Weakly-bound three-body nuclear systems: structure, reactions and astrophysical implications

PhD thesis

Jesús Casal Berbel

Departamento de Física Atómica, Molecular y Nuclear
Universidad de Sevilla

February 2016

Weakly-bound three-body nuclear systems: structure, reactions and astrophysical implications

(Sistemas nucleares de tres cuerpos débilmente ligados: estructura, reacciones e implicaciones astrofísicas)

Memoria para optar al título de Doctor en Física Nuclear

Jesús Casal Berbel

Dirigida por los Doctores

D. José Miguel Arias Carrasco
Dª. Manuela Rodríguez Gallardo

Departamento de Física Atómica, Molecular y Nuclear
Universidad de Sevilla

Febrero 2016

A mis padres

Y a Fran

Agradecimientos

Con esta memoria cierro una etapa marcada por cuatro años de trabajo y dedicación, que han dado sus frutos gracias al apoyo de un gran número de personas a las que debo mi más sincera gratitud. El desarrollo de este proyecto no habría sido posible sin la ayuda, en lo profesional y en lo personal, de todos aquellos cuya labor quiero reconocer en estas líneas. Resulta difícil plasmar en pocas palabras la importancia de cada conversación y cada gesto, y tengo que decir humildemente que me siento pequeño al estar rodeado de personas tan grandes.

En primer lugar quisiera reconocer la indispensable contribución de mis directores de tesis, Dr. José M. Arias Carrasco y Dra. Manuela Rodríguez Gallardo. De ellos he recibido una excelente formación, no sólo por los conocimientos que me han transmitido, sino también por su experiencia académica y profesional. Su atención, apoyo y confianza han servido como el motor fundamental de este trabajo. Quiero agradecer sus esfuerzos, su compromiso y su cercanía, que han facilitado el difícil camino que supone un doctorado. Gracias por las ideas, charlas y discusiones sobre el trabajo; por esas innumerables horas delante del ordenador ayudándome en los aspectos técnicos y estudiando los resultados.

Mi gratitud se hace extensible a todo el departamento. Durante estos años me he sentido cómodo e integrado, rodeado de personas de las que aprender y con las que compartir experiencias y vivencias. Tampoco puedo olvidar a aquellos que, estando fuera, han seguido formando parte del alma de este grupo. Sería injusto destacar unos nombres sobre otros, pues cada cual ha dejado su huella personal. Algunos han contribuido con su ayuda en el plano académico. Otros, con sus palabras de ánimo y sus buenos deseos. Dejo atrás una familia de compañeros con las que espero seguir teniendo contacto durante mi carrera investigadora.

Como parte de mi formación, he tenido la grata suerte de poder realizar dos estancias en el extranjero. Tuve la oportunidad de enriquecer mis conocimientos y de conocer a un grupo inigualable de personas. Mi viaje a Estados Unidos para trabajar con el profesor I. J. Thompson en el Laboratorio Nacional Lawrence Livermore fue una experiencia inolvidable. Le seguiría mi visita a la Universidad Libre de Bruselas bajo la tutela del profesor P. Descouvemont. Me siento muy agradecido por la atención recibida y la implicación de ambos con mi trabajo.

También quiero aprovechar la ocasión para dar las gracias a los profesores E. Garrido y A. Arazi por permitirme incluir en este trabajo algunos de los resultados preliminares de su investigación.

En el plano económico, quiero destacar que he podido realizar mi formación predoctoral gracias a la beca de Formación de Profesorado Universitario del Ministerio de Educación, Cultura y Deporte que he disfrutado durante estos años. La carrera profesional en investigación, especialmente en ciencia básica, no sería posible sin el apoyo económico de las instituciones. Sin embargo, la obsesión por el carácter aplicado de la investigación amenaza con relegar la ciencia básica a un lugar marginal dentro del panorama investigador. Debemos hacer un esfuerzo en reconocer y visibilizar la investigación fundamental, favoreciendo así el acceso a este campo a futuras promesas que podrían lograr, en los años venideros, avances verdaderamente importantes para la sociedad.

Dejando a un lado las formalidades, tengo que echar la vista atrás para reconocer que todo esto no habría sido posible sin el apoyo de mis padres. No sólo les debo mi vida y la posibilidad de haber realizado estudios superiores, sino que han demostrado una y otra vez a lo largo de mis años como estudiante y como doctorando que siempre están ahí para ayudarme en cada obstáculo. Os quiero y os doy las gracias por todo.

No puedo olvidarme de los amigos, la familia que elegimos para que forme parte de nuestras vidas. Gracias por nuestras reuniones en casa, por las risas y momentos felices; por esas charlas intrascendentes y disparatadas, y por aguantar mis excentricidades y mis cambios de humor. Todos, sin saberlo, habéis ayudado enormemente durante estos cuatro años.

Y por último, a Fran. Por todo y más.

Jesús

febrero 2016

Abstract

This PhD dissertation arises with the idea of studying nuclear systems of astrophysical interest. Understanding of nucleosynthesis processes requires a deep connection between nuclear physics and astrophysics. In general, the reaction networks describing the evolution in composition and energy production of different astrophysical scenarios rely on the properties of the involved nuclei. Reaction rates at stellar burning phases can be very slow, thus involving stable nuclei only. However, nucleosynthesis paths in explosive scenarios at the final stages of stellar evolution require also reactions with exotic nuclei far from stability.

Within this broad field, this work focuses on the structure of weakly-bound Borromean nuclei and the description of reactions involving them. Borromean nuclei are three-body systems whose binary subsystems are unbound. This is, for instance, the case of ^{9}Be ($\alpha+\alpha+n$). In order to describe properly the properties and dynamics of weakly-bound nuclei, a reasonable treatment of continuum states is required. However, the asymptotic behavior of continuum states for systems comprising several charged particles is not known in general. A possibility to address approximately this problem is the pseudo-state method, in which the system Hamiltonian is diagonalized in a basis of square-integrable functions. In this work, the analytical transformed harmonic oscillator (THO) basis serves as the main tool for this purpose.

Starting with a general introduction, the first chapter is intended to provide a brief overview regarding some recent advances and challenges in nuclear physics. Special attention is paid to halo nuclei, which consist of a core surrounded by one or more nucleons that form a diffuse nuclear cloud. Two-neutron halo nuclei such as ^{6}He ($\alpha + n + n$) and ^{11}Li (^{9}Li $+ n + n$) present a Borromean structure. The relevance of Borromean nuclei in astrophysics is discussed along a brief introduction to nucleosynthesis, focusing

on the case of radiative capture reactions. In order to describe three-body capture processes, a proper three-body model is required. In this regard, the formalisms used along this work are presented.

The bulk of this thesis is structured in three parts. In chapter 2, the analytical THO basis for three-body systems is introduced, and the computation of the Hamiltonian matrix elements is discussed. The formalism is applied to describe the structure of three Borromean systems comprising one, two and three-charged particles, respectively: the two-neutron halo nucleus ^{6}He, the weakly-bound ^{9}Be and the candidate for two-proton halo ^{17}Ne ($^{15}\mathrm{O} + p + p$). The eigenfunctions obtained upon diagonalization of the three-body Hamiltonian enable the evaluation of different observables, such as matter and charge radii or transition probabilities. The comparison with experimental data supports the robustness of the method in describing Borromean systems.

The three-body radiative capture reactions to produce these nuclei are studied in chapter 3. While the production of ^{6}He and ^{9}Be have been linked to the r-process in neutron rich environments, the formation of ^{17}Ne has been proposed to play a role in the rp-process. The production of Borromean nuclei in astrophysical environments has traditionally been studied as sequential processes. At low temperatures, however, the three particles may have no access to intermediate configurations and therefore they can fuse directly. This leads to an enhancement of the corresponding reaction rates at relatively low temperatures, which may have an impact on nucleosynthesis.

Reaction rates for three-body processes, which cannot be measured directly, carry an uncertainty related to the discrepancies between different theoretical approaches. An alternative procedure is proposed to estimate reaction rates from inclusive Coulomb breakup measurements. The method is tested for ^{11}Li, for which recent data on inclusive breakup data are available.

In chapter 4, direct reactions induced by three-body projectiles are studied within a four-body reaction framework. The continuum-discretized coupled-channel (CDCC) method is applied to describe the scattering of ^{9}Be on ^{208}Pb, ^{120}Sn and ^{27}Al at energies around the Coulomb barrier. Due to the weakly-bound nature of the projectile, continuum effects play an important role. The agreement with the available experimental data confirms the reliability of the method in describing reactions induced by three-body projectiles comprising more than one charged particle.

The main results and conclusion of this work are summarized in chapter 5, with solid remarks for future research. Preliminary calculations for the structure of ^{12}C and its formation via the famous triple-α process are presented in an additional chapter after the summary.

The document concludes with three formal appendixes which contain the mathematical derivations of some expressions and formulae presented throughout the main chapters. These appendixes are integral parts of this PhD thesis, since they include important results which have been developed along the doctoral period. They are presented in a compact manner at the end of the document so as not to obscure the main discussion thread in the chapters of this dissertation.

In addition to the physical and mathematical contents in this work, the computing aspects have been very important. A comprehensive three-body code has been developed to carry out calculations with the analytical THO basis. Subroutines from the FaCE code have been modified and integrated in the new code in order to enable the treatment of systems comprising two or three identical particles. The coupling-channel problem for reaction calculations has been solved using the FRESCO code, including coupling potentials generated externally. Original codes have also been developed for other general purposes, such as the computation of probabilities and cross section within the semiclassical Coulomb excitation theory or the generation of two- and three-dimensional wave-function probability plots.

Contents

List of Figures

List of Tables

Chapter 1

Introduction

While knowledge can create problems, it is not through ignorance that we can solve them.

Isaac Asimov

The present work covers a series of theoretical studies concerning the properties of three-body Borromean nuclei. These systems have changed our understanding of nucleosynthesis processes, acquiring a well-deserved position among the most studied nuclei over the past few years. A general overview, regarding the experimental and theoretical advances that have pushed forward our knowledge in nuclear physics, is given in section 1.1. Some general astrophysical questions concerning the origin of elements in the Universe are given in section 1.2. The theoretical models to describe the particular case of three-body systems are introduced in section 1.3, where the importance of continuum states is also discussed. In section 1.4, the description of direct reactions including continuum couplings is introduced. Finally, a brief outline is presented.

1.1 Background

The first studies on the atomic nucleus date back to the early 20th century, when Geiger and Marsden conducted the famous Rutherford experiment. The scattering of alpha particles on a gold target led Rutherford to formulate his atomic model, in which the nucleus contained almost all the atomic mass

in a tiny region compared to the size of the atom. Since then, every step towards a better understanding of the nuclear properties has brought new questions and motivations to carry out challenging experiments. The atomic nucleus provides a unique system to learn about the competition between the strong, weak and electromagnetic forces. As basic constituents of matter, understanding the nucleus structure and reaction mechanisms is essential for other fields, e.g. standard model and interaction theories, astrophysical questions such as nucleosynthesis, and a variety of medical and industrial applications.

In order to get reliable information from experiments carrying out nuclear reactions, theoretical models need to incorporate a detailed description of the interacting nuclei. The atomic nucleus, however, is a many-body system of strong-interacting particles. The strong interaction and the finite number of nucleons make difficult to address the problem by means of perturbative theories or statistical approaches, of great interest in other fields. This reveals that, in a quantum-mechanical perspective, the nucleus is one of the most challenging problems Nature has to offer.

While the chemical behavior of the atom is essentially determined by its atomic number Z defining the element, isotopes with different neutron number N may exhibit completely different nuclear properties. The nuclear chart[1] arranges the different isotopes according to their Z and N, out to the limits imposed by the neutron and proton driplines. Beyond them, no bound nuclei can exist. Among the more than three thousand known nuclei, only a few hundred are stable or have a half-life long enough to occur naturally. The remaining are known as exotic nuclei, and some of them appear as intermediate steps in the reaction networks that govern the evolution in composition and energy production in different astrophysical scenarios. In order to study exotic nuclei on Earth, they need to be artificially produced and characterized in Radioactive Ion Beam (RIB) facilities. Over the past decades, the advances in accelerator technologies, particle detectors and instrumentation for the production and detection of exotic nuclei have allowed nuclear physicists to explore regions of the nuclear chart far from the so-called valley of stability. Whenever novel techniques have been developed, new and often unexpected features have shown up. The experimental and

[1] Also referred to as Segrè chart. See, for instance, the updated database by the NNDC Brookhaven National Laboratory, `http://www.nndc.bnl.gov/chart/`.

theoretical efforts in this field are motivated by the necessity to assess the nuclear structure knowledge gained from stable nuclei, to explore the edges of the nuclear landscape, and to study the extremes of stability [1].

In an attempt to sort and classify nuclei, the Shell Model [2] was proposed in the 40s and developed in 50s by several physicists, most notably Eugene P. Wigner, Maria G. Mayer and Hans D. Jensen, who shared the 1963 Nobel Prize for their contributions. Searching the analogy with the atomic shell model, which describes the arrangement of electrons in an atom, in the nuclear shell model neutrons and protons fill successive layers according to specific ordering rules. A totally filled shell results in greater stability, so adding more nucleons decreases the binding energy of the system (and can potentially lead to an unstable nucleus). The numbers corresponding to closed shells received the name of magic numbers. Although the prevalence of the established magic numbers for stable nuclei is remarkable, the predictive capabilities of the Shell Model began to diminish when exotic nuclei came into play. Separation energies and spin-parity assignments suggested the disappearance of magic numbers and changes in the filling order for exotic nuclei, revealing that the simple ideas behind the periodic table in atomic physics were not sufficient to build up a similar picture in nuclear physics.

The complexity of the nuclear many-body problem has made nuclear physics a phenomena-driven research field. Discoveries in RIB facilities have revealed a substantial variety of exotic properties for nuclei far from stability. The theoretical efforts to describe these features have been mostly based on phenomenological principles. One of the observed features that have attracted more interest in the recent years is the appearance of nuclear halos for light nuclei close to the driplines. This term was introduced in 1969 [3] and established shortly thereafter. Halo nuclei consist of a core surrounded by one or more nucleons which are far from typical nuclear distances. When the binding energy of these nucleons is small, a significant part of the wave function describing its relative motion may define a diffuse nuclear cloud, which is typically called nuclear halo. The first experimental evidences for nuclear halos were found in the 80s, pointed out by an unexpectedly large dipole response for ^{11}Be [4], and large interaction cross sections for ^{6}He, ^{8}He and ^{11}Li [5]. Today, the ^{11}Be nucleus is understood as a one-neutron halo system on top of a ^{10}Be core, while ^{6}He and ^{11}Li are clear examples of two-neutron halos on ^{4}He and ^{9}Li, respectively. The nucleus of ^{8}He is

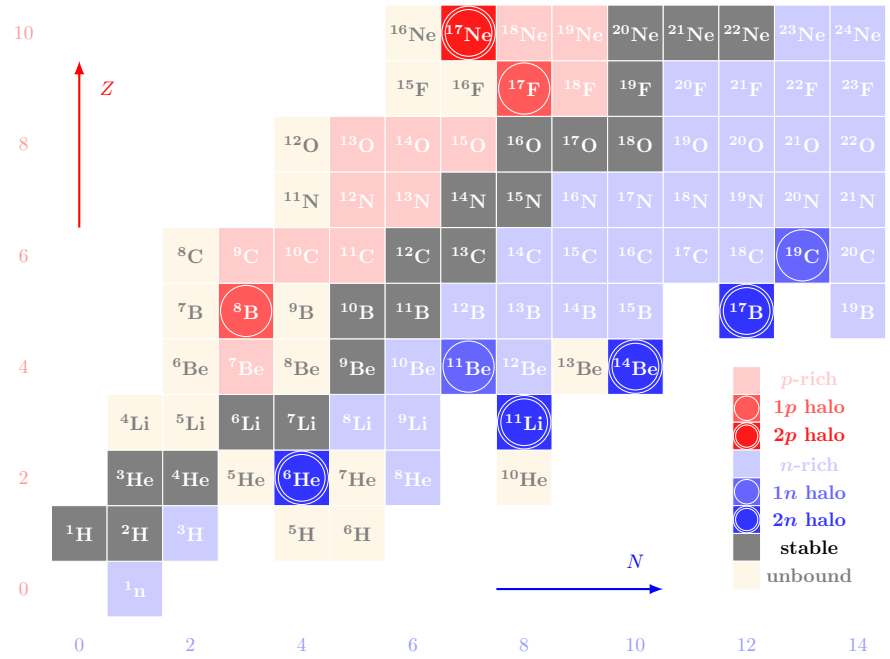

Figure 1.1: Nuclear chart for $Z \leq 10$, $N \leq 14$. Stable, unbound, neutron- and proton-rich nuclei are shown. One- and two-nucleon halo systems are highlighted with rings. See the legend for color reference.

proposed to have a four-neutron halo. The unexpectedly large interaction cross sections were associated to either large deformations or a spatially-extended matter distribution. Another experiment in 1992 [6] confirmed that the quadrupolar deformation of the ^{9}Li and ^{11}Li were quite similar, concluding that the diffuse neutron cloud was responsible for this large cross section. The properties of these nuclei and the mechanisms that govern nuclear reactions involving them have been extensively studied [7–11] and keep being the subject of many publications [12–14]. Other examples of halo nuclei are shown in Fig. 1.1, including the one-proton halo ^{8}B and the candidate for two-proton halo ^{17}Ne.

The case of two-nucleon halo systems, such as ^{6}He $(\alpha + n + n)$[2] or ^{11}Li (^{9}Li $+ n + n$), deserves special attention. They are what we call Borromean nuclei, or three-body systems whose binary subsystems are not bound [11]. The term Borromean is named after a Renaissance heraldic symbol consisting of three bound rings, but without bound pairs. This is schematically shown in Fig. 1.2. Other examples of three-body Borromean halo nuclei are ^{14}Be

[2] An α-particle is simply a ^{4}He nucleus.

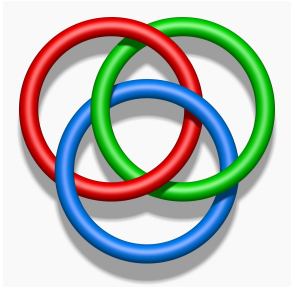

Figure 1.2: Borromean rings.

(^{12}Be$+n+n$) and ^{17}Ne (^{15}O$+p+p$). Well studied and characterized stable nuclei such as ^{9}Be ($\alpha+\alpha+n$) or ^{12}C ($\alpha+\alpha+\alpha$) have also a Borromean structure, so this feature is not restricted to exotic systems. The relevance of these systems in nucleosynthesis has motivated past and ongoing researchs (see Section 1.2).

From a theoretical perspective, the description of halo and Borromean systems can be addressed within few-body models, in which the internal degrees of freedom of the particles that compose the system can be neglected or simplified. One- and two-nucleon halo nuclei have been described in two- [15–18] and three-body [19–25] models, respectively, and the effect of core excitations on structure and reaction observables has also been studied [26, 27]. In general, systems far from stability are weakly-bound and exhibit a large breakup probability in nuclear reactions. In order to account for this effect, the theoretical models describing these systems need to include a proper description of continuum or scattering states. This is explained in detail in section 1.3.

Halo and Borromean nuclei are just a small piece within the nuclear landscape. The nuclear physics community has devoted enormous efforts to address several subjects of key importance to understand nuclear interactions and dynamics [28]. Nuclei far from stability enable to amplify and isolate particular features, helping to build up a unified theory of the nuclear matter and finite nuclei, from deeply- to weakly-bound systems, and from light to heavy elements. This objective requires a large network of research groups, working both in theory and experiments, to map the different features that appear at the very limits of the nuclear chart. The present contribution to the field addresses some specific questions that will be outlined at the end of this chapter.

1.2 Nucleosynthesis

The origin of nuclei in the Universe is one of the key questions in nuclear astrophysics. As a result of the extensive experimental and theoretical activity in the field, our current understanding of nucleosynthesis processes recognizes three main scenarios [29]: i) Big Bang nucleosynthesis (BBN), also called primordial nucleosynthesis, concerning nuclear reactions which occurred in the first few minutes of the Universe. ii) Hydrostatic equilibrium nucleosynthesis, or stellar nucleosynthesis. This covers the reactions which occur during the life of a star, providing the energy which prevents its gravitational collapse. iii) Explosive nucleosynthesis, involving more complex reactions at the final stages of stellar evolution, such as supernovae, X-ray bursts or neutron star mergers.

Primordial nucleosynthesis is one of the evidences supporting the Big Bang model. Observations of primitive astrophysical sites enable to deduce the primordial abundances of hydrogen (H, D), helium (^{3}He, ^{4}He) and lithium (^{7}Li) produced in the first nuclear reactions. Most of the reactions responsible for the production of these nuclei have been measured at the relevant energies, and the agreement between the BBN calculations and the observed abundances is remarkable [28]. The gradual transformation of these light elements into heavier ones is achieved through nuclear reactions in stars.

Stellar nucleosynthesis is driven by the balance between the gravitational contraction and an outward flow of energy produced by nuclear reactions. Stars burn H to produce He through the well known p-p chain and CNO cycles (see Ref. [29] for a detailed review). When the star exhausts its hydrogen fuel, gravity tends to collapse the system. This produces an enhancement of the star inner temperature, up to the point where He begins to fuse producing C and O. The process continues in a series of advanced burning phases involving C, O, Ne and finally Si. Beyond the synthesis of Fe, fusion reactions can no longer maintain the equilibrium against the gravitational collapse, leading to the final stage of the star. The rates at which the reactions occur depend on the temperature in the environment. At the (relatively) low temperatures during early stellar burning phases the rates can be very low, with nuclei existing for millions of years before being changed in a reaction. For this reason only stable nuclei are important. After the hydrogen burning, the formation of heavier nuclei needs to overcome

the instability gaps at mass numbers $A = 5$ and $A = 8$ [30]. This means that, within a stellar environment where mainly α-particles and nucleons are present, the formation of ^{9}Be or ^{12}C can proceed avoiding the unbound nuclei ^{5}He and ^{8}Be. At the helium burning phase of stars, the low neutron density makes the triple-α reaction for the formation of ^{12}C the main nucleosynthesis process [31]. Then, the α-particle capture on ^{12}C to produce ^{16}O is also considered to be crucial, as it occurs during the helium-burning phase and determines the abundance ratio between two elements which are fundamental for life: C and O. This process, in turn, influences the timescales of stellar evolution up to the final stages when the fuel burning ends. Despite the importance of the triple-α reaction, the production rate of such process has not yet been determined accurately (nor uniquely) for the entire temperature range relevant in astrophysics (see the relative differences in Refs. [32–36]). This is due to experimental problems to measure these processes as well as to discrepancies in the theoretical predictions about the structure of ^{12}C. Other reactions beyond O and C complete the cases of astrophysical interest, but it will not be discussed here. They account for the production of light elements via proton- and α-particle capture at thermal equilibrium conditions.

As heavier nuclei are formed, the Coulomb repulsion decreases drastically the capture cross sections. For this reason, charged-particle reactions at moderate stellar temperatures are not sufficient to explain the observed solar system abundances of nuclides with masses beyond $A \simeq 56$. It is therefore reasonable to assume that heavy nuclides can be synthesized by exposing lighter seed nuclei to a source of neutrons. About half of the element abundances between Fe and Bi are produced via slow neutron capture nucleosynthesis (s-process) during the hydrostatic burning phase of a star. Starting at iron seed nuclei, the s-process path runs close to the the valley of stability via a sequence of neutron captures and β-decays. This path will eventually reach ^{209}Bi, which is the most massive stable nuclide. Further neutron captures produce radioactive species that decay by α-particle emission, so Bi represents the termination point of the s-process. Neutrons are not stable[3], and they need to be produced during nuclear reactions in the stellar medium. Thus, the neutron flux for the s-process is small and cannot populate nuclei close to the driplines.

[3]The neutron has a lifetime of about ten minutes.

In more exotic, neutron-rich environments such as the cataclysmic events that follow the gravitational collapse of the star, the alternative rapid neutron capture nucleosynthesis (r-process) comes into play. Nucleosynthesis paths in explosive scenarios have the added complexity of requiring unstable nuclei. The networks of nuclear reactions to describe the evolution of classical novae, type Ia and type II supernovae or neutron stars involve thousands of nuclides [28, 37]. Although the site for the r-process is still unclear, the promising candidates are the neutrino-driven winds after core-collapse in type II supernovae [38, 39], prompt supernova explosions [40] or neutron star mergers [41]. In these neutron-rich environments, the formation of ^{9}Be and ^{6}He can proceed overcoming the instability gaps and affect the abundances of seed material for the r-process [42]. The process $\alpha + \alpha + n \rightarrow {}^{9}\mathrm{Be} + \gamma$ is key among the reactions involving light nuclides, since it provides an alternative path to ^{12}C via the capture of another α particle [37, 43], and it has been linked to the r-process in type II supernovae [37]. The reaction $\alpha + n + n \rightarrow {}^{6}\mathrm{He} + \gamma$ may have an impact on nucleosynthesis models for neutron star mergers [42].

It is interesting that the solar system abundances in the $A > 60$ range can be accounted for in terms of two extreme pictures, that is, by relatively low neutron densities achieved in the s-process and by very high neutron exposures characteristic of the r-process [44]. However, these processes have no access to the neutron-deficient[4] region in the nuclear chart. The path to reach these nuclides requires another type of reactions, the so-called rapid proton capture (rp-process) [45]. Explosive H and He burning at high temperatures can trigger the rp-process in Type I X-ray bursts. These are binary systems consisting of a red giant and a neutron star, where the neutron star accretes H-rich matter from the companion star. The proton flux is heated and compressed, leading the rp-process to potentially populate nuclides off the CNO cycle, i.e. Ne, F, Na [29, 45] via breakout reactions. Among the relevant reactions, the two-proton capture on ^{15}O to produce ^{17}Ne has been proposed as a key ingredient towards the production of heavier, neutron-deficient nuclei [46, 47].

Stellar models aiming to describe the evolution in composition, energy production and temperature of the different astrophysical environments rely on the knowledge of the reaction rates for the relevant processes. The direct

[4] Also commonly called proton-rich nuclei, although this term is not completely correct.

experimental measurement of the cross sections is, in principle, possible for two-body reactions, both for charged particles and neutrons. In many cases, however, reaction cross sections may not be measured directly. This may occur if the initial nucleus is short-lived [48], or when the capture process is a three-body reaction [49]. Theoretical models providing a reliable description of the system are then necessary. The formation of ^{6}He, ^{9}Be and ^{17}Ne, as in the case of ^{12}C, involve the description of a Borromean system. Radiative capture reactions for three-body Borromean nuclei have traditionally been studied as sequential processes [42, 49, 50]. For instance, in a first step towards the production of ^{12}C, two α-particles fuse to form ^{8}Be. This system is unbound but has a long enough lifetime to capture another α-particle producing ^{12}C. At low temperatures, however, the three particles may have no access to intermediate resonances and therefore they can fuse directly [34, 35]. A complete three-body formulation is needed to describe properly the reaction rates of such nuclei in the entire temperature range.

1.3 Three-body systems

In the case of Borromean nuclei, different approaches have been developed to describe structure and scattering observables [11]. Three-body models typically assume a simple cluster configuration, where the excitation of one of the particles, if applicable, can be taken into account [51]. The simplified three-body picture avoids some computational limitations behind more fundamental few-body *ab initio* approaches based on nucleon-nucleon interactions between all A constituents [52]. In turn, strict three-body models can be applied, from a practical purpose, to relatively heavier nuclei.

A common characteristic of exotic nuclei is their small separation energy and hence their large breakup probability in scattering processes. This can be understood as an excitation of the nucleus to unbound states that form a continuum of energies [53]. On the other hand, the synthesis of nuclei in stellar environments can be described as a decay from an unbound state of several particles that fuse together producing a bound system [54]. Both processes demand a reasonable treatment of continuum states.

In general, the treatment of unbound states of a quantum-mechanical system deals with the drawback that the corresponding wave functions are not square normalizable and their energies are not discrete values. Solving

this problem is a difficult task, especially as the number of charged particles increases, since the asymptotic behavior of continuum states is not known in general. Nevertheless, there are various procedures to address this problem such as the R-matrix method [24, 55, 56], not without difficulties. Another approach to solve the continuum problem consists in using the so-called discretization methods. These methods replace the actual continuum by a finite set of normalizable states, i.e., a discrete basis that can be truncated to a relatively small number of states providing a reasonable description of the system. Several discretization methods have been proposed [21, 55]. For instance, one can solve the Schrödinger equation in a box [54], being the energy level density governed by the size of the box. As this is larger, the level density increases but numerical problems begin to appear. Another method is the binning procedure, used traditionally in the continuum-discretized coupled-channels formalism [57]. In this method the continuum spectrum is truncated at a maximum energy and divided into a finite number of energy (or momentum) intervals or bins. For each bin, a normalizable state is constructed by superposition of the scattering states within that interval. This approach requires the calculation of unbound states with the correct asymptotic behavior. As mentioned above, the calculation of this asymptotic behavior for a three-body system with more than one charged particle is by no means an easy task.

An alternative method to obtain a discrete representation of the continuum spectrum is the so-called Pseudo-State (PS) method. This approach consists in diagonalizing the Hamiltonian of the system in a complete basis of square-integrable functions. The negative-energy solutions of that problem describe the bound states of the system, while positive-energy solutions are taken as a discrete representation of the continuum [58]. The PS method provides a unified description of bound, resonant and non-resonant continuum states in terms of discrete functions. A variety of bases have been proposed for two-body [15–17, 59] and three-body systems [19, 22, 23, 25], for which this method can be especially useful.

1.3.1 The Pseudo-State (PS) method

In order to describe three-body systems, Jacobi coordinates $\{\boldsymbol{x}_k, \boldsymbol{y}_k\}$ are introduced. The variable $\boldsymbol{x}_k$ is proportional to the relative coordinate between two particles and $\boldsymbol{y}_k$ is proportional to the distance from the center

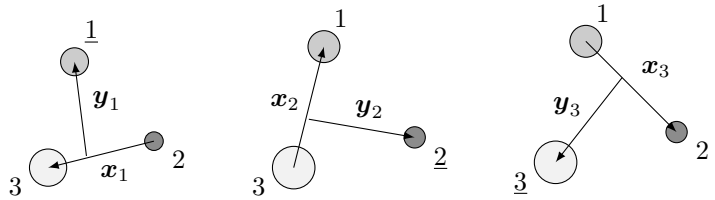

Figure 1.3: The three sets of scaled Jacobi coordinates.

of mass of the x-subsystem to the third particle, both with a scaling factor depending on their masses [21]. The label k identifies one the three possible Jacobi systems, as shown in Fig. 1.3. For convenience, the notation assumes that, for example, the Jacobi-$\underline{1}$ system corresponds to the system where the particles (2,3) are related by coordinate $\boldsymbol{x}_1$. From the Jacobi coordinates it is possible to define the hyperspherical coordinates $\{\rho, \alpha_k, \widehat{x}_k, \widehat{y}_k\}$, where the hyperradius (ρ) and the hyperangle (α_k) are given by

$$\rho = \sqrt{x_k^2 + y_k^2}, \tag{1.1}$$

$$\alpha_k = \tan\left(\frac{x_k}{y_k}\right), \tag{1.2}$$

and $\{\widehat{x}_k, \widehat{y}_k\}$ are the two-dimensional angular variables associated to $\{\boldsymbol{x}_k, \boldsymbol{y}_k\}$. Note that, while the hyperangle depends on k, the hyperradius is the same for the three Jacobi systems. More details about Jacobi and hyperspherical coordinates are shown in appendix A.1.

Using hyperspherical coordinates, the solutions of the Schrödinger equation in one of the Jacobi systems can be expanded as (k is not specified when it is fixed)

$$\phi_{nj\mu}(\rho, \Omega) = \rho^{-5/2} \sum_{\beta} \mathcal{R}^{j\mu}_{n\beta}(\rho) \mathcal{Y}_{\beta j\mu}(\Omega), \tag{1.3}$$

where n labels the eigenstate with associated eigenvalue ε_{nj}, $\Omega \equiv \{\alpha, \widehat{x}, \widehat{y}\}$ is introduced for the angular dependence and $\beta \equiv \{K, l_x, l_y, l, S_x, j_{ab}\}$ is a set of quantum numbers called channel. In this set, K is the hypermomentum, l_x and l_y are the orbital angular momenta associated with the Jacobi coordinates $\boldsymbol{x}$ and $\boldsymbol{y}$, respectively, l is the total orbital angular momentum ($\boldsymbol{l} = \boldsymbol{l_x} + \boldsymbol{l_y}$), S_x is the spin of the particles related by the coordinate $\boldsymbol{x}$, and j_{ab} results from the coupling $\boldsymbol{j_{ab}} = \boldsymbol{l} + \boldsymbol{S_x}$. If I denotes the spin of the third particle, which is assumed to be fixed, the total angular momentum j is given by $\boldsymbol{j} = \boldsymbol{j_{ab}} + \boldsymbol{I}$. The functions $\mathcal{Y}_{\beta j\mu}(\Omega)$ are states of good total

angular momentum j, expanded in Hyperspherical Harmonics (HH) $\Upsilon^{l_x l_y}_{Klm}$ as [11]

$$\mathcal{Y}_{\beta j\mu}(\Omega) = \left\{ \left[\Upsilon^{l_x l_y}_{Klm} \otimes \kappa_{S_x} \right]^{j_{ab}} \otimes \xi_I \right\}^{j}. \tag{1.4}$$

This expression follows the angular momentum couplings described in the preceding lines, being κ and ξ the spin functions. The HH are the eigenfunctions of the hypermomentum operator $\widehat{K}$, as shown in appendix A.2. The hyperradial functions $\mathcal{R}^{j\mu}_{n\beta}(\rho)$ are expanded in a basis of square-integrable functions,

$$\mathcal{R}^{j\mu}_{n\beta}(\rho) = \sum_{i=0}^{i_{\max}} C_n^{i\beta j} U_{i\beta}(\rho), \tag{1.5}$$

where i denotes the hyperradial excitation, so that $(i_{\max}+1)$ represents the number of hyperradial functions included for each channel, and $C_n^{i\beta j}$ are the diagonalization coefficients. Inserting Eq. (1.5) in Eq. (1.3), the eigenstates of the system are given by

$$\phi_{nj\mu}(\rho,\Omega) = \rho^{-5/2} \sum_{\beta} \sum_{i=0}^{i_{\max}} C_n^{i\beta j} U_{i\beta}(\rho) \mathcal{Y}_{\beta j\mu}(\Omega). \tag{1.6}$$

The hyperspherical formalism is an ideal tool to describe three-body Borromean systems [11, 21], since it considers the three components on an equal footing assuming no specific two-body structure. In principle, expansion (1.6) includes an infinite number of channels β, which account for all possible system configurations. However, the Hamiltonian diagonalization is performed in a truncated basis with a maximum hypermomentum K_{max}, which limits the number of channels included in the calculations and has to be large enough to provide converged results. Different PS methods differ in the basis choice. Different bases can be found in the literature, each one with its advantages and drawbacks. The results and the properties of the system are not dependent on the basis choice, provided the model space is large enough.

1.3.2 Three-body Hamiltonian

The specific properties of a system are described by its Hamiltonian. Using Jacobi coordinates, it is possible to express the Hamiltonian of a three-body

system as

$$\widehat{\mathcal{H}}(\boldsymbol{x},\boldsymbol{y}) = \widehat{T}(\boldsymbol{x},\boldsymbol{y}) + \widehat{V}(\boldsymbol{x},\boldsymbol{y}), \tag{1.7}$$

where the center of mass term has been subtracted and $\widehat{T}$, $\widehat{V}$ are the typical kinetic energy and potential operators. The kinetic energy has two terms, each one that can be separated into a radial part and an angular part,

$$\widehat{T}(\boldsymbol{x},\boldsymbol{y}) = \widehat{t}_x(\boldsymbol{x}) + \widehat{t}_y(\boldsymbol{y}) = -\frac{\hbar^2}{2m}\left[\left(\frac{1}{x}\frac{d^2}{dx^2}x - \frac{\widehat{l}_x^2}{x^2}\right) + \left(\frac{1}{y}\frac{d^2}{dy^2}y - \frac{\widehat{l}_y^2}{y^2}\right)\right], \tag{1.8}$$

where $\widehat{l}_x$ and $\widehat{l}_y$ are the angular momentum operators associated to $\boldsymbol{x}$ and $\boldsymbol{y}$, and m is a normalization mass which, for nuclear systems, is usually taken as the atomic mass unit. It is convenient, however, to write the Hamiltonian in hyperspherical coordinates. In appendix B.1 it is shown that the kinetic energy operator can be written equivalently as

$$\widehat{T}(\rho,\Omega) = -\frac{\hbar^2}{2m}\left[\frac{\partial^2}{\partial\rho^2} + \frac{5}{\rho}\frac{\partial}{\partial\rho} - \frac{1}{\rho^2}\widehat{K}^2(\Omega)\right], \tag{1.9}$$

where $\widehat{K}$ represents the hypermomentum operator. This expression is a specific case of the more general N-dimensional problem [21].

Concerning the potential $\widehat{V}$, the general expression for a three-body system can be written by means of binary terms as fundamental interactions,

$$\widehat{V}(\rho,\Omega) = \widehat{V}_{12} + \widehat{V}_{13} + \widehat{V}_{23}, \tag{1.10}$$

each one including different contributions depending on the particles involved. Calling r the modulus of the coordinate relating two particles, the general binary interaction has the form

$$\widehat{V}_{ij} = V_c(r) + V_{so}(r)\widehat{SO} + V_q(r)\widehat{Q} + V_t(r)\widehat{\mathcal{T}} + V_{ss}(r)\widehat{SS}, \tag{1.11}$$

where

- $V_c(r)$ is the central term,
- $\widehat{SO}$ and $V_{so}(r)$ are the spin-orbit operator and its radial form factor,
- $\widehat{Q}$ and $V_q(r)$ are the tensor operator and the radial form factor for a deformed potential if the excitation of one of the particles is considered,

- $\widehat{\mathcal{T}}$ and $V_t(r)$ are the standard tensor operator and the radial form factor for the nucleon–nucleon (NN) interaction, and
- $\widehat{SS}$ and $V_{ss}(r)$ are the spin-spin operator and its corresponding radial dependence.

Preceding expressions assume that the binary interactions V_{ij} are local, and they are adjusted to reproduce the phenomenology of the two-body subsystems, when experimental data is available. However, since three-body models are an approximation to the full many-body problem, including only binary interactions may lead to deviations from the experimental three-body energies [23, 51, 54]. Therefore, it is usual to add a structureless hyperradial three-body force V_{3b} in Eq. (1.10), whose parameters can be fixed to adjust the energy of the system without distorting its structure. Specific forms of this phenomenological force will be shown in the following chapters.

1.3.3 Pauli blocking

The solution of the Schrödinger equation,

$$\left(\widehat{T} + \widehat{V}_{12} + \widehat{V}_{13} + \widehat{V}_{23} + V_{3b} - \varepsilon_{nj}\right) \phi_{nj\mu} = 0, \tag{1.12}$$

does not take any account of Pauli blocking effects. In general, some components of the wave function would disappear under full antisymmetrization of the A–nucleon system. This problem is a common issue in few-body theories, where the Pauli principle can only be treated approximately.

The antisymmetrization of the full many-nucleon system would lead to exchange terms which are nonlocal in the two-body subsystem relative coordinates [60, 61]. These terms produce an l–dependence of the local phase-equivalent potentials V_{ij} included in Eqs. (1.10), (1.12), which accounts for the Pauli principle within the two-body subsystems. This is usually needed for the binary local potentials to be able to reproduce the two-body experimental phase shifts. However, the l–dependent local interactions typically have unphysical bound states that represent already occupied states of one of the clusters. An approximate way to deal with the antisymmetrization problem is to remove these two-body forbidden states prior to solving the three-body equation. For this, several different methods have been developed [24].

- *Projection operators.* It consists in projecting out the two-body unphysical states. The three-body Schrödinger equation is then solved within the allowed subspace. This can be done by using the pseudo-potential method [62] or directly with nonlocal projection operators [63].

- *Phase-equivalent potential.* It is possible to introduce an auxiliary repulsive interaction in the partial components of the local potential between clusters where forbidden states appear. The interaction defined in this way is fitted to reproduce the experimental phase shifts. Due to its application to systems formed by a core surrounded by valence nucleons which cannot enter the occupied core states, this method is typically called *repulsive core*.

- *Supersymmetric transformation.* For a potential having a two-body forbidden state, it is possible to use a supersymmetric transformation [64] to obtain a spectrally equivalent interaction without this state but with a repulsive singularity at the origin.

- *Adiabatic projection.* Projecting onto the hyperangular part of the wave function, it is possible to write down an adiabatic equation involving a hyperradial coupling matrix, which contains both the potential and centrifugal terms. Its eigenvalues define the adiabatic energy surfaces or adiabatic potentials. Those associated with unphysical bound states can be projected out, providing an effective coupling matrix without forbidden states [65].

These approaches provide essentially the same results when computing three-body bound states [11, 66], but may show differences for continuum-dependent observables like transition probability distributions [24]. This is a price one has to pay in order to simplify the complex many-body problem by a much simpler few-body picture. In some cases, a clever choice of the Jacobi set to describe the system simplifies the antisymmetrization between identical particles by removing components of the wave function with forbidden angular momenta. This will be clarified with specific examples in chapter 2.

1.4 Continuum-Discretized Coupled Channels

The Continuum-Discretized Coupled-Channel (CDCC) method [57, 67] was developed as a natural extension of the Coupled-Channel (CC) method, widely used to study the effect of (bound) excited states on reactions with stable nuclei. The explicit inclusion of states that are strongly coupled to the ground state of the system enables to evaluate the relevance of inelastic channels, in which either the projectile or the target ends up in an excited state. The influence of excitations on the elastic channel can also be studied. In the case of weakly-bound projectiles, continuum couplings may play an important role, and therefore the CC method cannot be applied directly. The CDCC method is an extension of the CC method to include continuum states in the formalism. Roughly speaking, the CDCC method consists in expanding the total wave function in a basis of projectile or target internal states, including both bound and continuum states. The method was originally introduced to address deuteron breakup in a three-body model, $(p + n) + X$. Typical examples that can be addressed with the CDCC method are reactions induced by ^{6}Li, by the proton-rich nucleus ^{8}B and by the neutron-rich nuclei ^{11}Be or ^{19}C, which contain only a single bound state characterized by a small binding energy. Then, the applicability of the method relies on a good description of the states (bound and continuum) of the involved nuclei.

The CDCC approach, however, solves an effective few-body problem approximately, via the expansion of the full wave function in a selected set of continuum wave functions of a given subsystem Hamiltonian. It was introduced as a practical way of solving the complicated scattering problem, avoiding the exact Faddeev equations [68] for the wave function components or the equivalent Alt, Grassberger and Sandhas (AGS) equations for the transition operators [69]. It has been argued that the CDCC solution approaches the exact (Faddeev or AGS) solution as the model space to describe the internal states is increased, but still some differences may appear. For $^{11}\mathrm{Be}+p$, the three-body CDCC based on a pn or $^{10}\mathrm{Be}+n$ expansion showed a good agreement with the exact AGS solutions only in certain angular regions depending on the basis choice [70]. In the case of reaction induced by weakly-bound projectiles on heavy, deeply-bound targets with large gaps between their ground state and the first excited state, the total wave function

is expanded in internal states of the projectile and this problem is typically ignored. But a word of caution is required for reactions where this separation is not evident.

Considering an N-body projectile colliding with a structureless target, the total scattering wave function $(N+1)$ will be solution of

$$[\mathcal{H} - E]\Psi^{(+)}_{\boldsymbol{K}}(\{\boldsymbol{r}_q\}, \boldsymbol{R}) = 0, \tag{1.13}$$

where $\boldsymbol{R}$ represents the projectile-target relative motion, $\{\boldsymbol{r}_q\}$ are the $(N-1)$ internal coordinates describing the projectile, and $\boldsymbol{K}$ is the incident wave vector in the center of mass frame. The total Hamiltonian is given by

$$\widehat{\mathcal{H}} = \widehat{T}_R + \widehat{U}_{pt} + \widehat{h}, \tag{1.14}$$

being $\widehat{T}_R$ the kinetic energy operator associated to the projectile-target relative motion and $\widehat{h}$ the internal Hamiltonian describing the projectile. The term $\widehat{U}_{pt}$ is the interaction between projectile and target, which depends on the position of the N particles with respect to the center of mass of the target, $\{\boldsymbol{R}_i\}$. It is assumed that each particle i interacts with the target through a potential $V_{it}(\boldsymbol{R}_i)$, which implies

$$\widehat{U}_{pt} = \sum_{i=1}^{N} V_{it}(\boldsymbol{R}_i). \tag{1.15}$$

Here, $V_{it}(\boldsymbol{R}_i)$ can be taken as the optical potential describing the elastic scattering for the i-target subsystem. These are typically central potentials with imaginary parts that account for the absorption from the elastic channel. Therefore, they describe implicitly the possible excitations of the target due to the interaction with each projectile component i. The projectile Hamiltonian $\widehat{h}$ must satisfy

$$\widehat{h}\phi_{nj\mu} = \varepsilon_{nj}\phi_{nj\mu}, \tag{1.16}$$

where $\phi_{nj\mu}$ are the projectile states labeled by its angular momentum j and corresponding projection μ. Notice that index n assumes implicitly a discrete representation. For simplicity, $w \equiv \{nj\mu\}$ is introduced to denote the states with definite labels. The projectile collides with the target being initially in a state ϕ_ω, that will be strongly distorted by the projectile-target interaction.

The solutions of Eq. (**??**) must reflect the nature of a scattering process, and therefore have the asymptotic form[5]

$$\Psi^{(+)}_{\boldsymbol{K},\omega}\left(\{\boldsymbol{r}_q\},\boldsymbol{R}\right) = e^{i\boldsymbol{K}\cdot\boldsymbol{R}}\phi_\omega + \{\text{outgoing waves}\}, \tag{1.17}$$

where the second term on the right side will be a linear combination of scattered spherical waves in the different states $\phi_{\omega'}$ accessible to the projectile. The coefficients in that expansion are the scattering amplitudes and determine the cross sections.

System wave functions for a definite initial state $\phi_\omega = \phi_{nj\mu}$ and total angular momentum $\boldsymbol{J} = \boldsymbol{j} + \boldsymbol{L}$, where $\boldsymbol{L}$ is the orbital angular momentum associated to the relative motion, can be expanded as

$$\Psi^{JM}_{Lnj}\left(\{\boldsymbol{r}_q\},\boldsymbol{R}\right) = \sum_{L'n'j'} \frac{i^L}{R}\chi^J_{Lnj,L'n'j'}(R)\left[Y_{L'}(\widehat{R})\otimes\phi_{n'j'}(\{\boldsymbol{r}_q\})\right]^{JM}, \tag{1.18}$$

which assumes an expansion in terms of excited states of the projectile. Defining a channel wave function

$$\Phi^{JM}_{Lnj}(\widehat{R},\{\boldsymbol{r}_q\}) = \left[Y_L(\widehat{R})\otimes\phi_{nj}(\{\boldsymbol{r}_q\})\right]^{JM}, \tag{1.19}$$

and introducing $c \equiv \{Lnj\}$, Eq. (1.18) can be written as

$$\Psi^{JM}_{c}\left(\{\boldsymbol{r}_q\},\boldsymbol{R}\right) = \sum_{c'} \frac{i^L}{R}\chi^J_{c,c'}(R)\Phi^{JM}_{c'}(\widehat{R},\{\boldsymbol{r}_q\}). \tag{1.20}$$

This notation is introduced to distinguish between ω, that represents the state of the projectile with fixed projection μ, and c, which is the reaction channel associated to ω that includes also the relative angular momentum L. Inserting expansion (1.20) in the Schrödinger equation leads to the set of coupled equations for the radial functions

$$\begin{aligned}\Big[-\frac{\hbar}{2m_r}\left(\frac{d^2}{dR^2}-\frac{L(L+1)}{R^2}\right)+E_\omega-E\Big]\chi^J_{c,c}(R)\\ +\sum_{c'} i^{L'-L}V^{JM}_{c,c'}(R)\chi^J_{c,c'}(R)=0,\end{aligned} \tag{1.21}$$

[5]The plane wave to describe the relative motion at large distances is valid only in absence of Coulomb interaction between projectile and target. The general case involves additional phase factors.

where E_ω is defined from ε_{nj} by subtracting the ground state energy, and m_r is the projectile-target reduced mass. In this expression, $V^{JM}_{c,c'}(R)$ are the coupling potentials that contain all the information related to the projectile internal states,

$$V^{JM}_{c,c'}(R) = \langle \Phi^{JM}_c | \widehat{U}_{pt} | \Phi^{JM}_{c'} \rangle. \tag{1.22}$$

The coupled-channel problem given by Eq. (1.21) must be solved for positive scattering energies $E > 0$. At large distances, the radial functions for open channels ($E > E_\omega$) are given by a combination of incoming ($H^{(-)}_c$) and outgoing ($H^{(+)}_c$) Coulomb functions [71],

$$\chi^J_{c,c'}(R) \longrightarrow \frac{i}{2}\left[H^{(-)}_c(K_cR)\delta_{c,c'} - S^J_{c,c'}H^{(+)}_c(K_cR)\right], \tag{1.23}$$

where c and c' refer to the entrance and exit channels, respectively. Here $\boldsymbol{K}_c$ is the wave vector and $S^J_{c,c'}$ is the scattering matrix. The coupled equations have to be integrated up to a maximum distance R_{max}, which has to be large enough before matching with the asymptotic form to extract the S-matrix. Convergence with respect to this parameter must be checked. Then, elastic, inelastic, and breakup cross sections are derived from the scattering matrices. A detailed review is available in Refs. [72–75].

Note that $\Psi^{JM}_c(\{\boldsymbol{r}_i\}, \boldsymbol{R})$ are not the general solutions of the scattering problem, but solutions for a given entrance channel and total angular momentum. The actual solutions of Eq. (1.13) will be a combination of these wave functions,

$$\Psi^{(+)}_{\boldsymbol{K},\omega}(\{\boldsymbol{r}_q\}, \boldsymbol{R}) = \sum_c \sum_{JM} \mathcal{C}^{JM}_c(\boldsymbol{K})\Psi^{JM}_c(\{\boldsymbol{r}_i\}, \boldsymbol{R}), \tag{1.24}$$

where the initial state ω is fixed. This means that the sum over entrance channels c is equivalent to a summation over L only. Coefficients $\mathcal{C}^{JM}_c$ are obtained with the condition that, in absence of interactions, Eq. (1.24) must reduce to the expansion of a plane wave times the initial state. For simplicity, let assume that these coefficients are known. Expanding explicitly the states Ψ^{JM}_c, the previous scattering solution with the asymptotic conditions (1.23) is given by

$$\Psi^{(+)}_{\boldsymbol{K},\omega}\left(\{\boldsymbol{r}_q\},\boldsymbol{R}\right) = \sum_c \sum_{JM} \mathcal{C}_c^{JM}(\boldsymbol{K}) \left[\sum_{c'} \frac{i^L}{R} \Phi_{c'}^{JM}(\widehat{R},\{\boldsymbol{r}_q\}) \right.$$
$$\left. \times \frac{i}{2}\Big(H_c^{(-)}(K_c R)\delta_{c,c'} - S^J_{c,c'} H_{c'}^{(+)}(K_{c'}R) \Big) \right]. \qquad (1.25)$$

This expansion remains to be compared with the general solutions introduced by Eq. (1.17),

$$\Psi^{(+)}_{\boldsymbol{K},\omega}\left(\{\boldsymbol{r}_q\},\boldsymbol{R}\right) = e^{i\boldsymbol{K}\cdot\boldsymbol{R}}\phi_\omega + \sum_{\omega'} f_{\omega',\omega}(\theta)\phi_{\omega'} e^{i\boldsymbol{K}'\cdot\boldsymbol{R}}. \qquad (1.26)$$

For that, the channel wave functions $\Phi_{c'}^{JM}$ have to be decoupled, the explicit expressions of the Coulomb functions $H_c^{(-)}$ and $H_{c'}^{(+)}$ are required, and coefficients $\mathcal{C}_c^{JM}$ need to be known. The general expression for the angular-dependent scattering amplitude[6] $f_{\omega',\omega}(\theta)$ to the projectile state ω' from initial state ω can be written as

$$f_{\omega'\omega}(\theta) = \delta_{\omega'\omega} F_{\rm coul}(\theta) + \sum_{L'} A^{L'}_{\omega'\omega} P_{L'}^{\mu'-\mu}(\cos\theta), \qquad (1.27)$$

where $F_{\rm coul}(\theta)$ is the Rutherford amplitude for pure Coulomb scattering (with no $e^{2i\sigma_0}$ factor),

$$F_{\rm coul}(\theta) = -\frac{\eta}{2K} \frac{\exp(-2i\eta\ln(\sin\theta/2))}{\sin^2\theta/2}, \qquad (1.28)$$

η is the Sommerfeld parameter and $A^{L'}_{\omega'\omega}$ are the Legendre coefficients of $P_{L'}^{\mu'-\mu}(\cos\theta)$. These coefficients are given by

$$A^{L'}_{\omega'\omega} = \sum_{LJ} \langle L0j\mu|J\mu\rangle \langle L' M'_L j'\mu'|J(M'_L+\mu')\rangle \ \frac{4\pi}{K}\sqrt{\frac{K'}{K}} \qquad (1.29)$$
$$\times\, e^{i(\sigma_L-\sigma_0)} e^{i(\sigma'_{L'}-\sigma'_0)} \left(\frac{i}{2}\right) \left[\delta_{c',c} - S^J_{c',c}\right] \sqrt{\frac{2L+1}{4\pi}} Y_{\rm coef}(L', M'_L),$$

[6] The scattering amplitudes depend, in general, on both spherical angles (θ,φ). When the colliding nuclei have no spin or the corresponding interaction are spin-independent, then scattering process possesses azimuthal symmetry and the scattering amplitude depends only on θ.

where $Y_{\rm coef}(L, M_L)$ is the coefficient of $P_L^{|M_L|}(\cos\theta)e^{iM_L\phi}$ in $Y_L^{M_L}(\theta,\phi)$, $\sigma_L = \arg\left[\Gamma(1+L+i\eta)\right]$ is the Coulomb phase shift, and (c, c') refer to the entrance and exit channels associated to initial and final states (ω, ω'), respectively. The differential cross section is obtained in terms of the scattering amplitudes in Eq. (1.27) as

$$\frac{d\sigma(\theta)}{d\Omega} = \frac{1}{2j+1}\sum_{\mu'\mu}|f_{\mu'\mu}(\theta)|^2. \tag{1.30}$$

Note that, in the previous equation, ω has been replaced by μ, as the remaining labels nj are fixed. Thus, it requires only a summation over the projections. The S-matrix elements can also be used to directly calculate the integrated cross sections

$$\sigma_{n'}(E) = \frac{4\pi}{K^2}\frac{K'}{K}\sum_{JLL'}\frac{2J+1}{2j+1}\left|S^J_{Lnj,L'n'j'}\right|^2. \tag{1.31}$$

This expression provides directly the inelastic scattering from the initial state nj to a final state $n'j'$. In the case of excitations to unbound states, which represents the breakup of the projectile, the specific cross section to a single continuum-discretized state has no physical meaning. However, the total breakup cross-section can be approximated by the contribution of all continuum states as

$$\sigma_{BU}(E) = \sum_{n'}\sigma_{n'}(E). \tag{1.32}$$

Previous expressions assume a process in which the target has no spin and there is no particle transfer between projectile and target. More general expressions can be found in Ref. [73].

This work is structured as follows. Chapter 2 introduces the analytical transformed harmonic oscillator (THO) basis to describe three-body systems using pseudo-states (PS). The method is applied to ^{6}He, ^{9}Be and ^{17}Ne (comprising one, two and three charged particles, respectively), for which structure observables are calculated. The radiative capture reaction rates for these systems are obtained in chapter 3. Since reaction rates have an important uncertainty related to the discrepancies in the different theoretical approaches, an alternative procedure to estimate them from inclusive breakup measurements is proposed. The method is tested for ^{11}Li, for which data on inclusive breakup has been measured recently. In chapter 4, the THO method is applied to describe reactions induced by three-body projectiles, focusing on the ^{9}Be case. Finally, chapter 5 summarizes the main results of this work and establishes an outlook for future research.

An additional chapter, regarding the structure and formation of ^{12}C, is presented after the summary. This is a work in progress whose final conclusions have not yet been inferred. The document ends with three appendixes, which supplement the expressions and mathematical derivations included in the main chapters. They show important results that are presented at the end of the document so as not to obscure the discussion thread.

Chapter 2

Description of three-body Borromean systems

It seems to be one of the fundamental features of nature that fundamental physical laws are described in terms of a mathematical theory of great beauty and power.

Paul Dirac

In this chapter, the main features of the theoretical formalism used throughout the work is presented. First, the analytical Transformed Harmonic Oscillator (THO) basis is introduced. Then, expressions for the corresponding Hamiltonian matrix elements in the THO basis are shown. Finally, the calculation of different observables in the Pseudo-State (PS) basis is discussed, and the relevant expressions for the matter radius, charge radius and electromagnetic transition probabilities between states are obtained. The formalism is applied to different cases of astrophysical interest: ^{6}He, ^{9}Be and ^{17}Ne.

2.1 The analytical transformed harmonic oscillator (THO) basis

The Transformed Harmonic Oscillator (THO) basis is based on a Local Scale Transformation (LST) of the Harmonic Oscillator (HO) functions. The

transformation is chosen to change the Gaussian asymptotic behavior of the HO functions into an exponential decay, which is the known behavior for physical bound systems. This relation is given by

$$U_{i\beta}^{\mathrm{THO}}(\rho) = \sqrt{\frac{ds}{d\rho}} U_{iK}^{\mathrm{HO}}[s(\rho)], \tag{2.1}$$

being $s(\rho)$ the transformation which provides the desired asymptotic behavior. As originally developed, this transformation was defined so that from the HO ground state one could recover the ground state of the system under study [76]. This provided a numerical transformation. By construction, the numerical THO reproduced the ground state of the system, independently on the size of the basis. The method was applied to two-body [16, 77, 78] and later to three-body systems [23, 79] in structure and reaction calculations. A different approach consists in defining an analytic LST, which presents several advantages over the numerical THO: i) The previous knowledge of the ground state of the system is not required. ii) The analytical form can be easily implemented in numerical codes. iii) The parameters of the transformation govern the radial extension of the THO basis functions. The analytical form of the transformation was proposed by Karataglidis *et al.* [80],

$$s(\rho) = \frac{1}{\sqrt{2}b} \left[\frac{1}{\left(\frac{1}{\rho}\right)^{\xi} + \left(\frac{1}{\gamma\sqrt{\rho}}\right)^{\xi}} \right]^{\frac{1}{\xi}}, \tag{2.2}$$

depending on parameters ξ, γ, and the oscillator length b. The role of the parameter ξ is related to the rate at which the analytic form of the LST deviates from the linear behavior at $\rho \to 0$. Previous works found a very weak dependence of the results on this parameter. It is then customary to fix it to $\xi = 4$. The HO hyperradial variable s is dimensionless according to the transformation defined by Eq. (2.2). In this way, b is taken as another parameter of the transformation. Note that the THO hyperradial wave functions depend, in general, on all the quantum numbers included in a channel β, however the HO hyperradial wave functions only depend on the hypermomentum K (see appendix A.3). This analytical transformation provides a suitable representation of bound and unbound states to calculate structure and scattering observables. The method was applied first to de-

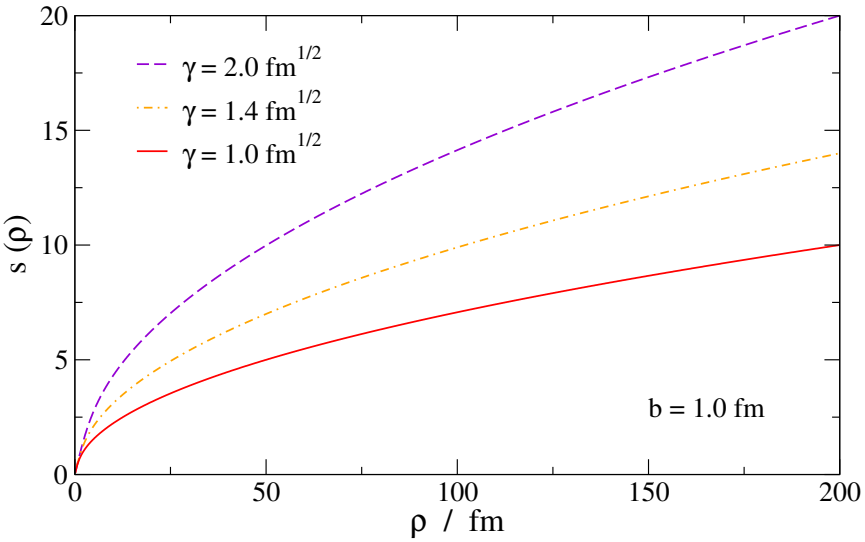

Figure 2.1: Analytic LST for three different values of the γ parameter, keeping the oscillator length fixed to $b = 1$ fm. As γ decreases, a given value of $s(\rho)$ corresponds to a larger hyperradius.

scribe two-body systems [17, 18], and it is generalized here for three-body problems. Using the transformation defined by Eq. (2.1), the basis states in hyperspherical coordinates are given by

$$\psi^{\mathrm{THO}}_{i\beta j\mu}(\rho,\Omega) = \rho^{-5/2} U^{\mathrm{THO}}_{i\beta}(\rho)\mathcal{Y}_{\beta j\mu}(\Omega), \tag{2.3}$$

where $\mathcal{Y}_{\beta j\mu}$ are states of good total angular momentum j given by Eq. (1.4). The previous expression, together with the general Eq. (1.6), provide the following system wave function after diagonalization of the three-body Hamiltonian:

$$\phi_{nj\mu}(\rho,\Omega) = \sum_{\beta}\sum_{i=0}^{i_{\max}} C_n^{i\beta j}\psi^{\mathrm{THO}}_{i\beta j\mu}(\rho,\Omega). \tag{2.4}$$

The function $s(\rho)$ behaves asymptotically as $\dfrac{\gamma}{b}\sqrt{\dfrac{\rho}{2}}$ and hence the analytical THO hyperradial wave functions obtained behave at large distances as $\exp\left(-\gamma^2\rho/2b^2\right)$. Therefore, the ratio γ/b governs the asymptotic behavior of the THO functions: as γ/b increases, the hyperradial extension of the basis decreases and some of the eigenvalues obtained by diagonalizing the Hamiltonian explore higher energies [17]. That is, γ/b determines the density

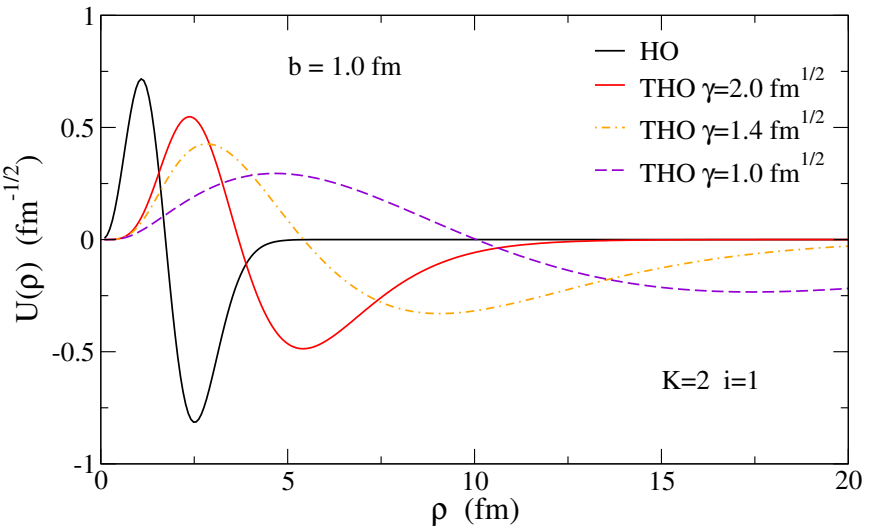

Figure 2.2: Hyperradial THO functions corresponding to analytical transformations with different γ parameters, keeping $b = 1$ fm. The original HO function is also shown. It is clear that the asymptotic behavior of the THO functions is an exponential decay, while that of the original HO function is Gaussian. As the parameter γ decreases, the THO functions explore larger distances.

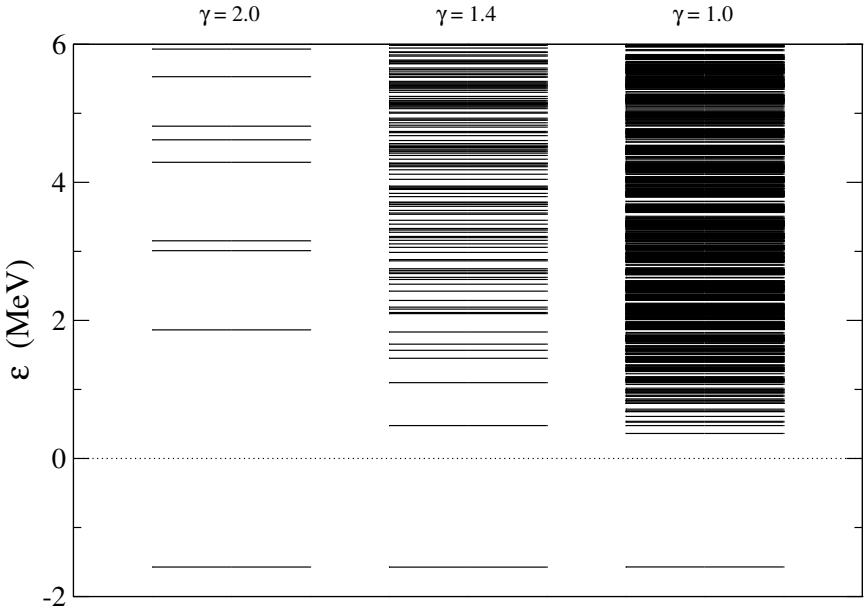

Figure 2.3: PS energy spectra for a given system and j^π configuration, as a function of the γ parameter, keeping b fixed. The only negative eigenvalue corresponds to a bound state, and the positive energy solutions are a representation of the continuum in the analytical THO basis. The level density close to the break-up threshold is strongly dependent on the γ parameter.

of PSs as a function of the energy. This allows to select an optimal basis depending on the observable of interest. In Figs. 2.1 and 2.2 the analytical form of the transformation and the corresponding extension of the hyperradial basis functions are shown for different values of the γ parameter, fixing the oscillator length b to 1 fm. For comparison, a HO function is also shown in Fig. 2.2. As an example, in Fig. 2.3, the resulting PS energy spectra for a given system are shown. The PS level density is very different for different values of these parameters, and a good γ/b choice can reduce noticeably the basis size needed to achieve converged calculations.

It is worth mentioning that the role of the ratio γ/b is somehow equivalent to the size of a box when solving the Schrödinger equation with box boundary conditions. The level density in that case is proportional to the size of the box. However, very large boxes lead typically to numerical instabilities solving the equation, so achieving large level densities at low energies can be a problem [54]. This limitation is absent when using the analytical THO method to solve the problem.

2.1.1 Hamiltonian matrix elements

Diagonalization of the three-body Hamiltonian requires the calculation of its matrix elements in the chosen basis. The kinetic energy and potential matrix elements can be computed separately. As shown in the previous chapter, the kinetic energy operator is given by Eq. (1.9) and involves the hypermomentum operator $\widehat{K}$. The matrix elements are calculated between basis states that separate in a hyperradial part and an angular part (Eq. (2.4)), represented in ket notation by

$$|i\beta j\mu\rangle = \rho^{-5/2} U_{i\beta}(\rho)\mathcal{Y}_{\beta j\mu}(\Omega). \tag{2.5}$$

It is shown in appendix B.1 that the kinetic energy matrix elements can be easily written as

$$\langle i\beta j|\widehat{T}(\rho,\Omega)|i'\beta' j\rangle = \langle i\beta j|\widehat{T}_U(\rho)|i'\beta' j\rangle\delta_{\beta\beta'} = \int d\rho\; U_{i\beta}(\rho)\widehat{T}_U(\rho)U_{i'\beta'}(\rho)\delta_{\beta\beta'}, \tag{2.6}$$

where projection μ has been omitted, and

$$\widehat{T}_U(\rho) = -\frac{\hbar^2}{2m}\left(\frac{d^2}{d\rho^2} - \frac{15/4 + K(K+4)}{\rho^2}\right). \tag{2.7}$$

This implies explicitly that the kinetic energy does not connect different channels β. It is, however, non diagonal with respect to index i.

The potential matrix elements are computed in two steps. First, the hyperradial coupling matrix is defined by integrating the potential $\widehat{V}$ between the basis angular functions (see appendix B.2),

$$V^{j}_{\beta\beta'}(\rho) = \langle \mathcal{Y}_{\beta j\mu} | \widehat{V}_{12}(\boldsymbol{r}_{12}) + \widehat{V}_{13}(\boldsymbol{r}_{13}) + \widehat{V}_{23}(\boldsymbol{r}_{23}) + V_{3b}(\rho) | \mathcal{Y}_{\beta' j\mu} \rangle. \tag{2.8}$$

Then, this coupling matrix is integrated between the hyperradial functions, providing the potential matrix elements

$$\langle i\beta j | \widehat{V}(\rho,\Omega) | i'\beta' j \rangle = \langle U_{i\beta} | V^{j}_{\beta\beta'}(\rho) | U_{i'\beta'} \rangle = \int d\rho \; U_{i\beta}(\rho) V^{j}_{\beta\beta'}(\rho) U_{i'\beta'}(\rho). \tag{2.9}$$

The preceding expression does connect different channels, and can include different contributions according to the potential decomposition given by Eq. (1.11). In the present work, the angular integration is performed following the prescriptions in the FaCE code [51]. The matrix elements given by Eqs. (2.6) and (2.9) can be calculated numerically using Gauss-Laguerre quadratures with the analytical THO basis functions $U^{\mathrm{THO}}_{i\beta}$.

2.2 Three-body observables

Diagonalization of the three-body Hamiltonian provides the eigenenergies and corresponding eigenfunctions. The wave functions so obtained enable the calculation of different observables by using the appropriate quantum operators. Comparison of these observables with the available experimental data for a given system will determine the degree of suitability of the model.

2.2.1 Matter and charge radius

The matter radius for an A-nucleon system is given by

$$r^2 = \frac{1}{A} \sum_{i=1}^{A} r_i^2, \tag{2.10}$$

where $\boldsymbol{r_i}$ is the position of each nucleon with respect to the center of mass of the system. Considering a three-cluster system, this vector can be separated

into two parts,

$$\boldsymbol{r_i} = \boldsymbol{R_q} + \boldsymbol{r_{i(q)}}. \tag{2.11}$$

Here, $\boldsymbol{R_q}$ are the position of the clusters and $\boldsymbol{r_{i(q)}}$ are the positions of each nucleon with respect to the center of mass of its cluster. Inserting Eq. (2.11) in (2.10) leads, after a simple derivation, to the final expression

$$r_{\text{mat}} = \sqrt{\langle r^2 \rangle} = \sqrt{\frac{1}{A}\left[\left(\sum_{q=1}^{3} A_q \langle r^2_{A_q} \rangle\right) + \langle \rho^2 \rangle\right]}, \tag{2.12}$$

where A_q and $\langle r^2_{A_q} \rangle$ are the mass number and known squared radius of each cluster, respectively, and $\langle \rho^2 \rangle$ remains to be calculated in the state of interest. Concerning the charge radius, the general definition gives

$$r^2_{\text{ch}} = \frac{1}{Z}\sum_{i=1}^{Z} r_i^2, \tag{2.13}$$

where $\boldsymbol{r_i}$ is now the position of each proton with respect to the center of mass of the system. In this sense, this is a point-nucleon charge radius. Following a similar procedure, the final expression in this case reads

$$r_{\text{ch}} = \sqrt{\langle r^2_{\text{ch}} \rangle} = \sqrt{\frac{1}{Z}\left[\left(\sum_{q=1}^{3} Z_q \langle r^2_{Z_q} \rangle\right) + \langle f(x,y) \rangle\right]}, \tag{2.14}$$

where Z_q and $\langle r^2_{Z_q} \rangle$ are the charge and squared charge radius of each cluster, respectively, and $f(x, y)$ is a function with a different form depending on the number of charged and/or identical clusters in the system. All details concerning the derivation and computation of the preceding formulae can be found in appendix B.3.

2.2.2 Electromagnetic transition probabilities

Electromagnetic observables probe the structure of the wave functions through multipole moments and gamma transitions. Both multipole deformations and electromagnetic transition probabilities can be measured experimentally, providing data to compare with. The electromagnetic radiation field is usually expanded in multipoles containing spherical harmonics,

and electric and magnetic terms can be treated separately. A transition from an initial nuclear state to a final state is, in this picture, mediated by one of the multipole terms [81]. Following the notation of Brink and Satchler [82], the reduced transition probability between two states labeled nj and $n'j'$ is defined as

$$\begin{aligned} B(\mathcal{O}\lambda)_{nj,n'j'} &\equiv B(\mathcal{O}\lambda; nj \to n'j') \\ &= |\langle nj \| \widehat{\mathcal{O}}_\lambda \| n'j' \rangle|^2 \left(\frac{2\lambda+1}{4\pi} \right), \end{aligned} \tag{2.15}$$

where $\widehat{\mathcal{O}}_{\lambda M_\lambda}$ is the electric or magnetic multipole operator of order λ, and $|nj\mu\rangle$ denotes the wave function given by Eq. (2.4).

For electric transitions, the electric multipole operator for a general three-body system takes the form in the Jacobi-k set

$$\widehat{Q}_{\lambda M_\lambda}(\boldsymbol{x}_k, \boldsymbol{y}_k) = \left(\frac{4\pi}{2\lambda+1} \right)^{1/2} \sum_{q=1}^{3} Z_q \; e \; r_q^\lambda Y_{\lambda M_\lambda}(\widehat{r}_q), \tag{2.16}$$

where Z_q is the atomic number of particle q, e is the electron charge, and $\boldsymbol{r}_q$ is the position of particle q with respect to the center of mass of the system. In the case of magnetic transitions, the magnetic multipole operator can be expressed as a sum of two terms: the orbital and spin parts [83]. Following again the notation of Brink ans Sachtler, these two terms are

$$\begin{aligned} \widehat{M}^{\text{orb}}_{\lambda M_\lambda}(\boldsymbol{x}_k, \boldsymbol{y}_k) &= \frac{e\hbar}{2mc} \sqrt{4\pi\lambda} \sum_q r_q^{\lambda-1} \frac{2g_l^{(q)}}{\lambda+1} \left[Y_{\lambda-1} l \right]^{(q)}_{(\lambda-1,1)\lambda,M_\lambda}, \\ \widehat{M}^{\text{spin}}_{\lambda M_\lambda}(\boldsymbol{x}_k, \boldsymbol{y}_k) &= \frac{e\hbar}{2mc} \sqrt{4\pi\lambda} \sum_q r_q^{\lambda-1} g_s^{(q)} \left[Y_{\lambda-1} s \right]^{(q)}_{(\lambda-1,1)\lambda,M_\lambda}. \end{aligned} \tag{2.17}$$

Here g_l and g_s are the orbital and spin g-factors, and $[Y_{\lambda-1}j]_{(\lambda-1,1)\lambda M_\lambda}$ is a tensorial product of order one,

$$\begin{aligned} [Y_{\lambda-1}j]_{(\lambda-1,1)\lambda,M_\lambda} &\equiv [Y_{\lambda-1} \otimes \boldsymbol{j}]_{(\lambda-1,1)\lambda,M_\lambda} \\ &= \sum_{\eta\nu} Y_{(\lambda-1)\eta} \widehat{j}_\nu \; \langle (\lambda-1)\eta 1\nu | \lambda M_\lambda \rangle. \end{aligned} \tag{2.18}$$

The position $\boldsymbol{r}_q$ appearing in both electric and magnetic operators are given in the Jacobi-q system by Eq. (A.7),

$$\boldsymbol{r}_q = \sqrt{\frac{m}{m_q}\frac{(M_T - m_q)}{M_T}}\boldsymbol{y}_q, \tag{2.19}$$

where M_T is the total mass of the system. This means that, in the Jacobi-q system, the position of particle q is given by a vector proportional to $\boldsymbol{y}_q$. However, wave functions are obtained in a preferred Jacobi-k system. For that reason, the wave functions $|nj\mu\rangle$ have to be rotated from Jacobi-k to Jacobi-q for each summand (i.e. for each particle) in Eq. (2.16), making use of the transformations between different Jacobi sets. For that, it is possible to write the wave functions using the notation

$$|k;nj\mu\rangle = \sum_{\beta_k}\sum_{i} C_n^{i\beta_k j}|i\beta_k j\mu\rangle = \sum_{\beta_k}\sum_{i} C_n^{i\beta_k j}|i\beta_k\rangle \otimes |k;\beta_k j\mu\rangle, \tag{2.20}$$

where the basis states separate in its radial part $|i\beta_k\rangle$ and its angular part $|k;\beta_k j\mu\rangle$. Note that index k just labels the preferred Jacobi set in which the Hamiltonian has been diagonalized. Taking into account that the angular functions are a complete basis of the angular subspace, it is clear that

$$|k;\beta_k j\mu\rangle = \sum_{\beta_q}|q;\beta_q j\mu\rangle\langle q;\beta_q j\mu|k;\beta_k j\mu\rangle = \sum_{\beta_q} N_{\beta_k\beta_q}|q;\beta_q j\mu\rangle. \tag{2.21}$$

The matrix elements $N_{\beta_k\beta_q}$ are related to the Raynal-Revai coefficients [84] and are given by Eqs. (B.37) and (B.38). This transformation preserves the hypermomentum K and the total orbital angular momentum l. Inserting Eq. (2.21) in (2.20),

$$|k;nj\mu\rangle = \sum_{\beta_k}\sum_{i} C_n^{i\beta_k j}|i\beta_k\rangle \sum_{\beta_q} N_{\beta_k\beta_q}|q;\beta_q j\mu\rangle. \tag{2.22}$$

The electric and magnetic multipole operator matrix elements by means of the basis states require some non-trivial algebra. The full derivation as well as the corresponding guides and references are shown with detail in appendixes B.4 and B.5. In practice, label k standing for the preferred Jacobi set can be omitted, making the notation much simpler. Doing so, the final

expression for the electric multipole operator reduced matrix element is

$$\langle nj||\widehat{Q}_\lambda||n'j'\rangle = \sum_q Z_q e \left(\frac{\sqrt{m a_{y_q}}}{m_q}\right)^\lambda \sum_{\beta\beta'}\sum_{ii'} C_n^{i\beta j} C_{n'}^{i'\beta' j'} \sum_{\beta_q\beta'_q} N_{\beta\beta_q} N_{\beta'\beta'_q}$$
$$\times \delta_{l_{x_q} l'_{x_q}} \delta_{S_{x_q} S'_{x_q}} \hat{l}_{y_q} \hat{l}'_{y_q} \hat{l}_q \hat{l}'_q \hat{j}_{ab_q} \hat{j}'_{ab_q} \hat{j}' (-1)^{j+l_{x_q}+l_{y_q}+l'_{y_q}+S_{x_q}-j_{ab_q}+j'_{ab_q}-I_q}$$
$$\times \begin{pmatrix} l_{y_q} & \lambda & l'_{y_q} \\ 0 & 0 & 0 \end{pmatrix} W(l_q l'_q l_{y_q} l'_{y_q}; \lambda l_{x_q}) W(j_{ab_q} j'_{ab_q} l_q l'_q; \lambda S_{x_q}) W(jj' j_{ab_q} j'_{ab_q}; \lambda I_q)$$
$$\times \int (\sin\alpha)^2 (\cos\alpha)^2 \, d\alpha \; d\rho \; \varphi_{K_q}^{l_{x_q} l_{y_q}}(\alpha) U_{i\beta}^{THO}(\rho) y_q^\lambda U_{i'\beta'}^{THO}(\rho) \varphi_{K'_q}^{l'_{x_q} l'_{y_q}}(\alpha). \qquad (2.23)$$

and the magnetic orbital and spin parts are

$$\langle nj||\widehat{M}_\lambda^{\rm orb}||n'j'\rangle = \frac{e\hbar}{2mc} \frac{\sqrt{\lambda}}{\lambda+1} (\lambda \hat{-} 1) \hat{\lambda} \hat{j}' (-1)^\lambda \sum_q \left(\frac{M_T - m_q}{M_T}\right)^\lambda \left(\frac{m}{a_{y_q}}\right)^{\frac{\lambda-1}{2}} 2 g_l^{(q)}$$
$$\times \sum_{\beta\beta'} \sum_{\beta_q\beta'_q} N_{\beta\beta_q} N_{\beta\beta'_q} \delta_{S_{x_q} S'_{x_q}} \delta_{l_{x_q} l'_{x_q}} \times (-1)^{2j-j'+l'_{y_q}-l_{y_q}+l_{x_q}-S_{x_q}+j_{ab_q}+j'_{ab_q}-I_q}$$
$$\times \sqrt{l'_{y_q}\left(l'_{y_q}+1\right)} \hat{l}_{y_q} \hat{l}'^2_{y_q} \hat{j}_{ab_q} \hat{j}'_{ab_q} \hat{l}_q \hat{l}'_q \begin{pmatrix} l_{y_q} & \lambda-1 & l'_{y_q} \\ 0 & 0 & 0 \end{pmatrix} W(l_{y_q} l'_{y_q} (\lambda-1) 1; \lambda l'_{y_q})$$
$$\times W(l_q l'_q l_{y_q} l'_{y_q}; \lambda l_{x_q}) W(l_q l'_q j_{ab_q} j'_{ab_q}; \lambda S_{x_q}) W(j_{ab_q} j'_{ab_q} jj'; \lambda I_q) \sum_{ii'} C_n^{i\beta j} C_n'^{i'\beta' j'}$$
$$\times \int\int d\alpha d\rho (\sin\alpha)^2 (\cos\alpha)^2 U_{i\beta}(\rho) \varphi_{K_q}^{l_{x_q} l_{y_q}}(\alpha) y^{\lambda-1} U_{i'\beta'}(\rho) \varphi_{K'_q}^{l'_{x_q} l'_{y_q}}(\alpha), \qquad (2.24)$$

$$\langle nj||\widehat{M}_\lambda^{\rm spin}||n'j'\rangle = \frac{e\hbar}{2mc} \sqrt{\lambda} (\lambda \hat{-} 1) \hat{\lambda} \hat{j}' \sum_q \left(\frac{M_T - m_q}{M_T}\right)^{\lambda-1} \left(\frac{m}{a_{y_q}}\right)^{\frac{\lambda-1}{2}} g_s^{(q)}$$
$$\times \sum_{\beta\beta'} \sum_{\beta_q\beta'_q} N_{\beta\beta_q} N_{\beta\beta'_q} \delta_{S_{x_q} S'_{x_q}} \delta_{l_{x_q} l'_{x_q}} (-1)^{j+j'+l_{x_q}-S_{x_q}-j_{ab_q}+2I_q}$$
$$\times \sqrt{I_q\left(I_q+1\right)} \hat{I}_q \hat{l}_{y_q} \hat{l}'_{y_q} \hat{j}_{ab_q} \hat{j}'_{ab_q} \hat{l}_q \hat{l}'_q \begin{pmatrix} l_{y_q} & \lambda-1 & l'_{y_q} \\ 0 & 0 & 0 \end{pmatrix} W(l_q l'_q l_{y_q} l'_{y_q}; (\lambda-1) l_{x_q})$$
$$\times W(l_q l'_q j_{ab_q} j'_{ab_q}; (\lambda-1) S_{x_q}) \begin{Bmatrix} j & j' & \lambda \\ j_{ab_q} & j'_{ab_q} & \lambda-1 \\ I_q & I_q & 1 \end{Bmatrix} \sum_{ii'} C_n^{i\beta j} C_n'^{i'\beta' j'}$$
$$\times \int\int d\alpha d\rho (\sin\alpha)^2 (\cos\alpha)^2 U_{i\beta}(\rho) \varphi_{K_q}^{l_{x_q} l_{y_q}}(\alpha) y^{\lambda-1} U_{i'\beta'}(\rho) \varphi_{K'_q}^{l'_{x_q} l'_{y_q}}(\alpha). \qquad (2.25)$$

In these expressions, a_{y_q} is the Jacobi y-coordinate scale (see appendix A.1), $\hat{j}$ represents a reduced form for the factor $\sqrt{2j+1}$, and $W(abcd;ef)$ is a Racah coefficient. Concerning the g-factors, it is known that their effective values in the nuclear medium are rather uncertain [85]. This will be discussed in the following chapters.

An alternative way to calculate the electric transition probability consists in expanding the harmonic polynomials $y_q^\lambda Y_{\lambda M_\lambda}(\widehat{y}_q)$ in Eq. (2.16) in terms of the Jacobi-k system. This can be done by using the relation between harmonic polynomials in different Jacobi sets [86],

$$\begin{aligned} y_q^\lambda Y_{\lambda M_\lambda}(\widehat{y}_q) = & \sum_{l=0}^{\lambda} (-1)^\lambda x_k^{\lambda-l} (\sin\varphi_{qk})^{\lambda-l} y_k^l (\cos\varphi_{qk})^l \\ & \times \sqrt{\frac{4\pi\,(2\lambda+1)!}{(2l+1)!\,(2\lambda-2l+1)!}} \\ & \times \left[Y_{\lambda-l}(\widehat{x}_k) \otimes Y_l(\widehat{y}_k)\right]^{\lambda M_\lambda}, \end{aligned} \tag{2.26}$$

with

$$\tan\varphi_{qk} = (-1)^P \sqrt{\frac{m_p M_T}{m_q m_k}}, \tag{2.27}$$

depending on the mass of the particles and the parity $(-1)^P$ of the permutation P of $\{k,p,q\}$. The identity transformation is given by $\varphi_{kk} = \pi$. Using Eq. (2.26) it is possible to rewrite the harmonic polynomial for each particle q, as a function of the Jacobi coordinates in the preferred Jacobi system k. This provides an expression for the electric operator to be used directly between the states in the Jacobi–k system, and is equivalent to the result given by Eq. (2.23). When the final expression for the operator so obtained has a simple form, this procedure is much more efficient computationally.

Electromagnetic transitions of a given multipolarity λ from an initial state labeled $|n_0 j_0 \mu_0\rangle$ to final states $|nj\mu\rangle$ define a total probability strength

$$S_T(E\lambda) = \sum_{nj} B(E\lambda)_{n_0 j_0, nj} = \left(\frac{2\lambda+1}{4\pi}\right) \sum_{nj} |\langle n_0 j_0 || \widehat{\mathcal{O}}_\lambda || nj\rangle|^2. \tag{2.28}$$

The reduced matrix element can be related to the projection-dependent

matrix element by [82]

$$|\langle n_0 j_0 || \widehat{\mathcal{O}}_\lambda || nj \rangle|^2 = \sum_{\mu M_\lambda} |\langle n_0 j_0 \mu_0 | \widehat{\mathcal{O}}_{\lambda M_\lambda} | nj\mu \rangle|^2, \tag{2.29}$$

which, together with Eq. (2.28), leads to

$$\begin{aligned} S_T(E\lambda) &= \left(\frac{2\lambda+1}{4\pi}\right) \sum_{nj} \sum_{\mu M_\lambda} |\langle n_0 j_0 \mu_0 | \widehat{\mathcal{O}}_{\lambda M_\lambda} | nj\mu \rangle|^2 \\ &= \left(\frac{2\lambda+1}{4\pi}\right) \sum_{nj} \sum_{\mu M_\lambda} \langle n_0 j_0 \mu_0 | \widehat{\mathcal{O}}^\dagger_{\lambda M_\lambda} | nj\mu \rangle \langle nj\mu | \widehat{\mathcal{O}}_{\lambda M_\lambda} | n_0 j_0 \mu_0 \rangle \\ &= \left(\frac{2\lambda+1}{4\pi}\right) \sum_{M_\lambda} \langle n_0 j_0 \mu_0 | \widehat{\mathcal{O}}^\dagger_{\lambda M_\lambda} \widehat{\mathcal{O}}_{\lambda M_\lambda} | n_0 j_0 \mu_0 \rangle. \end{aligned} \tag{2.30}$$

For a given operator, this expression is completely determined by the properties of the initial state $|n_0 j_0 \mu_0\rangle$, and defines the corresponding sum rule [87, 88]. Specific closed expressions can be obtained for different operators, which provide a quantity to compare with the total strength and allow to check the completeness of the basis used to diagonalize the Hamiltonian. See appendix B.4.1 for details.

Due to the discrete nature of the PS basis, transition probabilities given by Eq. (2.15) are a set of discrete values. In order to obtain a continuous energy distribution, in some cases one can calculate the actual continuum wave functions by solving the Schrödinger equation with the right asymptotic boundary conditions [89]. The PS energy distributions can be obtained by doing the overlap with these continuum wave functions, and enable the smoothing of the transition probability discrete values. However, the asymptotic behavior of continuum states for systems with several charged particles is not known in general, so this procedure is only applicable in very limited cases. An approximation to describe these distributions consists in considering that a PS with energy ε_n is the superposition of continuum states in the vicinity. Then, for each discrete value of $B(\mathcal{O}\lambda)_{\text{g.s.}\to nj} \equiv B(\mathcal{O}\lambda)(\varepsilon_n)$ it is possible to assign an energy distribution $D(\varepsilon; \varepsilon_n, w)$ with a Poisson form

$$D(\varepsilon; \varepsilon_n, w) = C(\varepsilon_n, w) \varepsilon^w \exp\left[-\kappa(\varepsilon_n, w)\varepsilon\right], \tag{2.31}$$

being $C(\varepsilon_n, w)$ and $\kappa(\varepsilon_n, w)$ totally determined by the following conditions

$$\int_0^\infty D(\varepsilon; \varepsilon_n, w) d\varepsilon = 1, \tag{2.32}$$

$$\int_0^\infty \varepsilon D(\varepsilon; \varepsilon_n, w) d\varepsilon = \varepsilon_n. \tag{2.33}$$

In this way the distributions are normalized to one and centered at the corresponding energy. Using these conditions, the distributions can be expressed as

$$D(\varepsilon, \varepsilon_n, w) = \frac{(w+1)^{w+1}}{\varepsilon_n^{w+1}\Gamma(w+1)} \varepsilon^w \exp\left(-\frac{w+1}{\varepsilon_n}\varepsilon\right),$$

so, finally, the smoothed transition probability distribution is given by

$$\frac{dB(\widehat{\mathcal{O}}\lambda)}{d\varepsilon}(\varepsilon, w) = \sum_n D(\varepsilon; \varepsilon_n, w)\ B(\widehat{\mathcal{O}}\lambda)(\varepsilon_n). \tag{2.34}$$

Poisson distributions tend smoothly to zero at the origin, which is the physical behavior expected for the energy distributions of the PSs. But this choice is not unique, and different distributions can be used to smear the discrete values [90, 91]. The parameter w controls the width of the distributions; as w decreases, the width of the distributions increases. The prescription to fix an appropriate w parameter consists in choosing the value of w that ensures a smooth $B(E1)$ distribution without spreading it unphysically. More details and a practical example are shown in the following sections.

2.3 Application to ^{6}He

The ^{6}He nucleus was produced for the first time back in 1936 [92], only a few years after the discovery of the neutron, although its halo features had to wait a few decades to be appreciated [5]. This system has attracted a lot of attention, especially in the recent few decades. After remarkable experimental and theoretical work, valuable information is available on the ground state of ^{6}He: total angular momentum 0^+, experimental binding energy of 0.975 MeV below the three-body threshold [93], a rms point nucleon matter radius of 2.5-2.6 fm [94], and a charge radius of 2.06 fm [95]. It shows also a well-known 2^+ resonance at 0.824 MeV over the breakup threshold [93].

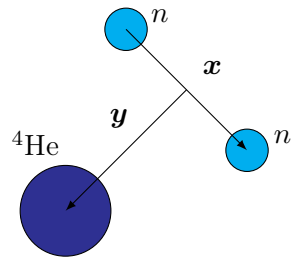

Figure 2.4: The Jacobi-T system used to describe the ^{6}He nucleus.

In a theoretical perspective, ^{6}He is the simplest halo, Borromean nuclei that has been studied. Described as an α particle and two neutrons, it comprises a single charged particle. In this case, the comparison with actual continuum wave functions (not always available) may serve as a reference for any other calculation. The α core is tightly bound and therefore can be considered inert, so its excited states will not play any role at the energies of interest. This assumption may not be valid for more complex exotic nuclei. Due to its relative simplicity, it provides an excellent case for benchmark calculations. Two-body models to describe the structure of ^{6}He must rely on the properties of either ^{5}He or the dineutron [42], none of which are bound. In a full three-body model, such as the one presented in this work, both configurations (and their relative importance in describing the system) are included consistently. It is worth noting that more fundamental few-body methods can be applied to ^{6}He considered as a six-nucleon system, such as the resonating group method [96] or the Lorentz integral transform method [97]. Recently, *ab initio* calculations based on NN and 3N interactions between all constituents have been used to describe both bound [52] and continuum [98] states of ^{6}He by means of the no-core shell model combined with the resonating-group method. The applicability of these methods to heavier nuclei faces computational limitations due to the complexity of the calculations, although important progress has been achieved in recent years. Moreover, *ab initio* approaches for Borromean nuclei need to include three-cluster dynamics to account for the intrinsic three-body nature of the systems.

The strict three-body picture provides a more intuitive description and, as will be shown, leads to reliable structure and scattering observables for nuclei of key importance in astrophysics. The Jacobi-T set, where the two

neutrons are related by coordinate $\boldsymbol{x}$, is used to describe ^{6}He. This is shown in Fig. 2.4 and enables the proper treatment of the Pauli principle between identical valence neutrons. This results in the suppression of specific channels of the wave function (1.6), since antisymmetrization can be achieved by imposing $l_x + S_x + T_x$ to be odd [51]. Here, $T_x = 1$ is the isospin of the two-neutron subsystem, and therefore the channels characterized by odd values of $l_x + S_x$ will be removed. The model Hamiltonian includes two-body n-n and α-n potentials. These interactions are typically adjusted to reproduce the phenomenology of the two-body scattering problems. In this work, the following interactions are used:

- The n-n GPT potential [99], with central $V_c(r)$, spin-orbit $V_{so}(r)$ and tensor $V_t(r)$ components in Eq. (1.11). Each component is defined as a sum of Gaussian-shaped potentials,

$$V_c^{(l)}(r) = \sum_{k=1}^{3} v_{c_k}^{(l)} \exp\left[-\left(r/r_{c_k}^{(l)}\right)^2\right], \tag{2.35}$$

$$V_{so}(r) = v_{so} \exp\left[-\left(r/r_{so}\right)^2\right], \tag{2.36}$$

$$V_t(r) = \sum_{k=1}^{3} v_{t_k} \exp\left[-\left(r/r_{t_k}\right)^2\right]. \tag{2.37}$$

  The parameters for the central part are l-dependent, as shown in the following table:

l	v_{c_1} (MeV)	r_{c_1} (fm)	v_{c_2} (MeV)	r_{c_2} (fm)	v_{c_3} (MeV)	r_{c_3} (fm)
s, d	+560.0	0.8109	−390.7	1.031	−1.501	3.205
p	+9.335	1.184	−1.37	2.099	+0.1663	3.193

  The spin-orbit term is given by a single Gaussian potential defined by parameters:

v_{so} (MeV)	r_{so} (fm)
−114.5	0.9296

  The parameters for the tensor potential are:

v_{t_1} (MeV)	r_{t_1} (fm)	v_{t_2} (MeV)	r_{t_2} (fm)	v_{t_3} (MeV)	r_{t_3} (fm)
+12.24	1.539	−31.64	0.4039	+0.8111	3.015

- The α-n potential from Refs. [24, 100], with central $V_c(r)$ and spin-orbit $V_{so}(r)$ terms which are expressed as Woods-Saxon potentials,

$$V_c(r) = \frac{v_c^{(l)}}{1 + \exp\left(\frac{r - r_c^{(l)}}{a_c^{(l)}}\right)}, \tag{2.38}$$

$$V_{\rm so}(r) = \frac{v_{\rm so}}{r a_{\rm so}} \frac{\exp\left(\frac{r - r_{\rm so}}{a_{\rm so}}\right)}{\left[1 + \exp\left(\frac{r - r_{\rm so}}{a_{\rm so}}\right)\right]^2} \ . \tag{2.39}$$

Again, the parameters for the central part are l-dependent:

l	v_c (MeV)	r_c (fm)	a_c (fm)
s	+48.0	2.0	0.7
p	−43.0	2.0	0.7
d	−21.5	2.0	0.7

The spin-orbit potential is given by:

$v_{\rm so}$ (MeV fm^2)	$r_{\rm so}$ (fm)	$a_{\rm so}$ (fm)
−40.0	1.5	0.35

In section 1.3.3, the problem of the Pauli blocking for three-body systems was discussed. As already stated, two-body forbidden states that would disappear under full antisymmetrization need to be removed for proper computation of three-body observables. In this work, the α-n potential includes a repulsive s-wave component to forbid the valence neutrons to enter the occupied α core states. The repulsive-core potential is introduced with the requirement that the experimental phase shifts are correctly reproduced [24]. This kind of interactions are sometimes called shallow potentials, as the counterpart of deep potentials including unphysical bound states.

As already discussed in the introduction (section 1.3.2), strict three-body models with binary interactions only may lead to deviations from the experimentally known energies. Therefore, it is customary to include a structureless hyperradial three-body force in order to adjust the energy of the system to experimental data, when available. As in Ref. [23], a possibility is to consider

$$V_{3b}(\rho) = \frac{v_{3b}}{1 + \left(\frac{\rho}{r_{3b}}\right)^{a_{3b}}}. \tag{2.40}$$

There are other choices in the literature, but the specific form of this interaction plays a negligible role on the final results. In this case, the parameters of the three-body force are chosen to adjust the energy of the 0^+ ground state and the 2^+ resonance in ^{6}He, -0.9736 and 0.824 MeV with respect to the three-body threshold [93], respectively. In the case of 1^- states, no low-lying resonance is available to fit the three-body force. A possible choice consists in accepting, for 1^- states, the same three-body interaction used to fit the 2^+ states. The following table shows the relevant parameters for each j^π configuration:

j^π	v_{3b} (MeV)	r_{3b} (fm)	a_{3b}
0^+	-2.45	5.0	3
1^-	-0.90	5.0	3
2^+	-0.90	5.0	3

The 0^+ states are obtained by diagonalizing the Hamiltonian in an analytical THO basis defined by parameters $b = 0.7$ fm and $\gamma = 1.4$ fm$^{1/2}$ (see Eq. (2.2)), trying to minimize the size of the basis needed to reach convergence of the ground state. It is found that a basis with a larger γ/b ratio has a too small hyperradial extension to provide a fast convergence for the ground state. On the other hand, a basis with smaller γ/b has a very large hyperradial extension and does not describe properly the interior region of the potential where the ground state probability is larger. In Fig. 2.5, the first THO hyperradial wave functions for the channel $\beta \equiv \{2, 0, 0, 0, 0, 0\}$, using the given analytical transformation, are shown. This channel is the most important ground-state channel, with a 78.6% contribution to the total norm. The figure shows that, as i increases, the functions are more oscillatory and explore larger distances.

In Fig. 2.6 the Hamiltonian eigenvalues for $j^\pi = 0^+$, for an increasing number of hyperradial excitations, $i_{\max}$, are presented up to 10 MeV. The calculated ground state is stable with respect to the size of the basis and has a binding energy of $|\varepsilon_B| = 0.9749$ MeV. With this value of the energy, and assuming that the α particle point nucleon matter and charge radii are 1.47 and 1.6755 fm [101], respectively, the computed matter and charge radii of the ^{6}He ground state are $r_{mat} = 2.554$ fm and $r_{ch} = 2.09$ fm. These values are in good agreement with the available experimental data [94, 95]. In Table 2.1 the ground state energy and the matter and charge radii are

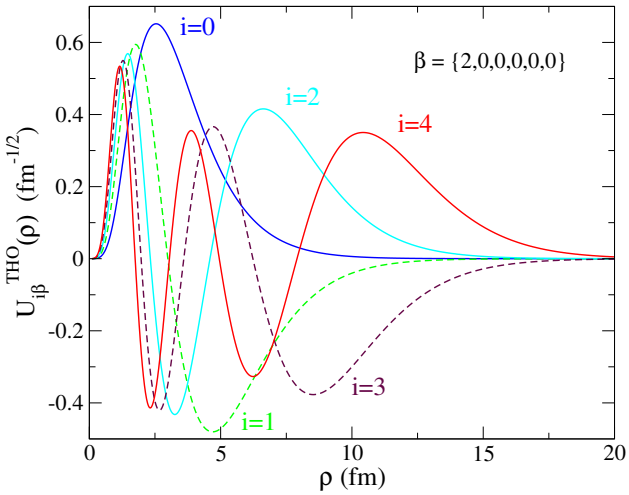

Figure 2.5: First five THO hyperradial wave functions for the channel $\beta \equiv \{2,0,0,0,0,0\}$, the most important channel in the g.s. wave function.

$i_{\max}$	ε_B (MeV)	r_{mat} (fm)	r_{ch} (fm)
5	-0.9452	2.511	2.069
10	-0.9744	2.552	2.085
15	-0.9748	2.554	2.090
20	-0.9749	2.554	2.090
25	-0.9749	2.554	2.090

Table 2.1: Ground-state energy ε_B, matter radius r_{mat} and charge radius r_{ch} of ^{6}He as a function of $i_{\max}$. A fast convergence is observed.

shown as a function of the maximum number of hyperradial excitations $i_{\max}$. A fast convergence is observed for both ground state observables within this THO basis. The model space in which the three-body wave functions are expanded is truncated by fixing a maximum value of the hypermomentum K_{max}. In this case, a value of $K_{max} = 20$ is sufficient to get convergence for the ground state energy and radius. This is shown in Figs. 2.7 and 2.8.

The first three hyperradial components of the ground state wave function for $i_{\max} = 20$ are presented in Fig. 2.9. The curves match a reference calculation of the ground state wave function corresponding to the same model Hamiltonian. This is presented in Ref. [24] and implemented in the codes FaCE [51] and sturmxx [102], using a suitable basis for bound states, the so-called Sturmian basis. The dominance of s waves in the Jacobi-T set is clear.

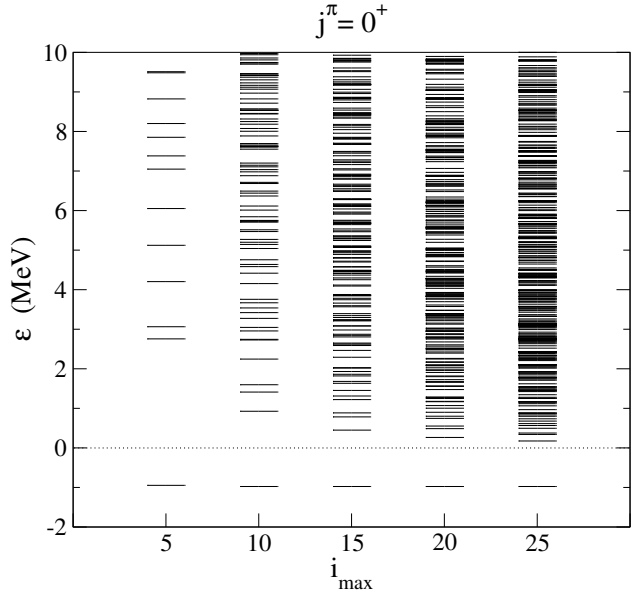

Figure 2.6: ^{6}He eigenvalues for $j^\pi = 0^+$ up to 10 MeV, as a function of the size of the basis given by i_{max}. Calculations are truncated at maximum hypermomentum $K_{max} = 20$, which is large enough to reach convergence of the ground state properties.

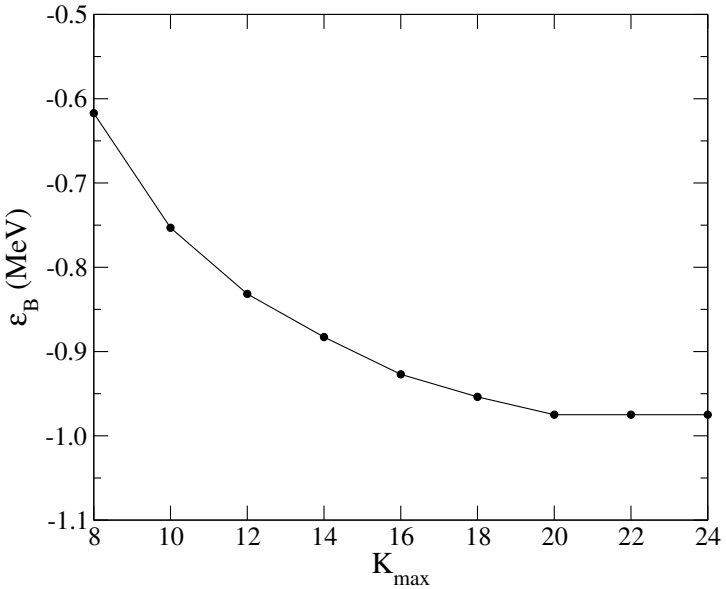

Figure 2.7: Convergence of the ^{6}He ground state energy ε_B with respect to the maximum hypermomentum K_{max}. Calculations use $i_{max} = 20$.

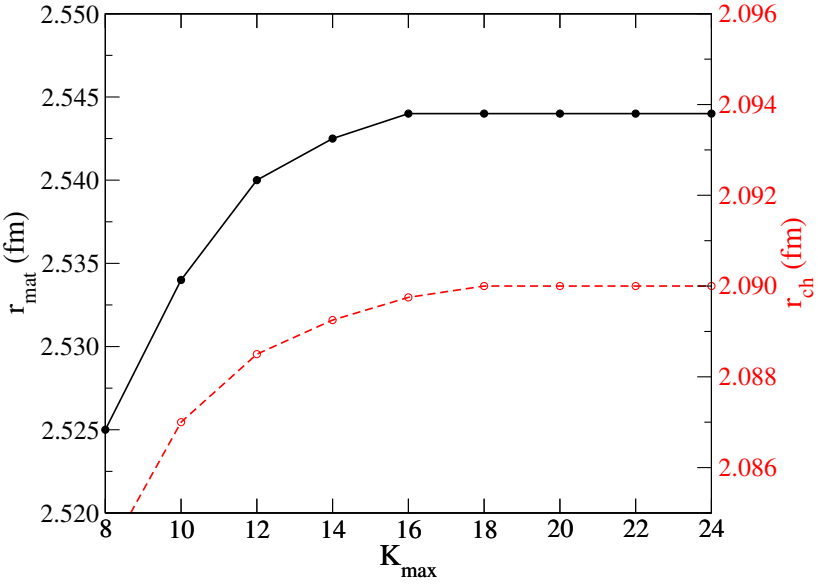

Figure 2.8: Convergence of the ^{6}He ground state matter and charge radii, r_{mat} (in black) and r_{ch} (in red), with respect to the maximum hypermomentum K_{max}. Calculations use $i_{max} = 20$. Notice the different scales for both observables.

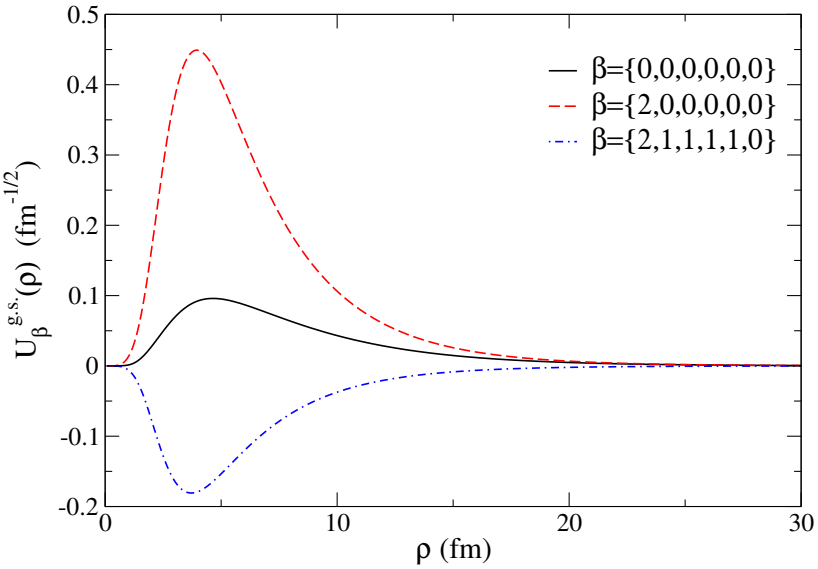

Figure 2.9: Hyperradial wave function, $U_\beta^{\text{g.s.}}(\rho)$, for the first three channels included in the ground state of ^{6}He.

l_x	l_y	l	S_x	$W(^6\text{He})$
0	0	0	0.0	84.0
1	1	1	1.0	12.4
2	2	0	0.0	2.4

Table 2.2: Angular components included for the 0^+ ground state of ^{6}He. $W(^6\text{He})$ indicates the contribution to the total norm of the wave function. Only those components contributing more than 1% are given.

In Table 2.2, the percentage of the total norm provided by each angular component $\{l_x, l_y, l, S_x\}$ to the ground state, is shown. Notice that the quantum number j_{ab} is not included since, for ^{6}He described in the Jacobi-T system, it is zero in all channels. The main contribution of 84% is from s waves, and less than 13% comes from p waves. Contributions from d waves and higher angular momenta are almost negligible. In particular, the two most important channels shown in Fig. 2.9, corresponding to $l_x = 0$ waves with $K = 0$ and $K = 2$, contain the 5% and 79% of the total norm, respectively. This dominance prevails when rotating the wave function to the Jacobi set where $\boldsymbol{x}$ connects the α core and one neutron, and is a signal of the dilute halo tail of the wave function.

Fig. 2.9 shows the ground state wave function hyperradial components, which hinders the visualization of the system spatial configuration. A detailed view is shown in Fig. 2.10, where the square of the three-body wave function is integrated over the direction of the two Jacobi coordinates. This gives the system probability. Here, r_x represents the distance between the two valence neutrons in ^{6}He, while r_y corresponds to the distance between the two-neutron center of mass and the α core. The probability shows a prominent peak for distances $r_x \simeq 2$ fm and $r_y \simeq 2.5$ fm. Another peak is found for corresponding distances of about 4.5 and 1 fm, respectively. These two shapes can be described as two neutrons either on the same side of the α core (at some distance apart) or at almost opposite sides of the core. In the literature, these peaks have been referred to as dineutron- and cigar-like configurations, respectively [11]. The shapes in this plot carry information about the underlying correlations in the system, halo particle correlations in this case, so they are mainly connected with the details of the binary potentials used to describe the system.

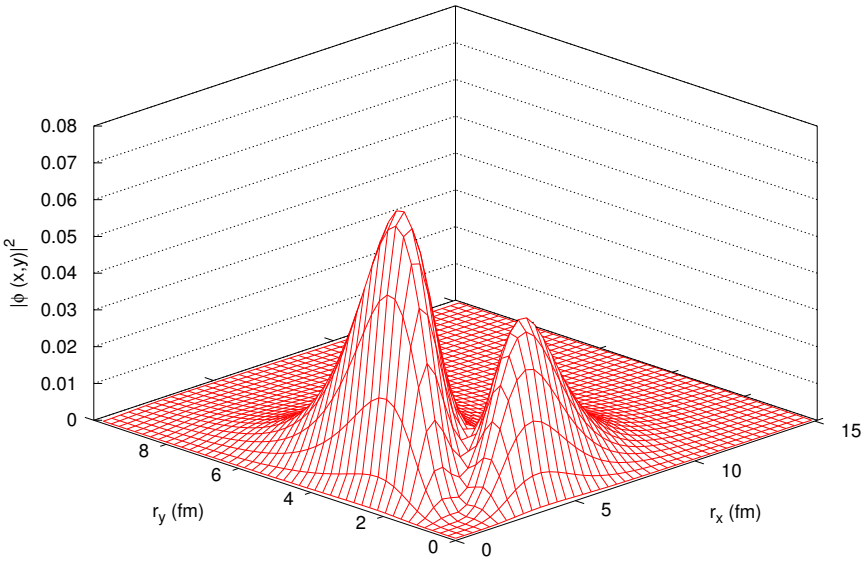

Figure 2.10: Probability distribution of the ^{6}He ground state.

The first resonance in ^{6}He is a 2^+ state at 0.824 MeV over the two-neutron separation energy [93]. The 2^+ states can be described in a basis defined by parameters $b = 0.7$ fm and $\gamma = 2.0$ fm$^{1/2}$. This basis has a small hyperradial extension and therefore spreads the eigenvalues obtained upon diagonalization at higher energies. This choice enables to have only one pseudostate presenting the features of the resonance, since the rest of states are sufficiently above the resonance energy for medium-size bases. In this way, it is possible to adjust the resonance energy to the experimentally known value using the phenomenological three-body force. In Fig. 2.11, the eigenvalues of the Hamiltonian for $j^\pi = 2^+$ states, for an increasing number of hyperradial excitations, are shown. Calculations use, again, $K_{max} = 20$. Note that the lowest state is rather stable. In Fig. 2.12, the hyperradial probability density of the 2^+ pseudostate representing the resonance is shown, compared with the 0^+ ground state probability. The contributions of the three most important channels for each one are shown. The 2^+ state has a large probability in the interior part, similar to a bound state. Note the different scales.

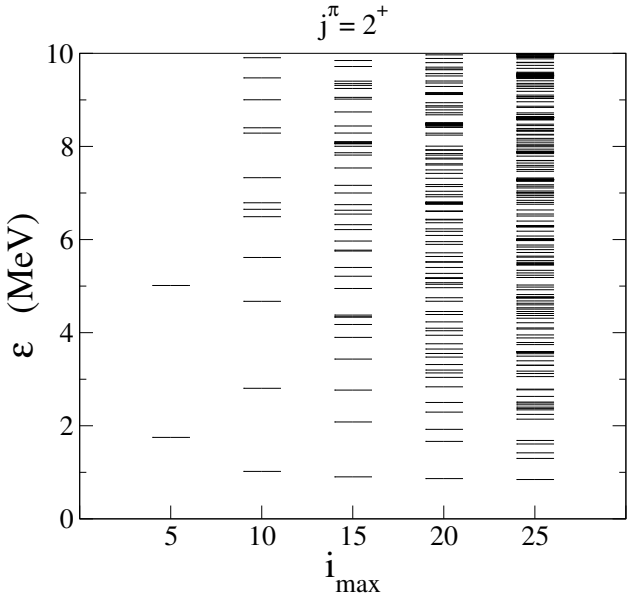

Figure 2.11: ^{6}He eigenvalues for $j^\pi = 2^+$ up to 10 MeV.

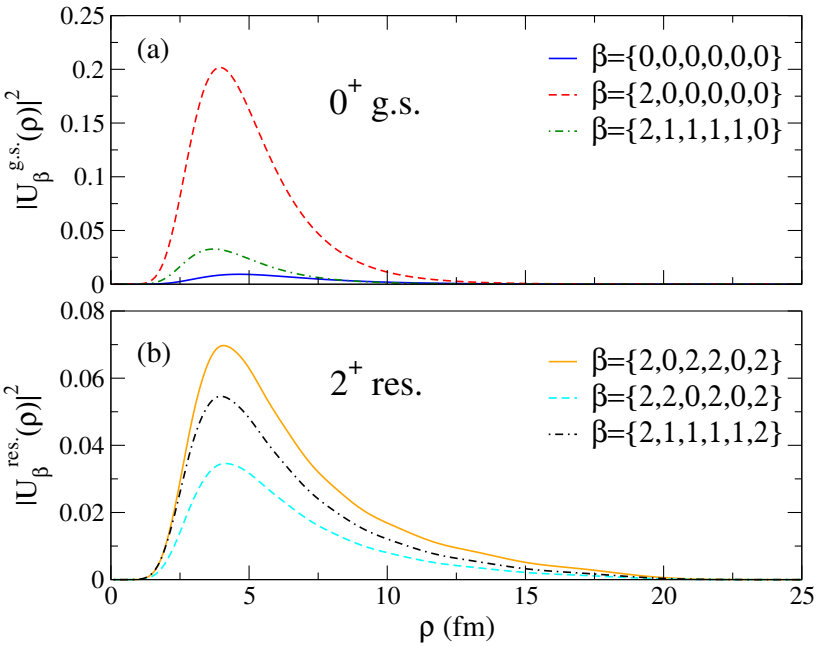

Figure 2.12: ^{6}He ground state (a) and 2^+ resonance state (b) probabilities.

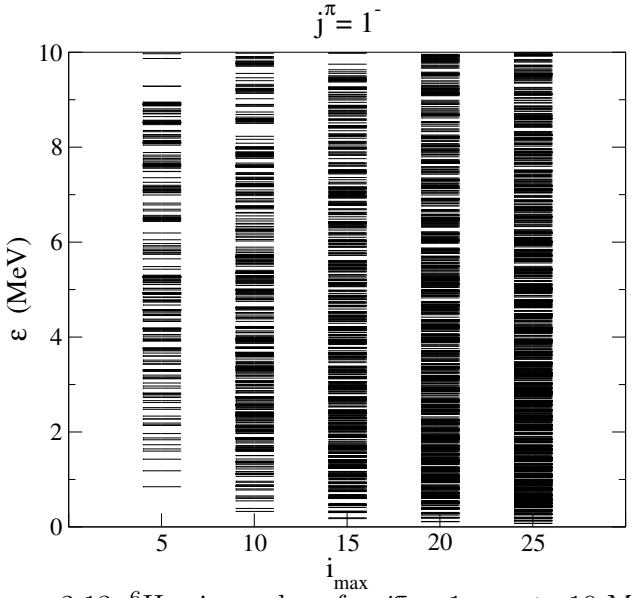

Figure 2.13: ^{6}He eigenvalues for $j^\pi = 1^-$ up to 10 MeV.

Dipole excitations from the ground state to continuum states are the most relevant dynamics in low-energy reactions involving halo nuclei [79, 103]. Thus, excitations from the 0^+ ground state to 1^- continuum states in ^{6}He will be of key importance in describing the system. This is typically reflected by relatively large electric dipolar transition probability strengths, $B(E1)$, at low energies. The Hamiltonian for 1^- states is diagonalized following the already shown prescriptions. Since no reference is available to fit the three-body force for 1^-, the same strength used for 2^+ states is considered. Calculations in this case use an analytical THO basis defined by parameters $b = 0.7$ fm and $\gamma = 1.0$ fm$^{1/2}$. This choice concentrates a large level density near the origin, and enables to build up a very detailed transition probability distribution at low energies. The eigenvalues of the Hamiltonian in this case are presented for different i_{max} values in Fig. 2.13. The comparison of this figure with those for 0^+ and 2^+ states points out the sensitivity of the pseudostate density on the parameters of the analytical transformation defining the basis.

For the evaluation of the transition probabilities, it is convenient to increase further the number of hyperradial excitations included in the calculations. This, together with the hyperradial extension of the basis, ensures a detailed description of the low-energy part of the $B(E1)$ distribution. As previously discussed, the transition probabilities obtained by using a

$i_{\max}$	$\sum B(E1)$ (e^{2}fm^2)
5	1.402
10	1.489
15	1.492
20	1.492
25	1.493
30	1.493
35	1.493

Table 2.3: Sum of $B(E1)$ discrete values, from the 0^+ ground state to 1^- continuum states in ^{6}He, as a function of $i_{\max}$.

discretization method to treat continuum states are a set of discrete values. Before any smoothing procedure, the completeness of the discrete, truncated basis must be evaluated. This can be done by comparing the sum over the discrete $B(E1)$ values, Eq. (2.28), with the sum rule provided by Eq. (2.30), which depends only on the properties of the ground state. For the particular case of a system comprising a charged core and two valence neutrons, the electric operator for dipolar transition (2.16) can be expressed as

$$Q_{1M_1}(\boldsymbol{y}) = \left(\frac{4\pi}{3}\right)^{1/2} Ze\frac{\sqrt{ma_y}}{m_c} y Y_{1M_1}(\widehat{y}), \tag{2.41}$$

where m_c is the mass of the core and Z its charge. Inserting the previous expression in Eq. (2.30) imposes (see appendix B.4.1)

$$S_T(E1) = \sum_n B(E1)_{g.s.,n1} = \frac{3}{4\pi}\frac{Z^2e^2ma_y}{m_c^2}\langle \text{g.s.}|y^2|\text{g.s.}\rangle. \tag{2.42}$$

Table 2.3 shows the sum of $B(E1)$ discrete values between the 0^+ ground state and 1^- continuum states as a function of the number of hyperradial excitations included, i_{max}. The summation converges to the exact value given by the sum rule, 1.493 e^{2}fm^2.

The $B(E1)$ distribution up to 6 MeV, after smoothing using Poisson distributions (see Eq. 2.34) on the discrete values given by Eq. (2.23), is shown in Fig. 2.14. The present calculation, given by the solid black line, uses $i_{max} = 35$. Fig 2.14 also contains a reference calculation obtained by using the actual three-body continuum wave functions which, in this simple case, can be computed easily [24] (dashed red line). To generate the continuum

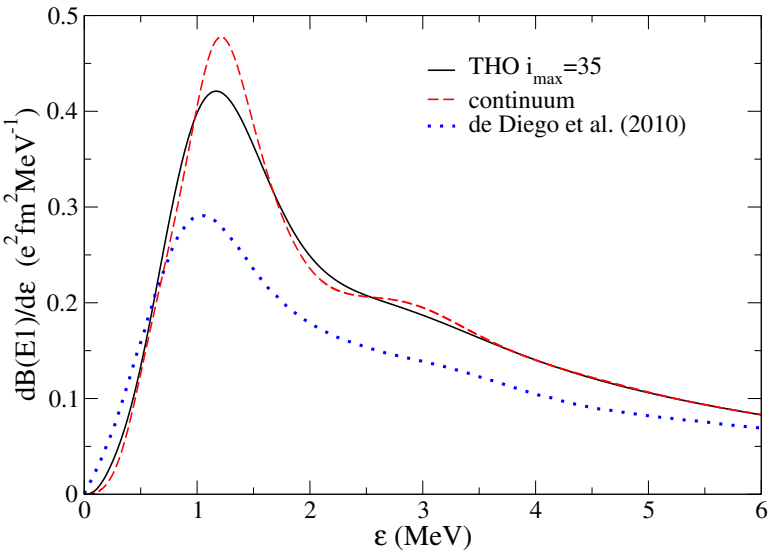

Figure 2.14: $B(E1)$ distribution for ^{6}He up to 6 MeV.

wave functions the codes FaCE [51] and sturmxx [102] have been used, for the same model Hamiltonian. If the smoothing of the THO calculation is done using the overlap with the continuum wave functions, the obtained $B(E1)$ distribution is indistinguishable from the reference one. This guarantees that the formalism presented here works correctly. However, in the case of other systems for which the actual continuum wave functions are difficult to obtain, the alternative smoothing procedure following Eq. (2.34) can provide a reasonable description. The Poisson distribution width parameter has been set to $w = 30\sqrt{\varepsilon_n}$, such that ensures a smooth $B(E1)$ distribution without spreading it unphysically. Due to the large number of basis states near the threshold, an energy dependence of w is convenient to produce a smooth distribution in that region. The total $B(E1)$ strength is the same for both calculations (solid and dashed lines) and the behavior is similar, although small differences are observed in the medium energy range.

It is also included in Fig. 2.14 a calculation taken from Ref. [104]. In that work, the hyperspherical adiabatic expansion method is used instead of the hyperspherical harmonic expansion. Then, the three-body states are calculated by box boundary conditions, obtaining a discrete spectrum. The discrete $B(E1)$ values are smoothed using the finite energy interval approximation. This calculation clearly have a different behavior at low energies. The difference comes from the difficulty to have a large energy level density

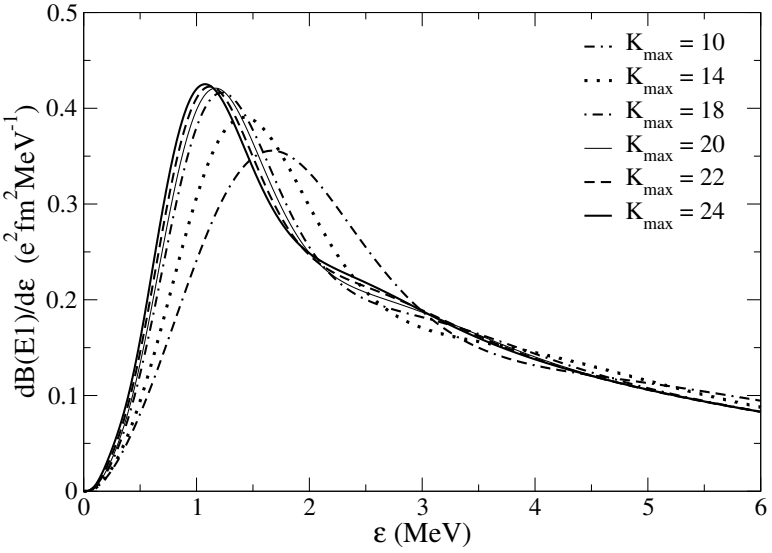

Figure 2.15: $B(E1)$ distribution for ^{6}He up to 6 MeV as $K_{\max}$ increases.

at low energies solving the problem in a box. It is also apparent that the total $B(E1)$ from this calculation is considerably lower than that of the THO method and the reference calculation. In the literature, one can find other $B(E1)$ distributions for ^{6}He using different three-body formalisms, such as [105] and [106], which globally agree with the results here presented. It is worth mentioning that the available experimental data [107] (not shown in Fig. 2.14) differ significantly from all published theoretical calculations. In particular the data do not show the enhancement at energies around 1 MeV. Either new experiment or reanalysis of the existing data is clearly needed. In order to show the convergence of calculations with $K_{\max}$ and that $K_{\max} = 20$ is sufficient to provide converged results, Fig. 2.15 shows the $B(E1)$ distribution for different $K_{\max}$ values. In these calculations the same two- and three-body forces are kept fixed. It is clear from the figure that the calculations for $K_{\max} = 20$, 22, and 24 are very close together.

These results for ^{6}He encourage the application of the analytical THO method to more complex three-body systems. The features and properties discussed here (and in the following sections) will be essential to describe nuclear reactions involving three-body nuclei. In particular, as will be derived in chapter 3, a reliable description of the $B(E1)$ distribution is a key ingredient for the computation of astrophysical three-body reaction rates.

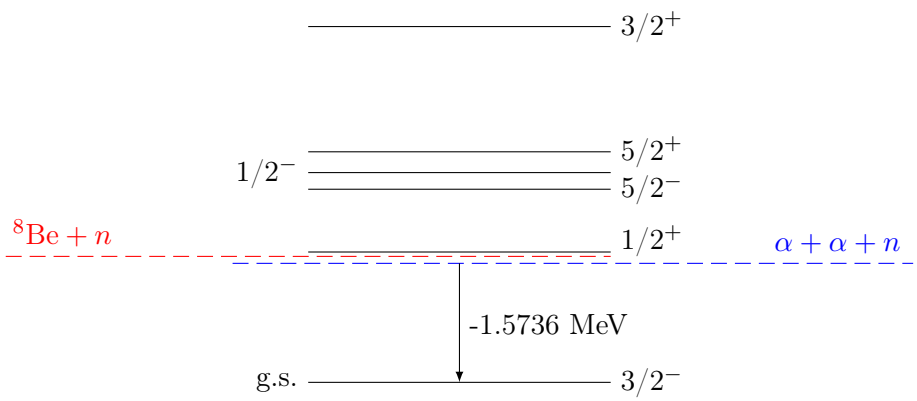

Figure 2.16: Low-lying states of ^{9}Be with respect to the two- and three-body thresholds.

2.4 Application to ^{9}Be

The ^{9}Be nucleus can be described as a three-body system, comprising two α particles and one neutron. Therefore, it shows a Borromean structure, since none of the binary subsystems, ^{5}He nor ^{8}Be, are bound. Unlike ^{6}He, the ^{9}Be nucleus lies on the stability line. Its $3/2^-$ ground state, however, has a small binding energy of 1.5736 MeV below the α+α+n threshold [108]. Information about the matter radius [109, 110], charge radius [101] and quadrupolar deformation [111] of ^{9}Be is also available in the literature, providing an excellent test to the THO method for systems comprising more than one charged cluster. This nucleus presents several low-energy resonances above the two- and three-body thresholds, as shown in Fig. 2.16. The lowest is a genuine three-body $1/2^+$ resonant state around 0.11 MeV with a relatively large width [112]. The spin-parity assignment of other low-lying resonances is still under debate [113].

Although ^{9}Be is not an exotic system in the same sense as ^{6}He and other halo nuclei, its weakly-bound nature and intrinsic three-body structure demand also a proper treatment of continuum states for describing structure and reaction observables. The Jacobi-T set, now connecting the two identical α particles, is used to describe ^{9}Be. This is shown in Fig. 2.17. The α particles are two identical bosons with spin 0^+, so they couple to $S_x = 0$. The symmetry of the wave function under permutation of the two identical particles can be fixed in this case by considering only even l_x components. In

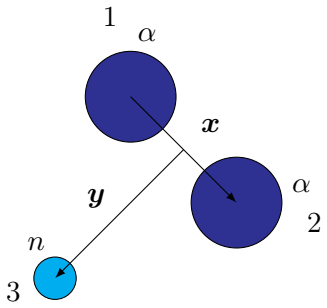

Figure 2.17: Jacobi-T system to describe ^{9}Be.

order to treat properly identical bosons, the FaCE subroutines regarding the generation of the channels β required some changes to distinguish between fermions and bosons. The model Hamiltonian includes α+n and α+α binary interactions adjusted to reproduce the experimental two-body phase shifts. The $\alpha + n$ interaction is the same used for ^{6}He calculations. For the $\alpha + \alpha$ interaction, an Ali-Bodmer-like [114] interaction is used, with only a central term defined by the sum of two Gaussian-shaped functions,

$$V_{\alpha\alpha}^{(l)}(r) = v_R^{(l)} \exp\left[-(r/1.53)^2\right] - 30 \exp\left[-(r/2.85)^2\right]. \tag{2.43}$$

Here, $v_R^{(l)}$ are repulsive terms that account for the α-α Pauli states and need to be different in order to reproduce the experimental phase shifts. Thus, as in the case of the $\alpha - n$ potential, this is an l-dependent interaction. The strength $v_R^{(l)}$ of the potential is taken as 125 MeV for $l = 0$, 20 MeV for $l = 2$, and 0 for the remaining $l > 2$ components. This potential, together with a hard-sphere Coulomb interaction with a Coulomb radius of $r_{\rm Coul} = 2.94$ fm,

$$V_{\alpha\alpha}^{Coul}(r) = Z^2e^2 \times \begin{cases} \left(\frac{3}{2} - \frac{r^2}{2r_{Coul}^2}\right)\frac{1}{r_{Coul}} & ; \quad r \le r_{Coul}, \\ \frac{1}{r} & ; \quad r > r_{Coul}, \end{cases} \tag{2.44}$$

reproduces the exact position of the two-body s-wave ^{8}Be resonance. This is crucial to obtain the right behavior of the low-lying ^{9}Be continuum.

As in the previous example of application, the binary interactions need to be complemented by a structureless hyperradial three-body force in order to fit the known states of the system to their experimentally known energies. The parameters for the three-body force, Eq. (2.40), are fixed to reproduce the energies of the ^{9}Be ground state and the $1/2^+$, $3/2^+$, $5/2^+$, $5/2^-$, and

j^π	v_{3b} (MeV)	r_{3b} (fm)	a_{3b}
$3/2^-$	+1.11	6.1	5
$1/2^+$	−2.45	6.1	5
$3/2^+$	−1.60	6.1	5
$5/2^+$	−0.18	6.1	5
$5/2^-$	+1.65	6.1	5
$1/2^-$	+0.20	6.1	5

Table 2.4: Three-body force parameters for each j^π configuration in ^{9}Be.

$1/2^-$ resonances. The values of these parameters are again different for each j^π, and they are given in Table 2.4.

The $3/2^-$ states are described with an analytical THO basis defined by parameters $b = 0.7$ fm, and $\gamma = 1.4$ fm$^{1/2}$, which minimizes the size of the basis needed to reach convergence of the ground state. In Figs. 2.18 and 2.19, the convergence of the ground-state energy and the matter and charge radii with respect to the maximum hypermomentum $K_{\max}$ is shown, with $i_{\max}$ fixed to 20. From Fig. 2.18, the value $K_{\max} = 30$ provides a well converged ground state with energy $\varepsilon_B = -1.5736$ MeV, fixed to the experimental value in Ref. [108]. Assuming that the α particle matter and charge radii are 1.47 and 1.6755 fm, respectively, the computed ^{9}Be ground state charge and matter radii are $r_{\rm ch} = 2.508$ fm and $r_{\rm mat} = 2.466$ fm. For the charge radius, calculations are in agreement with the experimental value of 2.519 ± 0.012 fm [101]. This reveals that the method is rather accurate. For the matter radius, the computed value is larger than that given in Ref. [109], 2.38 ± 0.01 fm, obtained with Glauber-model calculations from interaction cross sections at high energies. A different estimation from a simple microscopic model by using cross sections at intermediate energies gives a radius of 2.53 ± 0.07 fm [110], in better agreement with the present results. It has been pointed out [115] that the optical limit approximation of Glauber models, such as in Ref. [109], may underestimate the radius of loosely bound systems. In halo nuclei, the few-body structure implies strong spatial correlations between the core and valence nucleons, so the optical limit fails. ^{9}Be is not a halo system but it shows a strong few-body intrinsic configuration with the two α particles loosely bound by the remaining neutron, so the usual estimations of its radius from interaction cross sections may be misleading.

In this case, the system comprises two charged particles, and therefore the expression for the electric operator is not as simple as in the case of

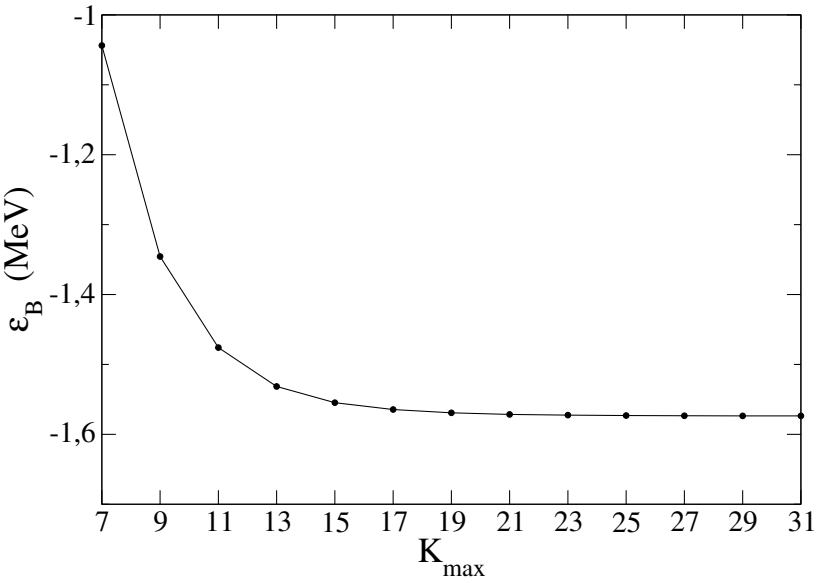

Figure 2.18: Convergence of the ground-state energy of ^{9}Be with respect to the maximum hypermomentum $K_{\max}$.

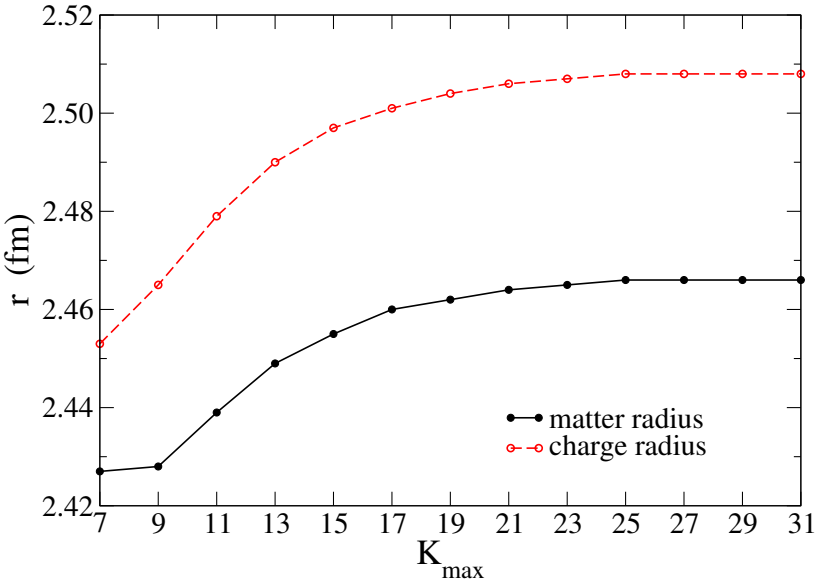

Figure 2.19: Convergence of the matter radius (solid line) and the charge radius (dashed line) of ^{9}Be with respect to the maximum hypermomentum $K_{\max}$.

$i_{\max}$	ε_B (MeV)	$r_{\rm mat}$ (fm)	$r_{\rm ch}$ (fm)	$S_T(E1)$ (e^2fm^2)
5	−1.5659	2.453	2.502	0.5565
10	−1.5734	2.465	2.507	0.5760
15	−1.5736	2.466	2.508	0.5762
20	−1.5736	2.466	2.508	0.5762
25	−1.5736	2.466	2.508	0.5762

Table 2.5: ^{9}Be ground-state energy ε_B, matter radius $r_{\rm mat}$, charge radius $r_{\rm ch}$ and sum rule $S_T(E1)$ as a function of $i_{\max}$ with $K_{\max} = 30$. A fast convergence is observed.

^{6}He. Using the relationship between harmonic polynomials in different Jacobi sets, given by Eq. (2.26), the electric operator for dipolar transitions can be written as

$$Q_{1M_1}(\boldsymbol{y}) = -\left(\frac{4\pi}{3}\right)^{1/2} 2(\cos\varphi_{23}) Z_2 e \frac{\sqrt{m a_{y2}}}{m_2} y Y_{1M_1}(\widehat{y}), \tag{2.45}$$

where indexes 2 and 3 refer to the α particle and the neutron labeled in Fig. 2.17, and φ_{23} is the mass-dependent phase given by Eq. (2.27). This expression is analogous to Eq. (2.41) for the case of ^{6}He, but including a factor $2(\cos\varphi_{23})$ which, for ^{9}Be, equals $2/\sqrt{10}$. With the above-given definition, the sum rule (2.30) for electric dipolar transitions from the ground state is given by

$$S_T(E1) = \sum_{nj} B(E1)_{g.s.,nj} = \frac{3}{4\pi} \frac{Z_2^2 e^2 m a_{y2}}{m_2^2} (2\cos\varphi_{23})^2 \langle \text{g.s.}|y^2|\text{g.s.}\rangle. \tag{2.46}$$

The convergence of the ground-state energy, its matter radius, the charge radius and the sum rule for electric dipolar transitions, as the number of hyperradial excitations $i_{\max}$ increases, is shown in Table 2.5. Calculations are performed for a fixed value of $K_{\max} = 30$, for which a rapid convergence is observed.

One of the consequences of the three-body structure of ^{9}Be is its large quadrupolar deformation, given by the system quadrupole moment $Q = 5.29 \pm 0.04$ e fm^2 [111]. The quadrupole moment is defined as

$$Q = \sqrt{\frac{16\pi}{5}} \langle n_0 j_0 j_0 | \widehat{Q}'_{20} | n_0 j_0 j_0 \rangle, \tag{2.47}$$

where $|n_0 j_0 j_0\rangle$ represents the ground-state wave function with angular momentum j_0 and maximum projection. This is the usual definition of Q, where the quadrupolar operator $\widehat{Q}'_{20}$ does not include the factor $\sqrt{4\pi/(2\lambda+1)}$ used in the notation from Brink and Satchler [82]. For a system comprising two identical charged particles described in the Jacobi-T set, this operator is

$$\widehat{Q}'_{2M_\lambda} = 2Z_2 e \frac{m a_{y_2}}{m_2^2} \left[(\sin\varphi_{23})^2 \, x^2 Y_{2M_\lambda}(\widehat{x}) + (\cos\varphi_{23})^2 \, y^2 Y_{2M_\lambda}(\widehat{y}) \right]. \quad (2.48)$$

For ^{9}Be, $\cos\varphi_{23} = 1/\sqrt{10}$ and $\sin\varphi_{23} = 3/\sqrt{10}$. Inserting (2.48) into Eq. (2.47) leads to the final expression

$$\begin{aligned} Q = \sqrt{\frac{16\pi}{5}} \langle n_0 j_0 j_0 | \widehat{Q'}_{20} | n_0 j_0 j_0 \rangle = \sqrt{\frac{16\pi}{5}} 2Z_2 e \frac{m a_{y2}}{m_2^2} \\ \times \langle n_0 j_0 j_0 | \, (\sin\varphi_{23})^2 \, x^2 Y_{20}(\widehat{x}) + (\cos\varphi_{23})^2 \, y^2 Y_{20}(\widehat{y}) | n_0 j_0 j_0 \rangle. \end{aligned} \quad (2.49)$$

The full derivation of this and other electromagnetic operator expressions, as well as its corresponding expansions in the THO basis, are shown with detail in appendix B. The three-body model provides a good description of the system deformation due to the alpha-alpha cluster configuration, and gives a quadrupole moment of 4.91 e fm^2, which is close to the experimental value. The system deformation can be clearly appreciated by plotting the probability distribution of the ground state. This is shown in Fig. 2.20, in a two-dimensional plot where $r_x = r_{\alpha\text{-}\alpha}$ and $r_y = r_{(\alpha\alpha)\text{-}n}$. The figure shows a maximum near $r_x \simeq 3$ fm and $r_y \simeq 2.5$ fm. This α-α distance is similar to the value found for the ground state of ^{12}C [22], and is also consistent with previous estimations for ^{9}Be [116].

Unlike ^{6}He, the ^{9}Be nucleus has half-integer angular momenta. This results in a splitting of the $B(\mathcal{O}\lambda)$ strength from the ground state to different j^π contributions. For instance, the $B(E1)$ strength will be distributed between $1/2^+$, $3/2^+$, and $5/2^+$ states, all connected to the ground state by electric dipolar transitions. The first resonance in ^{9}Be is a $1/2^+$ state at 0.11 MeV above the three-body threshold [108]. The structure of this state arises from three-body spatial correlations, and previous studies considering a two-body ^{8}Be-n resonance or a virtual state are inconsistent [112]. Only a three-body model can account for its relatively large width. The corresponding $B(E1)$ distribution from the ground state will show a broad peak just above the breakup threshold, with a large tail exploring higher energies. This is not the

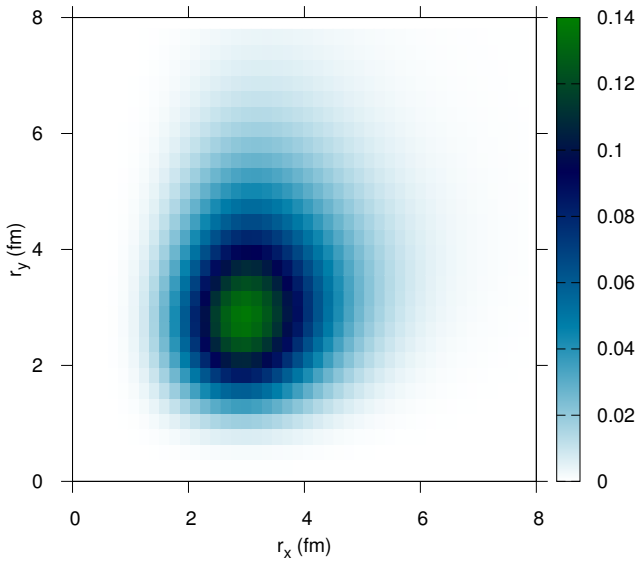

Figure 2.20: Two-dimensional probability of the ^{9}Be ground state.

typical behavior of low-energy resonances, which present usually a narrow distribution.

To get a well defined $B(E1)$ distribution at low energies, the Hamiltonian is diagonalized in a THO basis defined by parameters $b = 0.7$ fm and $\gamma = 0.7$ fm$^{1/2}$. Calculations, however, show a very slow convergence with respect to $K_{\max}$ for the low-energy $1/2^+$ continuum. The structure of the $1/2^+$ resonance is not well described with $K_{\max}$ values around 30-40, and going to larger hypermomenta involves the computation of very large basis sets, which is limited by computer power and calculation times. Since the $1/2^+$ resonance decay is known to proceed mainly through the two-body low-lying s-wave ^{8}Be resonance [112], the three-body resonance is expected to be mainly governed by α-α s-wave components. Thus, $K_{\max}$ can be fixed to 40, and the maximum hypermomentum for s-waves, $K^s_{\max}$, is further increased. Fig. 2.21 shows the $B(E1)$ distribution to $1/2^+$ states, as a function of $K^s_{\max}$. For these calculations, the THO basis includes $i_{\max} = 30$ hyperradial excitations, and the discrete values are smoothed using Poisson distributions with a width parameter $w = 30$. It can be clearly seen that

the structure of the resonance is strongly dependent on $K^s_{\max}$ and very large values are needed to reach convergence. For this reason, $K^s_{\max}$ is fixed to 140, maintaining the global $K_{\max} = 40$ for all the other partial waves.

Concerning the width of the Poisson distributions, w, note that it must ensure a smooth $B(E1)$ distribution without spreading it unphysically. As an example, Fig. 2.22 shows the $B(E1)$ distribution to the $1/2^+$ states calculated with different width parameters. For w values smaller than 30, the distributions are too wide to represent the PS energy distributions, and consequently the final distributions will not be able to reproduce the experimental width. For much larger values, however, the final distributions are distorted and show unphysical oscillations or peaks. This provides a possible prescription to select the optimal w value, choosing w as large as possible. In this case $w = 30$ is a reasonable choice.

The $3/2^+$, $5/2^+$, $1/2^-$ and $5/2^-$ resonances in ^{9}Be have excitation energies of 3.131, 1.475, 1.206 and 0.856 MeV, respectively [108]. The positive-parity states, as in the case of $1/2^+$, are connected to the ground state by E1 transitions. The sum over discrete $B(E1)$ values for the three contributions converges to the value given by the sum rule in Table 2.5, 0.576 $\mathrm{e^2fm^2}$. However, to populate $5/2^-$ or $1/2^-$ states one needs M1 or E2 transitions. The $5/2^-$ resonance presents a small width, which implies a very narrow peak in the corresponding transition probability. To illustrate this, the $B(M1)$ distribution will be shown.

The $5/2^-$ states are described with a THO basis defined by parameters $b = 0.7$ fm and $\gamma = 1.0$ $\mathrm{fm}^{1/2}$, that ensures enough states at low energies. The maximum hypermomentum is fixed to $K_{\max} = 30$, large enough to get converged strength distributions in this case, and $i_{\max}$ is taken as 30. The convergence problem shown in the previous case is absent here, since the properties of the resonance are less sensitive to the α-α s-wave contribution. Notice that, in order to fit the resonance to its experimentally known energy, the three-body potential strength v_{3b} has to be different. Section 2.2.2 provides all necessary expressions to compute magnetic transitions, which depend on the orbital and spin g factors of each particle. The α particles have spin zero, so it is reasonable to fix $g_s^{(\alpha)} = 0$, and $g_l^{(\alpha)}$ is taken as its charge. For the neutron it is customary to use the free value of $g_s^{(n)} = -3.82$, and no effective charge is assigned, i.e., $g_l^{(n)} = 0$. It is known that the effective g factor are rather uncertain [85], especially $g_s^{(n)}$ which could be reduced by

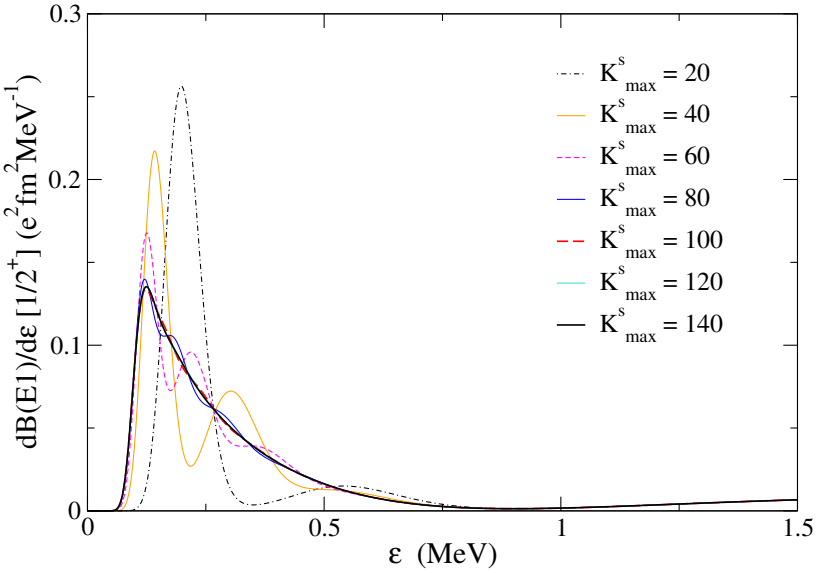

Figure 2.21: Dependence of the $1/2^+$ contribution to the ^{9}Be $B(E1)$ distribution on $K^s_{\max}$. Small K^s_{max} values do not provide converged results.

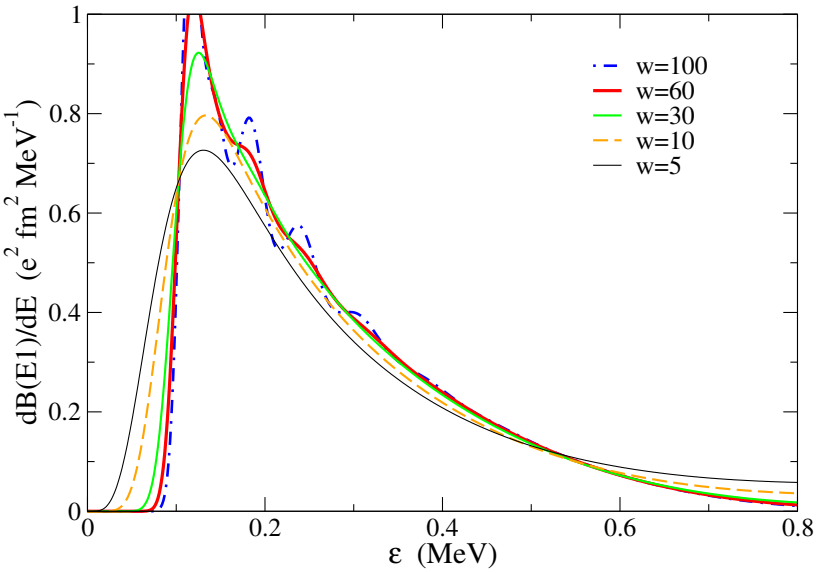

Figure 2.22: $B(E1)$ distribution to the $1/2^+$ states in ^{9}Be as a function of the Poisson width parameter w.

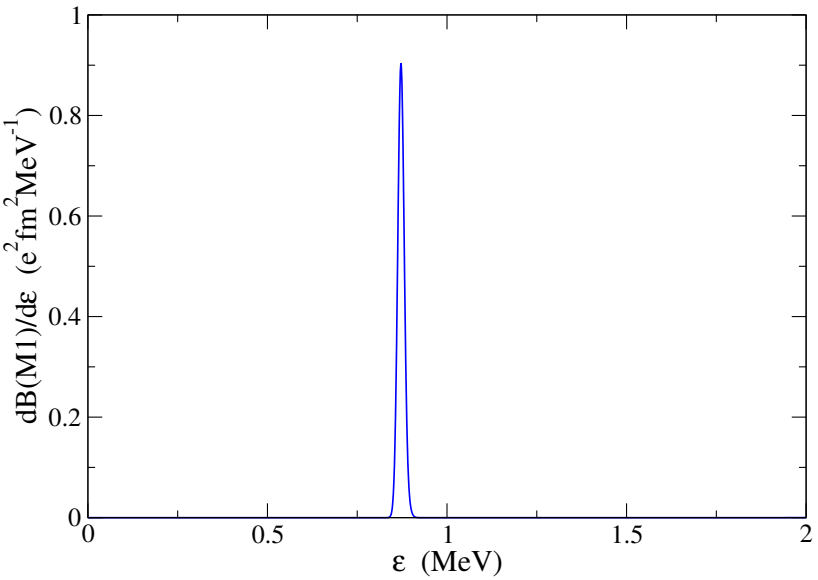

Figure 2.23: $B(M1)$ distribution to the $5/2^-$ states in ^{9}Be. The narrow peak corresponds to the experimental resonance at 0.856 MeV.

a factor of 2 due to spin polarization. This introduces an uncertainty in the corresponding magnetic transition probabilities which, in any case, will not change the order of magnitude. For the $5/2^-$ states a larger width parameter, which produces narrower distributions, is required, since the experimental width for the $5/2^-$ resonance is known to be extremely small. This was previously reported in Ref. [23], where a value of $w = 1300$ was used to describe properly the width of the narrow 2^+ resonance in ^{6}He. Thus, it is convenient fix $w = 10000$ around the resonance energy, keeping $w = 30$ for the non-resonant region. The magnetic transition probability distribution so obtained is shown in Fig. 2.23, which is consistent with the narrow $5/2^-$ state reported in the literature [117].

The present results support the reliability of the method in describing the ^{9}Be wave functions within a three-body approach. The pseudostate method in an appropriate Jacobi set enables the proper treatment of a system comprising two identical charged bosons. The formation of this nucleus will be addressed in the next chapter considering different j^π configurations. In chapter 4, the ^{9}Be wave functions will be used to describe reactions induced by this nucleus in a four-body framework, considering a three-body projectile plus a structureless target.

2.5 Application to ^{17}Ne

The ^{17}Ne nucleus can be seen as a three-body system comprising an ^{15}O core and two valence protons. It is a Borromean system, since ^{16}F and the diproton are not bound. This nucleus has attracted special interest over the last few years for two main reasons: i) it is the most promising known candidate to present a two proton halo, and ii) its formation through two proton capture can break out of the hot CNO cycle, with important implications for the rp-process. Despite the remarkable theoretical efforts to address the structure of ^{17}Ne, controversy still exists [118, 119]. The halo nature of ^{17}Ne has not yet been confirmed.

Compared with the previous cases of ^{6}He and ^{9}Be, a three-body model for ^{17}Ne needs to deal with the complication that the corresponding ^{15}O core has non-vanishing spin. Core excitations could play a relevant role in describing the structure and dynamics of ^{17}Ne. However, all the lowest excited states in the ^{15}O-core occur with positive parities between 5 and 9 MeV, with a single exception of $3/2^-$ about 6 MeV [120]. The ground state, first and second resonances in ^{17}Ne have negative parity and energies of -0.94 ($1/2^-$), 0.34 ($3/2^-$) and 0.82 MeV ($5/2^-$) from the two-proton separation threshold [121, 122]. This is shown in Fig. 2.24. These energies are small compared to the lowest-lying core-excited state, which would need to be combined with proton valence states of negative parity, only available in the next shell, to contribute in the states of ^{17}Ne [118]. Contributions to negative-parity ^{17}Ne states from the $3/2^-$ core-state at 6 MeV are the most likely, but its energy is relatively high. The same applies for contributions to the third excited, $1/2^+$ state in ^{17}Ne, from the other core states. Therefore, the assumption of a structureless core seems to be a reliable picture, although the effect of core excitations should be explicitly studied.

The same method applied to ^{6}He and ^{9}Be in the preceding sections will be employed to describe the structure of ^{17}Ne. Notice that, in addition to the core-excitation problem, a three-body model for ^{17}Ne comprises three charged particles. The computation of actual continuum states for a system of three-charged particles has no general solution. For that reason, the pseudostate method will be tested against this more complicated system. The Jacobi-T system is again used in this case, as shown in Fig. 2.25, where the two identical protons are related by coordinate $\boldsymbol{x}$. This choice enables

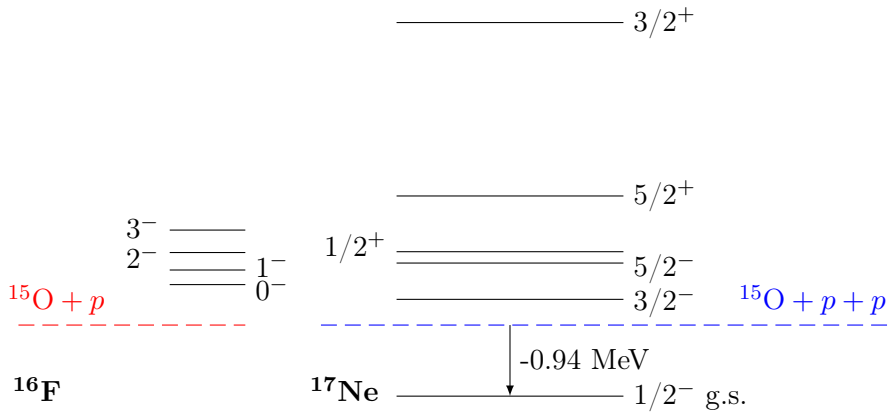

Figure 2.24: Low-lying states of ^{17}Ne and the ^{16}F (p + ^{15}O) subsystem. The energies are given with respect to the $2p$ and p thresholds, respectively.

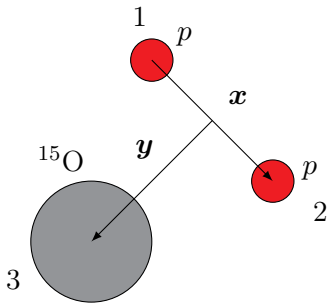

Figure 2.25: The Jacobi-T system used to describe the ^{17}Ne nucleus.

the proper treatment of the Pauli principle by removing the corresponding components of the wave functions that would disappear under antisymmetrization (see the case of two identical neutrons for ^{6}He). The model Hamiltonian for ^{17}Ne uses the p-p GPT potential [99], formally equivalent to the n-n interaction but including also the Coulomb repulsion. For the ^{15}O-p interaction, some prescription is needed to fit the potentials. Since there is no available experimental information on the scattering phase shifts, a possibility is to select the potential to fit the known resonances of the unbound system ^{16}F. The lowest negative-parity states in ^{16}F are shown together with the ^{17}Ne states in Fig. 2.24. Higher-energy states are also considered to adjust the potential. The available experimental data [123] on these states is shown in Table 2.6. The resulting ^{15}O-p interaction has central V_c, spin-orbit V_{so}, and spin-spin V_{ss} components. The central part follows the Woods-Saxon form in Eq. (2.38), with l-dependent strengths:

j^π	(E_R, Γ) (MeV)	j^π	(E_R, Γ) (MeV)
0^-	(0.535, 0.040)	1^+	(4.29, < 0.040)
1^-	(0.728, < 0.040)	2^+	(4.41, < 0.020)
2^-	(0.959, 0.040)	1^-	(5.81, –)
3^-	(1.256, < 0.015)	2^-	–

Table 2.6: Experimental two-body spectrum for ^{16}F [123]. Since the system is unbound, the values are given as the resonance energy and the corresponding width, (E_R, Γ).

l	v_c (MeV)	r_c (fm)	a_c (fm)
s	-50.0	3.13	0.67
p	-11.0	3.13	0.67
d	-48.4	3.13	0.67

The spin-orbit potential for the proton spin, $\boldsymbol{l_x} \cdot \boldsymbol{s_p}$, is given by a Woods-Saxon form in Eq. (2.39) with parameters:

$v_{\rm so}$ (MeV fm^2)	$r_{\rm so}$ (fm)	$a_{\rm so}$ (fm)
-30.0	3.13	0.67

Finally, the spin-spin potential, $\boldsymbol{s}_{\rm core} \cdot \boldsymbol{s_p}$, is a Woods-Saxon with the following parameters for each l component:

l	v_{ss} (MeV)	r_{ss} (fm)	a_{ss} (fm)
s	0.7	3.13	3.13
p	1.0	3.13	3.13
d	2.0	3.13	3.13

This potentials present unphysical bound states that correspond to the $s_{1/2}$ states occupied in the ^{15}O core. The Pauli principle has to be taken into account by forbidding these two-body states within the three-body calculations. This is achieved by using the adiabatic projection method [65] to eliminate the Pauli forbidden states. This potential, together with a hard-sphere Coulomb interaction (see Eq. (2.44)) with a Coulomb radius of $r_{\rm Coul} = 3.13$ fm, reproduces the experimental energies of the two-body ^{16}F resonances.

The three-body force used in this case has a Gaussian form,

$$V_{3b}(\rho) = v_{3b} \exp\Big[-(\rho/\rho_0)^2\Big], \tag{2.50}$$

which parameters are fixed to reproduce the energies of the ^{17}Ne ground state and the $3/2^-$, $5/2^-$, $1/2^+$, $5/2^+$ resonances. The $3/2^+$ is very high and its position is therefore not crucial. For that reason, no three-body force is included for $3/2^+$ states. The values of the three-body force parameters are:

j^π	v_{3b} (MeV)	ρ_0 (fm)
$1/2^-$	-1.94	5
$3/2^-$	-2.40	5
$5/2^-$	-4.25	5
$1/2^+$	-6.75	5
$5/2^+$	-1.00	5
$3/2^+$	–	–

To describe the ground state of ^{17}Ne, the $1/2^-$ states are obtained in an analytical THO basis defined by parameters $b = 0.7$ fm and $\gamma = 1.4$ fm$^{1/2}$. The convergence of the ground state with respect to the size of the model space, given by the maximum hypermomentum K_{max}, is found to be slower than in the previous examples. This is shown in Fig 2.26 for the ground state energy. This behavior is associated to the presence of three charged particles, which enhances Coulomb effects, and therefore the convergence of the hyperspherical expansion becomes slower. In Fig. 2.27, the convergence of the matter and charge radii is shown. These calculations are performed with a fixed value of $i_{max} = 20$. To achieve converged energy and radii, K_{max} has to be fixed to 30. With a ground state energy of -0.943 MeV, the computed matter and charge radii of ^{17}Ne result 2.78 and 2.92 fm, respectively. The calculated matter radius is in good agreement with the available experimental data of $r_{mat} = 2.75(7)$ fm [124]. For the charge radius, the present result underestimate the experimental value of $r_{ch} = 3.042(21)$ fm [125]. This could be a consequence of the approximations within the model. Nevertheless, the three-body model with the two-body interactions presented above describe the overall features of the system spatial distribution, with a charge radius being substantially large than the matter radius, as expected for a system comprising two valence protons. The ground-state probability distribution for ^{17}Ne in the Jacobi-T set is shown in Fig. 2.28, where r_x refers to the distance between the two valence proton. A prominent peak is observed for $r_x \simeq 2.5$ fm and $r_y \simeq 3$ fm. Another smaller peak is found for corresponding distances of about 5 and 1 fm, respectively. The third peak between the

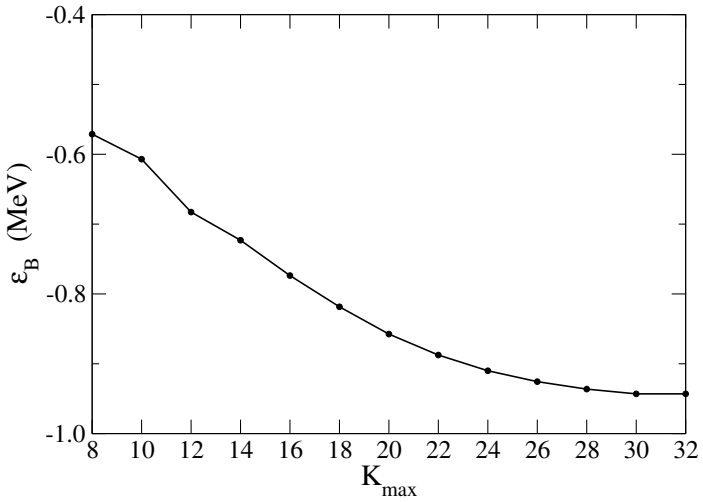

Figure 2.26: Convergence of the ground-state energy of ^{17}Ne with respect to the maximum hypermomentum $K_{\max}$.

other two is defined by $r_x \simeq 4$ fm and $r_y \simeq 2$ fm. The first two peaks can be described as two protons either on the same side of the core or at almost opposite sides. The third peak accounts for intermediate configurations.

In this case, the system includes three charged particles. If the two particles related by coordinate $\boldsymbol{x}$ are identical, such as the two protons in ^{17}Ne, the electric dipolar operator in the Jacobi-T set can be obtained as a sum of the Eqs. (2.41) and (2.45),

$$\widehat{Q}_{1M_\lambda} = \left(\frac{4\pi}{3}\right)^{1/2} \left[Z_3 e \frac{\sqrt{m a_{y_3}}}{m_3} - 2\ Z_2 e\,(\cos\varphi_{23})\,\frac{\sqrt{m a_{y_2}}}{m_2} \right]\ y Y_{1M_\lambda}(\widehat{y}), \tag{2.51}$$

where the charge and mass factors are different for the ^{15}O (labeled as 3) and the protons (labeled as 2). Then, the sum rule for dipolar transition (2.30) in this case is

$$S_T(E1) = \frac{3}{4\pi} \left[Z_3 e \frac{\sqrt{m a_{y_3}}}{m_3} - 2\ Z_2 e\,(\cos\varphi_{23})\,\frac{\sqrt{m a_{y_2}}}{m_2} \right]^2 \langle n_0 j_0 \mu_0 | y^2 | n_0 j_0 \mu_0 \rangle. \tag{2.52}$$

Here, Z_3, m_3 and Z_2, m_2 are the charge and mass numbers of ^{15}O and the proton, respectively, a_{y_3} and a_{y_2} are the Jacobi y-coordinate scales in the T and Y[1] sets, and $\cos\varphi_{23}$ is simply given by Eq. (2.27).

[1]For halo nuclei, it is common to call Jacobi-Y set the system where one valence nucleon is out the $\boldsymbol{x}$ coordinate.

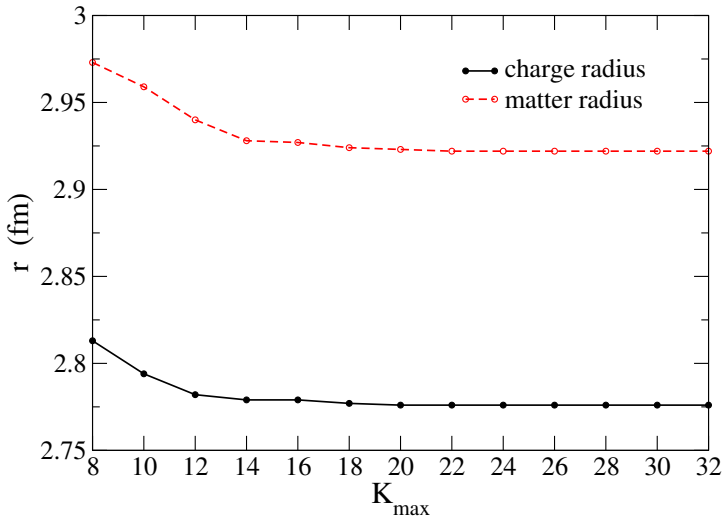

Figure 2.27: Convergence of the matter radius (solid line) and the charge radius (dashed line) of ^{17}Ne with respect to the maximum hypermomentum $K_{\max}$.

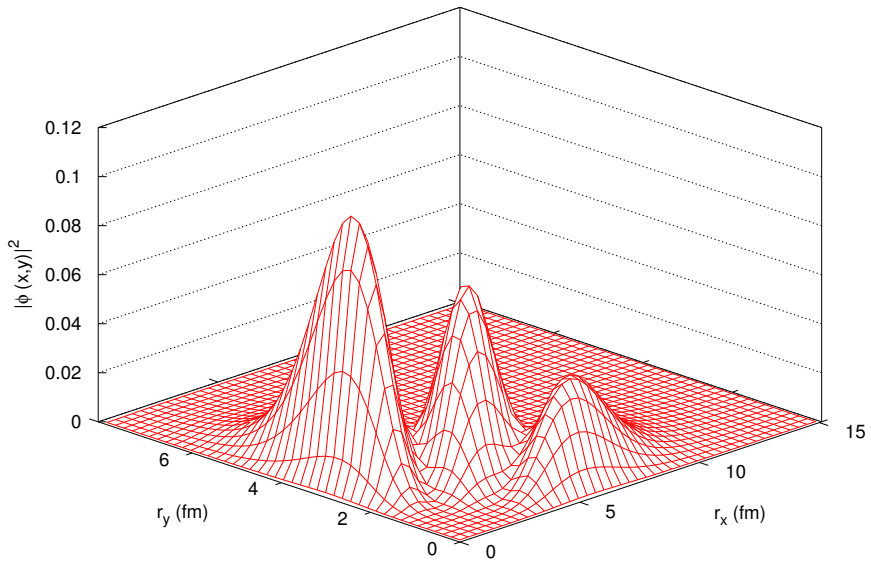

Figure 2.28: Probability distribution of the ^{17}Ne ground state.

$i_{\max}$	ε_B (MeV)	$r_{\rm mat}$ (fm)	$r_{\rm ch}$ (fm)	$S_T(E1)$ (e^2fm^2)
5	−0.5260	2.805	2.968	1.820
10	−0.8959	2.778	2.923	1.690
15	−0.9351	2.776	2.922	1.689
20	−0.9431	2.776	2.922	1.687
25	−0.9431	2.776	2.922	1.687

Table 2.7: ^{17}Ne ground-state energy ε_B, matter radius $r_{\rm mat}$, charge radius $r_{\rm ch}$ and sum rule $S_T(E1)$ as a function of $i_{\max}$ with $K_{\max} = 30$.

l_x	l_y	l	S_x	j_{ab}	$W(^{17}\text{Ne})$
0	0	0	0.0	0.0	82.0
1	1	1	1.0	0.0	12.9
2	2	0	0.0	0.0	4.5
0	0	0	0.0	0.0	9.7
0	0	0	1.0	1.0	32.1
2	2	0	0.0	0.0	10.4
2	2	1	1.0	0.0	2.9
2	2	1	0.0	1.0	3.7
2	2	0	1.0	1.0	28.1
2	2	1	1.0	1.0	6.6
1	1	0	0.0	0.0	1.5
1	1	0	1.0	1.0	4.5

Table 2.8: Angular components included for the $1/2^-$ ground state of ^{17}Ne in the Jacobi-T (upper part) and Jacobi-Y (lower part) sets. $W(^{17}\text{Ne})$ indicates the contribution to the total norm of the wave function. Only those components contributing more than 1% are given.

The convergence of the ground-state energy of ^{17}Ne, its matter radius, the charge radius and the sum rule for electric dipolar transitions, as the number of hyperradial excitations $i_{\max}$ increases, is shown in Table 2.7. Calculations are performed for a fixed value of $K_{\max} = 30$.

As in the case of ^{6}He previously presented, the ground state wave function of ^{17}Ne is dominated, in the Jacobi-T set, by s-wave components. This is shown in the upper part of Table 2.8, where the percentage of the total norm provided by each angular components $\{l_x, l_y, l, S_x, j_{ab}\}$ is given. The main contribution of 82% corresponds to $l_x = l_y = 0$ components, while $l_x = l_y = 2$ contains less than 5% of the norm. This does not provide information about the l content of the single particle proton wave function, which is hindered in the Jacobi-T set. To see these contributions, a rotation to the Jacobi-Y

set, where $\boldsymbol{x}$ connects the ^{15}O core and one proton, can be performed. This has already been used for the computation of electromagnetic transition probabilities (see section 2.2.2). The results are also shown in the lower part of Table 2.8. In that case, d waves contribute with roughly 52%, while 42% of the norm comes from s waves. A similar result was found previously by Garrido *et al.* [118] for the ground state of ^{17}Ne. Even though d waves have a important contribution, these numbers support the existence of a proton halo in ^{17}Ne [126], which is only suppressed for larger d-wave norms. This is also consistent with the experimental evidences of this nucleus showing a halo-like dilute tail in the density and charge distributions [119, 125]. However, previous data on reaction cross sections suggested that ^{17}Ne is not as large as typical halo nuclei [127]. This debate about the structure of ^{17}Ne is still unresolved. Since the Coulomb barrier prevents proton-halo formation, the number of known halo nuclides on the neutron-deficient side is smaller than that on the neutron-rich side. More experimental and theoretical efforts are required to shed some light on these questions.

The $3/2^-$, $5/2^-$, $1/2^+$, $5/2^+$ and $3/2^+$ states in ^{17}Ne can also been computed with the analytical THO method. For $3/2^-$, $5/2^-$ and $1/2^+$, the system exhibit narrow resonances at 0.34, 0.82 and 0.97 MeV, respectively [122]. The $5/2^+$ and $3/2^+$ resonances appear at higher energies and therefore have a broad energy distribution [121]. A good knowledge of the transition probabilities between these states and the ground state of the system can be essential to describe different processes where the continuum is involved. Considering only E1, M1 and E2 transitions, as in the case of ^{9}Be, electromagnetic excitations from the $1/2^-$ ground state can populate all the above-mentioned j^π states but $5/2^+$.

In this section, the case of $1/2^+$ states will be addressed in detail. The others will be relevant in chapter 3 and will be discussed therein. To isolate and identify the resonance, $1/2^+$ states are computed in an analytical THO basis defined by parameters $b = 0.7$ fm and $\gamma = 2.0$ fm$^{1/2}$. This choice decreases the level density at lower energies, implying that a single pseudostate carries the resonant behavior. Calculations are performed with $K_{max} = 30$, and the corresponding spectra for an increasing number of hyperradial excitations i_{max} is shown in Fig. 2.29. After fitting the spectrum with the three-body force, the lowest state stabilizes around the experimental resonance energy, 0.97 MeV.

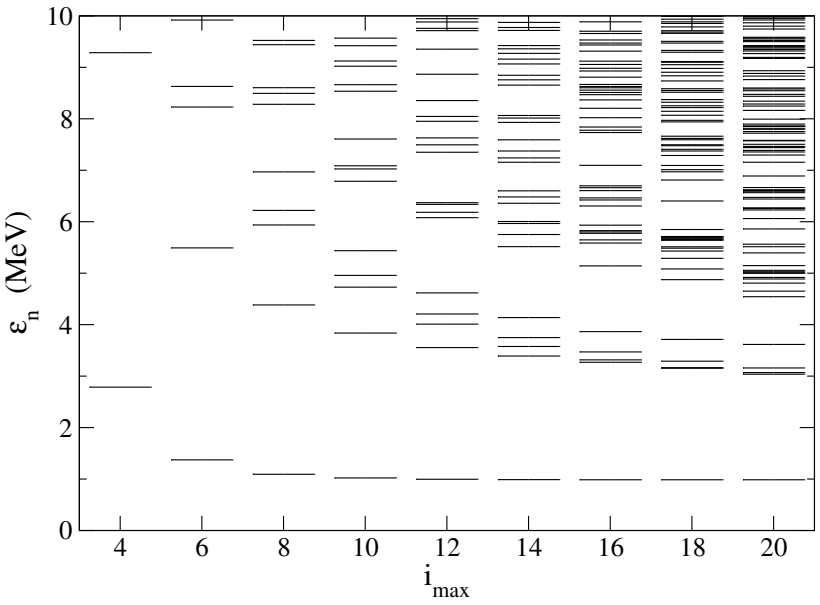

Figure 2.29: ^{17}Ne eigenvalues for $j^\pi = 1/2^+$ up to 10 MeV, as a function of the size of the basis given by i_{max}. Calculations are truncated at maximum hypermomentum $K_{max} = 30$. The lowest state, using a proper basis, is stable and carries the resonant behavior.

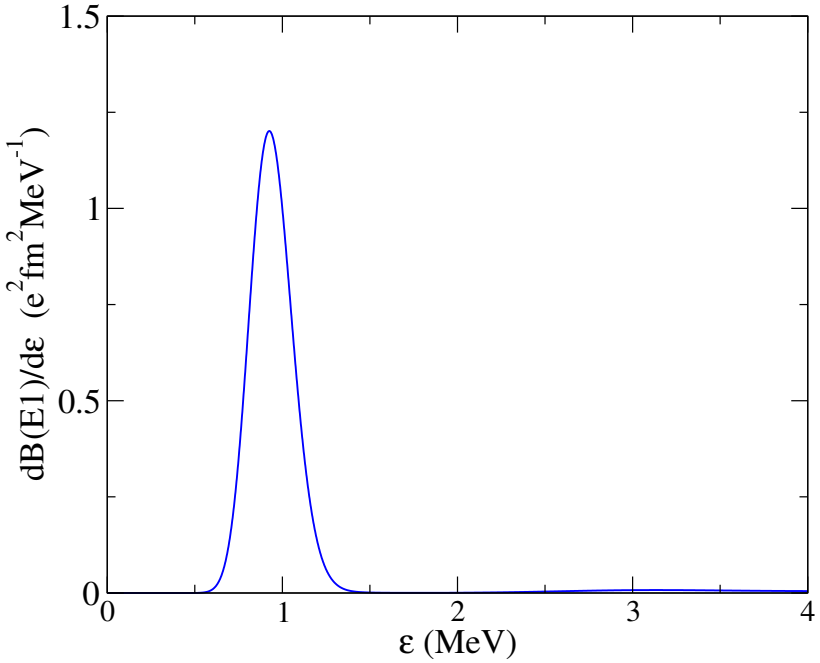

Figure 2.30: $B(E1)$ transition probability distribution from the $1/2^-$ ground state to $1/2^+$ continuum states in ^{17}Ne. The discrete values are smoothed using a Poisson distribution defined by $w = 60$.

In order to compute the corresponding transition probabilities between the ground state and $1/2^+$ states, the analytical basis parameter γ is changed from 1.4 to 1.0 fm$^{1/2}$. This produces a larger level density around the resonance, and allow to map the low-energy continuum with detail. The discrete values are then smoothed by using Poisson distributions with a width parameter of $w = 60$. The results are shown in Fig. 2.30. From this figure, it is clear that almost all the E1 strength goes to the resonance. The sum over all $B(E1)$ discrete values for transitions to $1/2^+$ states is 0.562 e^{2}fm^2. This value is far below the result provided by the sum rule in Table 2.7, 1.687 e^{2}fm^2. It has been checked that the remaining E1 strength is covered by transitions to $3/2^+$ states at higher energies.

In this chapter, the analytical THO method for three-body systems has been presented and applied to three different nuclei: ^{6}He, ^{9}Be and ^{17}Ne, comprising one, two and three-charged particles, respectively. The resulting wave functions provide a good description of the nuclear properties of these nuclei, and the comparison with experimental data (when available) supports the reliability of the method to describe Borromean systems. The three-body wave functions and transition probability distributions obtained here will be used as key ingredients for the applications presented in the following chapters.

Chapter 3

Radiative capture reactions

The cosmos is also within us. We're made of star-stuff. We are a way for the cosmos to know itself.

Carl Sagan

In this chapter, results from chapter 2 are used to calculate reaction rates of astrophysical interest. First, the three-body radiative capture reaction rate is obtained from the inverse photodissociation process. Then, the formation of ^{6}He, ^{9}Be and ^{17}Ne is studied in a common framework, paying special attention to the different nuclear structure properties of these nuclei. Finally, an alternative procedure to estimate reaction rates from inclusive Coulomb breakup measurements is proposed and applied to ^{11}Li, for which recent experimental data is available.

3.1 Three-body radiative capture reaction rates

As discussed in chapter 1, some weakly-bound nuclei are important for nucleosynthesis processes, and an accurate knowledge of their reaction and production rates in different scenarios is essential to understand the origin of the different elements in the Universe. We focus on radiative capture reactions of three particles, (abc), into a compound nucleus A of binding energy ε_B, *i.e.*

$$a + b + c \longrightarrow A + \gamma.$$

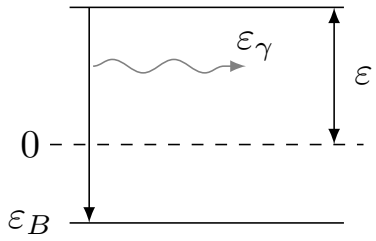

Figure 3.1: Schematic representation of the notation used for the different energies involved in the radiative capture reaction process (or in the inverse photodissociation process).

The energy-averaged reaction rate for such process, $\langle R_{abc}(\varepsilon)\rangle$, can be obtained from the inverse photodissociation process and is given as a function of the temperature T by the expression [34, 54] (see appendix C)

$$\langle R_{abc}(\varepsilon)\rangle(T) = \nu!\frac{\hbar^3}{c^2}\frac{8\pi}{(a_x a_y)^{3/2}}\frac{g_A}{g_a g_b g_c}\frac{1}{(k_B T)^3}e^{\frac{|\varepsilon_B|}{k_B T}} \times \int_{|\varepsilon_B|}^{\infty} \varepsilon_\gamma^2\ \sigma_\gamma(\varepsilon_\gamma)e^{\frac{-\varepsilon_\gamma}{k_B T}}d\varepsilon_\gamma, \tag{3.1}$$

where $\varepsilon = \varepsilon_\gamma + \varepsilon_B$ is the initial three-body kinetic energy, ε_γ is the energy of the photon emitted, ε_B is the binding energy of the compound nucleus below the three-body threshold (see Fig. 3.1), g_i are the spin degeneracy of the particles, ν is the number of identical particles in the three-body system, and a_x and a_y are the reduced masses of the subsystems related to the Jacobi coordinates $\{\boldsymbol{x}, \boldsymbol{y}\}$ (see Eqs. (A.3) and (A.4) in appendix A). The photodissociation cross-section $\sigma_\gamma(\varepsilon_\gamma)$ of the nucleus A can be expanded into electric and magnetic multipoles, λ, as [128, 129]

$$\sigma_\gamma^{(\lambda)}(\varepsilon_\gamma) = \frac{(2\pi)^3(\lambda+1)}{\lambda[(2\lambda+1)!!]^2}\left(\frac{\varepsilon_\gamma}{\hbar c}\right)^{2\lambda-1}\frac{dB(\mathcal{O}\lambda)}{d\varepsilon}. \tag{3.2}$$

Here, $B(\mathcal{O}\lambda)$ is the electric or magnetic transition probability ($\mathcal{O} = E, M$) of order λ. This means that the total photodissociation cross section is a sum over electric and magnetic terms of multipolarity λ. Accordingly to the traditional literature [130], the first multipole is the dominant one and the electric contribution dominates over the magnetic one at the same order. Then, processes sensitive to the $B(\mathcal{O}\lambda)$ transition probabilities are governed by E1 contributions, while M1 and E2 contributions compete at a lower level.

Higher order contributions are typically ignored. The photodissociation cross section enables the comparison between different $B(\mathcal{O}\lambda)$ terms[1] with a single observable that can be measured experimentally. This can be achieved only for stable nuclei such as ^{9}Be [49]. The $\mathcal{O}\lambda$ contribution to the total reaction rate is given by

$$\langle R_{abc}(\varepsilon);\mathcal{O}\lambda\rangle(T) = \mathcal{N}_\lambda(T)\int_{|\varepsilon_B|}^{\infty} d\varepsilon_\gamma\ \varepsilon_\gamma^{2\lambda+1}\ \frac{dB(\mathcal{O}\lambda)}{d\varepsilon} e^{\frac{-\varepsilon_\gamma}{k_B T}}, \qquad (3.3)$$

where $\mathcal{N}_\lambda(T)$ is a function of the temperature to be obtained directly from Eqs. (3.1) and (3.2). The previous expressions makes no assumption concerning the reaction mechanism, and therefore sequential and direct reactions are included implicitly on an equal footing.

The use of Eq. (3.3) relies on the knowledge of the $B(\mathcal{O}\lambda)$ energy distributions or the corresponding photodissociation cross sections. This can be available experimentally although in most cases of astrophysical interest it has not been measured (e.g. ^{17}Ne [131]) or there are different measurements with important discrepancies among them (e.g. ^{9}Be [49, 117]). Then, a reliable theoretical prediction of the electromagnetic transition probability distribution can provide a reaction rate estimation to be used within stellar evolution models. A possibility has been presented in chapter 2, using the analytical transformed harmonic oscillator (THO) method to describe the bound and continuum states of a system.

Note that the exponential in Eq. (3.3) determines the relevant energy range when computing the reaction rate from a given transition probability distribution. For a given temperature T, only energies of the order of $k_B T$ will be relevant. For instance, at $T = 10^{10}$ K (i.e. 10 GK), only the energies up to a few MeV will contribute to the integral. Temperatures at different astrophysical scenarios range from 10^{-2} GK in the center of a typical main-sequence star, to temperatures around 10 GK in explosive environments [132, 133]. This means that nucleosynthesis is driven by low-energy nuclear reactions. A reliable estimation of the reaction rate requires then a detailed description of the transition probability distributions at low energies. In this sense, the analytical THO method described in the preceding chapter allows to build up an optimal basis concentrating a large number of pseudo-states near the breakup threshold.

[1] Notice that the units of $B(\mathcal{O}\lambda)$ depend on λ.

3.2 Application to ^{6}He

The structure of ^{6}He has been addressed in chapter 2 using the analytical THO method. As already discussed, it is a Borromean system comprising an α particle and two valence neutrons, and its ground state is a 0^+ state at 0.973 MeV below the two-neutron separation threshold [93]. The halo nature of this nucleus entails a relatively large radius and a large $B(E1)$ distribution at low excitation energies. It also presents a quadrupolar resonance at 0.83 MeV above the threshold.

In nuclear astrophysics, the $^4\mathrm{He}(2n,\gamma)^6\mathrm{He}$ reaction is of particular importance. It was suggested first that a series of dineutron capture processes on ^{4}He and ^{6}He might contribute to nucleosynthesis in neutron-rich environments for the r-process [38, 134]. It was shown later that the rates for these reactions could change the abundance predictions for heavier element production only in low-entropy neutron-rich environments, such as supernovae or neutron star mergers [42]. The formation of ^{6}He, and ^{9}Be via the $^6\mathrm{He}(\alpha,n)^9\mathrm{Be}$ reaction, could bridge the instability gaps at mass numbers $A = 5$ and $A = 8$, affecting the production mechanism of seed material and the subsequent r-process abundance predictions. Thus, a reliable description of the three-body reaction $^4\mathrm{He}(2n,\gamma)^6\mathrm{He}$ can be of key importance for the stellar models of these cataclysmic events.

The radiative capture of two neutrons by an α particle producing ^{6}He is dominated, according to Eq. (3.2), by electric dipolar transitions from the 1^- continuum to the 0^+ ground state. No dipolar resonances have been observed for ^{6}He. However, due to the presence of a well known 2^+ resonance of ^{6}He, the electric quadrupolar contribution from 2^+ states could play a role. The $B(E1)$ distribution for ^{6}He was presented in the preceding chapter, Fig 2.14, using the analytical THO basis to achieve a detailed description at low energies. The transition probability distribution can be then inserted in Eq. (3.3) to obtain the corresponding reaction rate.

In Fig. 3.2, the reaction rate as a function of the temperature in GK for the radiative capture reaction $^4\mathrm{He}(2n,\gamma)^6\mathrm{He}$ is shown. Although it is not shown in the figure for clarity, E2 contribution from 2^+ states is of about five orders of magnitude smaller than the presented calculations. The result from the analytical THO method (black solid line) is compared to the reaction rate obtained using the actual three-body continuum wave functions

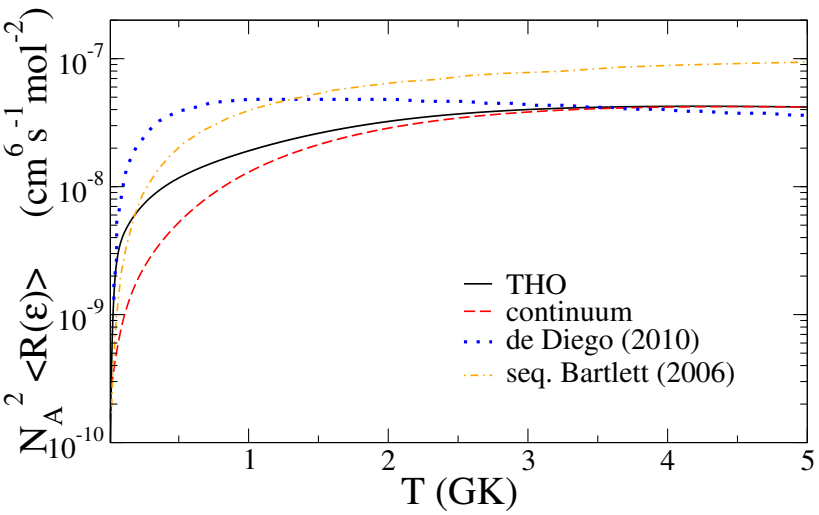

Figure 3.2: Reaction rate for ^{4}He$(2n,\gamma)^6$He as a function of the temperature in GK, with different models: this work (black solid), a reference calculation using the actual three-body continuum wave functions (red dashed), the results from Ref. [54] (blue dotted) and the results from a sequential calculation assuming a dineutron capture [42] (orange dot-dashed).

(red dashed line). Both calculations are in good agreement, although a small difference is observed in the region between 0.1 and 1.5 GK. Calculation from Ref. [54] is also shown (blue dotted line), which exhibits a different behavior at low energies. This is due to the difference of the $B(E1)$ distributions of the corresponding models at energies below 0.5 MeV. It has been checked that the differences in the $B(E1)$ distribution between 0.5 and 3.5 MeV do not affect the calculated reaction rate, provided the same total strength. Fig. 3.2 includes also the results from a sequential model for the radiative capture [42] (orange dot-dashed line). This calculation presents the same behavior as the THO but is a factor of two larger above 0.2 GK. Note that this sequential calculation assumes first the formation of a dineutron, which is controversial, and then the capture of this by an α particle. An alternative sequential process, presented also in [42], starts from a neutron capture by the α particle to give ^{5}He followed by the capture of a second neutron. This provides a reaction rate more than two orders of magnitude smaller in all studied ranges of temperatures. The separation between these two processes is not required within a full three-body model as presented in this work, which provides a consistent description of the reaction with no assumptions.

3.3 Application to ^{9}Be

Details about the structure of ^{9}Be using a three-body model have been shown in chapter 2. Reactions induced by ^{9}Be within a four-body framework will be addressed in chapter 4. The analytical THO method provides a proper description of the $3/2^-$ ground state of the system and, as will be shown, a reasonable agreement with the available experimental data on elastic scattering.

In astrophysics, the reaction $\alpha(\alpha n,\gamma)^9$Be followed by ^{9}Be$(\alpha,n)^{12}$C may provide an alternative path towards the production of heavier elements beyond the instability gaps at mass numbers $A = 5$ and $A = 8$ [49]. This process, however, competes with the triple-α reaction and will be important only in highly neutron-rich environments. The relevance of this process has been linked to the r-process in type II supernovae [37]. The formation of ^{9}Be has been addressed in several works assuming a sequential process [49, 117, 135, 136], but more recently it was suggested that the direct three-body capture could enhance the reaction rate at low temperatures [34, 54] by several orders of magnitude. In this temperature region, calculations on the reaction rate are extremely sensitive to the transition probability distributions at low energies. Thus, a detailed description of these distributions is required to study the effect of the three-body capture. It was shown in the preceding chapter that the low energy spectrum of ^{9}Be presents a series of resonances near the three-body threshold. These states are connected to the $3/2^-$ ground state of the system by electric (E1) and magnetic (M1) dipolar transitions. For the computation of σ_γ, only dipolar transitions are considered, since the λ-factors in Eq. (3.2) reduces the relevance of quadrupolar contributions. The cases of $1/2^+$ (E1) and $5/2^-$ (M1) were shown in the preceding chapter. For the remaining j^π states, the same THO basis used for $5/2^-$ states in chapter 2 is employed. The $B(E1)$ and $B(M1)$ discrete values are smoothed using Poisson distributions with a width parameter $w = 30, 60, 30$ for $3/2^+, 5/2^+, 1/2^-$, respectively.

In Fig. 3.3, the three electric dipolar contributions to the photodissociation cross section of ^{9}Be from $1/2^+$ (solid line), $3/2^+$ (dotted line) and $5/2^+$ states (dashed line), are shown. Magnetic dipolar contribution from $5/2^-$ states (dot dashed) and $1/2^-$ states (double dot dashed) are also given. The total cross section is represented by a thick solid line. It is clear that, at very

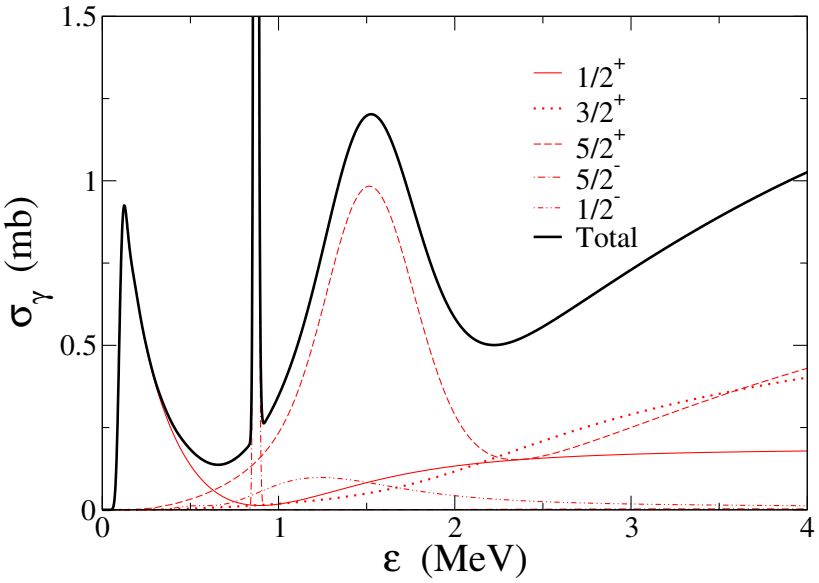

Figure 3.3: Contribution of the $1/2^+$ (thin solid), $5/2^+$ (dashed), $3/2^+$ (dotted), $5/2^-$ (dot dashed) and $1/2^-$ (double dot dashed) states to the total photodissociation cross section (thick solid) of ^{9}Be.

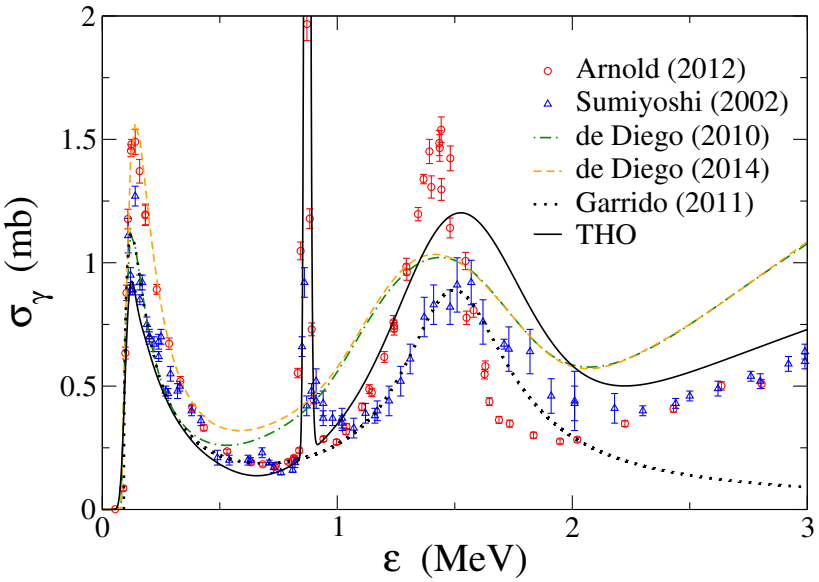

Figure 3.4: Total photodissociation cross section from the present three-body calculation (solid line) compared with the theoretical results by de Diego *et al.* (dashed line [54], dot dashed [137]) and Garrido *et al.* (dotted [34]), and experimental data by Sumiyoshi *et al.* (triangles [49]) and Arnold *et al.* (circles [117]).

low energies, only the $1/2^+$ states contribute to the cross section. The total photodissociation cross section is compared, in Fig. 3.4, with the experimental data from Arnold *et al.* [117] and Sumiyoshi *et al.* [49]. The agreement is quite good. The result is also in good agreement with other experimental data available in the literature [135, 136], although they are not shown in the figure for clarity. Recent calculations by de Diego *et al.* [54, 137], using a similar three-body model, are also shown. In those works, the continuum problem is solved by imposing box boundary conditions, for which obtaining a large density of states at the lowest energies is numerically challenging. So, the $1/2^+$ resonance peak for energies below 1.2 MeV is replaced by an energy-dependent Breit-Wigner distribution with the proper resonance parameters to reproduce the data. In Ref. [54], the $1/2^+$ parameters are adjusted to reproduce the 2002 data, while in Ref. [137] are fixed to describe the 2012 data. This procedure is applied by Garrido *et al.* [34] to fit the total cross section including Breit-Wigner distributions for the lowest ^{9}Be resonances, also presented in Fig 3.4. This calculation is adjusted to reproduce the data from Sumiyoshi *et al.*

In contrast, the present result for the $1/2^+$ peak is directly obtained by smoothing the transition strength with Poisson distributions, using a THO basis that concentrates a large density of states near the breakup threshold. In this sense, this model provides the first full three-body calculation of the ^{9}Be photodissociation cross section in the whole energy range. The experimental data for the $1/2^+$ contribution is underestimated (in particular compared to 2012 data), but it shows the right low-energy behavior and the corresponding tail of the resonance. The narrow $5/2^-$ resonance is also well reproduced. This contribution is not computed in Refs. [34, 54, 137]. Concerning the $5/2^+$ broad resonance, the present estimations agree better with Sumiyoshi *et al.* [49] than with those from the more recent experiment of Arnold *et al.* [117], in which a rather narrow peak is obtained. For that reason the position of the $5/2^+$ resonance is fixed to Sumiyoshi *et al.* data. In the calculations by de Diego *et al.*, the $5/2^+$ resonance is adjusted to the energy given by Sumiyoshi *et al.*, however due to the smoothing procedure the maximum is shifted to lower energies. The $3/2^+$ resonance plays a minor role and its contribution affects only in the high energy region. At these energies, the results here presented agree better with both sets of experimental data than those by de Diego *et al.* The overall difference between both calculations

could be associated to the different discretization methods and different two-body potentials. Concerning the M1 contribution to the $1/2^-$ states, it has a small effect on the cross section, as shown in Fig. 3.3.

Although the overall behavior is very similar in both sets of experimental data, there are important discrepancies between them. The accuracy of these experiments could then be questioned, since experimental normalization factors may lead to very different results. In Refs. [49] and [117], for instance, the energy and width of the $1/2^+$ resonance are found to be the same, but with different gamma widths by a factor of 1.3. This results in a different height for the resonant peak. For that reason it is not trivial to find an explanation to the differences between theory and experiment. On the other hand, three-body models are an approximation to the actual many-body problem, and consequently there might be effects on the cross section that are not considered explicitly, e.g. dynamical effects within the clusters or full antisymmetrization problems. Both calculations (this work and Refs. [54, 137]) are systematically above the data at energies larger than 2 MeV, but at this level it is not possible to determine whether this difference is related to many-body corrections or a possible normalization uncertainty of the data. Nevertheless, the overall agreement between the present calculations and the available experimental data supports the reliability of the method in describing the ^{9}Be wave functions within a three-body approach.

In Fig. 3.5, the contribution to the $\alpha(\alpha n,\gamma)^9$Be reaction rate from $1/2^+$ (solid line), $3/2^+$ (dotted line), $5/2^+$ (dashed line), $5/2^-$ (dot dashed) and $1/2^-$ (double dot dashed) states is shown as a function of the temperature in GK. As expected, the $1/2^+$ contribution dominates almost in the whole temperature range, with other contributions being relevant only at temperatures above 3 GK.

The total reaction rate is compared in Fig. 3.6 with sequential estimations from experimental cross sections from Refs [49] (triangles), [117] (circles) and [33] (squares). The present result converges to the sequential estimations at high temperatures, where the direct capture plays a minor role. Three-body calculations by de Diego *et al.* [54, 137] were included for the photodissociation cross section in Fig. 3.4. The subsequent results for the reaction rate are not included in Fig. 3.6 for clarity, but they agree with the present results in the temperature region between 0.1 and 5 GK. At low temperature, below 0.1 GK, the three-body capture enhances the reaction rate by several orders

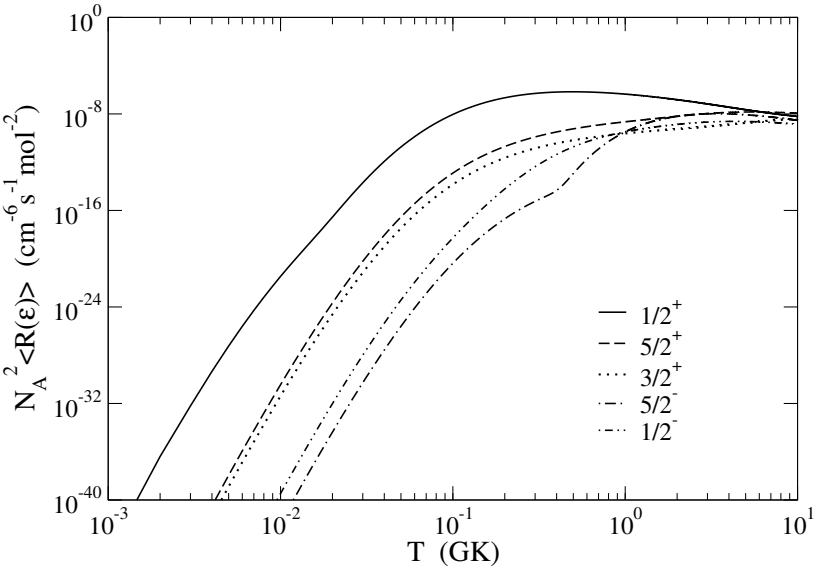

Figure 3.5: Contribution of the $1/2^+$ (solid), $5/2^+$ (dashed), $3/2^+$ (dotted), $5/2^-$ (dot dashed) and $1/2^-$ (double dot dashed) states to the total $\alpha(\alpha n,\gamma)^9$Be reaction rate.

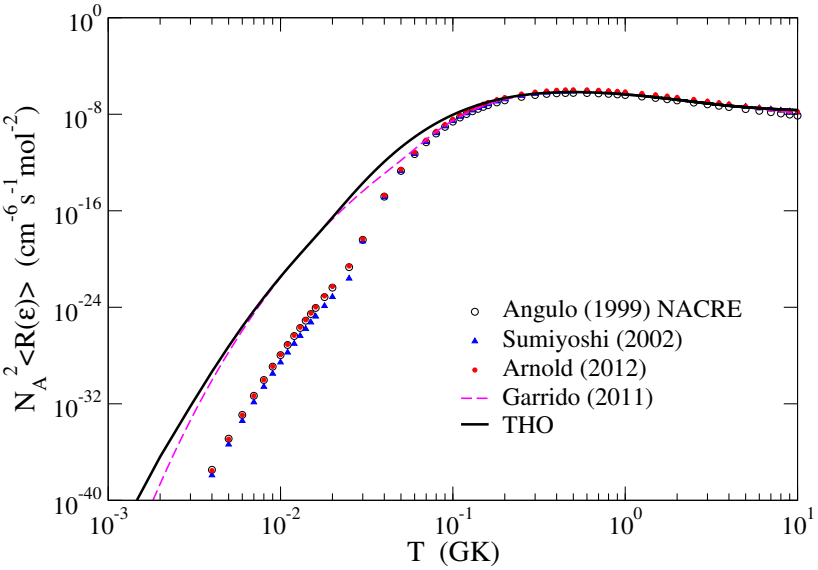

Figure 3.6: Total $\alpha(\alpha n,\gamma)^9$Be reaction rate (solid line) compared with the three-body Breit-Wigner estimation by Garrido *et al.* (dashed [34]) and sequential calculations from experimental data by Sumiyoshi *et al.* (triangles [49]), Arnold *et al.* (circles [117]) and Angulo *et al.* (squares [33]).

of magnitude, in good agreement with three-body Breit-Wigner estimations by Garrido *et al.* [34]. This confirms that the uncertainty related to the $1/2^+$ peak shown in chapter 2 is not crucial when computing the reaction rate. At such low temperatures, the three-body system has no energy to populate the two-body ^{8}Be resonance and, as expected, the direct capture begins to dominate. This effect cannot be described within sequential models.

3.4 Application to ^{17}Ne

As in the previous cases, the structure of ^{17}Ne has been addressed in chapter 2. This nucleus is a Borromean system with two valence protons on top of a ^{15}O core. Accordingly to the available experimental data, whether this system presents or not a halo structure is still an open problem.

Under the astrophysical conditions in X-ray bursts, the breakout from the hot CNO cycle can trigger the rp-process. Among the possible breakout reactions, $^{15}\mathrm{O}(2p,\gamma)^{17}\mathrm{Ne}$ has been proposed to play a significant role towards the production of heavier, neutron-deficient nuclei along the proton dripline. Experimental effort has been devoted to obtain the photodissociation cross section of ^{17}Ne from a Coulomb dissociation experiment at GSI, although conclusive results have not yet been published [131]. The resonant [47] and non-resonant [138] capture processes for the production of ^{17}Ne have been studied theoretically by Grigorenko *et al.*, showing the relevance of the three-body direct capture compared to sequential estimations [46].

As shown in the preceding chapter, the ^{17}Ne low-energy spectrum presents several resonances near the two-proton separation threshold. The analytical THO method presented in this work enables the description of resonant and non-resonant capture on the same footing. Therefore, the method provides a different approach to compare with the theoretical results in Refs. [47, 138]. Considering only dipolar transitions from the $1/2^-$ ground state, this requires the computation of the photodissociation cross section including $3/2^-$ (M1), $1/2^+$ (E1) and $3/2^+$ (E1) states. Electric quadrupolar transition (E2) to $3/2^-$ and $5/2^-$ could also compete with the M1 contribution, while is reasonable to neglect higher order multipoles. The case of $1/2^+$ (E1) was shown in the preceding chapter. For the remaining j^π states, the same THO basis is employed. The $B(E1)$ and $B(M1)$ discrete values are smoothed using Poisson distributions with a proper width parameter.

In Fig. 3.7, the E1 contributions to the photodissociation cross section of ^{17}Ne from $1/2^+$ (thin solid line) and $3/2^+$ (dotted line) are shown. The M1 contribution from the $3/2^-$ states (dot-dashed line) is also given. The total cross section is represented by a dashed line. The cross section is presented in linear (upper panel) and logarithmic scale (lower panel). Electric dipolar contributions, especially of $1/2^+$ states, dominate the photodissociation cross section. However, the lower panel suggests a non-negligible M1 contribution from $3/2^-$ states, which can affect the reaction rate at very low temperatures. No data is available on σ_γ to compare with the present calculations of ^{17}Ne. The distributions have been obtained following the same prescription presented in the previous cases, i.e., by selecting the Poisson width parameters to be as large as possible.

From the photodissociation cross section, the $^{15}\mathrm{O}(2p,\gamma)^{17}\mathrm{Ne}$ reaction rate can be easily calculated. In Fig. 3.8, the contribution from $1/2^+$ (thin solid line), $3/2^+$ (dotted line) and $1/2^-$ (dot-dashed line) states to the total reaction rate for ^{17}Ne formation (thick solid), is shown as a function of the temperature in GK. The $1/2^+$ contribution dominates at high temperatures, while the low-temperature tail is governed by transitions from $3/2^-$ states.

The reaction rate is compared in Fig. 3.9 (thick black solid) with previous calculations by Grigorenko *et al.* [138] (thick gray solid), which consider the resonant and non-resonant contributions separately. These are not actual three-body calculations, as the resonant part is estimated from experimental data on ^{17}Ne excited states and the non-resonant contribution is obtained by assuming specific s^2 and d^2 weights of the system ground state. It is remarkable that just the $1/2^+$ contribution in the present work (red solid) is noticeably larger than the total rate in Ref. [138] at high temperatures. The addition of $3/2^-$ states increases further this difference at low temperatures, while $3/2^+$ states play a negligible role in the whole temperature range. It is worth mentioning that E2 contributions have also been estimated, being even smaller. To asses the origin of these differences and the validity of the method here presented, a calculation by Garrido *et al.* [139] for the $1/2^+$ contribution is also shown (orange dashed). This corresponds to a three-body calculation similar to the present work, using different binary interactions and solving the Schrödinger equation with box boundary conditions to describe the ^{17}Ne states. Both approaches agree above 0.5 GK and question the results in Ref. [138].

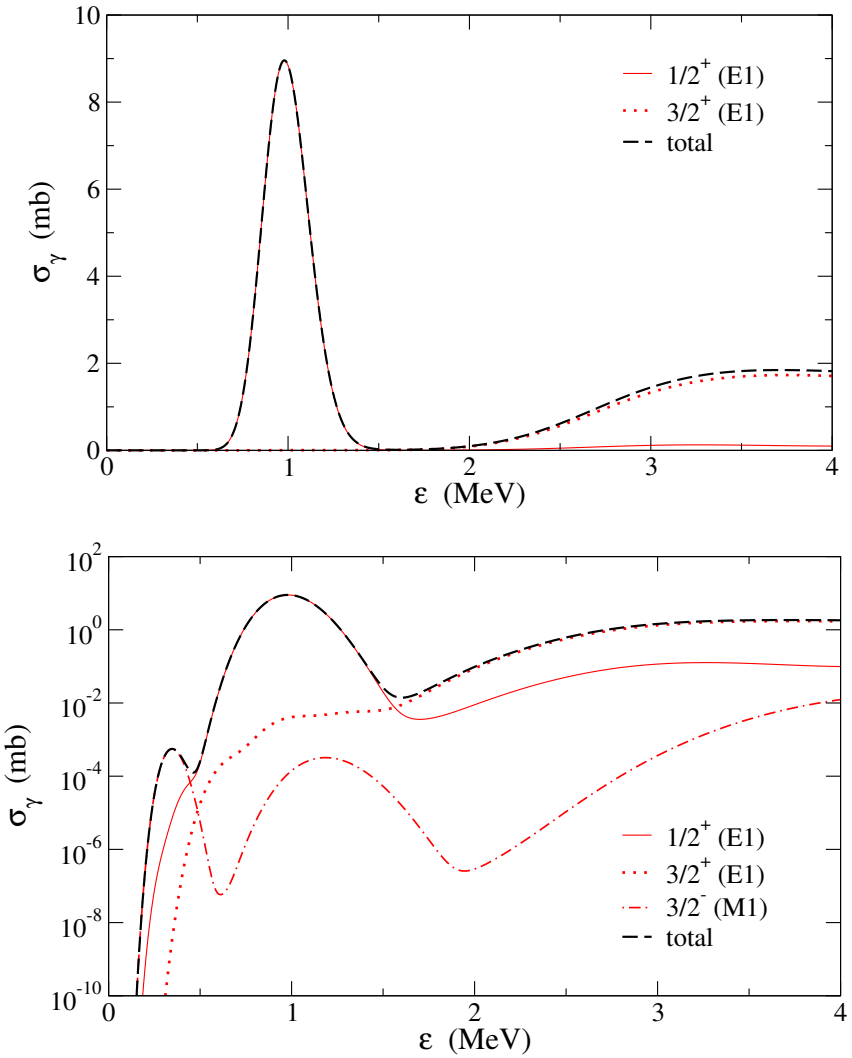

Figure 3.7: Contribution of the $1/2^+$ (thin solid), $3/2^+$ (dotted), and $3/2^-$ (dot-dashed) states to the total photodissociation cross section (thick solid) of ^{17}Ne in linear (upper panel) and logarithmic scale (lower panel). Note that the $3/2^-$ contribution cannot be appreciated in a linear scale, so it is not shown in the upper panel.

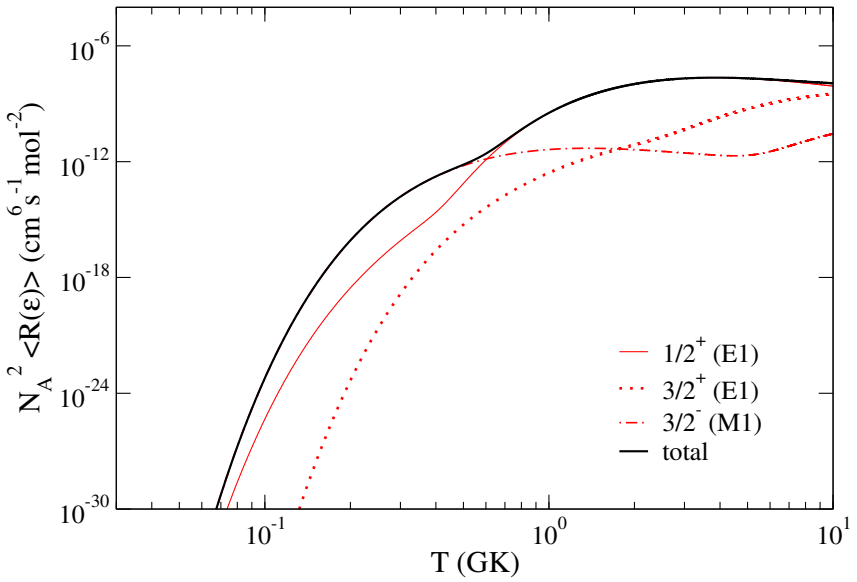

Figure 3.8: Contribution of the $1/2^+$ (thin solid), $3/2^+$ (dotted) and $1/2^-$ (dot-dashed) states to the total $^{15}\mathrm{O}(2p,\gamma)^{17}\mathrm{Ne}$ reaction rate (thick solid).

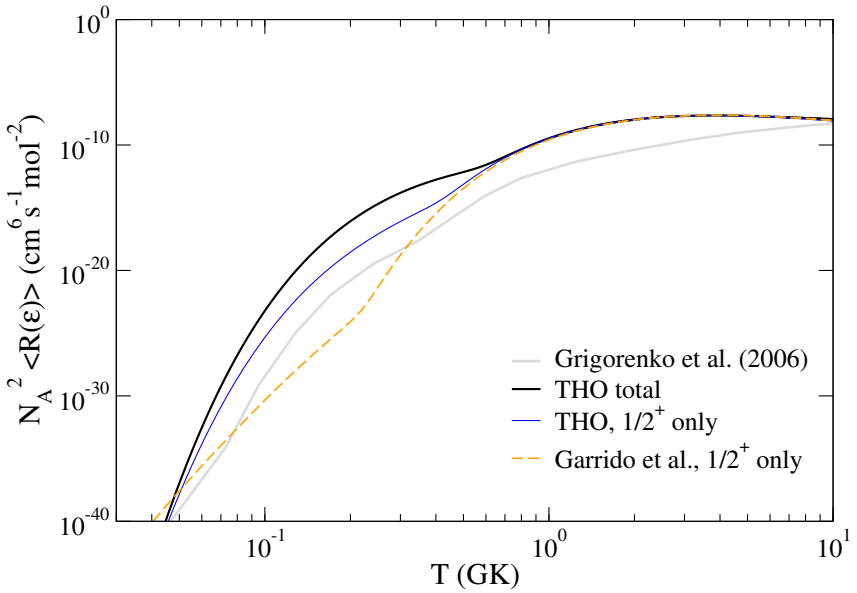

Figure 3.9: Total reaction rate (thick black solid) compared with the results in Ref. [138] (thick gray solid). The $1/2^+$ contribution in the present work (blue solid) and calculations by Garrido *et al.* [139] (orange dashed) are also shown.

The temperature range of astrophysical interest in novae and X-ray bursts is of the order of 0.3-3 GK (see, for instance, Ref. [140]). In this range, both three-body approaches (the present work and calculations by Garrido *at al.*) agree and provide a reaction rate several orders of magnitude larger than that in Ref. [138]. This could imply important differences in the temperature-density profile that determines the conditions for the $^{15}\mathrm{O}(2p,\gamma)^{17}\mathrm{Ne}$ reaction to be relevant. At lower temperatures, calculations show important differences that may be related to the discretization method or specific features of the system ground state derived from the different binary interactions. Nevertheless, this region is not important for the astrophysical site and, even though the origin of these differences should be investigated, implications in nucleosynthesis are expected to be small.

3.5 Capture reaction rates from inclusive Coulomb breakup

Reaction rates presented in previous sections for ^{6}He, ^{9}Be and ^{17}Ne have uncertainties related to the theoretical model used to describe the systems. Radiative capture reactions take place in stellar environments at very low energies, leading to very small productions rates, thus making them very difficult for direct measurements. Moreover, when the capture process is a three-body reaction or involves exotic nuclei, direct measurements are not feasible. Alternative procedures to estimate reaction rates are a necessity. In this section, a relationship between the inclusive Coulomb breakup probability and the radiative capture reaction rate for weakly-bound three-body projectiles is established. First, the semiclassical model for Coulomb excitation is introduced, and the breakup probability in the equivalent photon model (EPM) is obtained. Then, a direct link between the so-called reduced breakup probability and the three-body reaction rate is developed. Finally, the method is applied to ^{11}Li, for which recent data on inclusive breakup are available.

3.5.1 Semiclassical Coulomb excitation theory

Weakly-bound nuclei can be easily excited or dissociated in the presence of a strong electromagnetic field, such as the one generated by a heavy target.

Therefore, the properties of these nuclei can be accessed from the analysis of collisions at energies below the Coulomb barrier.

The semiclassical description of Coulomb excitation is largely due to Alder and Winther [141]. The theory considers classical trajectories and a quantum model for nuclear excitations. This enables the obtention of simple formulae for the scattering cross sections when the process is electromagnetically dominated. This applies at energies below the Coulomb barrier, or at higher energies in the angular region corresponding to large impact parameters. Within this approximation, the breakup cross section of the projectile due to the electromagnetic interaction with the target can be written as

$$\left(\frac{d\sigma}{d\Omega}\right)_{\mathrm{BU}} = \left(\frac{d\sigma}{d\Omega}\right)_{\mathrm{Ruth}} P(\Omega), \tag{3.4}$$

where $P(\Omega)$ is the breakup probability. The Rutherford cross section, which corresponds to a pure Coulomb trajectory, is simply given by

$$\left(\frac{d\sigma}{d\Omega}\right)_{\mathrm{Ruth}} = \frac{a_0^2}{4\sin^4(\theta/2)} \tag{3.5}$$

being θ the scattering angle in the center of mass frame and a_0 the half the distance of closest approach,

$$a_0 = \frac{Z_p Z_t e^2}{2E}. \tag{3.6}$$

Here, Z_p and Z_t are the charge numbers of the projectile and the target, respectively, and E is the energy in the center of mass frame. Considering only electric excitations, the λ contribution to the breakup cross section can be written as

$$\left(\frac{d\sigma_{E\lambda}}{d\Omega d\varepsilon_\gamma}\right)_{\mathrm{BU}} = \left(\frac{Z_t e}{\hbar v}\right)^2 a_0^{-2\lambda+2} \frac{dB(E\lambda)}{d\varepsilon} \frac{df_{E\lambda}(\theta,\xi)}{d\Omega}, \tag{3.7}$$

where ε_γ is the excitation energy[2], v is the relative velocity between projectile and target, ξ is a dimensionless variable given by $\xi = a_0\varepsilon_\gamma/\hbar v$, and $f_{E\lambda}(\theta,\xi)$ represents the *number of equivalent photons* incident on the projectile due to the interaction with the target. This quantity names the Equivalent Photon

[2]This section follows the same notation than section 3.1. See Fig. 3.1.

Model (EPM) and is given by

$$\frac{df_{E\lambda}(\theta,\xi)}{d\Omega} = \frac{4\pi^2}{(2\lambda+1)^3}\frac{1}{\sin^4(\theta/2)}\sum_{\mu}\left|Y_{\lambda\mu}\left(\frac{\pi}{2},0\right)\right|^2\left|I_{\lambda\mu(\theta,\xi)}\right|^2. \tag{3.8}$$

Here, $I_{\lambda\mu}(\theta,\xi)$ are the Coulomb integrals, and

$$Y_{\lambda\mu}\left(\frac{\pi}{2},0\right) = \begin{cases} \left(\dfrac{2\lambda+1}{4\pi}\right)^{1/2}\dfrac{[(\lambda-\mu)!(\lambda+\mu)!]^{1/2}}{(\lambda-\mu)!!(\lambda+\mu)!!}(-1)^{\frac{(\lambda+\mu)}{2}} & ;\ \lambda+\mu \text{ even} \\ 0 & ;\ \lambda+\mu \text{ odd.} \end{cases}$$

Thus, in the case that dipolar excitations (E1) dominate, the breakup probability in Eq. (3.4) can be written as

$$P(\Omega) = \left(\frac{Z_t e}{\hbar v a_0}\right)^2\frac{2\pi}{9}\int_{|\varepsilon_B|}^{\infty}d\varepsilon_\gamma\frac{dB(E1)}{d\varepsilon}\left(I_{1,1}^2+I_{1,-1}^2\right), \tag{3.9}$$

where ε_B is the ground state energy from the separation threshold, and therefore $|\varepsilon_B|$ represents the breakup energy. Note that this probability is explicitly proportional to $(Z_t)^2$, and implicitly proportional to $(Z_p)^2$ via the transition probability $B(E1)$. As a consequence, the cross section (3.4) increases with the Coulomb repulsion, and the breakup of the projectile is enhanced for reactions on heavy targets.

A detailed description of the Coulomb integrals in Eqs. (3.8), (3.9) is available in Refs. [141, 142]. In the small angle limit, these integrals can be approximated as [103]

$$I_{1,1}^2+I_{1,-1}^2 \approx \frac{8\pi a_0}{\hbar v}\sin(\theta/2)\ \varepsilon_\gamma\exp\left[-\frac{a_0}{\hbar v}\left(\pi+\frac{2}{\sin(\theta/2)}\right)\varepsilon_\gamma\right]. \tag{3.10}$$

Inserting this result in Eq. (3.9) leads to

$$P(\Omega) \approx \frac{16\pi^2}{9}\frac{(Z_t e)^2\sin^2(\theta/2)}{(\hbar v)^3 a_0}\int_{|\varepsilon_B|}^{\infty}d\varepsilon_\gamma\ \varepsilon_\gamma\frac{dB(E1)}{d\varepsilon}e^{-\frac{a_0}{\hbar v}\left(\pi+\frac{2}{\sin(\theta/2)}\right)\varepsilon_\gamma}. \tag{3.11}$$

It is convenient to introduce a collision time

$$t = \frac{a_0}{\hbar v}\left(\pi+\frac{2}{\sin(\theta/2)}\right), \tag{3.12}$$

in terms of which a reduced breakup probability $P_r(t)$ can be defined as

$$P_r(t) = P(\Omega)\frac{9t^2(\hbar v)^3 a_0}{16\pi^2 \left(Z_t e\right)^2 \sin^4\left(\theta/2\right)} = \int_{|\varepsilon_B|}^{\infty} d\varepsilon_\gamma \; \varepsilon_\gamma \frac{dB(E1)}{d\varepsilon} e^{-t\varepsilon_\gamma} t^2. \quad (3.13)$$

With the collision time t defined in Eq. (3.12), $P_r(t)$ is independent of the collision parameters. This makes t a scaling variable in such a way that experimental data on a given reaction at different energies can be merged together and analyzed using a single quantity, $P_r(t)$. At the right conditions, i.e., low incident energies and small scattering angles, the reduced breakup probability is then totally determined by the electric dipolar transition probability distribution of the projectile.

3.5.2 Reaction rate from break-up probability

The applicability of Eq. (3.13) relies on the knowledge of the $B(E1)$ distribution. This problem was also present in section 3.1 for the astrophysical reaction rate. Transition probability distributions are typically model dependent and introduce an uncertainty in both observables. When accurate reaction rates are needed to compute full nucleosynthesis networks in astrophysics, this can be a problem. A demanding reference is required to asses the validity of the different theoretical approaches that have been used to calculate reaction rates. Recently, it was proposed that inclusive Coulomb breakup measurements can provide information on the $B(E1)$ distribution of weakly-bound projectiles [103]. These results are used in the present work to establish a relationship between the inclusive Coulomb breakup probability and the three-body radiative capture reaction rate.

Accordingly to section 3.1 and following the same notation, the three-body radiative capture reaction rate can be written, in leading order, as

$$\langle R_{abc}(\varepsilon)\rangle(T) \simeq \mathcal{N}_1(T) \int_{|\varepsilon_B|}^{\infty} d\varepsilon_\gamma \; \varepsilon_\gamma^3 \; \frac{dB(E1)}{d\varepsilon} e^{\frac{-\varepsilon_\gamma}{k_B T}}, \quad (3.14)$$

where $\mathcal{N}_\lambda(T)$ is a function of the temperature to be obtained directly from Eqs. (3.1) and (3.2). This, for electric dipolar transitions, gives

$$\mathcal{N}_1(T) = \mathcal{C}\frac{1}{(k_B T)^3} e^{\frac{|\varepsilon_B|}{k_B T}}, \quad (3.15)$$

and $\mathcal{C}$ represents all the projectile-related constants,

$$\mathcal{C} = \nu! \frac{\hbar^2}{c^3} \frac{2^7 \pi^4}{3^2 (a_x a_y)^{3/2}} \frac{g_A}{g_a g_b g_c}. \tag{3.16}$$

At energies around the Coulomb barrier and at very forward angles, the reduced breakup probability of weakly-bound nuclei is given by Eq. (3.13) and also depends, in leading order, on the $B(E1)$ distribution. It is then clear that Eqs. (3.13) and (3.14) are formally equivalent except for a factor ε_γ^2. This means that both observables, reaction rate and reduced breakup probability, are strongly correlated in the range for which the EPM holds. This opens the possibility of getting reliable information on the astrophysical reaction rate from experimental measurements of the breakup probability. The maximum correlation is established when the exponentials in Eqs. (3.13) and (3.14) are equal, i.e.,

$$t = \frac{1}{k_B T}, \tag{3.17}$$

which, together with Eq. (3.12), establishes a direct correspondence between the scattering angle θ and the temperature T. This relation is not unique since it depends on the bombarding energy through the parameter a_0 and the velocity v. This enables the possibility of exploring different temperature ranges of relevance in astrophysics by measuring breakup probabilities at different energies. For larger energies, one gets information for the same angle on shorter collision times, which corresponds to exploring higher temperatures. It is straightforward to see from Eqs. (3.13), (3.14) and (3.17) that

$$\langle R_{abc}(\varepsilon) \rangle (T) = \mathcal{C}\ t^3 e^{|\varepsilon_B| t} \frac{d^2}{dt^2} \left(\frac{1}{t^2} P_r(t) \right). \tag{3.18}$$

This equation is the main result of this section. The reaction rate in a stellar environment at a given temperature T is related with the inclusive reduced break-up probability $P_r(t)$ obtained in a Coulomb scattering experiment, for certain collision times corresponding to given scattering angles and energies.

To evaluate from a practical purpose the second derivative in Eq. (3.18) it is convenient to fit a suitable function to the experimental data. The main t-dependence of $P_r(t)$ is through the exponential factor $e^{-|\varepsilon_B| t}$, as it can be deduced from Eq. (3.13). Thus, without any loss of generality, $P_r(t)$ can be expressed as an expansion,

$$P_r(t) \simeq e^{-|\varepsilon_B| t} \left(b_0 + b_1 t + b_2 t^2 + \dots \right). \tag{3.19}$$

The parameters $b_0, b_1, b_2, \ldots$ are fitted to the experimental values of $P_r(t)e^{|\varepsilon_B|t}$, over the range which is Coulomb dominated. From these values, the reaction rate given by Eq. (3.18) is

$$\begin{aligned}\langle R_{abc}(\varepsilon)\rangle(T) = \quad & \mathcal{C} \quad \left[b_0\left(|\varepsilon_B|^2 k_B T + 4|\varepsilon_B| + 6/(k_B T)\right)\right. \\ & + \quad b_1\left(|\varepsilon_B|^2 (k_B T)^2 + 2|\varepsilon_B| k_B T + 2\right) \\ & + \quad \left. b_2\left(|\varepsilon_B|^2 (k_B T)^3\right) + \ldots\right]. \end{aligned} \tag{3.20}$$

The parameters $b_0, b_1, b_2, \ldots$ fitted in Eq. (3.19) will have some uncertainties, given by a covariance matrix. These uncertainties can be implemented in Eq. (3.20) to estimate the uncertainties in the reaction rate.

3.5.3 Example of application: ^{11}Li

The breakup of ^{11}Li on ^{208}Pb was recently measured at TRIUMF [103]. Experimental breakup cross sections can be used to illustrate the method, evaluating the two-neutron radiative capture by ^{9}Li to produce ^{11}Li. This reaction, $^{9}\mathrm{Li}(2n,\gamma)^{11}\mathrm{Li}$, could appear in the α-process in type II supernovae or in the Inhomogeneous Big Bang [143]. Although ^{9}Li radiative capture might not be a key reaction in astrophysical sites, this case is chosen to show a procedure that can be used in general for three-body capture reactions.

The ^{11}Li nucleus is a two-neutron halo system with a Borromean structure, comprising a ^{9}Li core surrounded by two loosely-bound neutrons. The reported values of the $B(E1)$ of ^{11}Li deduced from exclusive breakup measurements (i.e., all outgoing fragments are detected) give a large E1 strength at low excitation energies. However, there are considerable discrepancies in the absolute values between breakup cross sections in different experiments (see, for instance, Refs. [144, 145]). Structure models for ^{11}Li differ also in their predictions, leading to uncertainties on the $B(E1)$ distribution. As a consequence, the $^{9}\mathrm{Li}(2n,\gamma)^{11}\mathrm{Li}$ reaction rate, which relies on the transition probability distribution, is not well determined. Similar problems have been shown in this chapter for nuclei of astrophysical interest.

Information on the $B(E1)$ distribution, and consequently on the reaction rate, can also be obtained from inclusive measurements in which only a heavy fragment is detected. In the case of ^{11}Li breakup, this implies to measure the ^{9}Li fragments. For weakly-bound systems such as ^{11}Li colliding on heavy

targets, the strong Coulomb repulsion decreases the elastic cross section and produces large breakup probabilities, even at low incident energies. At energies around the Coulomb barrier, the method presented in the previous section can be used within a wide angular range where the Coulomb interaction dominates. This enables the use of Eq. (3.17) to find a correspondence between scattering angles (or collision times) in the breakup process and temperatures for the radiative capture reaction. Note that the expressions in the previous section are referred to the center of mass of ^{11}Li fragments, but inclusive measurements imply to detect only the core fragment. It was checked in Ref. [103] that the effect of taking this angle instead of the experimentally determined ^{9}Li scattering angle is negligible. This is somehow expectable, since at low incident energies and small scattering angles the center of mass of the system and the core fragment are close enough.

In Fig. 3.10, the ^{11}Li + ^{208}Pb reduced break-up probability is presented. It is clear that, in the region from $t = 5$ to 15 MeV^{-1}, data are reasonably smooth and follow an exponential decay. The product of the break-up probability $P_r(t)$ times $e^{|\varepsilon_B|t}$ is fitted by a second degree polynomial, Eq. (3.19), obtaining the values $b_0 = 7.8$ e^{2}fm^{2}MeV^{-1}, $b_1 = -0.4$ e^{2}fm^2, $b_2 = 0.02$ e^{2}fm^{2}MeV, with the corresponding covariance matrix, which is given in Table 3.1. In this fit, $|\varepsilon_B|$ has been taken as 0.37 MeV, the experimental two-neutron separation energy of ^{11}Li [146]. In Fig. 3.10 the solid black line is the result of the quadratic fit and the shadow region around is the 1-σ region coming from the uncertainties in the determination of the parameters. This is given by

$$\begin{aligned}\sigma_P^2 &= (F_{\chi^2}\ e^{-|\varepsilon_B|t})^2\sigma^2\left(b_0 + b_1 t + b_2 t^2\right) \\ &= (F_{\chi^2}\ e^{-|\varepsilon_B|t})^2\left[\sigma^2(b_0) + \sigma^2(b_1)t^2 + \sigma^2(b_2)t^4\right. \\ &\quad \left. + 2\sigma(b_0,b_1)t + 2\sigma(b_0,b_2)t^2 + 2\sigma(b_1,b_2)t^3\ \right].\end{aligned} \tag{3.21}$$

Here, the factor F_{χ^2} is simply the square root of the reduced χ^2 of the fit and enhances the uncertainty band, accounting for the experimental data dispersion and the possible degree of unsuitability of the quadratic model. For comparison, Fig. 3.10 shows also the results obtained by integrating two different B(E1) distribution directly through Eq. (3.13): i) the experimental B(E1) measured at RIKEN [144] (dot-dashed red line), and ii) a theoretical calculation of the B(E1) in a three-body model [103] (dashed blue line). It

is shown that the quadratic fit reproduces fairly well the experimental data on the break-up probability.

From the knowledge of parameters b_0, b_1 and b_2, the reaction rate for the two-neutron capture by ^{9}Li can be estimated using Eq. (3.20) in the range of temperatures from 0.7 to 2.3 GK, corresponding to collision times from $t = 15$ to $t = 5$ MeV^{-1}. This range of temperatures is relevant since it corresponds to the burning of elements ranging from helium to silicon in a typical massive star [147]. One could try to explore a larger temperature range by doing Coulomb excitation experiments at different energies. The present work requires to be certain that nuclear effects, or higher order Coulomb effects, do not affect significantly the break-up cross sections. This can be checked using reliable reaction calculations, as shown in Ref. [103].

The reaction rate so obtained is shown in Fig. 3.11 as a function of the temperature in GK. The results from the quadratic fit and its corresponding 1-σ uncertainty band are shown by the full black line and the shaded region around, respectively. In the same figure, the results obtained by inserting different $B(E1)$ energy distributions in Eq. (3.14) are also shown: i) the experimental RIKEN data [144] (dot-dashed red line), ii) a theoretical three-body model of ^{11}Li which presents a resonance at 0.69 MeV [103] (dashed blue line), and iii) a theoretical two-body model of ^{11}Li with a dipolar resonance at the same position [148] (dotted green line). The results obtained from the RIKEN experimental data include an estimation of the uncertainty in the reaction rate, which is due to the statistical uncertainties of the $B(E1)$ points, and also to the uncertainty in the break-up energy, which is given [144] as $\Delta E = 0.17\sqrt{\varepsilon}$, with ε in MeV. This uncertainty is especially important, in relative terms, for the energies close to the threshold, which are the most relevant for the reaction rate.

As shown in Fig 3.11, the reaction rate extracted from this work is significantly larger than the reaction rate extracted from the RIKEN $B(E1)$ values, although these have considerable uncertainties. The difference is also seen in the break-up probability, in Fig. 3.10. This discrepancy may be an indication that the ^{11}Li reaction mechanism at the energies involved is not fully described by the one-photon method. Indeed, continuum-discretized coupled channels [103] indicate that higher order coupling effect may play a role. On the other hand, the $B(E1)$ values close to the threshold, and the corresponding energies, have uncertainties. However, it should be remarked

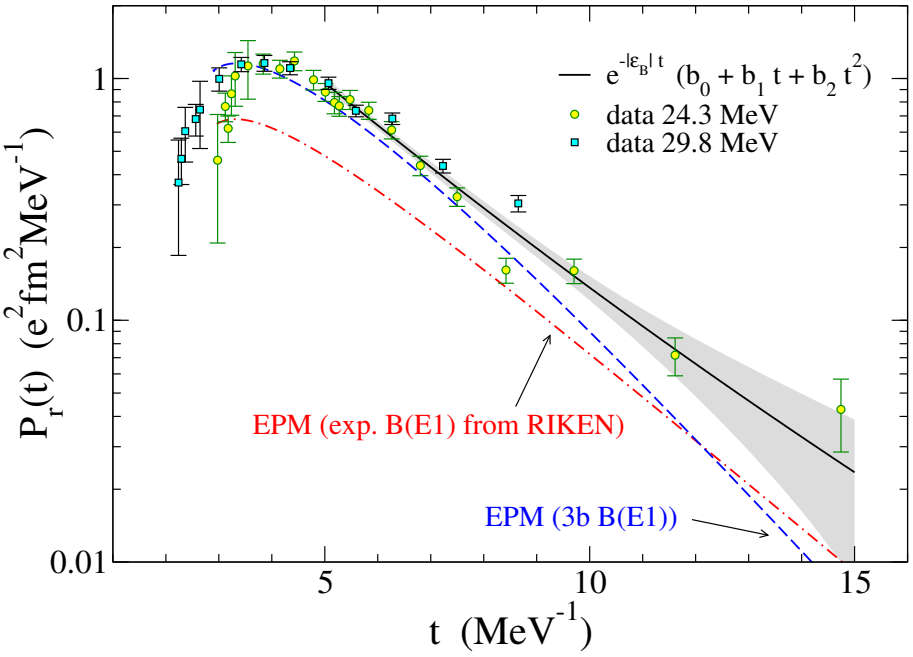

Figure 3.10: ^{11}Li + ^{208}Pb reduced break-up probability as a function of the collision time, t. Data are from Ref. [103], at two different incident energies. The continuous black line is the result of the fit with Eq. (3.19) and the shadow marks the 1-σ region around the fit. The results integrating in Eq. (3.13) the $B(E1)$ energy distribution from RIKEN data [144] (dot-dashed red line) and a theoretical three-body $B(E1)$ distribution [103] (dashed blue line) are also shown for comparison.

	b_0	b_1	b_2
b_0	3.893	-1.064	0.068
b_1		0.296	-0.019
b_2			0.001

Table 3.1: Covariance matrix of quadratic fit.

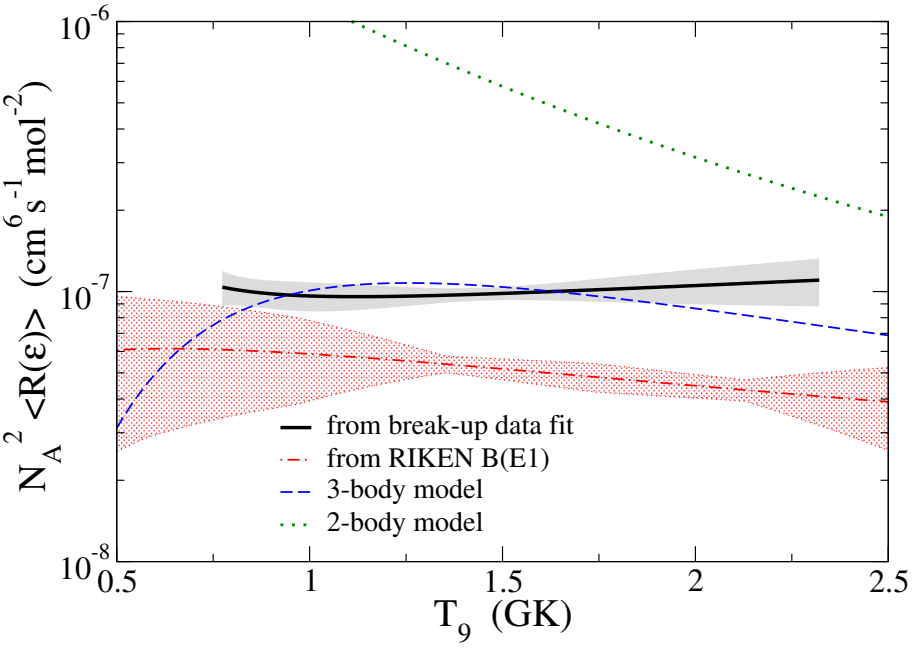

Figure 3.11: Reaction rate as a function of temperature (in GK). The estimation from inclusive break-up data using the quadratic fit, given by Eq. (3.20), is shown by the full black line. The shaded region around corresponds to the 1–σ uncertainty related to the fit. Other lines are calculations using different $B(E1)$ energy distributions directly in Eq. (3.14) (See text for details).

that both sets of experimental data allow to extract information on the astrophysical reaction rate, and give results in the same order of magnitude. It is seen in Fig 3.11 that the three-body calculation of [103] is in very good agreement with the reaction rate calculated in this work in the region of temperatures for which the EPM model holds. On the contrary, the two-body calculation [148] including a resonance at the same energy that the three-body model is clearly out of the values and trend calculated by the method here presented.

In this chapter, radiative capture reactions for the formation of ^{6}He, ^{9}Be and ^{17}Ne have been studied, making use of the results and considerations given in chapter 2. The reaction rates so obtained treat the resonant and non-resonant, sequential and direct contributions on an equal footing. Full nucleosynthesis network calculations are asked for to test the sensitivity of r-process (^{6}He, ^{9}Be) and rp-process models (^{17}Ne) to these updated reaction rates.

In the last section, a relation between the astrophysical reaction rate and the inclusive Coulomb break-up probability for three-body systems has been established, in the region in which first order dipole Coulomb interaction is dominant. The temperature of the stellar environment is directly related to the collision time of the reaction, which depends on the scattering angle and the incident energy. This implies that detailed measurements on inclusive break-up probabilities of these systems will provide a direct estimation of the corresponding reaction rates of astrophysical interest in a given range of temperatures. This result provides a new experimental tool to determine astrophysical reaction rates for short-lived three-body nuclei and provides an additional motivation to carry out Coulomb scattering experiments of exotic nuclei in radioactive ion beam facilities. The method could be used, for instance, to assess the validity of the reaction rates presented for the $^{4}\mathrm{He}(2n,\gamma)^{6}\mathrm{He}$ and $^{15}\mathrm{O}(2p,\gamma)^{17}\mathrm{Ne}$ capture process. Experimental data on ^{6}He or ^{17}Ne breakup could help in estimating the corresponding reaction rate. There are experimental data on ^{6}He inclusive Coulomb breakup at low energies [149, 150], but not in the angular region required by the new method. Dedicated experiments are desirable.

Chapter 4

Direct reactions induced by three-body projectiles

Experiments are the only means of knowledge at our disposal. The rest is poetry, imagination.

Max Planck

In this chapter, reactions induced by three-body projectiles are described within a four-body framework. The general expansion of the scattering wave functions by means of projectile internal states was presented in section 1.4, leading to a coupled-channel problem. The relevant expressions for the particular case of three-body projectiles are given in this chapter. The method is applied to reactions induced by ^{9}Be, for which some of the results and considerations presented in chapter 2 will be of key importance.

4.1 Three-body projectiles

The Continuum-Discretized Coupled-Channel (CDCC) method was introduced originally for two-body projectiles, in particular for deuteron ($p + n$) induced reactions. The traditional discretization method for two-body projectiles, whose continuum states can be easily calculated, is the *binning* procedure, in which the continuum spectrum is truncated at a maximum excitation energy and divided into energy (or momentum) intervals. For each interval, or bin, a normalizable state is built up by superposition of

the scattering states within the interval. This method has been extended to three-body projectiles such as the halo nuclei ^{6}He [151] and ^{11}Li [103], which consist of a core and two valence neutrons. However, as discussed in chapter 2, the calculation of actual continuum states for three-body systems comprising more than one charged particle is a very involved problem, since the asymptotic behavior of the wave functions is not known in general. An alternative to the binning procedure is the Pseudo-State (PS) method presented in chapter 2. The three-body projectile states will be then described approximately as square-integrable functions.

All the expressions in section 1.4 were presented with a general notation, and therefore can be applied for the case of three-body projectiles. Although the same ideas prevail, typical level densities in the description of three-body projectiles are much larger than that for two-body projectiles. As three-body wave functions contain many components (see chapter 2), the Schrödinger equation associated with the internal degrees of freedom of the projectile (1.16) provides many eigenvalues. The three-body continuum is therefore approximated by a large number of square-integrable wave functions. It was shown in Ref. [79] that the level densities for ^{6}He (α+n+n) were much higher than for two-body projectiles. As a consequence, the coupled-channel system in Eq. (1.21) involves a large number of equations. Moreover, the final expressions for the coupling potentials given by Eq. (1.22) in the case of three-body projectiles are rather complicated, as will be shown.

In the literature, the application of the method for three-body projectiles is typically referred to as four-body CDCC. The method is an ideal tool to describe reactions induced by Borromean nuclei, as it does not assume any specific two-body structure based on the properties of unbound nuclei. Fig. 4.1 shows schematically the four-body framework, where Jacobi coordinates $\{\boldsymbol{x}, \boldsymbol{y}\}$ are used to describe the projectile.

Expanding the angular couplings in Eq. (1.19), the four-body wave function in Eq. (1.18) can be written as

$$\Psi^{JM}(\boldsymbol{R}, \boldsymbol{x}, \boldsymbol{y}) \equiv \sum_{nj\mu LM_L} \phi^{\mathrm{THO}}_{nj\mu}(\boldsymbol{x}, \boldsymbol{y}) \langle LM_L j\mu | JM \rangle \times i^L Y_{LM_L}(\widehat{R}) \frac{1}{R} \chi^J_{Lnj}(R), \tag{4.1}$$

where the projectile states $\phi^{\mathrm{THO}}_{nj\mu}$ are obtained by diagonalizing the three-

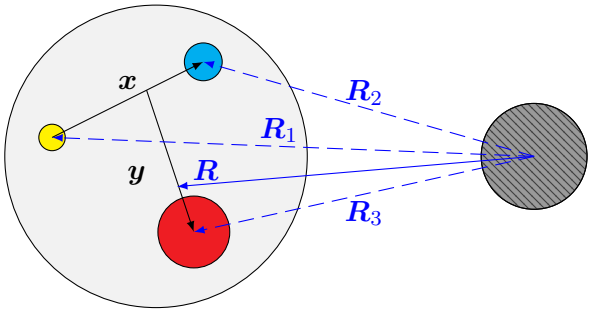

Figure 4.1: Scattering of a three-body projectile by a structureless target.

body internal Hamiltonian in an analytical transformed harmonic oscillator (THO) basis. This is a particular choice, although other bases can be used [116].

To generate the coupling potentials (1.22), a multipole expansion of the projectile-target interaction is introduced. According to Eq. (1.15), this interaction is the sum of the interaction between each projectile particle and the target, $V_{qt}(\boldsymbol{R}_q)$, with $q = 1, 2, 3$. For each pair potential, the appropriate Jacobi set is chosen so that the corresponding coordinate $\boldsymbol{R}_q$ depends only on vectors $\boldsymbol{R}$ and $\boldsymbol{y}_q$. Assuming central potentials, each component can be expanded as

$$V^{(q)}(r_q) = \sum_Q (2Q+1)\mathcal{V}_Q^{(q)}(R, y_q)P_Q(z_q), \tag{4.2}$$

where Q denotes the multipole, $P_Q(z_q)$ is a Legendre polynomial, and $z_q = \widehat{y}_q \cdot \widehat{R}$ is the cosine of the angle between $\boldsymbol{y}_q$ and $\boldsymbol{R}$. In this expansion, $\mathcal{V}_Q^{(q)}(R, y_q)$ are the multipole coefficients given by

$$\mathcal{V}_Q^{(q)}(R, y_q) = \frac{1}{2}\int_{-1}^{+1} dz_q V^{(q)}(r_q)P_Q(z_q). \tag{4.3}$$

Using the above-given definitions, and after some algebra, the coupling potentials can be expressed as

$$V^{JM}_{Lnj,L'n'j'}(R) = \sum_Q (-1)^{J-j}\hat{L}\hat{L}' \begin{pmatrix} L & Q & L' \\ 0 & 0 & 0 \end{pmatrix} \times W(LL'jj', QJ)F^Q_{nj,n'j'}(R), \tag{4.4}$$

where all the dependence on the projectile states is contained in the radial form factors $F^{Q}_{nj,n'j'}(R)$ given by

$$
\begin{aligned}
F^{Q}_{nj,n'j'}(R) = (-1)^{Q+2j-j'}\hat{j}\hat{j}'\,(2Q+1)\sum_{\beta\beta'}\sum_{q=1}^{3}\sum_{\beta_q\beta'_q} N_{\beta\beta_q}N_{\beta_q\beta'_q} \\
\times (-1)^{l_{x_q}+S_{x_q}+j'_{ab_q}-j_{ab_q}-I_q}\delta_{l_q l'_q}\delta_{S_{x_q}S'_{x_q}}\hat{l}_{y_q}\hat{l}'_{y_q}\hat{l}_q\hat{l}'_q\hat{j}_{ab_q}\hat{j}'_{ab_q} \\
\times \begin{pmatrix} l_{y_q} & Q & l'_{y_q} \\ 0 & 0 & 0 \end{pmatrix} W(l_q l'_q l_{y_q} l_{y'_q}, Q l_{x_q}) W(j_{ab_q} j'_{ab_q} l_q l'_q, Q S_{x_q}) \\
\times W(jj' j_{ab_q} j'_{ab_q}, Q I_q)\left[\int\int (\sin\alpha_q)^2(\cos\alpha_q)^2 d\alpha_q d\rho\right. \\
\left.\times\, \mathcal{R}^{\mathrm{THO}}_{n\beta j}(\rho)\varphi^{l_{x_q}l_{y_q}}_{K_q}(\alpha_q)\mathcal{V}^{(q)}_{Q}(R,y_q)\varphi^{l_{x_q}l'_{y_q}}_{K'_q}(\alpha_q)\mathcal{R}^{\mathrm{THO}}_{n'\beta'j'}(\rho)\right]. \quad (4.5)
\end{aligned}
$$

Here, $\mathcal{R}^{\mathrm{THO}}_{n\beta j}(\rho)$ are the hyperradial functions of the projectile wave functions, which can be expanded in the corresponding THO basis using the diagonalization coefficients $C^{i\beta j}_{n}$ (see (Eq. 1.5)). As already mentioned, for each particle q composing the projectile, the wave function components $\beta = \{K, l_x, l_y, l, S_x, j_{ab}\}$ obtained in a preferred Jacobi set are rotated to the corresponding Jacobi-q set so that the interactions can be easily calculated. This requires the components β_q and the transformations between Jacobi sets $N_{\beta\beta_q}$. These transformations were already introduced in chapter 2. More details are provided in appendix B.

Once the coupling potentials $V^{JM}_{Lnj\mu,L'n'j'\mu'}(R)$ are calculated, the coupled equations (1.21) can be solved. This can be achieved, for instance, by means of the Numerov method or using the R-matrix theory [152, 153]. The later is more time consuming but has the advantage of being numerically more stable. In this work, the integration of the coupled-channel problem is addressed by using the FRESCO code [73], which can employ both approaches. The code is prepared to read and use the form factors calculated externally via Eq. (4.5)

4.2 Application to reactions induced by ^{9}Be

The structure of ^{9}Be has been addressed in chapter 2. It can be described in a three-body model as two alpha particles loosely bound by the remaining neutron, and has a Borromean structure. The ground state of ^{9}Be has

total angular momentum $j^\pi = 3/2^-$ and a separation energy of 1.5736 MeV [108]. ^{9}Be shows several low-energy resonances with angular momenta $j^\pi = 1/2^+, 5/2^-, 1/2^-, 5/2^+, 3/2^+$ and possibly others, whose positions and widths have been studied by many authors in different experiments [49, 117, 136]. The spin-parity assignment for some of these states is still under discussion [113], although there are no implications for the lowest $1/2^+$ and $5/2^-$ resonances. The states of the system were described using the analytical THO method, and the agreement with the available experimental data on ^{9}Be radius and deformation revealed the suitability of the three-body description. The details concerning the interactions, ground state observables and energy distributions are omitted here.

Calculations shown in chapter 2 truncate the maximum hypermomentum at large values of K_{max}, which determines the size of the model space. For ^{9}Be, it is necessary to consider $K_{max} \geq 30$ in order to obtain a well converged ground state, and more importantly to achieve converged energy distributions. However, such values imply to work with very large basis sets when considering several j^π configurations for the coupled-channels problem, which is computationally challenging. It is convenient then to fix smaller K_{max} values, and adjust the three-body force parameters to recover the same energy and radius of the relevant states. In the following, unless stated otherwise, the calculations presented are performed with $K_{max} = 10$. This value provides converged results with respect to the hypermomentum, as will be shown in the following section.

With the analytical THO basis, it is possible to adjust the parameters of the local scale transformation in order to concentrate more states at low energy. However, if the level density is very high, coupled-channel calculations will become more and more demanding computationally. The THO parameters are fixed to $b = 0.7$ fm and $\gamma = 1.2$ fm$^{1/2}$ for all the j^π states considered. These values ensure a fast convergence of the ground state with respect to the number of hyperradial excitations i_{max}, and also allows to concentrate a reasonable number of continuum states close to the breakup threshold. As an example, Fig. 4.2 shows the energy spectra for different j^π configurations calculated with $i_{max} = 8$. The only negative eigenstate for $j^\pi = 3/2^-$ corresponds to the bound state, and the positive energy eigenvalues represent the continuum in the THO basis up to 10 MeV.

In the following sections, four-body CDCC calculations are performed for

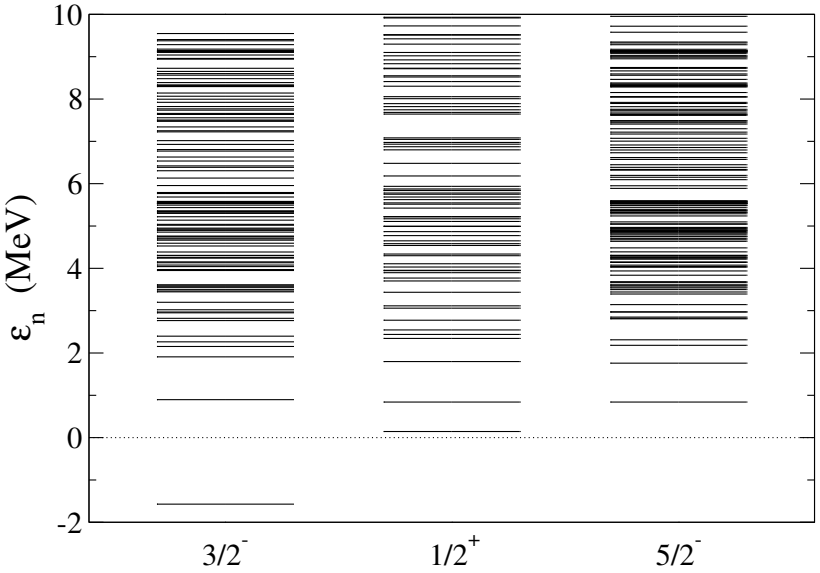

Figure 4.2: Energy spectra for ^{9}Be states with $j^\pi = 3/2^-, 1/2^+, 5/2^-$ up to 10 MeV. Calculations are performed for an analytical THO basis with $K_{max} = 10$ and $i_{max} = 8$.

^{9}Be-induced reactions on ^{208}Pb, ^{27}Al and ^{120}Sn, for which elastic scattering and breakup data are available in the literature.

4.2.1 ^{9}Be on ^{208}Pb

In this section, the scattering of ^{9}Be on a ^{208}Pb target at different energies is addressed. There are two different experiments available in the literature for this reaction [154, 155]. The ^{9}Be projectile wave functions are described as the eigenstates obtained with the analytical THO method. States with very high excitation energies will not be relevant for the description of the scattering process, since their couplings will be weak. Thus, only the states up to a given cutoff energy are included in the CDCC calculations. This parameter has to be large enough to provide converged results.

The Coulomb barrier for the ^{9}Be + ^{208}Pb system is around 47 MeV. Coupled-channels calculations have been performed at energies above, around and below the barrier. Since ^{9}Be is a weakly-bound system, a strong absorption is expected even at low energies, with an important coupling to breakup channels. This effect is widely known for exotic systems such as halo nuclei [12, 79]. The coupling potentials in Eq. (4.4) are generated

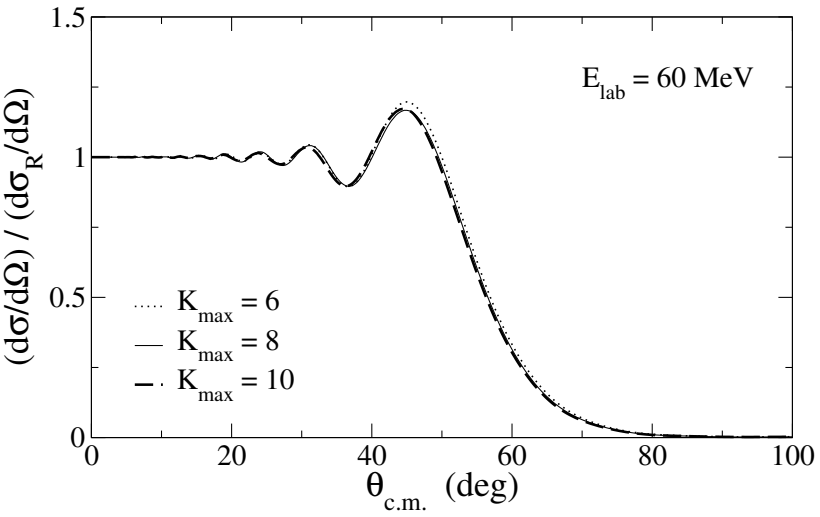

Figure 4.3: Convergence of the angular distribution of the elastic cross section relative to Rutherford with respect to K_{max} for the reaction ^{9}Be + ^{208}Pb at $E_{lab} = 60$ MeV. Calculations are performed with $i_{max} = 6$ and $\varepsilon_{max} = 6$ MeV.

considering the n-^{208}Pb potential from the Koning and Delaroche global parametrization [156] and the α-^{208}Pb interaction from Ref. [157]. Note that these potentials are in general energy-dependent. The coupled equations are solved up to $J = 301/2$, including projectile-target interaction multipole couplings to all orders.

The model space to describe the ^{9}Be projectile includes $j^\pi = 3/2^\pm, 1/2^\pm$ and $5/2^\pm$ states up to a maximum energy ε_{max}. The states are obtained with a THO basis with maximum hypermomentum K_{max} and i_{max} hyperradial excitations in each channel. First, the the convergence of calculations with respect to the hypermomentum must be checked. In Fig. 4.3, the elastic cross section at $E_{lab} = 60$ MeV is shown for different values of $K_{max} = 6, 8, 10$ using the same value of $i_{max} = 6$. In all cases, the three-body force in the model Hamiltonian is adjusted in order to recover the same energy and radius of the $3/2^-$ ground state and the same position of different projectile resonances. Calculations with $K_{max} = 8$ and 10 are almost identical, confirming the convergence of the results with respect to this parameter. For the reaction at lower energies, the same behavior is observed. At $E_{lab} = 60$ MeV, calculations show a very fast convergence with respect to i_{max} and the cutoff energy ε_{max}. For the reaction at energies around and below the

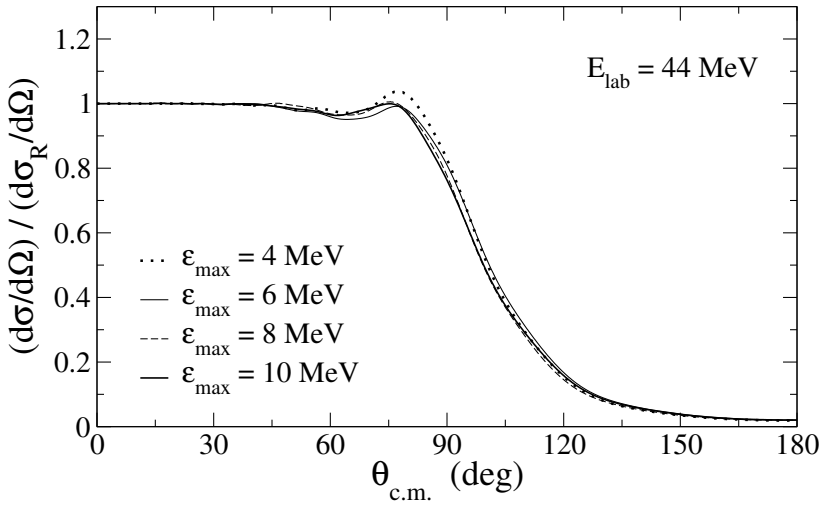

Figure 4.4: Convergence of the angular distribution of the elastic cross section relative to Rutherford with respect to ε_{max} for the reaction ^{9}Be + ^{208}Pb at $E_{lab} = 44$ MeV. Calculations are performed with $i_{max} = 6$.

Coulomb barrier, however, a slower convergence is observed. To illustrate this point, Fig. 4.4 shows the convergence of the elastic cross section at $E_{lab} = 44$ MeV with respect to ε_{max}, for a fixed value of $i_{max} = 6$. Calculations with $\varepsilon_{max} = 8$ MeV and 10 MeV are almost indistinguishable. For calculations with larger i_{max} values, the same behavior is observed. The dependence of the calculations at $E_{lab} = 44$ MeV on the parameter i_{max} is shown in Fig. 4.5, with a fixed cutoff energy of 8 MeV. Calculations are very close, with small differences only in the angular region between 60° and 90°. Working with $i_{max} > 10$ is computationally very time-consuming, and no significant changes are expected. The same features are observed at lower energies, far below the Coulomb barrier. The slower convergence at low energies was already reported for reactions induced by weakly-bound projectiles on heavy targets [79].

Once convergence with respect to all relevant parameters has been checked, calculations can be confronted with experimental data at energies above, around and below the Coulomb barrier to assess the validity of the model. Fig. 4.6 shows the final results at $E_{lab} = 60$, 44 and 38 MeV compared with the experimental data from Refs. [154, 155]. The error bars are very small and, for clarity, they are not shown. Calculations use $i_{max} = 6$, $\varepsilon_{max} = 6$ MeV for the reaction at $E_{lab} = 60$ MeV and $i_{max} = 10$, $\varepsilon_{max} = 8$

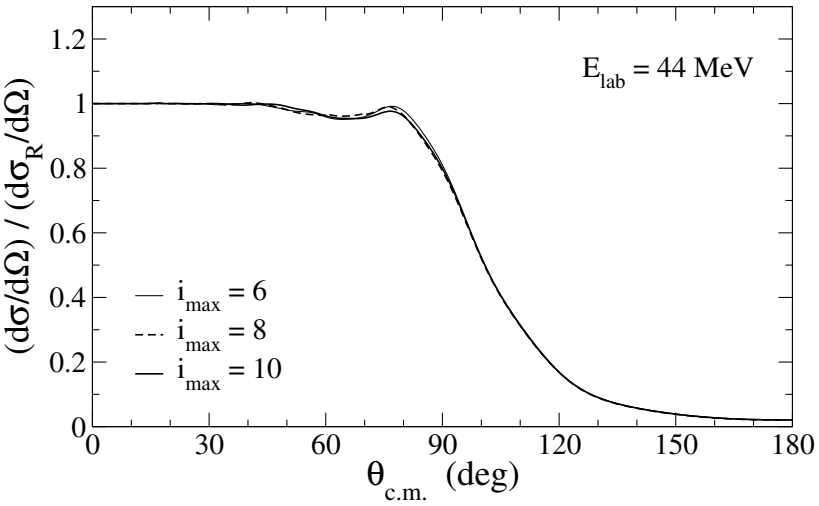

Figure 4.5: Convergence of the angular distribution of the elastic cross section relative to Rutherford with respect to i_{max} for the reaction ^{9}Be + ^{208}Pb at $E_{lab} = 44$ MeV. Calculations are performed with $\varepsilon_{max} = 8$ MeV.

MeV at $E_{lab} = 44$ and 38 MeV. In this figure, dashed lines correspond to calculations including the ground state only, and solid lines are the full CDCC calculations. In all cases, the agreement between the present calculations and the data is improved when the coupling to breakup channels is included. Calculations describe reasonably well the experimental data in the complete angular range. Around ($E_{lab} = 44$ MeV) and below (38 MeV) the Coulomb barrier, there is an uncertainty related to the difference between the two data sets. This indicates a possible data normalization problem. At $E_{lab} = 44$ MeV, the calculation underestimates the data between 60 and 90°, i.e. in the nuclear-Coulomb interference region. At $E_{lab} = 38$ MeV, the calculation seems to overestimate the data at backward angles and slightly underestimate the data in the nuclear-Coulomb interference region.

It is worth mentioning that these features were not observed in a recent work by Descouvemont *et al.* [158] using also pseudo-states to describe the continuum. In that work, the Lagrange-mesh basis was used, and different α–n, α–α potentials were considered. Calculations in [158] seem to match the experimental data in the nuclear-Coulomb interference region at both $E_{lab} = 44$ and 38 MeV. However, these calculations involve only $j^\pi = 3/2^-, 1/2^+, 5/2^-$ states. If the present calculations are performed including the same ^{9}Be angular momenta, the experimental data in the

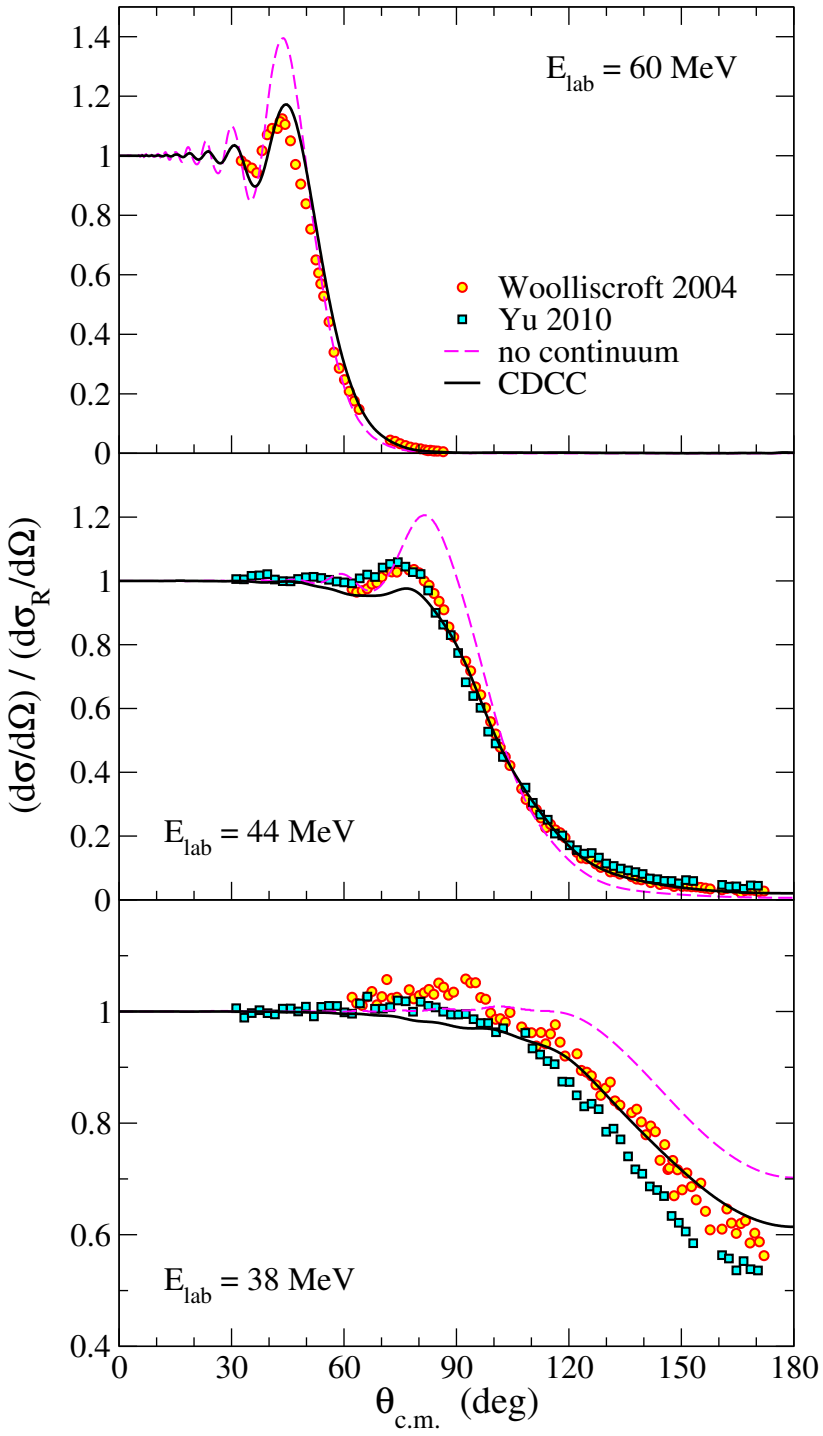

Figure 4.6: Angular distribution of the elastic cross section relative to Rutherford for the reaction ^{9}Be + ^{208}Pb at E_{lab} = 60, 44 and 38 MeV. Dashed lines correspond to calculations including the ground state only, and solid lines are the full CDCC calculations. The experimental data are shown with circles (Wolliscroft 2004: [154]) and squares (Yu 2010: [155]).

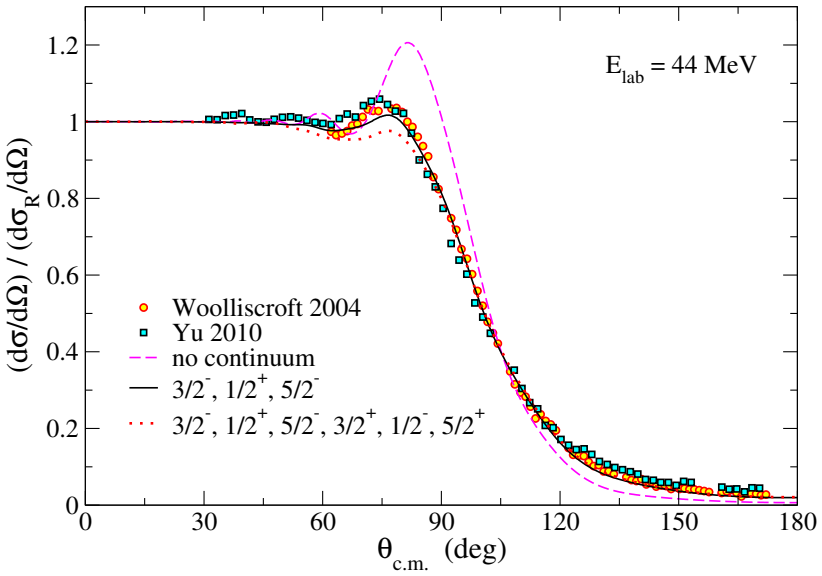

Figure 4.7: Effect of the model space truncation on the elastic cross section relative to Rutherford for the reaction ^{9}Be + ^{208}Pb at E_{lab} = 44 MeV. Calculations use $i_{max} = 10$ and $\varepsilon_{max} = 8$ MeV.

rainbow region is also reproduced. This is shown for clarity in Fig. 4.7. However, in the most recent publication by the same authors [116], calculations involve the same model space ($j^{\pi} = 3/2^{\pm}, 1/2^{\pm}, 5/2^{\pm}$ states) included in the present work. Results therein are in good agreement with calculations here presented and show the above-mentioned underestimation of the data in the interference region. Thus, both theoretical approaches are consistent if the same model space is used. A limited model space including only $j^{\pi} = 3/2^{-}, 1/2^{+}, 5/2^{-}$ states is not sufficient to reach convergence.

The source of the discrepancies, between the converged calculations (Ref. [116] and the present work) and the experiment in the nuclear-Coulomb interference region, could be due to either the experimental data analysis or the theoretical models used. First, we expect that the scattering of a weakly-bound nucleus such as ^{9}Be on a heavy target at energies around and below the Coulomb barrier follows the same behavior reported both, experimentally and theoretically, for other weakly-bound nuclei such as ^{6}He [159, 160], ^{11}Li [12] and ^{11}Be [161]. All these nuclei present a suppression of the rainbow at the interference region when colliding with heavy targets, at energies around and below the Coulomb barrier. This is due to the strong dipolar Coulomb coupling to the continuum states. This suppression is not

present in the experimental data on ^{9}Be+^{208}Pb at E_{lab} = 44 MeV and is smaller than the theoretical predictions at E_{lab} = 38 MeV.

Concerning the data analysis, a small uncertainty in the angle determination can produce an important deviation on the measured elastic cross section with respect to Rutherford at small angles. This is due to the elastic cross section behavior ($\sin^{-4}(\theta/2)$). In particular, it is necessary to be extremely careful with the beam misalignment. This issue has been addressed in different experimental works (see for example Refs. [12, 160, 162]) and could imply a slope change in the elastic cross section in the rainbow region. On the theoretical side, models describing this kind of reactions depend on several approximations, including the use of optical potentials between the projectile fragments and the target and a truncation of the model space describing the projectile states. At this point we cannot asses whether the source of the discrepancy arises from experimental problems or theoretical issues. However, CDCC calculations agree with the experimental data, elastic and breakup, in the rainbow region for other weakly-bound projectiles under similar scattering conditions (heavy target, energy around the Coulomb barrier). This is the case of ^{11}Li+^{208}Pb [12, 103] and ^{11}Be+^{197}Au [161], in which the observed enhancement of the breakup cross section in the nuclear-Coulomb interference region produces a systematic reduction of the elastic cross section at the same angles. Regardless, differences between the data on ^{9}Be+^{208}Pb and the four-body CDCC calculations at this region are below 6%, and the overall agreement is quite good considering that there is no parameter fitting. This affirms the reliability of a three-body model in describing the structure of ^{9}Be.

CDCC calculations involve a large set of coupled equations with coupling multipolarities Q, which determine the allowed transitions between projectile states. In order to study the effect of the j^{π} contributions and coupling multipolarities Q on the results, Fig. 4.8 shows different calculations at E_{lab} = 44 MeV. The monopolar (Q = 0) contribution allows to connect the $3/2^{-}$ ground state to the $3/2^{-}$ continuum. Then, the dipolar (Q = 1) contribution connects the ground state with $1/2^{+}$, $3/2^{+}$ and $5/2^{+}$ states. From them, dipolar and higher order contributions introduce couplings between all j^{π} configurations considered. This figure reveals that the main contributions to reducing the cross section, the monopole and dipole terms, are of the same order. This result differs from the case of ^{6}He and ^{11}Li

on ^{208}Pb, where dipolar contributions produce the largest reduction with respect to the calculation without continuum couplings [12, 79]. This dipole effect in halo nuclei, such as ^{6}He and ^{11}Li, is due to the deviation of the center of charge with respect to the center of mass because of the presence of two valence particles far away from the charged core (^{4}He or ^{9}Li). This produces a strong dipole moment and large $B(E1)$ strengths at low energy. On the contrary, the ^{9}Be system is not a halo nucleus and does not present such a large deviation; so dipolar effects, although present, are smaller. This is related to the fact that the sum rule for dipolar transitions is smaller in this case. Higher order contributions, especially the quadrupolar terms, produce a correction which improves the description of the experimental data at backward angles.

The ^{9}Be system has some low-energy resonances, characterized by different angular momenta, which have an important impact on the reaction mechanism. This effect has been reported for both elastic and breakup processes involving weakly-bound nuclei [12]. To illustrate this point, the resonance positions can be changed by introducing a different three-body strength in the model Hamiltonian for the $1/2^{\pm}$, $5/2^{\pm}$ and $3/2^{+}$ states. Fig. 4.9 shows the result of a calculation "without" resonances, i.e. including a strong repulsive three-body force so that the resonances appear at very high energies and play no role in the CDCC calculations. In that case the cross section exhibits a smaller reduction than the calculation with the resonance positions fitted to the experimental values. Although the resonant and non-resonant parts of the spectrum cannot be separated directly, these calculations clearly show the relevance of the resonance positions for the reaction mechanism.

In light of these results, the influence of breakup channels on the elastic scattering is clear. The explicit inclusion of continuum states in the formalism enables a proper description of the elastic cross section at energies around the Coulomb barrier. Most of the absorbed flux will then go to the breakup of the projectile, and this will be reflected by large breakup cross sections and probabilities [103]. Fig. 4.10 shows the breakup angular distributions in the center of mass frame at 44 and 38 MeV. The large breakup probability in the nuclear-Coulomb interference region is associated with the reduction of the elastic cross section at the corresponding angles (see Fig. 4.6). No data are available in the literature on this quantity. However it could be measured by performing an exclusive Coulomb dissociation experiment. This would

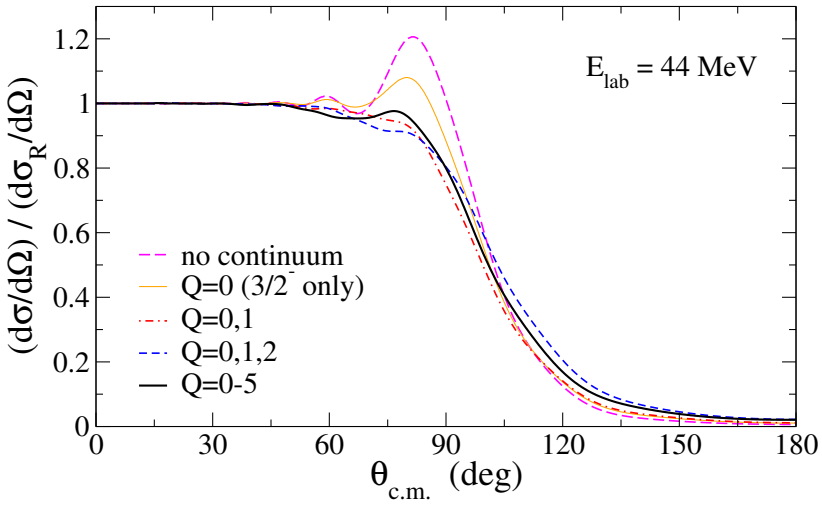

Figure 4.8: Effect of the different coupling multipolarities Q on the elastic cross section relative to Rutherford for the reaction ^{9}Be + ^{208}Pb at $E_{lab} = 44$ MeV. Calculations use $i_{max} = 10$ and $\varepsilon_{max} = 8$ MeV. See the text for details.

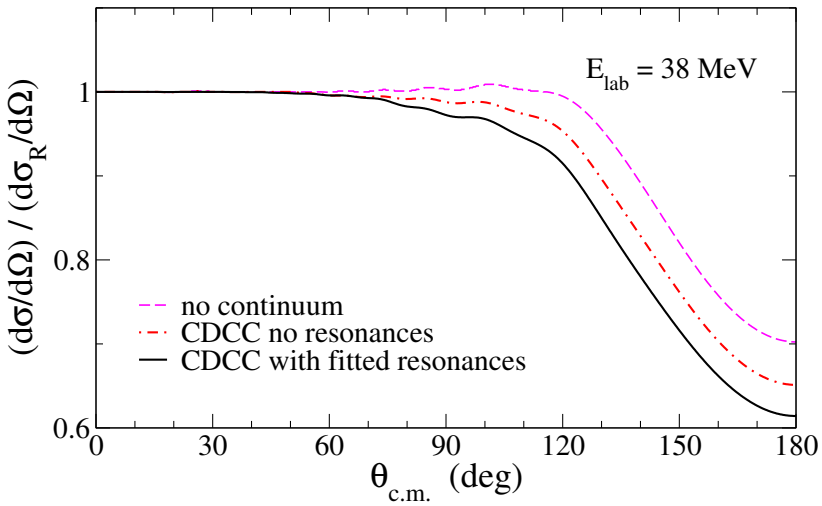

Figure 4.9: Effect of the position of the resonances on the elastic cross section for the reaction ^{9}Be + ^{208}Pb at $E_{lab} = 38$ MeV. Calculations use $i_{max} = 10$ and $\varepsilon_{max} = 8$ MeV.

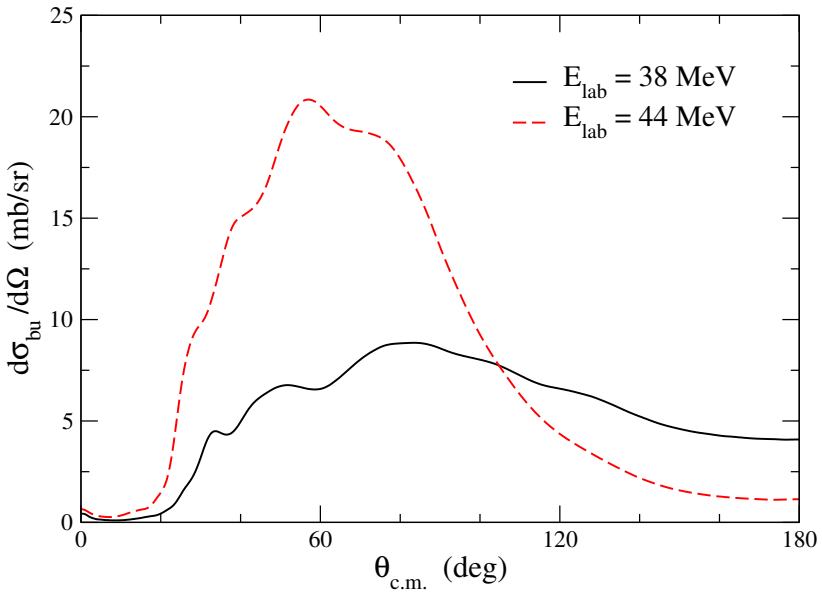

Figure 4.10: Breakup angular distribution ^{9}Be + ^{208}Pb at 44 MeV (red dashed) and 38 MeV (black solid).

allow to asses the validity of the model to describe the elastic and breakup processes on the same footing. The integrated breakup cross sections at 44 and 38 MeV are 112.0 and 80.5 mb, respectively. These values are in fair agreement with the experimentally reported values of 92.1 and 84.1 mb [163]. As expected, the total breakup increases with the incident energy. Breakup effects are important even below the Coulomb barrier, as already shown for the elastic scattering.

4.2.2 ^{9}Be on ^{27}Al

In order to study the effect of the target mass on the reaction mechanism, it is convenient to study the scattering of ^{9}Be on a lighter target using the same formalism. For ^{27}Al, elastic scattering data are available in the literature at near barrier energies [164]. In this reference it is shown that the coupling to breakup and/or transfer channels may be relevant even at energies below the Coulomb barrier.

For the coupling potentials, the n–target interaction from Ref. [156] already used for ^{208}Pb is adjusted for ^{27}Al. For the $\alpha-^{27}$Al interaction, the code by S. Kailas [165] provides suitable optical model parameters for α particle scattering using the results from Ref. [166]. Calculations with

light targets converge faster with respect to parameters K_{max}, i_{max} and ε_{max}, due to the weaker Coulomb interaction. The results here presented correspond to $K_{max} = 10$, $i_{max} = 6$ and $\varepsilon_{max} = 6$ MeV, including again $j^\pi = 3/2^\pm, 1/2^\pm, 5/2^\pm$ continuum states to describe the projectile. These values ensure convergence at the energies considered, $E_{lab} = 12, 14, 22$ and 32 MeV. In this section only final results are shown, although a convergence analysis similar to the case of the ^{208}Pb target has been carried out.

In Fig. 4.11 we show the elastic cross section above (32, 22 MeV) and around (14, 12 MeV) the Coulomb barrier. In all cases, the differences between calculations including only the ground state (dashed lines) and full CDCC calculations (solid lines) are significantly smaller with respect to the reaction on ^{208}Pb. This indicates that breakup effects are less important with light targets and confirms that Coulomb breakup is the dominant process at low incident energies. The agreement with the experimental data is reasonable but our calculations underestimate the elastic cross section at backward angles, especially at 14 and 22 MeV. For light targets the Coulomb repulsion is weak, so nuclear effects begin to dominate, and the internal structure of the target plays a more important role. This problem may be neglected for heavy targets, but a comprehensive study for light targets is needed. Moreover, the nuclear-dominated region depends on the features of the phenomenological optical potentials between the projectile fragments and the target at the corresponding energy per nucleon. This produces an uncertainty in the nuclear potential that makes difficult, in general, to reproduce with high precision the backward-angle region, where nuclear effects dominate.

4.2.3 ^{9}Be on ^{120}Sn

Preceding sections address the scattering of ^{9}Be on two different targets (heavy ^{208}Pb and a light ^{27}Al). The convergence of the calculations with heavy target has been shown to be slower, due to the large Coulomb breakup effects. Continuum couplings for the light target are much less relevant, and nuclear effects could play a more significant role. An interesting case between these two limits is the scattering on an mid-mass target.

Quasielastic scattering of ^{9}Be on ^{120}Sn has been recently measured at TANDAR laboratory [167]. In this case, the first 2^+ excited state of the target lies at 1.2 MeV above its 0^+ ground state. The charge of Sn is significantly

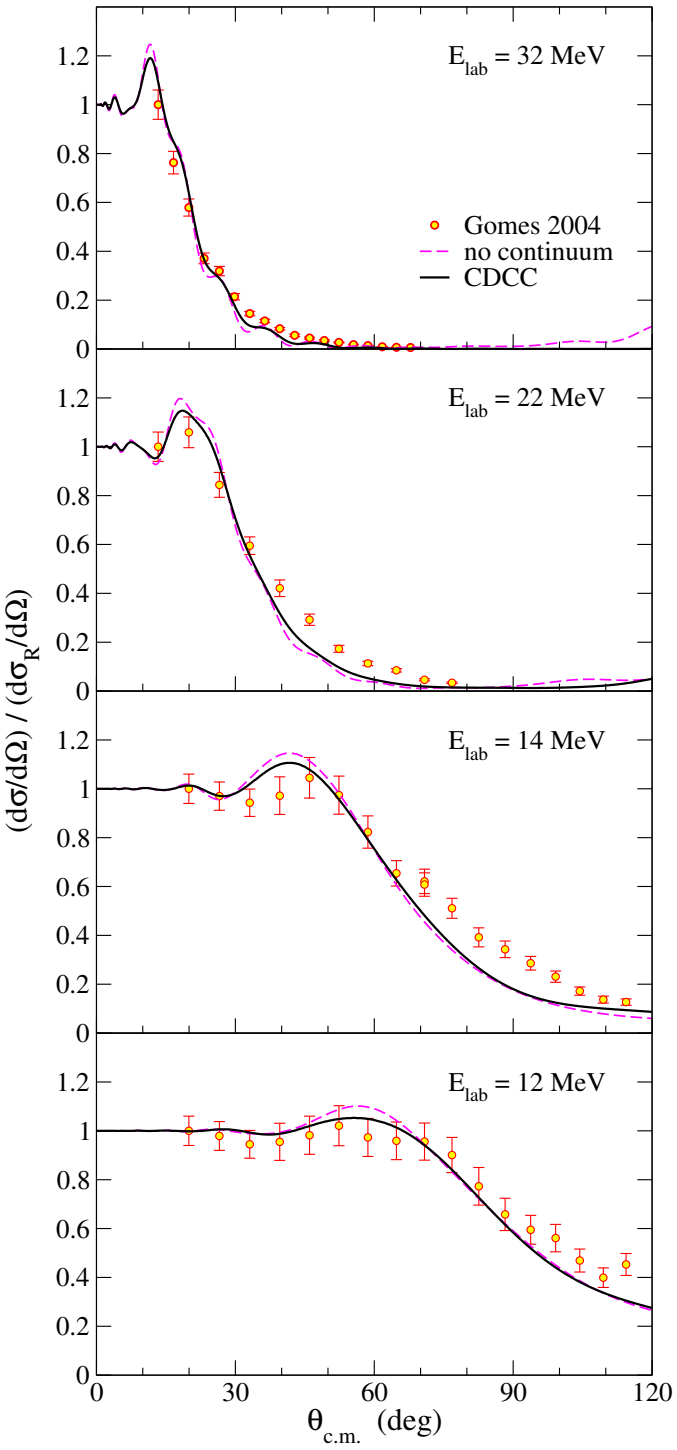

Figure 4.11: Angular distribution of the elastic cross section relative to Rutherford for the reaction ^{9}Be + ^{27}Al at $E_{lab} = 32, 22, 14$ and 12 MeV. Calculations use $i_{max} = 6$ and $\varepsilon_{max} = 6$ MeV. The experimental data are shown with circles (Gomes 2004: [164]).

smaller than that of Pb, so the Coulomb repulsion should be weaker and therefore the internal structure of the target may play an important role. Thus, reactions at energies around and above the Coulomb barrier will likely excite the target. As in the case of ^{27}Al, this effect cannot be explicitly included within the CDCC method as presented in this work, where the scattering wave functions are expanded in internal states of the projectile and the target is considered to be inert. Nevertheless, comparison between the CDCC results and experimental data can still provide insight into the reaction mechanism.

The coupling potentials are generated considering again the global parametrizations of Koning-Delaroche [156] and Kailas *et al.* [165] for the n-target and α-target interactions, respectively. To get convergence of the calculations in this case, a ^{9}Be basis with $K_{max} = 10$, $i_{max} = 8$ and $\varepsilon_{max} = 8$ MeV is required. As in the previous cases, all $j^{\pi} = 3/2^{\pm}, 1/2^{\pm}, 5/2^{\pm}$ continuum states are considered to describe the projectile excitations. These values ensure convergence of the calculation at the different energies considered and, as in the case of the ^{27}Al target, the corresponding convergence analysis is not shown.

The experimental data on this reaction is still to be published in collaboration with the Sevilla group. The preliminary results at energies below the Coulomb barrier are compared with the four-body CDCC calculations in Fig. 4.12. Continuum effects are not as large as in the case of ^{208}Pb, but larger than in the ^{27}Al case. This is another indication that the dominating process at low energies is Coulomb breakup. The agreement between calculations and the preliminary data is rather accurate and suggests that the explicit inclusion of target excitations is not required to cover the main features of the reaction.

As the incident energy E_{lab} is increased, the reaction approaches the Coulomb barrier and this behavior no longer holds. The experimental data at 29.5, 31 and 42 MeV, compared with the corresponding CDCC calculations, are shown in Fig. 4.13. Calculations show a suppression of the rainbow at 29.5 MeV, and the nuclear-Coulomb interference pattern begins to form at higher energies. The experimental data, however, presents a pronounced rainbow at 29.5 MeV, in disagreement with the CDCC calculations. This apparent difference is not shown at 31 and 42 MeV. The experimental data give a rainbow-like structure at 29.5 MeV but not so pronounced at 31 MeV. The

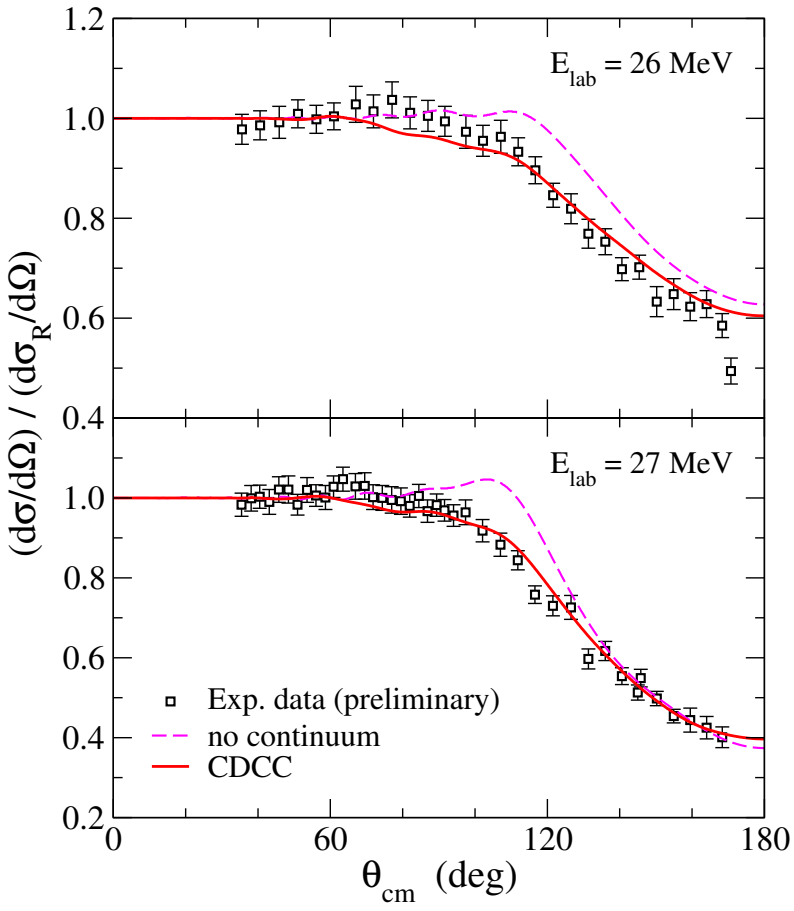

Figure 4.12: Angular distribution of the elastic cross section relative to Rutherford for the reaction ^{9}Be + ^{120}Sn at E_{lab} = 26 and 27 MeV. Calculations use $i_{max} = 8$ and $\varepsilon_{max} = 8$ MeV. The experimental data are shown with squares (Arazi *et al.*, preliminary).

rainbow is expected to appear as the incident energy increases and nuclear effects begin to have a relevance in the nuclear-Coulomb interference region, as indicated by the trend in the CDCC calculations. This issue at energies around the Coulomb barrier has already been discussed in the case of the ^{208}Pb target. At energies closer to the Coulomb barrier, technical problems related to the beam misalignment [12, 160, 162] could imply an slope change in the elastic cross section at the nuclear-Coulomb interference region. The different behaviors shown by the data at increasing energies supports this argument.

Apart from that difference at 29.5 MeV in the rainbow region, which could be due to a problem with the data, the agreement with the CDCC calculations is remarkable. Nevertheless, CDCC calculations do not consider explicitly inelastic excitations of the target. This effect, which becomes more relevant as the incident energy increases, could explain the small difference in the angular position of the rainbow between calculations and the data at 31 and 42 MeV. A proper treatment of target excitations should be employed in order to study this effect on the reaction mechanism. This has been addressed for the scattering of ^{6}He on ^{9}Be at energies above the barrier [168] by using a simple coupled-channel calculation, showing that the effect of ^{9}Be excitation was negligible compared to that of the ^{6}He projectile. However, in that work only the rotational states on top of the $3/2^{-}$ states were considered, with the first one being at around 2.5 MeV over the ground state of ^{9}Be. In the case of the ^{120}Sn target, the lowest excited state at around 1 MeV belongs to the ground-state rotational band, which could imply an important difference in terms of influence on the elastic cross section.

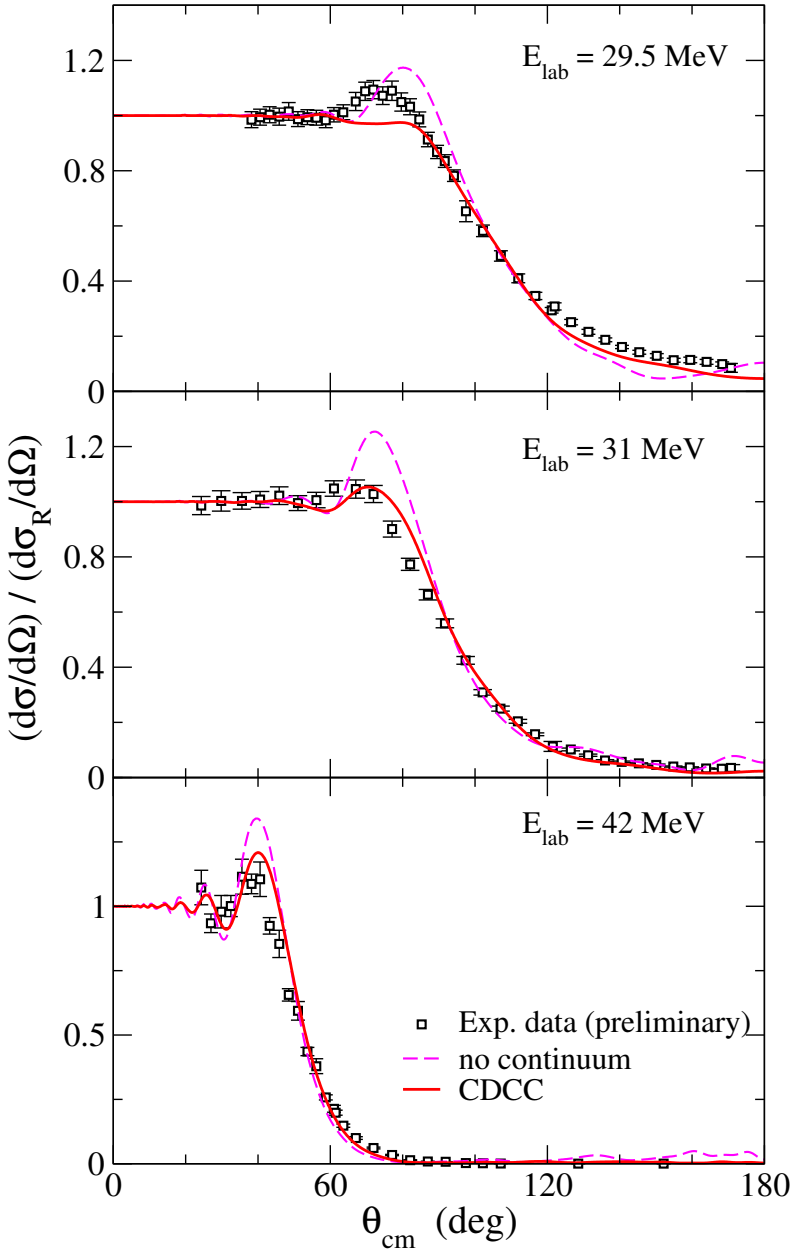

Figure 4.13: Angular distribution of the elastic cross section relative to Rutherford for the reaction ^{9}Be + ^{120}Sn at $E_{lab} = 29.5, 31$ and 42 MeV. Calculations use $i_{max} = 8$ and $\varepsilon_{max} = 8$ MeV. The experimental data are shown with squares (Arazi *et al.*, preliminary)

In this chapter, the four-body CDCC framework has been presented as a method to describe reactions induced by three-body projectiles. Including explicitly the continuum states of the projectile, the influence of breakup channels on the elastic cross section can be studied. For that, projectile states have been described using the analytical THO method as presented in chapter 2. The method has been applied to reactions induced by the weakly-bound Borromean nucleus ^{9}Be on three different targets: ^{208}Pb, ^{27}Al and ^{120}Sn, at energies around the Coulomb barrier. Continuum effects indicate that the dominating process at low energies is Coulomb breakup of the projectile. The agreement with the available experimental data is remarkable considering that there is no parameter fitting, and supports the reliability of the method (CDCC + analytical THO) in describing reactions induced by three-body projectiles comprising more than one charged particle.

Chapter 5

Summary and conclusions

An expert is a person who has found out by his own painful experience all the mistakes that one can make in a very narrow field.

Niels Bohr

Along the pages of this work, theoretical approaches to study the structure and reactions of three-body Borromean nuclei have been presented. These are three-body systems whose binary subsystems are unbound, which has important consequences on the theoretical description. The hyperspherical formalism is an ideal tool to describe three-body Borromean systems, since it considers the three components on an equal footing assuming no specific two-body structure.

A particular case of Borromean nuclei are those presenting a two-nucleon halo. Close to the driplines, some valence nucleons are so barely bound that, in some cases, they can explore large distances giving rise to a dilute matter cloud around a more compact structure or *core*. Halo nuclei are weakly-bound systems characterized by large interaction cross sections and important breakup effects in scattering processes even at Coulomb-barrier energies. This is the case of the $2n$ halo nuclei ^{6}He and ^{11}Li, and the candidate for $2p$ halo ^{17}Ne. The Borromean structure, however, is not restricted to exotic systems, and also appears for nuclei along the stability line such as the weakly-bound ^{9}Be nucleus or ^{12}C nucleus.

The formation of Borromean nuclei is of relevance in nucleosynthesis, with three-body capture reactions being, in some cases, key ingredients for stellar models. The synthesis of nuclei in stellar environments can be described as a decay from an unbound state of several particles that fuse together producing a bound system. In order to understand the underlying mechanisms that govern the structure and dynamics of these nuclei, experimental constraints can be used to assess the validity of theoretical models describing their properties. For instance, exotic nuclei present typically a small separation energy and consequently large breakup probabilities in scattering processes. The breakup of the system can be understood as an excitation of the nucleus to unbound states that form a continuum of energies. Thus, a reliable theoretical description of these systems must include a proper treatment of continuum states.

In the present work, the three-body problem is solved using the Pseudo-State (PS) method in hyperspherical coordinates, which consists in diagonalizing the system Hamiltonian in a basis of square-integrable functions. While the negative-energy solutions of that problem describe the bound states of the system, positive-energy eigenstates provide a discrete representation of the continuum. The analytical Transformed Harmonic Oscillator (THO) basis, previously applied to describe two-body systems, is selected for the PS method and generalized for the case of three-body systems. This basis is obtained by performing a simple local scale transformation to the Harmonic Oscillator (HO) functions. The transformation corrects the Gaussian asymptotic behavior of the HO functions in order to match the exponential decay of the bound solutions for potentials with finite depth and range, providing a suitable representation of the system states to calculate structure and scattering observables. The parameters defining the analytical transformation govern the radial extension of the basis, which determines the density of PSs as a function of the excitation energy. This allows to select an optimal basis depending on the observable of interest. The kinetic energy matrix elements have an analytic form and are calculated by Gauss-Laguerre quadratures. The computation of potential matrix elements is performed in two steps: first, the angular integration is achieved by following the prescriptions in the FaCE code. Then, the resulting hyperradial matrix is integrated numerically. After diagonalization of the three-body Hamiltonian, the PSs enable the cal-

culation of different observables, such as matter and charge radii or transition probabilities, provided the appropriate quantum operators are known. Note that, within few-body models, the Pauli principle cannot be treated exactly. In general, some components of the system wave functions would disappear under full antisymmetrization, which has to be taken into account by using approximated theories.

The method has been first applied to ^{6}He (α+n+n), a paradigmatic two-neutron halo nucleus. The $j^\pi = 0^+$ ground state is characterized by a two-neutron separation energy of 0.975 MeV. As a halo system, it exhibits a large dipole response at low energies. The system presents also a well-known 2^+ resonance at 0.824 MeV over the breakup threshold. The model Hamiltonian considers n-n and α-n binary interactions which are fitted to reproduce the experimental data on two-body scattering. In addition, a phenomenological three-body force is required to adjust the position of three-body states to their experimentally known energies. A good agreement with the system matter and charge radii is achieved when the ground state is fixed to the experimental energy. Describing the system in the Jacobi-T set, the ground state wave function shows a predominance of s-wave components in the relative n-n motion. This prevails when rotating the wave function to the Jacobi set where the x-coordinate relates the α core and one neutron, and it is a signal of the dilute halo tail of the wave function. The two-dimensional probability distribution for the ground state exhibits two peaks, which are typically associated with the so-called dineutron and cigar configurations.

As for the excited states in ^{6}He, it is shown that a proper choice of the basis parameters enables the isolation of the 2^+ resonance in a single PS. Its wave function resembles the behavior of a bound state, with a slightly larger hyperradial distribution. Since dipole excitations from the ground state to continuum states are the most relevant dynamics in low-energy reaction involving halo nuclei, the transition strengths to the 1^- state are computed. The $B(E1)$ distribution is described using a basis of 1^- states defined by a large hyperradial extension, which concentrates a large level density near the threshold. This enables to build up a detailed transition probability distribution. The electric dipolar strength is highly concentrated at low excitation energies, which is another signal of a typical halo nucleus. The sum over discrete $B(E1)$ values converges rapidly to the sum rule for dipolar transitions, confirming that the basis and calculations are well converged.

These results encourage the application of the analytical THO method to more complex three-body Borromean systems.

Then, the method has been applied to ^{9}Be, comprising two α particles and one neutron. This nucleus is stable but has a small binding energy of 1.574 MeV below the three-body threshold. Therefore, the system shares some properties with exotic nuclei. The ground state in this case has a spin-parity assignment of $3/2^-$, and the system presents several low-energy resonances characterized by $1/2^{\pm}$, $3/2^{\pm}$ and $5/2^{\pm}$. The lowest is a genuine three-body $1/2^+$ resonant state around 0.11 MeV with a relatively large width. As in the case of ^{6}He, a phenomenological three-body force is required, in addition to the corresponding binary interactions, in order to fit the energy of the three-body known states to their experimental values. The computed matter and charge radii for the $3/2^-$ ground state are in good agreement with the experimental data on these observables. This reveals that the method is rather accurate also for systems comprising more than one charged particle. The ^{9}Be system is a significantly deformed nucleus and exhibits a large quadrupole moment. The calculated quadrupole moment agrees reasonably with the experimental value and is consistent with the ground state probability showing a large deformation. As for the excited states, the three-body model provides a reliable description of the lowest $1/2^+$ resonance. The corresponding $B(E1)$ distribution from the $3/2^-$ ground state shows a broad peak just above the breakup threshold, with a large tail exploring higher energies. This is not the typical behavior of low-energy resonances, which present usually narrow widths. The $B(M1)$ distribution to $5/2^-$ states is also calculated and shows a peak which is consistent with the narrow $5/2^-$ resonance around 0.85 MeV. The results for ^{9}Be validate the reliability of the method in describing three-body systems comprising more than one charged particle, for which the computation of actual continuum states is a very involved problem.

A case comprising three charged particles is ^{17}Ne, which can be considered as an ^{15}O core plus two valence protons. It has been proposed to have a two-proton halo, but evidences and theoretical studies are not yet conclusive. The ^{17}Ne ground state has the same spin-parity assignment than its ^{15}O core, $1/2^-$. It is a weakly-bound system close to the proton dripline, with an experimental two-proton separation energy of 0.94 MeV. The contribution of core excitations for structure calculations cannot be completely neglected,

especially for excited states in ^{17}Ne, but the parity and high energy of the first ^{15}O excited states suggests that the assumption of a frozen core is a reliable picture. The binary interaction ^{15}O-p has been fitted to reproduce the experimental spectrum of the unbound nucleus ^{16}F. The computed ground state, once adjusted to the experimental two-proton separation energy of 0.94 MeV, gives matter and charge radii in reasonable agreement with experimental data. The probability distribution of ^{17}Ne shows two peaks that are related to two protons either on the same side or at almost opposite sides of the oxygen core. The ground state wave function in the Jacobi-Y set, where coordinate x connects the ^{15}O and one proton, presents contributions from s- and d-waves of about 40 and 50%, respectively. These numbers can support the existence of a proton halo in ^{17}Ne, although the system radius and that of its core are not noticeably different. As in the previous cases, electromagnetic transition probabilities between the ground state and continuum states are calculated. For $1/2^+$ states, the $B(E1)$ distribution concentrates all the strength in a narrow resonance around 0.97 MeV. Computation of j^π excited states agrees with the experimentally known resonances of ^{17}Ne, confirming the reliability of the method for systems which comprise three charged particles.

Radiative capture reactions for the formation of three-body Borromean nuclei have traditionally been studied as sequential processes. At low temperatures, however, the initial particles may have not enough energy to populate intermediate configurations and therefore they can fuse directly. This requires a full three-body model with no assumption about the reaction mechanism. The reaction rate of such process is governed by electromagnetic transitions and can be obtained from the time-reversed photodissociation process. This relies on the knowledge of the electric and magnetic transition probability distributions, either experimentally or from a reliable theoretical model. The analytical THO method is applied to generate these distributions for systems of astrophysical interest, such as the already presented ^{6}He, ^{9}Be and ^{17}Ne nuclei, to compute their reaction rates in the whole temperature range.

The ^{4}He$(2n,\gamma)^6$He reaction has been linked to the r-process in neutron star mergers. The reaction rate is governed by electric dipolar transitions between the 0^+ ground state and the 1^- continuum. The contribution from quadrupolar transitions to 2^+ states is negligible. Results are tested against the computation of the reaction rate from actual continuum calculations of

the $B(E1)$ distribution, which can be generated easily in this simple case comprising a single charged particle. The agreement supports the suitability of the THO method to describe these reactions. The present results are compared with those from a sequential model and another three-body calculation. The differences give rise to an uncertainty for the reaction rate depending on the model. Nevertheless, the analytical THO method provides a detailed description of the transition probability distribution at low energies. This, together with the good agreement with the actual continuum calculation, indicates the robustness of the present results.

The formation of ^{9}Be through the $\alpha(\alpha n,\gamma)^9$Be reaction can also be relevant for the r-process, but especially in supernova nucleosynthesis. The reaction rate is computed including E1 contributions to $1/2^+$, $3/2^+$, and $5/2^+$ states, and M1 contributions to $1/2^-$ and $5/2^-$ states. From the transition probabilities, the total photodissociation cross section is calculated and compared with two sets of experimental data and with previous estimations. The lowest peak corresponding to $1/2^+$ states governs the cross section and shows the right behavior, but underestimates the experimental data. The narrow peak corresponding to the $5/2^-$ resonance is also well reproduced. The present results provide the first full three-body calculation of the ^{9}Be photodissociation cross section in the whole energy range, and agrees reasonably with features observed in the experiments. Although the behavior is very similar in both sets of data, there are important discrepancies between them. This makes difficult the comparison with calculations, so the origin of the underestimation at low energies is unclear. Nevertheless, the overall agreement between the present calculations and the available data supports the reliability of the method in describing the ^{9}Be wave functions within a three-body approach. From the total photodissociation cross section, the reaction rate is easily computed. As expected, the $1/2^+$ contribution dominates almost in the whole temperature range, with others being relevant only at the highest temperatures. The reaction rate converges to sequential estimations from experimental data at high temperatures, but shows an enhancement of several orders of magnitude in the low-temperature tail. This effect comes from the direct capture and cannot be described within sequential models.

The case of the $^{15}\mathrm{O}(2p,\gamma)^{17}$Ne reaction is studied as a possible breakout reaction of the hot CNO cycle, which has implications for the rp-process towards the production of neutron-deficient nuclei. Previous calculations by

Grigorenko *et al.* suggested that the three-body capture is significantly larger than the sequential capture in the whole temperature range. The dominant contributions to the photodissociation cross section and the corresponding reaction rates come from $1/2^+$ states (E1), at high temperatures, and from $3/2^-$ states (M1) at low temperatures. However, the present calculations are noticeably larger than those by Grigorenko *et al.* at high temperatures. The present results are supported by Garrido *et al.* using different model and interactions to describe the structure of ^{17}Ne. Experimental data on ^{17}Ne photodissociation could help in understanding these differences.

In general, the presented reaction rates treat the resonant and non-resonant, sequential and direct contributions on an equal footing for different systems. The method provides a powerful tool for the computation of stellar evolution models. Full nucleosynthesis network calculations are asked for to test the sensitivity of r-process and rp-process models to these updated reaction rates.

Since reaction rates have an important uncertainty related to the differences in the different theoretical approaches, an alternative procedure has been proposed to estimate them from inclusive breakup measurements. A relation between the three-body capture reaction rate and the inclusive Coulomb breakup probability has been established, in the region in which the first order dipole Coulomb interaction is dominant and can be described using the semiclassical theory. The temperature of the stellar environment is directly related to the collision time of the reaction, which is related to the scattering angle through the kinematic parameters. This allows to explore different temperature ranges by measuring Coulomb breakup at different energies. The method is tested for ^{11}Li, for which data on inclusive breakup has been measured recently at TRIUMF. The computed $^{9}\mathrm{Li}(2n,\gamma)^{11}\mathrm{Li}$ reaction rate is compared to that obtained within two- and three-body models for ^{11}Li, and with the reaction rate obtained by integrating directly the experimental $B(E1)$ from exclusive breakup at RIKEN. The reaction rate in the present work is significantly larger than the reaction rate extracted from the RIKEN data, although these have considerable uncertainties. However, it should be remarked that both sets of experimental data allow to extract information on the astrophysical reaction rate, giving results in the same order of magnitude. The new method provides an additional motivation to carry out Coulomb scattering experiments of exotic nuclei, and establishes a

demanding reference to assess the validity of the different theoretical models that have been used to calculate reaction rates.

Direct reactions involving three-body projectiles can also be studied using the analytical THO method to describe projectile couplings. In the case of weakly-bound projectiles, continuum couplings may play an important role, which is reflected by large breakup probabilities. The Continuum-Discretized Coupled-Channel (CDCC) method enables the inclusion of continuum states in the formalism. It consists in expanding the total scattering wave function in a basis of projectile or target internal states. Reactions induced by three-body projectiles can be addressed in a four-body CDCC framework, including bound and continuum states of the projectile and considering a structureless target. In the present work, the projectile states are described using THO pseudo-states. This enables the computation of reactions involving projectiles with several charged particles. The method is applied to ^{9}Be-induced reactions on different targets: ^{208}Pb, ^{27}Al and ^{120}Sn, at energies around the Coulomb barrier. The model space to describe ^{9}Be includes $j^{\pi} = 3/2^{\pm}, 1/2^{\pm}$ and $5/2^{\pm}$ states. The coupling potentials are generated externally and then used by the FRESCO code to solve the coupled equations, including projectile-target interaction multipole couplings to all orders.

Continuum effects indicate that the dominating process at low incident energies is Coulomb breakup. The role of low-energy resonances on the reaction mechanism is shown to be important. The agreement with the available experimental data on elastic scattering and breakup is remarkable considering that CDCC calculations involve no parameter fitting, which confirms the reliability of the method. However, some differences between the present calculations and the experimental data are observed. For the scattering on ^{208}Pb around the Coulomb barrier, the computed elastic cross section underestimates the experimental cross section in the nuclear-Coulomb interference region. This behavior is also observed in recent four-body CDCC calculations by Descouvemont *et al.* and is consistent with the observed enhancement of the breakup cross section in the nuclear-Coulomb interference region for the scattering of other weakly-bound nuclei, such as ^{11}Li or ^{11}Be, on heavy targets. As for the scattering on ^{27}Al and ^{120}Sn, small differences are associated to the possible effect of target excitations which are not explicitly included in the model.

In conclusion, the analytical THO method has been used to describe the structure and reactions of Borromean nuclei, providing reasonable results for ^{6}He, ^{9}Be and ^{17}Ne. The method has been applied to three-body radiative capture reactions and four-body direct reactions, and the present results support its reliability for systems comprising several charged particles. Other Borromean nuclei and reactions involving them can be addressed using the same ingredients, which makes the analytical THO method a powerful and versatile tool. A new method to estimate reaction rates from inclusive Coulomb breakup measurements has also been proposed and tested for the case of ^{11}Li. Experimental data on ^{6}He or ^{17}Ne breakup could help in estimating the corresponding reaction rate and understanding the differences between different theoretical approaches.

Further applications of the analytical THO method are subjects for future research. Among them, the method can be used to describe quasifree scattering reactions induced by three-body projectiles. These reactions have been used as a tool to extract spectroscopic information of nuclei, such as separation energies, spin-parity assignments, and occupation probabilities. Three-body models of nuclei carry information about the underlying correlations between core and valence particles. The derivation of full energy and angular correlations between fragments for direct reactions with three-body projectiles is a work to be done. Finally, it would be also interesting to study the case of direct reactions involving three-body nuclei with core excitations.

Chapter 6

Work in progress: The case of ^{12}C

The ^{12}C nucleus has been mentioned in several parts of this thesis, mainly due to its relevance in stellar nucleosynthesis. The triple-α reaction ($\alpha + \alpha + \alpha$) can bridge the instability gaps at mass numbers $A = 5$ and $A = 8$ [30], and it serves as a key process towards the production of heavier elements. Fred Hoyle postulated the existence of a 0^+ resonance close to the three-body threshold to justify the observed abundances of ^{12}C in stars [31], state that was experimentally confirmed shortly thereafter. Since then, the accepted mechanism for the triple-α capture was a two-step process via ^{8}Be to populate the so-called Hoyle state. However, if the energy of the α particles is not sufficient to populate ^{8}Be resonances, the three-body direct capture can play a significant role [34]. Recent estimations on the reaction rate for such process present noticeable differences at low temperatures [32–36].

The structure of ^{12}C can be addressed within a three-body model, as it presents a Borromean structure. The spectrum of ^{12}C is shown in Fig. 6.1. The ground state is a 0^+ state at 7.27 MeV below the three-body threshold [169]. This is not strictly a weakly-bound system, as those presented in chapter 2. The 0^+ Hoyle state is a genuine three-body state at 0.38 MeV above the breakup threshold [170]. It has been found that the triple-α radiative capture reaction is governed by E2 transitions between 0^+ states and the first 2^+ state at 2.83 MeV below the threshold [35, 104]. Therefore, a reliable theoretical estimation of the reaction rate requires a proper description of the 0^+ and 2^+ states in a three-body model. This involves the treatment of three identical charged bosons.

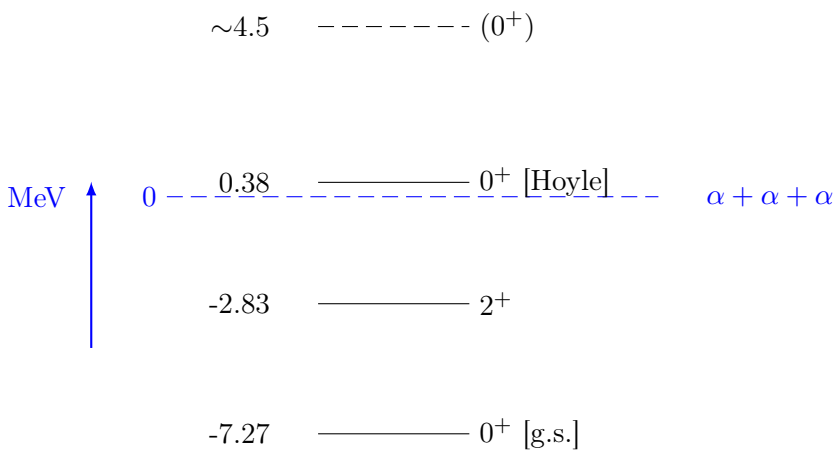

Figure 6.1: Spectrum of ^{12}C with respect to the three-body threshold.

The presence of three identical particles in the formalism implies that all Jacobi sets are equivalent. In a fixed Jacobi system, the interacting pair of α particles are two identical bosons with spin 0^+. As in the case of ^{9}Be (see section 2.4), the symmetry of the wave function is imposed by considering only even l_x components. In this case, however, the condition holds for the three Jacobi sets. This considerations have to be taken into account in the FaCE subroutines used to generate the wave function components. The model Hamiltonian includes the α-α interaction, which can be taken as the same used for ^{9}Be calculations. The three-body force is parametrized with a simple Gaussian form (Eq. 2.50), whose parameters are fixed to reproduce the positions of the 2^+ bound state and the Hoyle resonance. Note that the ground state of the system, which is also a 0^+ state, is disregarded for this study.

The three-body problem is solved using the pseudo-state method with the analytical transformed harmonic oscillator (THO) basis, as introduced in chapter 2. In order to describe properly the bound state, a THO basis with parameters $b = 0.7$ fm and $\gamma = 1.4$ fm$^{1/2}$ is selected. The computed 2^+ state is characterized by well converged energy and radius. This is shown in Figs. 6.2 and 6.3 (solid black lines), in which the convergence of these observables with respect to the maximum hypermomentum K_{max} is presented. Remember that K_{max} defines the size of the model space. From these pictures it is clear that $K_{max} = 20$ provides a well converged bound state. Assuming an α-particle radius of 1.47 fm, the calculated matter radius

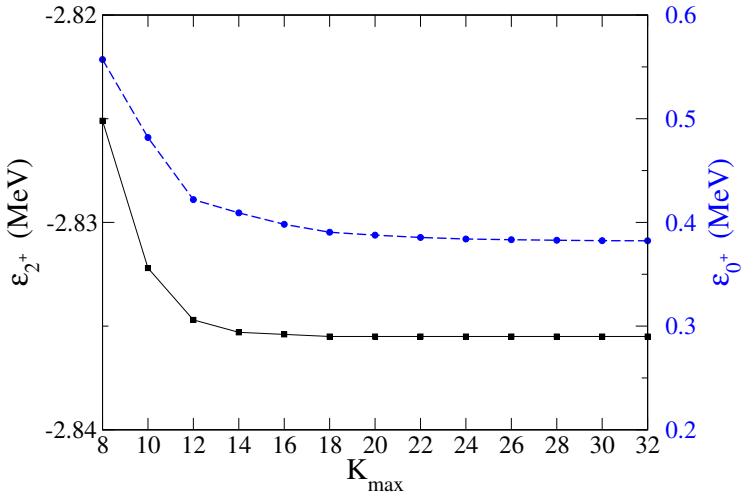

Figure 6.2: Energy of the 2^+ bound state (black line) and the Hoyle state (dashed blue line) in ^{12}C with respect to the maximum hypermomentum K_{max}. Notice the different scales.

for the 2^+ state is 2.46 fm. This number is similar to the result obtained in a microscopic calculation in Ref. [170]. The agreement validates the three-body approximation for the 2^+ bound state.

In order to study the Hoyle resonance, 0^+ states are first generated using a THO basis with a small hyperradial extension, i.e. $b = 0.7$ fm and $\gamma = 2.0$ fm$^{1/2}$. This, as discussed in chapter 2, provides a low density of states just above the breakup threshold and enables the isolation of the resonant behavior in a single pseudo-state. The convergence of the resonance energy and matter distribution with respect to K_{max} is also shown in Figs. 6.2 and 6.3 (dashed blue lines). In this case, a value of K_{max} around 26 is required to achieve convergence. The computed matter radius for the Hoyle resonance is 3.71 fm, also in agreement with Ref. [170].

The spatial configuration of three α particles within the 2^+ bound state and the Hoyle resonance can be studied by constructing the two-dimensional probability distributions. This is shown in Fig. 6.4, where r_x is the distance between two α particles, and r_y is the distance from their center of mass to the third α. The dominant configuration for the 2^+ bound state (upper panel in Fig. 6.4) is found at $r_x \simeq 3$ fm and $r_y \simeq 2.5$ fm, which is consistent with an equilateral triangle in which each pair of α particles is around 3 fm apart. This result is in agreement with the three-body calculation in Ref. [35], in

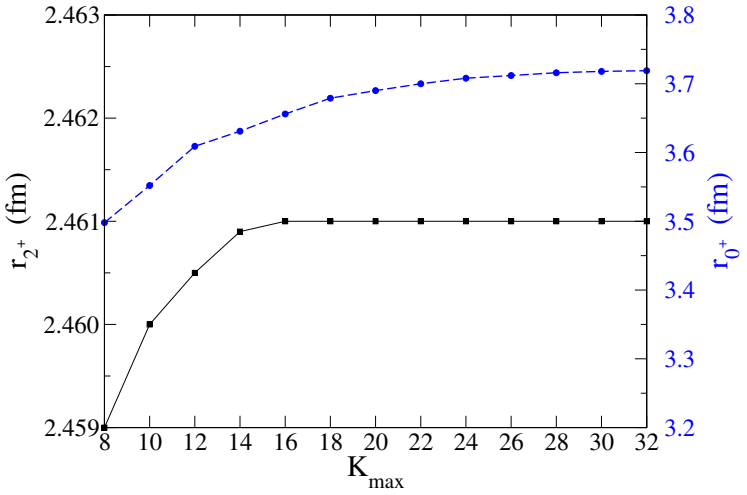

Figure 6.3: Matter radius of the 2^+ bound state (black line) and the Hoyle state (dashed blue line) in ^{12}C with respect to the maximum hypermomentum K_{max}. Notice the different scales.

which the hyperspherical harmonic expansion is applied to find solutions of the coupled-channel problem for bound states. Therefore, the pseudo-state method presented in this work provides, for bound states, the same result than that obtained by solving numerically the differential equations. This was already discussed in chapter 2 for the case of ^{6}He.

The lower panel in Fig. 6.4 shows the probability distribution for the Hoyle state. The dominant configuration is described by a probability maximum around $r_x \simeq 2.5$ fm and $r_y \simeq 3.5$ fm, which corresponds again to an almost equilateral triangle. This maximum features a long tail exploring distances up to $r_x \simeq 5$ fm and $r_y \simeq 6$ fm, which can be associated to a triangle where two α particles are close to each other and further away from the third. Another structure, shown as a dilute blur in Fig. 6.4, appears around $r_x \simeq 6.5$ fm and $r_y \simeq 2$ fm. These three structures agree with those obtained in Ref. [35], although their relative weights are different. In this reference, the so-called "prolate triangle" dominates, while in the present work it appears as a dilute tail in the probability distribution. Note that, in Ref. [35], the actual continuum problem is solved at the Hoyle energy, while in the present method this state is represented by a pseudo-state. By definition, pseudo-states contain information about all continuum states in the vicinity, and even with an optimal basis some non-resonant background is unavoidable.

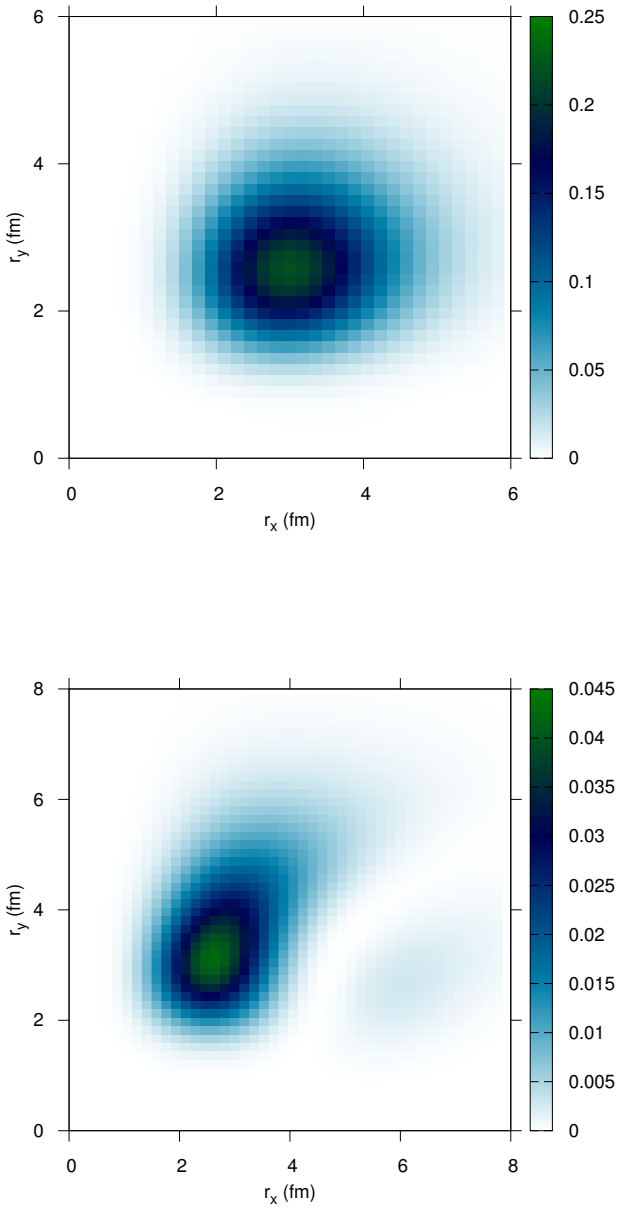

Figure 6.4: Probability distribution for the 2^+ bound state (upper panel) and for the Hoyle state (lower panel).

Electric quadrupolar transitions (E2) between the 2^+ bound state and 0^+ continuum states can be computed making use of the general Eq. (2.23). Equivalently, the electric quadrupolar operator can be expanded by using the relationship between harmonic polynomials in different Jacobi sets (see Eq. (2.26) and its application to different systems in chapter 2). This leads to a separation of the operator into two terms,

$$\widehat{Q}_{2M_\lambda}(\boldsymbol{x},\boldsymbol{y}) = \left(\frac{4\pi}{5}\right)^{1/2} Z_\alpha e \, \frac{m}{m_\alpha} \left[x^2 Y_{2M_\lambda}(\widehat{x}) + y^2 Y_{2M_\lambda}(\widehat{y})\right], \tag{6.1}$$

where Z_α and m_α are the charge and mass of an α particle. Therefore, the reduced transition probability in Eq. (2.15) can be written as a sum of two matrix elements,

$$B\left(E2\right)_{nj\to n'j'} = \left(\frac{5}{4\pi}\right) \left[\langle nj||\widehat{Q}_2||n'j'\rangle_x + \langle nj||\widehat{Q}_2||n'j'\rangle_y\right]^2. \tag{6.2}$$

After working out the algebra, these terms are

$$\begin{aligned}
&\langle nj||\widehat{Q}_2||n'j'\rangle_x = Ze\left(\frac{m}{m_c}\right)\hat{j}'\sum_{\beta\beta'}\sum_{ii'} C_n^{i\beta j} C_{n'}^{i'\beta' j'} \\
&\times \delta_{l_y l'_y}\delta_{S_x S'_x}\hat{l_x}\hat{l'_x}\hat{l}\hat{l}'\hat{j}_{ab}\hat{j}'_{ab}(-1)^{j+l_y+l_x+l'_x+S_x-j_{ab}+j'_{ab}-I+l+l'} \\
&\times \begin{pmatrix} l_x & 2 & l'_x \\ 0 & 0 & 0 \end{pmatrix} W(ll'l_x l'_x;\lambda l_y) W(j_{ab}j'_{ab}ll';\lambda S_x) W(jj'j_{ab}j'_{ab};\lambda I) \\
&\times \int\int (\sin\alpha)^2 (\cos\alpha)^2 \, d\alpha \; d\rho \; \varphi_K^{l_x l_y}(\alpha) U_{i\beta}^{THO}(\rho) x^2 U_{i'\beta'}^{THO}(\rho) \varphi_{K'}^{l'_x l'_y}(\alpha),
\end{aligned} \tag{6.3}$$

$$\begin{aligned}
&\langle nj||\widehat{Q}_2||n'j'\rangle_y = Ze\left(\frac{m}{m_c}\right)\hat{j}'\sum_{\beta\beta'}\sum_{ii'} C_n^{i\beta j} C_{n'}^{i'\beta' j'} \\
&\times \delta_{l_x l'_x}\delta_{S_x S'_x}\hat{l_y}\hat{l'_y}\hat{l}\hat{l}'\hat{j}_{ab}\hat{j}'_{ab}(-1)^{j+l_x+l_y+l'_y+S_x-j_{ab}+j'_{ab}-I} \\
&\times \begin{pmatrix} l_y & 2 & l'_y \\ 0 & 0 & 0 \end{pmatrix} W(ll'l_y l'_y;\lambda l_x) W(j_{ab}j'_{ab}ll';\lambda S_x) W(jj'j_{ab}j'_{ab};\lambda I) \\
&\times \int\int (\sin\alpha)^2 (\cos\alpha)^2 \, d\alpha \; d\rho \; \varphi_K^{l_x l_y}(\alpha) U_{i\beta}^{THO}(\rho) y^2 U_{i'\beta'}^{THO}(\rho) \varphi_{K'}^{l'_x l'_y}(\alpha).
\end{aligned} \tag{6.4}$$

As in the cases presented in chapter 2, the transition probabilities are computed in a basis providing a large density of pseudo-states near the breakup threshold. The discrete $B(E2)(\varepsilon_n) \equiv B(E2)_{12\to n0}$ values are shown

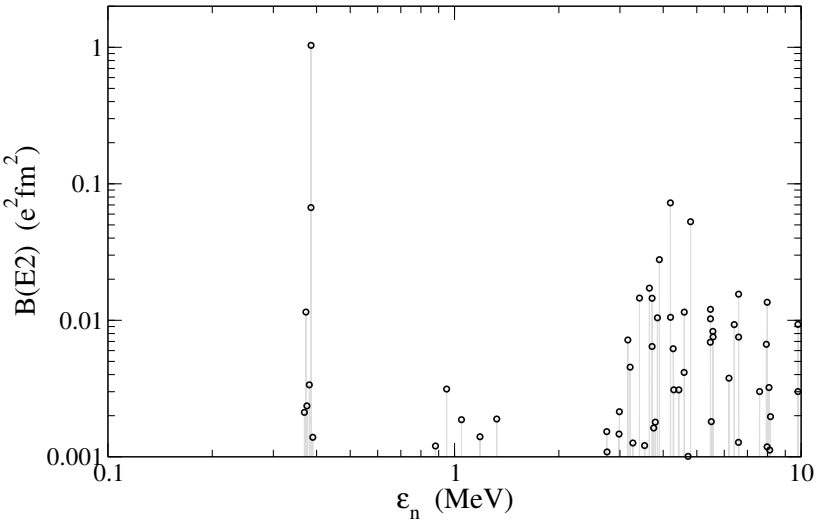

Figure 6.5: Discrete $B(E2)$ values corresponding to transitions from the 2^+ bound state to 0^+ continuum states in ^{12}C. Each circle represent the E2 strength to a single pseudo-state.

in Fig. 6.5. For clarity, a lower limit at 0.001 e^2fm^4 is established, and logarithmic scales are used. The total transition probability up to 10 MeV is 1.58 e^2fm^4, while states between 0.38 and 0.39 MeV carry 1.11 e^2fm^4. This indicates that the Hoyle resonance extinguishes around 70% of the quadrupolar strength.

A second, broad peak is found in Fig. 6.5 at energies around 4.5 MeV, which could indicate the presence of a second 0^+ resonance above the Hoyle resonance (see Fig. 6.1). The quadrupolar strength between 3 and 5 MeV is 0.28 e^2fm^4, which corresponds to 18% of the total transition probability. Note that calculations for 0^+ states include a phenomenological three-body force to fix the Hoyle resonance at 0.38 MeV, and therefore the position of this structure is somewhat arbitrary. This 0^+ state, which appears naturally in the present three-body model, has been observed experimentally [171] and is also predicted by algebraic cluster models [172].

The computation of the radiative capture reaction rate for the triple-α requires the photodissociation cross section associated to the inverse process. This is calculated from the $B(E2)$ values using Poisson distributions with an appropriate width parameter (see section 2.4 for a discussion regarding this matter). Results are shown in Fig. 6.6 up to 1 MeV, since higher energies

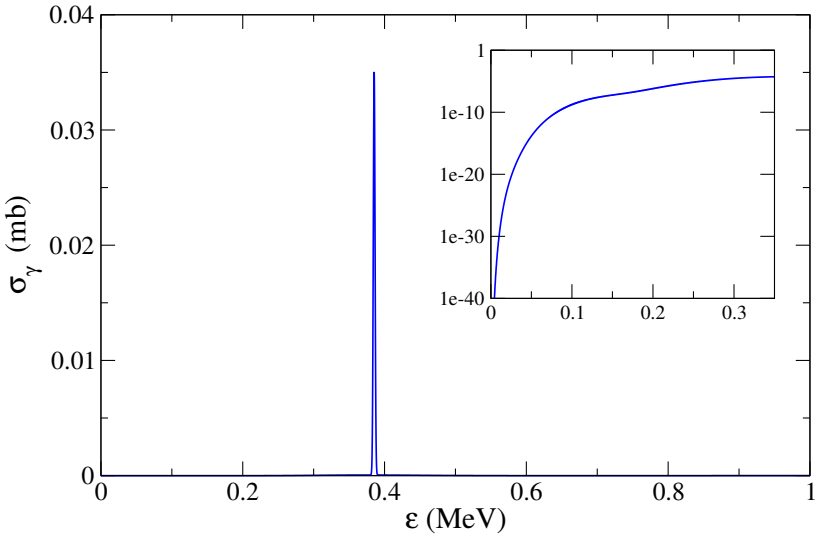

Figure 6.6: Photodissociation cross section of ^{12}C up to 1 MeV, considering only E2 transitions between the 2^+ bound state and 0^+ continuum states. The inset shows the cross section in a logarithmic scale at energies below the Hoyle resonance.

have little influence on the reaction rate at low temperatures. The photodissociation cross section is concentrated at the Hoyle resonance. However there is a non-negligible contribution at lower energies. This is shown in the inset of Fig. 6.6 using a logarithmic scale.

The reaction rate for ^{12}C formation is shown in Fig. 6.7. Previous estimations available in the literature are shown for comparison: i) The reference rate from the NACRE compilation [33] (black solid line), based on a sequential model. ii) The first three-body estimation of the triple-α reaction rate by Ogata *et al.* [32] (black dashed line). iii) The three-body Breit-Wigner estimation by Garrido *et al.* [34] (gray line) iv) The calculation by Nguyen *et al.* [35], in which actual three-body continuum wave functions are used (circled-solid line). These rates show considerable discrepancies at low temperatures. A recent estimation using the imaginary-time theory [173] agrees with the NACRE results, although it is not shown in the figure for clarity.

Three different calculations of the present work are presented together with the previous estimations. The first one corresponds to the reaction rate including only the Hoyle state (red dotted). This calculation matches the sequential estimation at high temperatures, which indicates that the dominating process in that region is a two-step capture reaction. The second

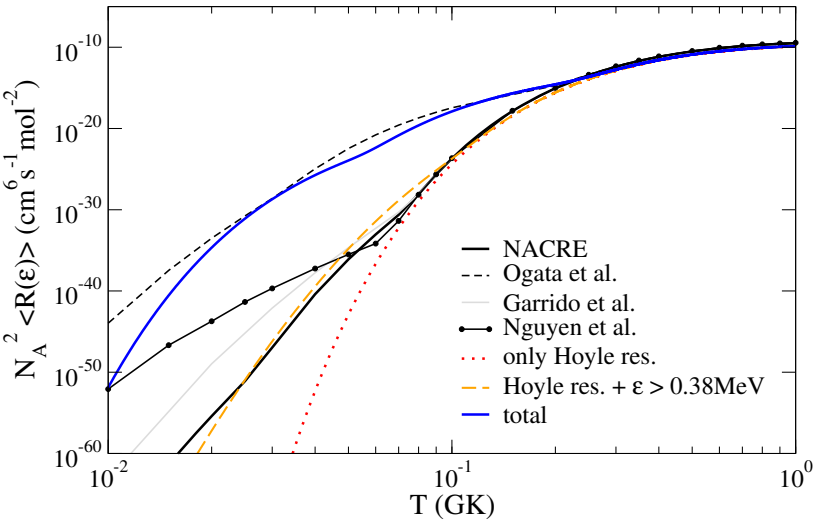

Figure 6.7: Reaction rate for the triple-α process as a function of the temperature in GK.

calculation includes, besides the Hoyle state, all pseudo-states above the resonance (orange dashed). This produces an enhancement of the reaction rate in fair agreement with the extrapolation of the NACRE results at low temperatures.

However, when the full calculation is performed (blue solid), the reaction rate at temperatures below 0.2 GK is several orders of magnitude larger than that of the NACRE compilation. A similar result was obtained by Ogata *et al.* [32], using also a discretization procedure to describe ^{12}C continuum states. This enhancement affects astrophysical studies and produces results which are incompatible with observations [174, 175]. The present model seems to provide too large non-resonant $B(E2)$ transition strengths at low excitation energies, i.e., below the Hoyle resonance at 0.38 MeV. At this point, the source of this effect is not well understood. Discretization methods cannot reproduce the correct asymptotic behavior of three charged particles, and pseudo-states are an approximation to actual continuum states. As the energy decreases, this approximation can eventually fail. The triple-α problem has also the complexity regarding the symmetry of the wave function for three identical bosons. In the present work, this problem is addressed approximately by considering two identical α particles (related by $\boldsymbol{x}$) in each Jacobi set, being the third α an spectator. A further analysis concerning these problems is in order.

Appendix A

Three-body formalism

This Appendix supplements the information provided in chapter 2, and presents some useful tools to treat three-body systems. More details can be found, for instance, in Refs. [11, 21, 84].

A.1 Jacobi and hyperspherical coordinates

A three-body system in three dimensions has nine degrees of freedom, three of them related to the center of mass motion and the remaining six tied to the relative motion. Thus, subtracting the center of mass energy, the system Hamiltonian has six dimensions. If m_i and $\boldsymbol{r}_i$ are the masses and positions of the particles, the three possible sets of Jacobi coordinates $(\boldsymbol{x}_i, \boldsymbol{y}_i)$ are

$$\boldsymbol{x}_i = (\boldsymbol{r}_j - \boldsymbol{r}_k)\sqrt{\frac{a_{x_i}}{m}}, \tag{A.1}$$

$$\boldsymbol{y}_i = \left(\boldsymbol{r}_i - \frac{m_j\boldsymbol{r}_j + m_k\boldsymbol{r}_k}{M_T - m_i}\right)\sqrt{\frac{a_{y_i}}{m}}, \tag{A.2}$$

where $\boldsymbol{x}_i$ is the relative coordinate between particles j and k, and $\boldsymbol{y}_i$ is the coordinate that connects the center of mass of the $\{j,k\}$ subsystem with particle i. Constants a_{x_i} and a_{y_i} are the relevant reduced masses, also referred to as the x- and y-coordinate scales, and take the values

$$a_{x_i} = \frac{m_j m_k}{M_T - m_i}, \tag{A.3}$$

$$a_{y_i} = \frac{m_i\,(M_T - m_i)}{M_T}. \tag{A.4}$$

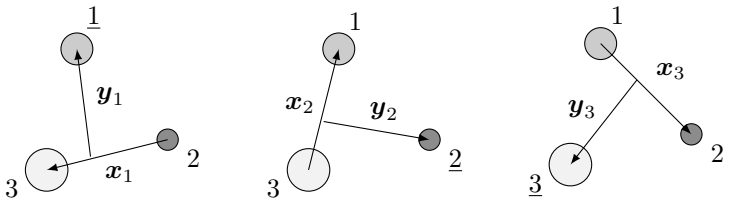

Figure A.1: The three sets of scaled Jacobi coordinates.

In the previous expressions, $M_T = (m_i + m_j + m_k)$ is the total mass of the three-body system and m is an arbitrary normalization mass, taken as the atomic mass unit.

The three Jacobi sets are determined by even permutations of $\{i, j, k\}$. For convenience, they are defined so that the particle out the x coordinate labels the Jacobi set, i.e. $\underline{1} \equiv \{1, 2, 3\}$, $\underline{2} \equiv \{2, 3, 1\}$ and $\underline{3} \equiv \{3, 1, 2\}$. This is shown for clarity in Fig. A.1. The three Jacobi sets, combined with the center of mass coordinate $\boldsymbol{R}$, describe the system. The positions of the three particles in the Jacobi–$\underline{i}$ system are given by

$$\boldsymbol{r}_i = \boldsymbol{R} + \frac{m_j + m_k}{M_T}\sqrt{\frac{m}{a_{y_i}}}\boldsymbol{y}_i, \tag{A.5}$$

$$\boldsymbol{r}_j = \boldsymbol{R} - \frac{m_i}{M_T}\sqrt{\frac{m}{a_{y_i}}}\boldsymbol{y}_i + \frac{m_k}{m_j + m_k}\sqrt{\frac{m}{a_{x_i}}}\boldsymbol{x}_i, \tag{A.6}$$

$$\boldsymbol{r}_k = \boldsymbol{R} - \frac{m_i}{M_T}\sqrt{\frac{m}{a_{y_i}}}\boldsymbol{y}_i - \frac{m_j}{m_j + m_k}\sqrt{\frac{m}{a_{x_i}}}\boldsymbol{x}_i, \tag{A.7}$$

where the center of mass position is

$$\boldsymbol{R} = \frac{m_i\boldsymbol{r}_i + m_j\boldsymbol{r}_j + m_k\boldsymbol{r}_k}{M_T}. \tag{A.8}$$

The connection between different Jacobi sets is given by

$$\boldsymbol{x}_k = -\cos\varphi_{ki}\ \boldsymbol{x}_i + \sin\varphi_{ki}\ \boldsymbol{y}_i, \tag{A.9}$$

$$\boldsymbol{y}_k = -\sin\varphi_{ki}\ \boldsymbol{x}_i - \cos\varphi_{ki}\ \boldsymbol{y}_i, \tag{A.10}$$

where

$$\tan\varphi_{ki} = (-1)^P\sqrt{\frac{m_j M_T}{M_T - m_j}}, \tag{A.11}$$

and $(-1)^P$ is the sign of the permutation $\{i, j, k\}$.

From Jacobi coordinates $(\boldsymbol{x}_i, \boldsymbol{y}_i)$ one can define a set of hyperspherical coordinates $(\rho, \alpha_i, \widehat{x}_i, \widehat{y}_i)$ that satisfy

$$\rho^2 = x_i^2 + y_i^2, \qquad \tan\alpha_i = \frac{x_i}{y_i}, \tag{A.12}$$

or equivalently,

$$x_i = \rho\sin\alpha_i, \qquad y_i = \rho\cos\alpha_i, \tag{A.13}$$

where ρ is the hyperradius and α_i is the hyperangle in the Jacobi-i set, confined by $0 < \alpha_i < \pi/2$. Notice that the hyperradius does not depend on the Jacobi system. The quantity $\Omega_i \equiv (\alpha_i, \widehat{x}_i, \widehat{y}_i)$ is usually introduced for the angular dependence, so that (ρ, Ω_i) represents the full set of hyperspherical coordinates. With the above given definitions, the volume element corresponding to the relative motion is

$$d^3\boldsymbol{x}_i d^3\boldsymbol{y}_i \equiv \rho^5(\sin\alpha_i)^2(\cos\alpha_i)^2\; d\rho d\alpha_i d\widehat{x}_i d\widehat{y}_i \equiv \rho^5 d\rho d\Omega_i. \tag{A.14}$$

A.2 Hyperspherical Harmonics

The spherical harmonics Y_{lm} are the eigenfunctions of the square of the angular momentum operator $\widehat{l}^2$,

$$\widehat{l}^2 Y_{lm_l}(\widehat{r}) = l(l+1)Y_{lm_l}(\widehat{r}), \tag{A.15}$$

and they can be defined so that,

$$\widehat{l}_z Y_{lm_l}(\widehat{r}) = m_l Y_{lm_l}(\widehat{r}). \tag{A.16}$$

Operators $\{\widehat{l}^2, \widehat{l}_z\}$ are a complete set of commuting observables in the three-dimensional angular subspace, and functions Y_{lm_l} define a complete and orthonormal basis.

The hyperspherical harmonics (HH) $\Upsilon_K^{l_x l_y m_x m_y}$ are the natural extension of the spherical harmonics for six-dimensional problems, being eigenfunctions of the square of the hypermomentum operator $\widehat{K}^2$,

$$\widehat{K}^2 \Upsilon_K^{l_x l_y m_x m_y}(\Omega_i) = K(K+4)\Upsilon_K^{l_x l_y m_x m_y}(\Omega_i). \tag{A.17}$$

They are chosen to be also eigenfunctions of the square of the angular

momenta associated to coordinates $\boldsymbol{x}_i$ and $\boldsymbol{y}_i$, $\widehat{l}_x^2$ and $\widehat{l}_y^2$, and that of its corresponding z components, $\widehat{l}_{x_z}$ and $\widehat{l}_{y_z}$. Thus,

$$\widehat{l}_x^2 \Upsilon_K^{l_x l_y m_x m_y}(\Omega_i) = l_x(l_x+1)\Upsilon_K^{l_x l_y m_x m_y}(\Omega_i), \tag{A.18}$$

$$\widehat{l}_y^2 \Upsilon_K^{l_x l_y m_x m_y}(\Omega_i) = l_y(l_y+1)\Upsilon_K^{l_x l_y m_x m_y}(\Omega_i), \tag{A.19}$$

$$\widehat{l}_{x_z} \Upsilon_K^{l_x l_y m_x m_y}(\Omega_i) = m_x \Upsilon_K^{l_x l_y m_x m_y}(\Omega_i), \tag{A.20}$$

$$\widehat{l}_{y_z} \Upsilon_K^{l_x l_y m_x m_y}(\Omega_i) = m_y \Upsilon_K^{l_x l_y m_x m_y}(\Omega_i). \tag{A.21}$$

This implies that $\{\widehat{K}^2, \widehat{l}_x^2, \widehat{l}_y^2, \widehat{l}_{x_z}, \widehat{l}_{y_z}\}$ is a complete set of observables in the three-body angular subspace, and the HH define a complete and orthonormal basis. They can be written by means of the spherical harmonics associated to $\boldsymbol{x}_i$ and $\boldsymbol{y}_i$,

$$\Upsilon_K^{l_x l_y m_x m_y}(\Omega_i) = \varphi_K^{l_x l_y}(\alpha_i) Y_{l_x m_x}(\widehat{x}_i) Y_{l_y m_y}(\widehat{y}_i), \tag{A.22}$$

where

$$\varphi_K^{l_x l_y}(\alpha_i) = N_K^{l_x l_y} (\sin\alpha_i)^{l_x} (\cos\alpha_i)^{l_y} P_n^{l_x+\frac{1}{2}, l_y+\frac{1}{2}}(\cos 2\alpha_i). \tag{A.23}$$

Here, $P_n^{a,b}$ represents a Jacobi polynomial of order

$$n = \frac{K - l_x - l_y}{2}, \tag{A.24}$$

and the normalization constant takes the value

$$N_K^{l_x l_y} = \left[\frac{2n!(K+2)(n+l_x+l_y+1)!}{\Gamma(n+l_x+3/2)\Gamma(n+l_y+3/2)} \right]^{1/2}. \tag{A.25}$$

Since n has to be integer or zero, Eq. (A.24) implies that K possible values go from $(l_x + l_y)$ to infinity in steps of two units.

The observable set choice is not unique, and one can define HH being eigenfunctions of $\{\widehat{K}^2, \widehat{l}_x^2, \widehat{l}_y^2, \widehat{l}^2, \widehat{l}_z\}$, where $\boldsymbol{l} = \boldsymbol{l}_x + \boldsymbol{l}_y$ and l_z is its third component. These functions are

$$\Upsilon_{K l m_l}^{l_x l_y}(\Omega_i) = \sum_{m_x m_y} \langle l_x m_x l_y m_y | l m_l \rangle \Upsilon_K^{l_x l_y m_x m_y}(\Omega_i), \tag{A.26}$$

and define also a complete set of the angular subspace. The HH given by Eq. (A.26) have a good total orbital angular momentum l, and their orthog-

onality relationship reads

$$\int d\Omega_i \Upsilon^{l_x l_y}_{Klm_l}(\Omega_i)\Upsilon^{l_x l_y}_{Klm_l}(\Omega_i) = \delta_{KK'}\delta_{l_x l'_x}\delta_{l_y l'_y}\delta_{ll'}\delta_{m_l m'_l}. \tag{A.27}$$

The square of the hypermomentum operator[1] as a function of the angles in hyperspherical coordinates is given by the expression

$$\widehat{K}^2(\Omega_i) = -\frac{\partial^2}{\partial\alpha_i^2} - 4\cot(2\alpha_i)\frac{\partial}{\partial\alpha_i} + \frac{1}{\cos^2\alpha_i}\widehat{l}^2_{y_i} + \frac{1}{\sin^2\alpha_i}\widehat{l}^2_{x_i}\ , \tag{A.28}$$

operator that is invariant under transformations between different Jacobi sets, i.e.

$$\widehat{K}^2(\Omega_i) = \widehat{K}^2(\Omega_j) = \widehat{K}^2(\Omega_k). \tag{A.29}$$

This relation implies that the corresponding eigenfunctions in a given Jacobi system can be expanded in terms of another set,

$$\Upsilon^{l_{x_i} l_{y_i}}_{Klm_l}(\Omega_i) = \sum_{l_{x_k} l_{y_k}} \langle l_{x_i} l_{y_i} | l_{x_k} l_{y_k}\rangle_{lK} \Upsilon^{l_{x_k} l_{y_k}}_{Klm_l}(\Omega_k), \tag{A.30}$$

where $\langle l_{x_i} l_{y_i} | l_{x_k} l_{y_k}\rangle_{lK}$ are the Raynal-Revai coefficients [84]. Notice that the transformation preserves the hypermomentum K, as well as the total orbital angular momentum l and its projection m_l.

A.3 HO basis

The harmonic oscillator (HO) functions in 6 dimensions have the form[2]

$$\phi^{\rm HO}_{iKl_x l_y l m_l}(s,\Omega) = R^{\rm HO}_{iK}(s)\Upsilon^{l_x l_y}_{Klm_l}(\Omega), \tag{A.31}$$

where i is the main quantum number and denotes the hyperradial excitation. Functions $\Upsilon^{l_x l_y}_{Klm_l}(\Omega)$ are the HH described in A.2, while the hyperradial functions are given by

$$R^{\rm HO}_{iK}(s) = \sqrt{\frac{2\Gamma(i+1)}{\Gamma(i+K+3)}}\, s^K L_i^{K+2}(s^2)\exp(-s^2/2), \tag{A.32}$$

[1] The operator $\widehat{K}$ is also called in the literature grand momentum operator.
[2] For clarity, the label that specifies the Jacobi set has been omitted.

being L_i^{K+2} a generalized Laguerre polynomial. These hyperradial functions fulfill the orthonormality relation

$$\int_0^\infty ds\ s^5 R_{iK}^{\mathrm{HO}}(s) R_{i'K}^{\mathrm{HO}}(s) = \delta_{ii'}. \tag{A.33}$$

It is convenient to introduce hyperradial functions $U_{iK}^{\mathrm{HO}}(s)$ as

$$U_{iK}^{\mathrm{HO}}(s) = s^{5/2} R_{iK}^{\mathrm{HO}}(s), \tag{A.34}$$

so that the orthonormality relationship is

$$\int_0^\infty ds\ U_{iK}^{\mathrm{HO}}(s) U_{i'K}^{\mathrm{HO}}(s) = \delta_{ii'}. \tag{A.35}$$

With this definition, the Jacobian term ρ^5 involved in all hyperradial integrals can be omitted. This is the prescription already presented in chapters 1 and 2.

Note that the angular part of the HO basis functions are simply hyperspherical harmonics, which do not account for the spin of the system. When the spins of the particles are considered, the HH have to be coupled to the corresponding spin functions to provide a total angular momentum j (see Eq. (1.4) in chapter 2).

Appendix B

Operator matrix elements and other relevant expressions

B.1 Kinetic energy matrix elements

The kinetic energy operator for a three-body system can be written, using Jacobi coordinates, as

$$\widehat{T}(\boldsymbol{x},\boldsymbol{y}) = -\frac{\hbar^2}{2m}\left[\left(\frac{1}{x}\frac{\partial^2}{\partial x^2}x - \frac{\widehat{l}_x^2}{x^2}\right) + \left(\frac{1}{y}\frac{\partial^2}{\partial y^2}y - \frac{\widehat{l}_y^2}{y^2}\right)\right], \tag{B.1}$$

which excludes the center of mass kinetic energy. Here, $\widehat{l}_x$ and $\widehat{l}_y$ are the angular momentum operators associated to coordinates $\boldsymbol{x}$ and $\boldsymbol{y}$, respectively, and m is a normalization mass. It is convenient to express this operator using hyperspherical coordinates, which are related with the Jacobi coordinates by Eq. (A.12). Accordingly to these relationships, the Jacobian matrix is given by

$$\frac{\partial\rho}{\partial x} = \sin\alpha, \tag{B.2}$$

$$\frac{\partial\alpha}{\partial x} = \left(\frac{1}{y}\right)\frac{1}{1+\left(\frac{x}{y}\right)^2} = \frac{\cos\alpha}{\rho}, \tag{B.3}$$

$$\frac{\partial\rho}{\partial y} = \cos\alpha, \tag{B.4}$$

$$\frac{\partial\alpha}{\partial y} = -\left(\frac{x}{y^2}\right)\frac{1}{1+\left(\frac{x}{y}\right)^2} = -\frac{\sin\alpha}{\rho}. \tag{B.5}$$

Considering that the operator $\widehat{T}$ acts on wave functions of the form $g(\rho,\alpha)$[1], the following useful expressions can be introduced

$$f_x(\rho,\alpha) = x\ g(\rho,\alpha), \tag{B.6}$$

$$h_x(\rho,\alpha) = \frac{\partial f_x}{\partial x}, \tag{B.7}$$

$$f_y(\rho,\alpha) = y\ g(\rho,\alpha), \tag{B.8}$$

$$h_y(\rho,\alpha) = \frac{\partial f_y}{\partial y}, \tag{B.9}$$

so that

$$\frac{1}{x}\frac{\partial^2}{\partial x^2}\left[x\ g(\rho,\alpha)\right] = \frac{1}{x}\frac{\partial^2 f_x}{\partial x^2} = \frac{1}{x}\frac{\partial h_x}{\partial x}, \tag{B.10}$$

$$\frac{1}{y}\frac{\partial^2}{\partial y^2}\left[y\ g(\rho,\alpha)\right] = \frac{1}{y}\frac{\partial^2 f_y}{\partial y^2} = \frac{1}{y}\frac{\partial h_y}{\partial y}. \tag{B.11}$$

Accordingly to the chain rule for multiple derivatives, previous functions satisfy

$$\frac{\partial f_x}{\partial x} = \frac{\partial f_x}{\partial \rho}\frac{\partial \rho}{\partial x} + \frac{\partial f_x}{\partial \alpha}\frac{\partial \alpha}{\partial x}\ , \tag{B.12}$$

$$\frac{\partial f_y}{\partial y} = \frac{\partial f_y}{\partial \rho}\frac{\partial \rho}{\partial y} + \frac{\partial f_y}{\partial \alpha}\frac{\partial \alpha}{\partial y}\ . \tag{B.13}$$

The two terms (B.10) and (B.11) are needed to compute the kinetic energy. Starting with the x coordinate, the derivatives of f_x with respect to ρ and α can be obtained from Eq. (B.6) as

$$\frac{\partial f_x}{\partial \rho} = \sin\alpha\left(g(\rho,\alpha) + \rho\ \frac{\partial g}{\partial \rho}\right), \tag{B.14}$$

$$\frac{\partial f_x}{\partial \alpha} = \rho\left(\cos\alpha\ g(\rho,\alpha) + \sin\alpha\ \frac{\partial g}{\partial \alpha}\right). \tag{B.15}$$

Inserting these expressions in Eq. (B.12), and using relations (B.2) and (B.3),

$$h_x = \frac{\partial f_x}{\partial x} = \sin^2\alpha\left(g(\rho,\alpha) + \rho\frac{\partial g}{\partial \rho}\right) + \cos^2\alpha\ g(\rho,\alpha) + \frac{\sin(2\alpha)}{2}\ \frac{\partial g}{\partial \alpha}. \tag{B.16}$$

Eq. (B.10) requires the h_x derivative with respect to x. Using again the chain

[1] The angular dependence on $\widehat{x}, \widehat{y}$ can be omitted.

rule,

$$\frac{\partial h_x}{\partial x} = \frac{\partial h_x}{\partial \rho}\frac{\partial \rho}{\partial x} + \frac{\partial h_x}{\partial \alpha}\frac{\partial \alpha}{\partial x}. \tag{B.17}$$

Performing the derivatives with respect to ρ and α, and collecting terms,

$$\begin{aligned}\frac{\partial h_x}{\partial x} = {} & \frac{\partial g}{\partial \rho}\left[2\sin^3\alpha + \cos^2\alpha\ \sin\alpha + 2\sin\alpha\ \cos^2\alpha\right] + \frac{\partial^2 g}{\partial \rho^2}\left[\rho\sin^3\alpha\right] \\ & + \frac{\partial g}{\partial \alpha}\left[\frac{\sin^2\alpha\ \cos\alpha}{\rho} + \frac{\cos^3\alpha}{\rho} + \frac{\cos(2\alpha)\cos\alpha}{\rho}\right] + \frac{\partial^2 g}{\partial \alpha^2}\left[\frac{\sin\alpha\ \cos^2\alpha}{\rho}\right] \\ & + \frac{\partial^2 g}{\partial \rho \partial \alpha}\left[\sin(2\alpha)\sin\alpha\right]. \end{aligned} \tag{B.18}$$

Following the same derivation for h_y, a similar result is obtained,

$$\begin{aligned}\frac{\partial h_y}{\partial y} = {} & \frac{\partial g}{\partial \rho}\left[2\cos^3\alpha + \sin^2\alpha\ \cos\alpha + 2\cos\alpha\ \sin^2\alpha\right] + \frac{\partial^2 g}{\partial \rho^2}\left[\rho\cos^3\alpha\right] \\ & + \frac{\partial g}{\partial \alpha}\left[-\frac{\cos^2\alpha\ \sin\alpha}{\rho} - \frac{\sin^3\alpha}{\rho} + \frac{\cos(2\alpha)\sin\alpha}{\rho}\right] + \frac{\partial^2 g}{\partial \alpha^2}\left[\frac{\cos\alpha\ \sin^2\alpha}{\rho}\right] \\ & + \frac{\partial^2 g}{\partial \rho \partial \alpha}\left[-\sin(2\alpha)\cos\alpha\right]. \end{aligned} \tag{B.19}$$

Evaluating now the sum of terms (B.10) and (B.11),

$$\begin{aligned}\left(\frac{1}{x}\ \frac{\partial h_x}{\partial x} + \frac{1}{y}\ \frac{\partial h_y}{\partial y}\right) = {} & \frac{\partial^2 g}{\partial \rho^2} + \frac{5}{\rho}\ \frac{\partial g}{\partial \rho} + \frac{1}{\rho^2}\ \frac{\partial^2 g}{\partial \alpha^2} \\ & + \frac{1}{\rho^2}\ \frac{\partial g}{\partial \alpha}\left[\underbrace{\left(\frac{\cos^3\alpha}{\sin\alpha} - \frac{\sin^3\alpha}{\cos\alpha}\right)}_{A} + \underbrace{\left(\frac{\cos(2\alpha)\cos\alpha}{\sin\alpha} + \frac{\cos(2\alpha)\sin\alpha}{\cos\alpha}\right)}_{B}\right]. \end{aligned} \tag{B.20}$$

Terms A and B can be simply reduced as

$$\begin{aligned} A &= \frac{\cos^3\alpha}{\sin\alpha} - \frac{\sin^3\alpha}{\cos\alpha} = \frac{\cos^4\alpha - \sin^4\alpha}{\sin\alpha\cos\alpha} = \frac{\cos(2\alpha)}{\sin\alpha\cos\alpha} \\ &= \frac{\cos(2\alpha)}{\sin\alpha\cos\alpha} = 2\ \frac{\cos(2\alpha)}{\sin(2\alpha)} = 2\cot(2\alpha), \end{aligned} \tag{B.21}$$

$$B = \frac{\cos(2\alpha)\cos\alpha}{\sin\alpha} + \frac{\cos(2\alpha)\sin\alpha}{\cos\alpha} = \frac{\cos(2\alpha)\cos^2\alpha + \cos(2\alpha)\sin^2\alpha}{\sin\alpha\cos\alpha}$$
$$= \frac{\cos(2\alpha)}{\sin\alpha\cos\alpha} = 2\,\frac{\cos(2\alpha)}{\sin(2\alpha)} = 2\cot(2\alpha) = A, \tag{B.22}$$

so finally

$$\left(\frac{1}{x}\,\frac{\partial h_x}{\partial x} + \frac{1}{y}\,\frac{\partial h_y}{\partial y}\right) = \frac{\partial^2 g}{\partial\rho^2} + \frac{5}{\rho}\frac{\partial g}{\partial\rho} + \frac{1}{\rho^2}\frac{\partial^2 g}{\partial\alpha^2} + \frac{1}{\rho^2}4\cot(2\alpha)\frac{\partial g}{\partial\alpha}. \tag{B.23}$$

Adding terms in $\widehat{l}_x$ and $\widehat{l}_y$ included in Eq. (B.1), the kinetic energy operator in hyperspherical coordinates can be written as

$$\widehat{T}(\rho,\alpha) = -\frac{\hbar^2}{2m}\left[\frac{\partial^2}{\partial\rho^2} + \frac{5}{\rho}\frac{\partial}{\partial\rho} + \frac{1}{\rho^2}\frac{\partial^2}{\partial\alpha^2} + \frac{1}{\rho^2}4\cot(2\alpha)\frac{\partial}{\partial\alpha}\right.$$
$$\left. -\frac{\widehat{l}_x^2}{\rho^2\sin^2\alpha} - \frac{\widehat{l}_y^2}{\rho^2\cos^2\alpha}\right], \tag{B.24}$$

and considering the expression for the hypermomentum operator introduced in Appendix A, Eq. (A.28),

$$\widehat{K}^2(\Omega) = -\frac{\partial^2}{\partial\alpha^2} - 4\cot(2\alpha)\frac{\partial}{\partial\alpha} + \frac{\widehat{l}_x^2}{\sin^2\alpha} + \frac{\widehat{l}_y^2}{\cos^2\alpha},$$

the final expression for the kinetic energy operator reads

$$\widehat{T}(\rho,\alpha) = -\frac{\hbar^2}{2m}\left[\frac{\partial^2}{\partial\rho^2} + \frac{5}{\rho}\frac{\partial}{\partial\rho} - \frac{1}{\rho^2}\widehat{K}^2(\Omega)\right]. \tag{B.25}$$

The expression (B.25) is totally general. This operator can act over three-body wave functions which factorize in hyperradial and angular parts,

$$\psi_{i\beta j\mu}(\rho,\Omega) = \rho^{-5/2}U_{i\beta}(\rho)\mathcal{Y}_{\beta j\mu}(\Omega), \tag{B.26}$$

where β denotes all quantum numbers coupled to a total angular momentum j, as introduced in chapter 1. Since the kinetic energy operator ignores the spin functions, for the computation of its matrix elements the effect of $\widehat{T}$ over angular functions $\mathcal{Y}_{\beta j\mu}(\Omega)$ is equivalent than that over hyperspherical harmonics. The effect of the operator on the basis functions is

$$\widehat{T}(\rho,\Omega)\left[\rho^{-5/2}U(\rho)\Upsilon(\Omega)\right] = \tag{B.27}$$
$$= -\frac{\hbar^2}{2m}\left(\underbrace{\frac{d^2}{d\rho^2}\left(\rho^{-5/2}U\right)}_{D} + \underbrace{\frac{5}{\rho}\frac{d}{d\rho}\left(\rho^{-5/2}U\right)}_{C} - \frac{K(K+4)}{\rho^2}\rho^{-5/2}U\right)\Upsilon,$$

where the relation $\widehat{K}^2\ \Upsilon = K(K+4)\Upsilon$, presented in Appendix A, has been used. Evaluating C and D,

$$C = \frac{5}{\rho}\frac{d}{d\rho}\left(\rho^{-\frac{5}{2}}U\right) = \frac{5}{\rho}\left(-\frac{5}{2}\rho^{-\frac{7}{2}}U + \rho^{-\frac{5}{2}}\frac{dU}{d\rho}\right) = \frac{-25}{2}\rho^{-\frac{9}{2}}U + 5\rho^{-\frac{7}{2}}\frac{dU}{d\rho}, \tag{B.28}$$

$$D = \frac{d}{d\rho}\left[\frac{d}{d\rho}\left(\rho^{-\frac{5}{2}}U\right)\right] = \frac{5}{2}\frac{7}{2}\rho^{-\frac{9}{2}}U - \frac{5}{2}\rho^{-\frac{7}{2}}\frac{dU}{d\rho} - \frac{5}{2}\rho^{-\frac{7}{2}}\frac{dU}{d\rho} + \rho^{-\frac{5}{2}}\frac{d^2U}{d\rho^2}. \tag{B.29}$$

These results lead to,

$$\widehat{T}(\rho,\Omega)\left[\rho^{-5/2}U(\rho)\Upsilon(\Omega)\right] = \rho^{-5/2}\widehat{T}_U(\rho)\left[U(\rho)\Upsilon(\Omega)\right], \tag{B.30}$$

where the new operator has the form

$$\widehat{T}_U(\rho) = \frac{-\hbar^2}{2m}\left[\frac{d^2}{d\rho^2} + \frac{15/4 + K(K+4)}{\rho^2}\right]. \tag{B.31}$$

Then, if $|i\beta j\mu\rangle$ represents the basis function in Eq. (B.26), the kinetic energy matrix elements can be computed as

$$\begin{aligned}\langle i\beta j\mu|\widehat{T}(\rho,\Omega)|i'\beta' j\mu\rangle &= \delta_{\beta\beta'}\langle i\beta j|\widehat{T}_U(\rho)|i'\beta' j\rangle \\ &= \delta_{\beta\beta'}\int_0^\infty d\rho\ U_{i\beta}(\rho)\ \widehat{T}_U(\rho)\ U_{i'\beta'}(\rho),\end{aligned} \tag{B.32}$$

where the ρ factors cancel, and the angular integral imposes diagonality in the channels β.

B.2 Potential matrix elements

As shown in chapter 2, potential matrix elements are computed in two steps. First, the angular integration is performed using the prescriptions by the FaCE code [51]. This program solves the Faddeev [68] equations for a three-body system with possible excitations of one of the particles. The three-body wave function with total angular momentum j is given in the Faddeev formalism as

$$\psi^{(j\mu)} = \psi_1^{(j\mu)}(\boldsymbol{x}_1, \boldsymbol{y}_1) + \psi_2^{(j\mu)}(\boldsymbol{x}_2, \boldsymbol{y}_2) + \psi_3^{(j\mu)}(\boldsymbol{x}_3, \boldsymbol{y}_3), \tag{B.33}$$

where $\{\boldsymbol{x}_k, \boldsymbol{y}_k\}$ are the Jacobi coordinates in the k set, and functions $\psi_k^{(j\mu)}$ satisfy the Faddeev coupled equations,

$$\begin{aligned}
\left(\widehat{T}_1 + \widehat{h} + \widehat{V}_1 - \varepsilon\right)\psi_1^{(j\mu)} &= -\widehat{V}_1\left(\psi_2^{(j\mu)} + \psi_3^{(j\mu)}\right), \\
\left(\widehat{T}_2 + \widehat{h} + \widehat{V}_2 - \varepsilon\right)\psi_2^{(j\mu)} &= -\widehat{V}_2\left(\psi_3^{(j\mu)} + \psi_1^{(j\mu)}\right), \\
\left(\widehat{T}_3 + \widehat{h} + \widehat{V}_3 - \varepsilon\right)\psi_3^{(j\mu)} &= -\widehat{V}_3\left(\psi_1^{(j\mu)} + \psi_2^{(j\mu)}\right).
\end{aligned} \tag{B.34}$$

These equations contain $\widehat{h} = \sum_k \widehat{h}_k$ the sum of the internal Hamiltonian of each particle $\widehat{h}_k$, the relative kinetic energy in each coordinate set $\widehat{T}_k = \widehat{T}_{x_k} + \widehat{T}_{y_k}$ and the two-body interaction between the corresponding pair $\widehat{V}_k = \widehat{V}_{pq}(r_{pq})$. The indexes (k, p, q) run through $(1, 2, 3)$ in circular order. Typically, the label $\mathbf{X}$ refers to the pair $\{\boldsymbol{x}_1, \boldsymbol{y}_1\}$, $\mathbf{Y}$ refers to $\{\boldsymbol{x}_2, \boldsymbol{y}_2\}$ and $\mathbf{T}$ refers to $\{\boldsymbol{x}_3, \boldsymbol{y}_3\}$. For a given Jacobi set, the corresponding Faddeev component is expanded following the angular momentum coupling presented in chapter 2. Using ket notation, the total three-body wave function in Eq. (B.33) can be written as

$$|j\mu\rangle = \sum_{k=1}^{3} |k; j\mu\rangle = \sum_{k=1}^{3} \sum_{\beta_k} |k; \beta_k j, \beta_k j\mu\rangle, \tag{B.35}$$

where $|k; \beta_k j, \beta_k j\mu\rangle$ represents the factorization of hyperradial and angular parts

$$|k; \beta_k j, \beta_k j\mu\rangle = |k; \beta_k j\rangle \otimes |k; \beta_k j\mu\rangle. \tag{B.36}$$

Potential matrix elements involve overlaps between pairs of the over-complete basis set $\{|k; \beta_k j\mu\rangle\}$. The calculation of these overlaps requires transformation matrices between angular components in different Jacobi sets,

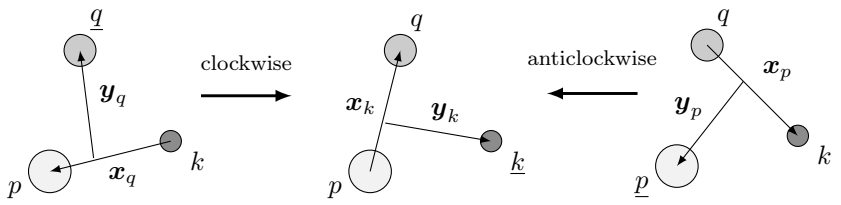

Figure B.1: Transformations between Jacobi sets.

which are rotations $|q;\beta_q j\mu\rangle \to |k;\beta_k j\mu\rangle$ clockwise and $|k;\beta_k j\mu\rangle \leftarrow |p;\beta_p j\mu\rangle$ anticlockwise. This is shown schematically in Fig. B.1. Considering $\{k,p,q\}$ in circular order, the transformations in both directions are

$$\begin{aligned}|k;\beta_k j\mu\rangle = &\sum_{K_q}\sum_{l_{x_q}l_{y_q}}\sum_{l_q S_{x_q}}\sum_{j_{ab_q}}\sum_{S_t}(-1)^{2\left(j-S_{x_q}-s_q\right)+S_t+S_{x_k}-s_k}\hat{S}_t^2\hat{S}_{x_q}\hat{S}_{x_k}\hat{j}_{ab_q}\hat{j}_{ab_k}\\ &\times W(l_k S_{x_k} j s_k; j_{ab_k} S_t) W(s_q s_p S_t s_k; S_{x_k} S_{x_q}) W(s_q S_{x_q} j l_q; S_t j_{ab_q})\\ &\times \langle l_{x_k} l_{y_k} | l_{x_q} l_{y_q}\rangle_{l_q K_q} \delta_{K_k K_q}\delta_{l_k l_q} |q;\beta_q j\mu\rangle, \qquad \text{(B.37)}\\ |k;\beta_k j\mu\rangle = &\sum_{K_p}\sum_{l_{x_p}l_{y_p}}\sum_{l_p S_{x_p}}\sum_{j_{ab_p}}\sum_{S_t}(-1)^{2\left(j-S_{x_p}-s_p\right)+S_t+S_{x_p}-s_p}\hat{S}_t^2\hat{S}_{x_p}\hat{S}_{x_k}\hat{j}_{ab_p}\hat{j}_{ab_k}\\ &\times W(l_k S_{x_k} j s_k; j_{ab_k} S_t) W(s_p s_q S_t s_k; S_{x_k} S_{x_p}) W(s_p S_{x_q p} j l_p; S_t j_{ab_p})\\ &\times \langle l_{x_k} l_{y_k} | l_{x_p} l_{y_p}\rangle_{l_p K_p} \delta_{K_k K_p}\delta_{l_k l_p} |p;\beta_p j\mu\rangle, \qquad \text{(B.38)}\end{aligned}$$

where $\langle l_{x_k} l_{y_k} | l_{x_p} l_{y_p}\rangle_{l_p K_p}$ are the Raynal-Revai coefficients in Eq. (A.30), and S_t is the total spin, $\boldsymbol{S}_t = \boldsymbol{S}_{x_p} + \boldsymbol{I}_p$. Equations (B.37) and (B.38) define two kinds of norm matrices, $\tilde{N}_{\beta_k\beta_q}$ and $N_{\beta_k\beta_p}$, such that

$$|k;\beta_k j\mu\rangle = \sum_{\beta_q}\tilde{N}_{\beta_k\beta_q}|q;\beta_q j\mu\rangle = \sum_{\beta_p} N_{\beta_k\beta_p}|p;\beta_p j\mu\rangle, \qquad \text{(B.39)}$$

which means that the matrix elements $N_{\beta_k\beta_p}$ are just the state overlaps

$$N_{\beta_k\beta_p} = \langle p;\beta_p j\mu | k;\beta_k j\mu\rangle, \qquad \text{(B.40)}$$

so that

$$\sum_{\beta_p} N_{\beta_k\beta_p} N_{\beta_p\beta_q} = \tilde{N}_{\beta_k\beta_q}. \qquad \text{(B.41)}$$

Note that these transformations conserve the total orbital angular momentum l and the hypermomentum K.

Eq. (1.11) in chapter 1 describes the general binary potential between an interacting pair. In this work, neither deformed potentials nor excited states of the particles are considered, so

$$\widehat{V}_{pq} = \widehat{V}_k(x_k) = V_c(x_k) + V_{so}(x_k)\widehat{SO} + V_t(x_k)\widehat{\mathcal{T}} + V_{ss}(x_k)\widehat{SS}, \qquad \text{(B.42)}$$

where $V_c(x_k)$ is the central term, $\widehat{SO}$ and $V_{so}(x_k)$ are the spin-orbit operator and its radial form factor, $\widehat{\mathcal{T}}$ and $V_t(x_k)$ are the standard tensor operator and the radial form factor for the NN interaction, and finally $\widehat{SS}$ and $V_{ss}(x_k)$ are the spin-spin operator and its corresponding radial dependence.

The matrix elements of $\widehat{V}_k(x_k)$ are calculated between basis states of the same Faddeev component k. The norm matrices introduced by Eq. (B.40) can be used to express general potential matrix elements in mixed representations, in terms of the preferred Jacobi set k. For example,

$$\langle p;\beta'_p j||\widehat{V}_k||k;\beta_k j\rangle = \sum_{\beta'_k} N_{\beta'_k\beta'_p}\langle k;\beta'_k j||\widehat{V}_k||k;\beta_k j\rangle, \qquad \text{(B.43)}$$

or, for cases in which the potential is easily represented in one particular Jacobi set,

$$\langle p;\beta'_p j||\widehat{V}_k||p;\beta_p j\rangle = \sum_{\beta'_k\beta_k} N_{\beta'_k\beta'_p}\langle k;\beta'_k j||\widehat{V}_k||k;\beta_k j\rangle N_{\beta_k\beta_p}. \qquad \text{(B.44)}$$

First, the angular and spin parts are considered, leading to a set of matrix elements to be later multiplied by numerical integrals over the hyperangle α_k. For that, it is convenient to separate further the angular wave functions,

$$|k;\beta_k j\mu\rangle = |k;K_k l_{x_k} l_{y_k}\rangle \otimes |k;\gamma_k j\mu\rangle, \qquad \text{(B.45)}$$

where $|k;K_k l_{x_k} l_{y_k}\rangle$ represents the hyperangular degree of freedom, given by function $\varphi_{K_k}^{l_{x_k} l_{y_k}}$ in Eq. (A.23), and $\beta_k \equiv \{K_k, \gamma_k\}$. Factors $W_{kk'}$ are then introduced to denote the potential matrix elements over the angular momentum basis states $|k;\gamma_k j\mu\rangle$, leading to

$$\begin{aligned}\langle k;\gamma'_k j||\widehat{V}_k||k;\gamma_k j\rangle = {} & W^c_{kk'}V^c_k(x_k) + W^{SO}_{kk'}V^{SO}_k(x_k) \\ & + W^{\mathcal{T}}_{kk'}V^{\mathcal{T}}_k(x_k) + W^{SS}_{kk'}V^{SS}_k(x_k). \qquad \text{(B.46)}\end{aligned}$$

The potential matrix element for the central part is diagonal in all angular and spin variables. Considering the spin-orbit part, since all three particles may have non-vanishing spin, a general spin operator $\widehat{\Sigma}_k \equiv \Gamma_{kp}\widehat{s}_p + \Gamma_{kq}\widehat{s}_q$ is introduced. Here Γ_{kp} and Γ_{pq} select which of the spins are to be dynamically coupled, and with which relative strength. The matrix elements for the resulting spin-orbit operator are

$$\begin{aligned}
&\langle k;\gamma'_k j||\widehat{l}_{x_k}\cdot\widehat{\Sigma}_k||k;\gamma_k j\rangle = \delta_{s'_k s_k}\delta_{s'_p s_p}\delta_{s'_q s_q}\delta_{j'_{ab_k} j_{ab_k}}\delta_{l'_{y_k} l_{y_k}}\delta_{l'_{x_k} l_{x_k}} \\
&\times(-1)^{2j+3j'_{ab_k}+l_{y_k}+l'_{x_k}+2s_k+s_p+s_q}\hat{S}'_{x_k}\hat{S}_{x_k}\hat{l}'_k\hat{l}_k\hat{l}_{x_k}\sqrt{l_{x_k}(l_{x_k}+1)} \\
&\times\begin{Bmatrix} l'_k & l_k & 1 \\ S_{x_k} & S'_{x_k} & j_{ab_k}\end{Bmatrix}\begin{Bmatrix} l'_k & l_k & 1 \\ l_{x_k} & l'_{x_k} & l'_{y_k}\end{Bmatrix} \\
&\times\left[\Gamma_{kp}(-1)^{S_{x_k}}\hat{s}_p\sqrt{s_p(s_p+1)}\begin{Bmatrix} S'_{x_k} & S_{x_k} & 1 \\ s_p & s'_p & s'_q\end{Bmatrix}\right. \\
&\left.+\,\Gamma_{kq}(-1)^{S_{x_k}}\hat{s}_q\sqrt{s_q(s_q+1)}\begin{Bmatrix} S'_{x_k} & S_{x_k} & 1 \\ s_q & s'_q & s'_p\end{Bmatrix}\right].
\end{aligned} \tag{B.47}$$

When considering spin-spin interactions there are three possibilities depending on the Faddeev components, $\langle s'_k||\widehat{s}_k\cdot\widehat{s}_p||s_k\rangle$, $\langle s'_k||\widehat{s}_k\cdot\widehat{s}_q||s_k\rangle$ and $\langle s'_k||\widehat{s}_p\cdot\widehat{s}_q||s_k\rangle$. The expression for these matrix elements are

$$\begin{aligned}
&\langle k;\gamma'_k j||\widehat{s}_k\cdot\widehat{s}_p||k;\gamma_k j\rangle = (-1)^{3j+j'_{ab_k}-j_{ab_k}+l'_k+2S_{x_k}-s_k+s_p+s_q} \\
&\times\delta_{s'_k s_k}\delta_{s'_p s_p}\delta_{s'_q s_q}\delta_{l'_k l_k}\hat{j}'_{ab_k}\hat{j}_{ab_k}\hat{S}'_{x_k}\hat{S}_{x_k}\hat{s}_k\hat{s}_p\sqrt{s_k(s_k+1)}\sqrt{s_p(s_p+1)} \\
&\times\begin{Bmatrix} j'_{ab_k} & j_{ab_k} & 1 \\ S_{x_k} & S'_{x_k} & l'_k\end{Bmatrix}\begin{Bmatrix} S'_{x_k} & S_{x_k} & 1 \\ s_p & s'_p & s'_q\end{Bmatrix}\begin{Bmatrix} s'_k & s_k & 1 \\ j_{ab_k} & j'_{ab_k} & j\end{Bmatrix},
\end{aligned} \tag{B.48}$$

$$\begin{aligned}
&\langle k;\gamma'_k j||\widehat{s}_k\cdot\widehat{s}_q||k;\gamma_k j\rangle = (-1)^{3j+j'_{ab_k}-j_{ab_k}+l'_k+S_{x_k}+S'_{x_k}-s'_k+s'_p+s_q} \\
&\times\delta_{s'_k s_k}\delta_{s'_p s_p}\delta_{s'_q s_q}\delta_{l'_k l_k}\hat{j}'_{ab_k}\hat{j}_{ab_k}\hat{S}'_{x_k}\hat{S}_{x_k}\hat{s}_k\hat{s}_q\sqrt{s_k(s_k+1)}\sqrt{s_q(s_q+1)} \\
&\times\begin{Bmatrix} j'_{ab_k} & j_{ab_k} & 1 \\ S_{x_k} & S'_{x_k} & l'_k\end{Bmatrix}\begin{Bmatrix} S'_{x_k} & S_{x_k} & 1 \\ s_q & s'_q & s'_p\end{Bmatrix}\begin{Bmatrix} s'_k & s_k & 1 \\ j_{ab_k} & j'_{ab_k} & j\end{Bmatrix},
\end{aligned} \tag{B.49}$$

$$\langle k;\gamma'_k j||\widehat{s}_p\cdot\widehat{s}_q||k;\gamma_k j\rangle = (-1)^{S_{x_k}+s_p+s_q}\delta_{s'_k s_k}\delta_{s'_p s_p}\delta_{s'_q s_q}\delta_{j'_{ab_k} j_{ab_k}}\delta_{S'_{x_k} S_{x_k}}\delta_{l'_k l_k}$$
$$\times\,\hat{s}_p\hat{s}_q\sqrt{s_p(s_p+1)}\sqrt{s_q(s_q+1)}\left\{\begin{array}{ccc} s'_p & s_p & 1\\ s_q & s'_q & S'_{x_k}\end{array}\right\}. \tag{B.50}$$

A realistic NN force contains a tensor interaction of the type $T_2(\widehat{s}_p\widehat{s}_q)\cdot C_2(\widehat{l}_{x_k})$ which also needs to be considered. Here, $C_2(\widehat{l}_{x_k})$ is a spherical harmonic in the notation of Brink and Satchler [82]. The expression for these matrix elements after working out the algebra is

$$\langle k;\gamma'_k j||T_2(\widehat{s}_p\widehat{s}_q)\cdot C_2(\widehat{l}_{x_k})||k;\gamma_k j\rangle = \delta_{s'_k s_k}\delta_{s'_p s_p}\delta_{s'_q s_q}\delta_{j'_{ab_k} j_{ab_k}}\delta_{l'_k l_k}$$
$$\times\,(-1)^{3j_{ab_k}+l_{y_k}-S'_{x_k}}\hat{2}\hat{S}'_{x_k}\hat{S}_{x_k}\hat{l}'_k\hat{l}_k\hat{l}'_{x_k}\hat{l}_{x_k}\hat{s}'_p\hat{s}'_q\sqrt{s_p(s_p+1)}\sqrt{s_q(s_q+1)}$$
$$\times\left\{\begin{array}{ccc} S'_{x_k} & S_{x_k} & 2\\ l_k & l'_k & j'_{ab_k}\end{array}\right\}\left\{\begin{array}{ccc} l'_k & l_k & 2\\ l_{x_k} & l'_{x_k} & l'_{y_k}\end{array}\right\} \tag{B.51}$$
$$\times\left(\begin{array}{ccc} l'_{x_k} & 2 & l_{x_k}\\ 0 & 0 & 0\end{array}\right)\left\{\begin{array}{ccc} S'_{x_k} & S_{x_k} & 2\\ s'_p & s_p & 1\\ s'_q & s_q & 1\end{array}\right\}.$$

As already discussed in the main body of this thesis, few-body models often include three-body effective potentials to describe the influence of dynamics not explicitly considered by two-body interactions. This is typically parametrized with a simple diagonal form,

$$\langle k';\gamma'_k j||\widehat{V}_{3b}||k;\gamma_k j\rangle = \delta_{k'k}\delta_{\gamma'_k\gamma_k}V_{3b}(\rho). \tag{B.52}$$

After computing these $W_{kk'}$ factors and performing the hyperangular integration in Eq. (B.46), the hyperradial $V_{\beta\beta'}(\rho)$ coupling matrix is obtained. In this work, instead of solving the Faddeev equations, the Schrödinger equation in the preferred Jacobi set k is solved by computing the potential matrix elements over the hyperradial functions and diagonalizing the full three-body Hamiltonian. This leads to the pseudo-state method in chapters 1 and 2.

B.3 Expressions for the matter and charge radii

The matter radius for an A-nucleon system is given by

$$r^2 = \frac{1}{A}\sum_{i=1}^{A} r_i^2, \tag{B.53}$$

where $\boldsymbol{r_i}$ is the position of each nucleon with respect to the center of mass of the system. Considering a three-cluster system, this vector can be separated into two parts,

$$\boldsymbol{r_i} = \boldsymbol{R_q} + \boldsymbol{r_{i(q)}}. \tag{B.54}$$

Here, $\boldsymbol{R_q}$ are the position of the clusters, given by Eqs. (A.5), (A.6), and (A.7) in the preferred Jacobi set as

$$\boldsymbol{R_1} = -\frac{m_3}{M_T}\sqrt{\frac{m}{a_y}}\boldsymbol{y} - \frac{m_2}{m_1+m_2}\sqrt{\frac{m}{a_x}}\boldsymbol{x}, \tag{B.55}$$

$$\boldsymbol{R_2} = -\frac{m_3}{M_T}\sqrt{\frac{m}{a_y}}\boldsymbol{y} + \frac{m_1}{m_1+m_2}\sqrt{\frac{m}{a_x}}\boldsymbol{x}, \tag{B.56}$$

$$\boldsymbol{R_3} = \frac{m_1+m_2}{M_T}\sqrt{\frac{m}{a_y}}\boldsymbol{y}, \tag{B.57}$$

and $\boldsymbol{r_{i(q)}}$ are the positions of each nucleon with respect to the center of mass of its cluster. Inserting Eq. (B.54) in (B.53) and separating the three clusters with mass numbers A_q provides

$$r^2 = \frac{1}{A}\left[\sum_{q=1}^{3}\sum_{i=1}^{A_q}\left(R_q^2 + r_{i(q)}^2 + 2\boldsymbol{R_q}\cdot\boldsymbol{r_{i(q)}}\right)\right]. \tag{B.58}$$

Considering that the clusters are symmetric and spherical, the sum over A_q cancels all the terms $2\boldsymbol{R_q}\cdot\boldsymbol{r_{i(q)}}$,

$$r^2 = \frac{1}{A}\left[\left(\sum_{q=1}^{3}\sum_{i=1}^{A_q} r_{i(q)}^2\right) + \sum_{q=1}^{3} A_q R_q^2\right], \tag{B.59}$$

which seems a reasonable approximation in many cases. Taking into account that Eq. (B.53) can be applied to each individual cluster,

$$r^2 = \frac{1}{A}\left[\left(\sum_{q=1}^{3} A_q r_{A_q}^2\right) + \sum_{q=1}^{3} A_q R_q^2\right], \tag{B.60}$$

where r_{A_q} is the known radius of each cluster. Since these numbers need to be known previously, the preceding expression could be applied even if the clusters are known to be deformed, by just changing its effective radius. The second term in Eq. (B.60) can be expanded using Eqs. (B.55), (B.56),

and (B.57), leading to

$$\sum_{q=1}^{3} A_q R_q^2 = \left[A_1 \left(\frac{m_2}{m_1+m_2} \sqrt{\frac{m}{a_x}} \right)^2 + A_2 \left(\frac{m_1}{m_1+m_2} \sqrt{\frac{m}{a_x}} \right)^2 \right] x^2 \tag{B.61}$$
$$+ \left[A_1 \left(\frac{m_3}{M_T} \sqrt{\frac{m}{a_y}} \right)^2 + A_2 \left(\frac{m_3}{M_T} \sqrt{\frac{m}{a_y}} \right)^2 + A_3 \left(\frac{m_1+m_2}{M_T} \sqrt{\frac{m}{a_y}} \right)^2 \right] y^2$$
$$+ \left[2A_1 \frac{m_2}{m_1+m_2} \sqrt{\frac{m}{a_x}} \frac{m_3}{M_T} \sqrt{\frac{m}{a_y}} - 2A_2 \frac{m_1}{m_1+m_2} \sqrt{\frac{m}{a_x}} \frac{m_3}{M_T} \sqrt{\frac{m}{a_y}} \right] \boldsymbol{x} \cdot \boldsymbol{y}.$$

In the previous expression, terms in $\boldsymbol{x} \cdot \boldsymbol{y}$ cancel regardless of the masses. The remaining terms reduce to $x^2 + y^2 \equiv \rho^2$, thus providing

$$r_{\text{mat}} = \sqrt{\langle r^2 \rangle} = \sqrt{\frac{1}{A} \left[\left(\sum_{q=1}^{3} A_q \langle r_{A_q}^2 \rangle \right) + \langle \rho^2 \rangle \right]}. \tag{B.62}$$

For the charge radius, a similar definition is introduced,

$$r_{\text{ch}}^2 = \frac{1}{Z} \sum_{i=1}^{Z} r_i^2, \tag{B.63}$$

where $\boldsymbol{r_i}$ is now the position of each proton with respect to the center of mass of the system. In this sense, this is a point-nucleon charge radius. Following the same decomposition leads in this case to

$$r^2 = \frac{1}{Z} \left[\left(\sum_{q=1}^{3} Z_q r_{Z_q}^2 \right) + \sum_{q=1}^{3} Z_q R_q^2 \right], \tag{B.64}$$

where Z_q and $\langle r_{Z_q}^2 \rangle$ are the charge and squared charge radius of each cluster, respectively. Expanding again the second term by using expressions (B.55), (B.56), and (B.57),

$$\sum_{q=1}^{3} Z_q R_q^2 = \left[Z_1 \left(\frac{m_2}{m_1+m_2} \sqrt{\frac{m}{a_x}} \right)^2 + Z_2 \left(\frac{m_1}{m_1+m_2} \sqrt{\frac{m}{a_x}} \right)^2 \right] x^2 \tag{B.65}$$
$$+ \left[Z_1 \left(\frac{m_3}{M_T} \sqrt{\frac{m}{a_y}} \right)^2 + Z_2 \left(\frac{m_3}{M_T} \sqrt{\frac{m}{a_y}} \right)^2 + Z_3 \left(\frac{m_1+m_2}{M_T} \sqrt{\frac{m}{a_y}} \right)^2 \right] y^2$$
$$+ \left[2Z_1 \frac{m_2}{m_1+m_2} \sqrt{\frac{m}{a_x}} \frac{m_3}{M_T} \sqrt{\frac{m}{a_y}} - 2Z_2 \frac{m_1}{m_1+m_2} \sqrt{\frac{m}{a_x}} \frac{m_3}{M_T} \sqrt{\frac{m}{a_y}} \right] \boldsymbol{x} \cdot \boldsymbol{y}.$$

For the charge radius, the terms in $\boldsymbol{x}\cdot\boldsymbol{y}$ cancel only if particles 1 and 2 are identical. Then, the charge radius can be written in general as

$$r_{\rm ch}=\sqrt{\langle r_{\rm ch}^2\rangle}=\sqrt{\frac{1}{Z}\left[\left(\sum_{q=1}^{3}Z_q\langle r_{Z_q}^2\rangle\right)+\langle f(x,y)\rangle\right]}, \tag{B.66}$$

where $f(x,y)$ will be different depending on the number of charged and/or identical particles in the system. If particles 1 and 2 are identical, i.e., $Z_2=Z_1$ and $A_2=A_1$, this function can be reduced to

$$f(x,y)\equiv f(x^2,y^2)=\frac{Z_1}{A_1}x^2+\frac{1}{A}\left(\frac{A_3}{A_1}Z_1+\frac{2A_1}{A_3}Z_3\right)y^2. \tag{B.67}$$

The computation of matter and charge radii requires some expectation values in the state considered, typically the ground state of the system. The state labeled $|nj\mu\rangle$ is given by

$$\phi_{nj\mu}(\rho,\Omega)=\sum_{\beta i}C_n^{i\beta j}\psi_{i\beta j\mu}(\rho,\Omega), \tag{B.68}$$

where $\psi_{i\beta j\mu}(\rho,\Omega)$ are the basis functions and $C_n^{i\beta j}$ the diagonalization coefficients. Following the angular momentum coupling given by Eq. (1.4), the basis functions can be expanded explicitly as

$$\psi_{i\beta j\mu}(\rho,\Omega)=\rho^{-5/2}U_{i\beta}(\rho)\sum_{\nu\iota}\langle j_{ab}\nu I\iota|j\mu\rangle\xi_I^{\iota}\sum_{m_l\sigma}\langle lm_lS_x\sigma|j_{ab}\nu\rangle\Upsilon_{Klm_l}^{l_xl_y}(\Omega)\kappa_{S_x}^{\sigma}, \tag{B.69}$$

being m_l,σ,ν and ι the projections of $\boldsymbol{l},\boldsymbol{S_x},\boldsymbol{j_{ab}}$ and $\boldsymbol{I}$, respectively. Considering that the operator x^2 is independent on the spin variables,

$$\begin{aligned}\langle nj\mu|x^2|nj\mu\rangle=&\sum_{\beta\beta' ii'}C_{\rm n}^{i\beta j}C_{\rm n}^{i'\beta' j}\sum_{\nu\nu'\iota\iota'}\langle j_{ab}\nu I\iota|j\mu\rangle\langle j'_{ab}\nu' I\iota'|j\mu\rangle\delta_{\iota\iota'}\\ &\times\sum_{m_lm'_l\sigma\sigma'}\langle lm_lS_x\sigma|j_{ab}\nu\rangle\langle l'm'_lS'_x\sigma'|j'_{ab}\nu'\rangle\delta_{S_xS'_x}\delta_{\sigma\sigma'}\\ &\times\int\int d\Omega\ d\rho\Upsilon_{Klm_l}^{l_xl_y}(\Omega)^*U_{i\beta}(\rho)x^2U_{i'\beta'}(\rho)\Upsilon_{K'l'm'_l}^{l'_xl'_y}(\Omega).\end{aligned} \tag{B.70}$$

Using Eqs. (A.22) and (A.26), which contain the explicit dependence of the hyperspherical harmonics, and separating the hyperradial and angular parts,

$$\begin{aligned}
\langle njm|x^2|njm\rangle &= \sum_{\beta\beta' ii'} C_{\mathrm{n}}^{i\beta j} C_{\mathrm{n}}^{i'\beta' j} \sum_{\nu\nu'\iota\iota'} \langle j_{ab}\nu I\iota|j\mu\rangle\langle j'_{ab}\nu' I\iota'|j\mu\rangle\delta_{\iota\iota'} \\
&\times \sum_{m_l m'_l \sigma\sigma'} \langle lm_l S_x\sigma|j_{ab}\nu\rangle\langle l'm'_l S'_x\sigma'|j'_{ab}\nu'\rangle\delta_{S_x S'_x}\delta_{\sigma\sigma'} \\
&\times \sum_{m_x m'_x} \sum_{m_y m'_y} \langle l_x m_x l_y m_y|lm_l\rangle\langle l'_x m'_x l'_y m'_y|l'm'_l\rangle \\
&\times \int\int (\sin\alpha)^2 (\cos\alpha)^2 \, d\alpha \; d\rho \; \varphi_K^{l_x l_y}(\alpha) U_{i\beta}(\rho) x^2 U_{i'\beta'}(\rho) \varphi_{K'}^{l'_x l'_y}(\alpha) \\
&\times \int d\widehat{x} Y^*_{l_x m_x}(\widehat{x}) Y_{l'_x m'_x}(\widehat{x}) \int d\widehat{y} Y^*_{l_y m_y}(\widehat{y}) Y_{l'_y m'_y}(\widehat{y}).
\end{aligned} \tag{B.71}$$

Considering that

$$\int d\widehat{x} Y_{l_x m_x}(\widehat{x})^* Y_{l'_x m'_x}(\widehat{x}) = \delta_{l_x l'_x}\delta_{m_x m'_x}, \tag{B.72}$$

$$\int d\widehat{y} Y_{l_y m_y}(\widehat{y})^* Y_{l'_y m'_y}(\widehat{y}) = \delta_{l_y l'_y}\delta_{m_y m'_y}, \tag{B.73}$$

it is possible to write

$$\begin{aligned}
\langle njm|x^2|njm\rangle &= \sum_{\beta\beta' ii'} C_{\mathrm{n}}^{i\beta j} C_{\mathrm{n}}^{i'\beta' j} \sum_{\nu\nu'\iota} \langle j_{ab}\nu I\iota|j\mu\rangle\langle j'_{ab}\nu' I\iota|j\mu\rangle \\
&\times \sum_{m_l m'_l \sigma} \langle lm_l S_x\sigma|j_{ab}\nu\rangle\langle l'm'_l S'_x\sigma|j'_{ab}\nu'\rangle\delta_{S_x S'_x} \\
&\times \sum_{m_x m_y} \langle l_x m_x l_y m_y|lm_l\rangle\langle l'_x m_x l'_y m_y|l'm'_l\rangle\delta_{l_x l'_x}\delta_{l_y l'_y} \\
&\times \int\int (\sin\alpha)^2 (\cos\alpha)^2 \, d\alpha \; d\rho \; \varphi_K^{l_x l_y}(\alpha) U_{i\beta}(\rho) x^2 U_{i'\beta'}(\rho) \varphi_{K'}^{l'_x l'_y}(\alpha),
\end{aligned} \tag{B.74}$$

which, taking into account the selection rules for Clebsh-Gordan coefficients, leads to

$$\begin{aligned}
\langle njm|x^2|njm\rangle &= \sum_{\beta\beta' ii'} C_{\mathrm{n}}^{i\beta j} C_{\mathrm{n}}^{i'\beta' j} \delta_{l_x l'_x}\delta_{l_y l'_y}\delta_{ll'}\delta_{S_x S'_x}\delta_{j_{ab} j'_{ab}} \\
&\times \int\int (\sin\alpha)^2 (\cos\alpha)^2 \, d\alpha \; d\rho \; \varphi_K^{l_x l_y}(\alpha) U_{i\beta}(\rho) x^2 U_{i'\beta'}(\rho) \varphi_{K'}^{l'_x l'_y}(\alpha).
\end{aligned} \tag{B.75}$$

For the expectation value of y^2, it is obtained analogously that

$$\langle njm|y^2|njm\rangle = \sum_{\beta\beta' ii'} C_{\rm n}^{i\beta j} C_{\rm n}^{i'\beta' j} \delta_{l_x l'_x} \delta_{l_y l'_y} \delta_{ll'} \delta_{S_x S'_x} \delta_{j_{ab} j'_{ab}} \tag{B.76}$$
$$\times \int\int (\sin\alpha)^2 (\cos\alpha)^2 \, d\alpha \; d\rho \; \varphi_K^{l_x l_y}(\alpha) U_{i\beta}(\rho) y^2 U_{i'\beta'}(\rho) \varphi_{K'}^{l'_x l'_y}(\alpha).$$

These expressions can be easily computed considering that, using hyperspherical coordinates, $x = \rho \sin\alpha$ and $y = \rho\cos\alpha$. In the case of $\rho^2 = x^2 + y^2$, the expectation value is simply

$$\langle njm|\rho^2|njm\rangle = \sum_{\beta ii'} C_{\rm n}^{i\beta j} C_{\rm n}^{i'\beta j} \int d\rho \; U_{i\beta}(\rho) \rho^2 U_{i'\beta}(\rho). \tag{B.77}$$

B.4 Electric transitions

Following the notation of Brink and Satchler [82], the reduced electromagnetic transition probability between states of a system is defined as

$$\begin{aligned} B(\mathcal{O}\lambda)_{nj,n'j'} &\equiv B(\mathcal{O}\lambda; nj \to n'j') \\ &= |\langle nj\|\widehat{\mathcal{O}}_\lambda\|n'j'\rangle|^2 \left(\frac{2\lambda+1}{4\pi}\right), \end{aligned} \tag{B.78}$$

The electric multipole operator takes the form in the Jacobi-k set

$$\widehat{Q}_{\lambda M_\lambda}(\boldsymbol{x}_k, \boldsymbol{y}_k) = \left(\frac{4\pi}{2\lambda+1}\right)^{1/2} \sum_{q=1}^{3} Z_q \; e \; r_q^\lambda Y_{\lambda M_\lambda}(\widehat{r}_q), \tag{B.79}$$

where Z_q is the atomic number of the particle q, e is the electron charge, and $\boldsymbol{r}_q$ is the position of particle q with respect to the center of mass of the system, which in the Jacobi-q system is given by (see Appendix A)

$$\boldsymbol{r}_q = \sqrt{\frac{m}{m_q}\frac{(M_T - m_q)}{M_T}}\boldsymbol{y}_q = \frac{\sqrt{m a_y}}{m_q}\boldsymbol{y}_q. \tag{B.80}$$

The reduced matrix element, $\langle nj||\widehat{Q}_\lambda||n'j'\rangle$, is related to the projection-dependent matrix element by the Wigner-Eckart theorem,

$$\langle njm|\widehat{Q}_{\lambda M_\lambda}|n'j'm'\rangle = (-1)^{2\lambda}\langle jm|j'm'\lambda M_\lambda\rangle\langle nj||\widehat{Q}_\lambda||n'j'\rangle, \tag{B.81}$$

where the ket $|nj\mu\rangle$ denotes the state wave function in the Jacobi-k set given by Eq. (B.68). The operator matrix elements are then given by

$$\begin{aligned}\langle nj\mu|\widehat{Q}_{\lambda M_\lambda}|n'j'\mu'\rangle = \frac{\sqrt{4\pi}}{\hat{\lambda}}\sum_{q=1}^{3} Z_q e\left(\frac{\sqrt{ma_{y_q}}}{m_q}\right)^{\lambda} \\ \times \langle nj\mu|y_q^{\lambda}Y_{\lambda M_\lambda}(\widehat{y_q})|n'j'\mu'\rangle.\end{aligned} \tag{B.82}$$

In order to compute these matrix elements, the system states $|nj\mu\rangle$ can be rotated to the Jacobi-q set using the transformations given by Eqs. (B.37) and (B.38). This can be done for each summand in Eq. (B.82) In ket notation, system states are written as

$$|nj\mu\rangle = \sum_{\beta i} C_n^{i\beta j}|i\beta j\mu\rangle = \sum_{\beta i} C_n^{i\beta j}|i\beta j\rangle \otimes |\beta j\mu\rangle, \tag{B.83}$$

where $|i\beta j\rangle$ describes the hyperradial part and $|\beta j\mu\rangle$ the angular and spin degrees of freedom. The transformation from the preferred Jacobi set k to the Jacobi-q system is defined by

$$|\beta j\mu\rangle = \sum_{\beta_q} N_{\beta\beta_q}|q:\beta_q j\mu\rangle. \tag{B.84}$$

Notice that, for simplicity, the index k is omitted. Then, the term labeled by q in Eq. (B.82) is given by

$$\begin{aligned}\langle nj\mu|y_q^{\lambda}Y_{\lambda M_\lambda}(\widehat{y_q})|n'j'\mu'\rangle &= \sum_{\beta\beta'}\sum_{ii'} C_n^{i\beta j}C_{n'}^{i'\beta' j'}\langle i\beta j\mu|y_q^{\lambda}Y_{\lambda M_\lambda}(\widehat{y_q})|i'\beta' j'\mu'\rangle \\ &= \sum_{\beta\beta'}\sum_{ii'} C_n^{i\beta j}C_{n'}^{i'\beta' j'}\sum_{\beta_q\beta'_q} N_{\beta\beta_q}N_{\beta'\beta'_q} \\ &\times \langle i\beta; q:\beta_q j\mu|y_q^{\lambda}Y_{\lambda M_\lambda}(\widehat{y_q})|i'\beta'; q:\beta'_q j'\mu'\rangle.\end{aligned} \tag{B.85}$$

Writing down explicitly the basis functions (see Eq. (B.69), expanding all momentum couplings and considering that the operator does not depend on the spins,

$$\begin{aligned}
\langle njm|y_q^\lambda Y_{\lambda M_\lambda}(\widehat{y}_q)|n'j'm'\rangle &= \sum_{\beta\beta'}\sum_{ii'} C_n^{i\beta j} C_{n'}^{i'\beta' j'} \sum_{\beta_q\beta'_q} N_{\beta\beta_q} N_{\beta'\beta'_q} \\
&\times \sum_{\nu_q\nu'_q\iota_q\iota'_q} \langle j_{abq}\nu_q I_q\iota_q|j\mu\rangle\langle j'_{abq}\nu'_q I_q\iota'_q|j'\mu'\rangle\delta_{\iota_q\iota'_q} \\
&\times \sum_{m_{lq}m'_{lq}\sigma_q\sigma'_q} \langle l_q m_{lq} S_{xq}\sigma_q|j_{abq}\nu_q\rangle\langle l'_q m'_{lq} S'_{xq}\sigma'_q|j'_{abq}\nu'_q\rangle\delta_{S_{xq}S'_{xq}}\delta_{\sigma_q\sigma'_q} \\
&\times \int\int d\Omega_q\; d\rho\; \Upsilon^{l_{xq}l_{yq}\;*}_{K_q l_q m_{lq}}(\Omega_q) U_{i\beta}(\rho) y_q^\lambda Y_{\lambda M_\lambda}(\widehat{y}_q) U_{i'\beta'}(\rho) \Upsilon^{l'_{xq}l'_{yq}}_{K'_q l'_q m'_{lq}}(\Omega_q),
\end{aligned} \tag{B.86}$$

where ν, ι, m_l, σ are the projections of j_{ab}, I, l, S_x. Note that the hyperradial functions are expressed in the original Jacobi-k set as the transformation conserves the hyperradius.

The hyperangular part in the previous expression can be separated making use of Eqs. (A.22) and (A.26), which contain the explicit dependence of the hyperspherical harmonics. This leads to

$$\begin{aligned}
\langle njm|y_q^\lambda Y_{\lambda M_\lambda}(\widehat{y}_q)|n'j'm'\rangle &= \sum_{\beta\beta'}\sum_{ii'} C_n^{i\beta j} C_{n'}^{i'\beta' j'} \sum_{\beta_q\beta'_q} N_{\beta\beta_q} N_{\beta'\beta'_q} \\
&\times \sum_{\nu_q\nu'_q\iota_q\iota'_q} \langle j_{abq}\nu_q I_q\iota_q|j\mu\rangle\langle j'_{abq}\nu'_q I_q\iota'_q|j'\mu'\rangle\delta_{\iota_q\iota'_q} \\
&\times \sum_{m_{lq}m'_{lq}\sigma_q\sigma'_q} \langle l_q m_{lq} S_{xq}\sigma_q|j_{abq}\nu_q\rangle\langle l'_q m'_{lq} S'_{xq}\sigma'_q|j'_{abq}\nu'_q\rangle\delta_{S_{xq}S'_{xq}}\delta_{\sigma_q\sigma'_q} \\
&\times \sum_{m_{xq}m'_{xq}} \sum_{m_{yq}m'_{yq}} \langle l_{xq} m_{xq} l_{yq} m_{yq}|l_k m_{lq}\rangle\langle l'_{xq} m'_{xq} l'_{yq} m'_{yq}|l'_q m'_{lq}\rangle \\
&\times \int (\sin\alpha_q)^2 (\cos\alpha_q)^2\, d\alpha_q\; d\rho\; \varphi^{l_{xq}l_{yq}}_{K_q}(\alpha_q) U_{i\beta}(\rho) y_q^\lambda U_{i'\beta'}(\rho) \varphi^{l'_{xq}l'_{yq}}_{K'_q}(\alpha_q) \\
&\times \int d\widehat{x}_q Y^*_{l_{xq}m_{xq}}(\widehat{x}_q) Y_{l'_{xq}m'_{xq}}(\widehat{x}_q) \int d\widehat{y}_q Y^*_{l_{yk}m_{yq}}(\widehat{y}_q) Y_{\lambda M_\lambda}(\widehat{y}_q) Y_{l'_{yq}m'_{yq}}(\widehat{y}_q).
\end{aligned} \tag{B.87}$$

Using Eq. (B.72) and considering that

$$\begin{aligned}
&\int d\widehat{y}_q Y^*_{l_{yq}m_{yq}}(\widehat{y}_q) Y_{\lambda M_\lambda}(\widehat{y}_q) Y_{l'_{yq}m'_{yq}}(\widehat{y}_q) \\
&\quad = (-1)^{m_{yq}} \frac{\hat{l_{yq}}\hat{\lambda}\hat{l'_{yq}}}{\sqrt{4\pi}} \begin{pmatrix} l_{yq} & \lambda & l'_{yq} \\ 0 & 0 & 0 \end{pmatrix} \begin{pmatrix} l_{yq} & \lambda & l'_{yq} \\ -m_{yq} & M_\lambda & m'_{yq} \end{pmatrix},
\end{aligned} \tag{B.88}$$

the matrix element is

$$\begin{aligned}\langle nj\mu|y_q^\lambda Y_{\lambda M_\lambda}(\widehat{y_q})|n'j'\mu'\rangle &= \sum_{\beta\beta'}\sum_{ii'} C_n^{i\beta j} C_{n'}^{i'\beta' j'} \sum_{\beta_q\beta_q'} N_{\beta\beta_q} N_{\beta'\beta_q'} \\ &\times \int (\sin\alpha_q)^2 (\cos\alpha_q)^2 \, d\alpha_q \; d\rho \; \varphi_{K_q}^{l_{xq}l_{yq}}(\alpha_q) U_{i\beta}(\rho) y_q^\lambda U_{i'\beta'}(\rho) \varphi_{K_q'}^{l'_{xq}l'_{yq}}(\alpha_q) \\ &\times \delta_{l_{xq}l'_{xq}} \delta_{S_{xq}S'_{xq}} \hat{l_{yq}} \hat{l'_{yq}} \begin{pmatrix} l_{yq} & \lambda & l'_{yq} \\ 0 & 0 & 0 \end{pmatrix} \Delta, \end{aligned} \tag{B.89}$$

where

$$\begin{aligned}\Delta = &\sum_{\nu_q\nu'_q\iota_q} \langle j_{abq}\nu_q I_q \iota_q | j\mu\rangle \langle j'_{abq}\nu'_q I_q \iota_q | j'\mu'\rangle \\ &\times \sum_{m_{lq}m'_{lq}\sigma_q} \langle l_k m_{lq} S_{xq}\sigma_q | j_{abq}\nu_q\rangle \langle l'_q m'_{lq} S_{xq}\sigma_q | j'_{abq}\nu'_q\rangle \\ &\times \sum_{m_{yq}m'_{yq}m_{xq}} \langle l_{xq}m_{xq}l_{yq}m_{yq}|l_k m_{lq}\rangle \langle l_{xq}m_{xq}l'_{yq}m'_{yq}|l'_q m'_{lq}\rangle \\ &\times (-1)^{m_{yq}} \begin{pmatrix} l_{yq} & \lambda & l'_{yq} \\ -m_{yq} & M_\lambda & m'_{yq} \end{pmatrix}. \end{aligned} \tag{B.90}$$

These Clebsch-Gordan coefficients can be expressed by means of 3-j symbols, according to

$$\langle ab\alpha\beta|c-\gamma\rangle = (-1)^{a-b-\gamma}\hat{c} \begin{pmatrix} a & b & c \\ \alpha & \beta & \gamma \end{pmatrix}. \tag{B.91}$$

Using this relation, (for simplicity q will be omitted)

$$\begin{aligned}\Delta = &\sum_{\nu\nu'\iota} \sum_{m_l m'_l \sigma} \sum_{m_y m'_y m_x} \hat{j}\hat{j}'\hat{j}_{ab}\hat{j}'_{ab}\hat{l}\hat{l}' \\ &\times (-1)^{j_{ab}+j'_{ab}-2I+l+l'-2S_x+l_y+l'_y+\mu+\mu'+\nu+\nu'+m_l+m'_l+m_y} \\ &\times \begin{pmatrix} j_{ab} & I & j \\ \nu & \iota & -\mu \end{pmatrix} \begin{pmatrix} j'_{ab} & I & j' \\ \nu' & \iota & -\mu' \end{pmatrix} \begin{pmatrix} l & S_x & j_{ab} \\ m_l & \sigma & -\nu \end{pmatrix} \begin{pmatrix} l' & S_x & j'_{ab} \\ m'_l & \sigma & -\nu' \end{pmatrix} \\ &\times \begin{pmatrix} l_x & l_y & l \\ m_x & m_y & -m_l \end{pmatrix} \begin{pmatrix} l_x & l'_y & l' \\ m_x & m'_y & -m'_l \end{pmatrix} \begin{pmatrix} l_y & \lambda & l'_y \\ -m_y & M_\lambda & m'_y \end{pmatrix}. \end{aligned} \tag{B.92}$$

Considering that the Racah symbols W are defined by

$$W(abcd;ef)\begin{pmatrix} c & a & f \\ \gamma & \alpha & \phi \end{pmatrix} = \sum_{\beta\delta\epsilon}(-1)^{f-e-\alpha-\delta}\begin{pmatrix} a & b & e \\ \alpha & \beta & -\epsilon \end{pmatrix} \times \begin{pmatrix} d & c & e \\ \delta & \gamma & \epsilon \end{pmatrix}\begin{pmatrix} b & d & f \\ \beta & \delta & -\phi \end{pmatrix}, \tag{B.93}$$

it is straightforward to get

$$\begin{aligned}
&\sum_{m_x m_y m'_y}(-1)^{m_y}\begin{pmatrix} l_x & l_y & l \\ m_x & m_y & -m_l \end{pmatrix}\begin{pmatrix} l_y & \lambda & l'_y \\ -m_y & M_\lambda & m'_y \end{pmatrix}\begin{pmatrix} l_x & l'_y & l' \\ m_x & m'_y & -m'_l \end{pmatrix} \\
&= (-1)^{l+l'_y+m'_l}\sum_{m_x m_y m'_y}(-1)^{l-l'_y+m'_l-m_y}\begin{pmatrix} l_x & l_y & l \\ m_x & m_y & -m_l \end{pmatrix} \\
&\times \begin{pmatrix} l_y & \lambda & l'_y \\ m_y & -M_\lambda & -m'_y \end{pmatrix}\begin{pmatrix} l' & l_x & l'_y \\ -m'_l & m_x & m'_y \end{pmatrix} \\
&= (-1)^{l+l'_y+m'_l}W(l'l_x\lambda l_y; l'_y l)\begin{pmatrix} \lambda & l' & l \\ -M_\lambda & -m'_l & m_l \end{pmatrix} \\
&= (-1)^{\lambda+l_x+m'_l}W(ll'l_y l'_y; \lambda l_x)\begin{pmatrix} \lambda & l' & l \\ -M_\lambda & -m'_l & m_l \end{pmatrix}.
\end{aligned}$$

The phase $(-1)^{m'_l}$ cancels the same term in expression (B.92). Using the 3-j symbol and applying again Eq. (B.93),

$$\begin{aligned}
&\sum_{m_l m'_l \sigma}(-1)^{m_l}\begin{pmatrix} l & S_x & j_{ab} \\ m_l & \sigma & -\nu \end{pmatrix}\begin{pmatrix} \lambda & l' & l \\ -M_\lambda & -m'_l & m_l \end{pmatrix}\begin{pmatrix} l' & S_x & j'_{ab} \\ m'_l & \sigma & -\nu' \end{pmatrix} \\
&= (-1)^{l+j'_{ab}+2S_x-\nu'}\sum_{m_l m'_l \sigma}(-1)^{j_{ab}-l'+\nu'-m_l}\begin{pmatrix} S_x & l & j_{ab} \\ \sigma & m_l & -\nu \end{pmatrix} \\
&\times \begin{pmatrix} l & \lambda & l' \\ m_l & -M_\lambda & -m'_l \end{pmatrix}\begin{pmatrix} j'_{ab} & S_x & l' \\ -\nu' & \sigma & m'_l \end{pmatrix} \\
&= (-1)^{l+j'_{ab}+2S_x-\nu'}W(j'_{ab}S_x\lambda l; l' j_{ab})\begin{pmatrix} \lambda & j'_{ab} & j_{ab} \\ -M_\lambda & -\nu' & \nu \end{pmatrix} \\
&= (-1)^{\lambda+3S_x+l+l'-j_{ab}+j'_{ab}-\nu'}W(j_{ab}j'_{ab}ll'; \lambda S_x)\begin{pmatrix} \lambda & j'_{ab} & j_{ab} \\ -M_\lambda & -\nu' & \nu \end{pmatrix},
\end{aligned}$$

where the factor $(-1)^{-\nu'}$ cancels with $(-1)^{\nu'}$ in expression (B.92). Following the same procedure with the remaining 3-j symbols,

$$\begin{aligned}
&\sum_{\nu\nu'\iota}(-1)^{\nu}\begin{pmatrix} j_{ab} & I & j \\ \nu & \iota & -\mu \end{pmatrix}\begin{pmatrix} \lambda & j'_{ab} & j_{ab} \\ -M_\lambda & -\nu' & \nu \end{pmatrix}\begin{pmatrix} j'_{ab} & I & j' \\ \nu' & \iota & -\mu' \end{pmatrix} \\
&= (-1)^{\lambda+j+2j'+3j_{ab}+\mu'}\sum_{\nu\nu'\iota}(-1)^{j-j'_{ab}-\mu'+\nu}\begin{pmatrix} I & j_{ab} & j \\ -\iota & -\nu & \mu \end{pmatrix} \\
&\times\begin{pmatrix} j_{ab} & \lambda & j'_{ab} \\ -\nu & M_\lambda & \nu' \end{pmatrix}\begin{pmatrix} j' & I & j'_{ab} \\ \mu' & -\iota & -\nu' \end{pmatrix} \\
&= (-1)^{\lambda+j+2j'+3j_{ab}+\mu'}W(j'I\lambda j_{ab};j'_{ab}j)\begin{pmatrix} \lambda & j' & j \\ M_\lambda & \mu' & -\mu \end{pmatrix} \\
&= (-1)^{I+2j'+3j_{ab}-j'_{ab}+\mu'}W(jj'j_{ab}j'_{ab};\lambda I)\begin{pmatrix} \lambda & j' & j \\ M_\lambda & \mu' & -\mu \end{pmatrix}.
\end{aligned}$$

In this case, $(-1)^{2j'+\mu'}$ cancels the phase $(-1)^{\mu'}$ in expression (B.92). This leads to

$$\begin{aligned}
\Delta &= (-1)^{\mu}\hat{j}\hat{j}'\begin{pmatrix} \lambda & j' & j \\ M_\lambda & \mu' & -\mu \end{pmatrix}\hat{l}\hat{l}'\hat{j}_{ab}\hat{j}'_{ab}(-1)^{l_x+l_y+l'_y+S_x-j_{ab}+j'_{ab}-I} \\
&\times W(ll'l_yl'_y;\lambda l_x)W(j_{ab}j'_{ab}ll';\lambda S_x)W(jj'j_{ab}j'_{ab};\lambda I).
\end{aligned} \tag{B.94}$$

Inserting this in Eq. (B.89) (and specifying again the label q)

$$\begin{aligned}
&\langle nj\mu|y^\lambda_q Y_{\lambda M_\lambda}(\widehat{y_q})|n'j'\mu'\rangle = (-1)^{\mu}\hat{j}\hat{j}'\begin{pmatrix} \lambda & j' & j \\ M_\lambda & \mu' & -\mu \end{pmatrix} \\
&\times\sum_{\beta\beta'}\sum_{ii'}C^{i\beta j}_{n}C^{i'\beta'j'}_{n'}\sum_{\beta_q\beta'_q}N_{\beta\beta_q}N_{\beta'\beta'_q} \\
&\times\delta_{l_{xq}l'_{xq}}\delta_{S_{xq}S'_{xq}}\hat{l_{yq}}\hat{l'_{yq}}\hat{l_q}\hat{l'_q}\hat{j}_{abq}\hat{j}'_{abq}(-1)^{l_{xq}+l_{yq}+l'_{yq}+S_{xq}-j_{abq}+j'_{abq}-I_q} \\
&\times\begin{pmatrix} l_{yq} & \lambda & l'_{yq} \\ 0 & 0 & 0 \end{pmatrix}W(l_ql'_ql_{yq}l'_{yq};\lambda l_{xq})W(j_{abq}j'_{abq}l_ql'_q;\lambda S_{xq})W(jj'j_{abq}j'_{abq};\lambda I_q) \\
&\times\int(\sin\alpha_q)^2(\cos\alpha_q)^2\,d\alpha_q\;d\rho\;\varphi^{l_{xq}l_{yq}}_{K_q}(\alpha_q)U_{i\beta}(\rho)y^\lambda_qU_{i'\beta'}(\rho)\varphi^{l'_{xq}l'_{yq}}_{K'_q}(\alpha_q).
\end{aligned} \tag{B.95}$$

Equations (B.89) and (B.95) determine the electric operator matrix elements.

Taking into account that

$$\begin{pmatrix} \lambda & j' & j \\ M_\lambda & \mu' & -\mu \end{pmatrix} = (-1)^{\lambda+j+j'} \begin{pmatrix} j' & \lambda & j \\ \mu' & M_\lambda & -\mu \end{pmatrix} = \frac{(-1)^{j-\mu}}{\hat{j}} \langle j'\mu'\lambda M_\lambda | j\mu \rangle, \tag{B.96}$$

and using Eq. (B.81), the reduced matrix element is given by

$$\begin{aligned} &\langle nj||\widehat{Q}_\lambda||n'j'\rangle = (-1)^{-2\lambda} \frac{\langle nj\mu|\widehat{Q}_{\lambda M_\lambda}|n'j'\mu'\rangle}{\langle j'\mu'\lambda M_\lambda|j\mu\rangle} \\ &= \sum_q Z_q e \left(\frac{\sqrt{m a_{y_q}}}{m_q}\right)^\lambda \sum_{\beta\beta'} \sum_{ii'} C_n^{i\beta j} C_{n'}^{i'\beta' j'} \sum_{\beta_q\beta'_q} N_{\beta\beta_q} N_{\beta'\beta'_q} \\ &\times \delta_{l_{x_q} l'_{x_q}} \delta_{S_{x_q} S'_{x_q}} \hat{l_{y_q}} \hat{l'_{y_q}} \hat{l}_q \hat{l}'_q \hat{j}_{ab_q} \hat{j}'_{ab_q} \hat{j}' (-1)^{j+l_{x_q}+l_{y_q}+l'_{y_q}+S_{x_q}-j_{ab_q}+j'_{ab_q}-I_q} \\ &\times \begin{pmatrix} l_{y_q} & \lambda & l'_{y_q} \\ 0 & 0 & 0 \end{pmatrix} W(l_q l'_q l_{y_q} l'_{y_q}; \lambda l_{x_q}) W(j_{ab_q} j'_{ab_q} l_q l'_q; \lambda S_{x_q}) W(jj' j_{ab_q} j'_{ab_q}; \lambda I_q) \\ &\times \int (\sin\alpha)^2 (\cos\alpha)^2 \, d\alpha \; d\rho \; \varphi_{K_q}^{l_{x_q} l_{y_q}}(\alpha) U_{i\beta}(\rho) y_q^\lambda U_{i'\beta'}(\rho) \varphi_{K'_q}^{l'_{x_q} l'_{y_q}}(\alpha), \end{aligned} \tag{B.97}$$

which is the final expression presented in chapter 2, Eq. (2.23).

B.4.1 Electric dipole sum rules

Electromagnetic transitions of a given multipolarity λ from an initial state labeled $|n_0 j_0 \mu_0\rangle$ to final states $|nj\mu\rangle$ define a total probability strength

$$S_T(E\lambda) = \sum_{nj} B(E\lambda)_{n_0 j_0, nj} = \left(\frac{2\lambda+1}{4\pi}\right) \sum_{nj} |\langle n_0 j_0 || \widehat{\mathcal{O}}_\lambda || nj \rangle|^2. \tag{B.98}$$

Taking into account that λ is an integer, Eq. (B.81) gives

$$\langle n_0 j_0 \mu_0 | \widehat{Q}_{\lambda M_\lambda} | nj\mu \rangle = \langle n_0 j_0 || \widehat{Q}_\lambda || nj \rangle \langle j_0 \mu_0 | j\mu\lambda M_\lambda \rangle. \tag{B.99}$$

The square of the previous equation, summing over all projections, leads to

$$|\langle n_0 j_0 || \widehat{Q}_\lambda || nj \rangle|^2 = \sum_{\mu M_\lambda} |\langle n_0 j_0 \mu_0 | \widehat{Q}_{\lambda M_\lambda} | nj\mu \rangle|^2, \tag{B.100}$$

where the normalization of the Clebsch-Gordan coefficients has been taken into account.

Inserting Eq. (B.100) in Eq. (B.98) leads to

$$\begin{aligned} S_T(E\lambda) &= \left(\frac{2\lambda+1}{4\pi}\right)\sum_{nj}\sum_{\mu M_\lambda}|\langle n_0 j_0\mu_0|\widehat{\mathcal{O}}_{\lambda M_\lambda}|nj\mu\rangle|^2 \\ &= \left(\frac{2\lambda+1}{4\pi}\right)\sum_{nj}\sum_{\mu M_\lambda}\langle n_0 j_0\mu_0|\widehat{\mathcal{O}}^\dagger_{\lambda M_\lambda}|nj\mu\rangle\langle nj\mu|\widehat{\mathcal{O}}_{\lambda M_\lambda}|n_0 j_0\mu_0\rangle \\ &= \left(\frac{2\lambda+1}{4\pi}\right)\sum_{M_\lambda}\langle n_0 j_0\mu_0|\widehat{\mathcal{O}}^\dagger_{\lambda M_\lambda}\widehat{\mathcal{O}}_{\lambda M_\lambda}|n_0 j_0\mu_0\rangle. \end{aligned} \tag{B.101}$$

In the particular case of electric dipolar transitions for a system comprising a single charged particle, the electric operator can be written as

$$\widehat{Q}_{1M_\lambda}(\boldsymbol{y}) = \left(\frac{4\pi}{3}\right)^{1/2} Z_c e\frac{\sqrt{ma_y}}{m_c} y Y_{1M_\lambda}(\widehat{y}). \tag{B.102}$$

Here, the label c refers to the charged particle. Inserting Eq. (B.102) in Eq. (B.101) involves the sum

$$\begin{aligned} &\sum_{M_\lambda}\langle n_0 j_0\mu_0|y^2 Y^*_{1M_\lambda}(\widehat{y})Y_{1M_\lambda}(\widehat{y})|n_0 j_0\mu_0\rangle \\ &= \langle n_0 j_0\mu_0|y^2\left(\sum_{M_\lambda}Y^*_{1M_\lambda}(\widehat{y})Y_{1M_\lambda}(\widehat{y})\right)|n_0 j_0\mu_0\rangle. \end{aligned} \tag{B.103}$$

Using the relationship

$$Y_{\lambda M_\lambda}Y_{\lambda -M_\lambda} = \frac{2\lambda+1}{\sqrt{4\pi}}\sum_c Y_{c0}\sqrt{2c+1}\begin{pmatrix}\lambda & \lambda & c\\ M_\lambda & M_\lambda & 0\end{pmatrix}\begin{pmatrix}\lambda & \lambda & c\\ 0 & 0 & 0\end{pmatrix}, \tag{B.104}$$

one can write

$$\begin{aligned} Y_{1M_\lambda}Y_{1-M_\lambda} = \frac{3}{\sqrt{4\pi}}\Bigg[&-\frac{1}{\sqrt{3}}Y_{00}\begin{pmatrix}1 & 1 & 0\\ M_\lambda & -M_\lambda & 0\end{pmatrix} \\ &+\sqrt{\frac{2}{15}}Y_{20}\sqrt{5}\begin{pmatrix}1 & 1 & 2\\ M_\lambda & -M_\lambda & 0\end{pmatrix}\Bigg]. \end{aligned} \tag{B.105}$$

Considering also that

$$Y^*_{\lambda M_\lambda}(\widehat{r}) = (-1)^{M_\lambda}Y_{\lambda -M_\lambda}, \tag{B.106}$$

the summation of spherical harmonics in Eq. (B.103) is

$$\sum_{M_\lambda} Y^*_{1M_\lambda}(\widehat{y}_i)Y_{1M_\lambda}(\widehat{y}_i) = \frac{3}{\sqrt{4\pi}}\sum_{M_\lambda}(-1)^{M_\lambda}\left[-\frac{1}{\sqrt{3}}Y_{00}\begin{pmatrix} 1 & 1 & 0 \\ M_\lambda & -M_\lambda & 0 \end{pmatrix} + \sqrt{\frac{2}{15}}Y_{20}\sqrt{5}\begin{pmatrix} 1 & 1 & 2 \\ M_\lambda & -M_\lambda & 0 \end{pmatrix}\right]. \tag{B.107}$$

These two terms can be evaluated, leading to

$$\sum_{M_\lambda}(-1)^{M_\lambda}\begin{pmatrix} 1 & 1 & 0 \\ M_\lambda & -M_\lambda & 0 \end{pmatrix} = -\sqrt{3}, \tag{B.108}$$

$$\sum_{M_\lambda}(-1)^{M_\lambda}\begin{pmatrix} 1 & 1 & 2 \\ M_\lambda & -M_\lambda & 0 \end{pmatrix} = 0, \tag{B.109}$$

so that the second term cancels. Therefore, the expression (B.107) gives

$$\sum_{M_\lambda} Y^*_{1M_\lambda}(\widehat{y}_i)Y_{1M_\lambda}(\widehat{y}_i) = \frac{3}{\sqrt{4\pi}}Y_{00} = \frac{3}{4\pi} \tag{B.110}$$

Using this result, together with (B.101), (B.102) and (B.103), the electric dipole sum rule for a system comprising a single charged particle is

$$S_{T_1}(E1) = \frac{3}{4\pi}\frac{Z_c^2 e^2 m a_y}{m_c^2}\langle n_0 j_0 \mu_0 | y^2 | n_0 j_0 \mu_0\rangle. \tag{B.111}$$

In the case of a system comprising two identical charged particles related by coordinate $\boldsymbol{x}$ in the preferred Jacobi set, the electric dipolar operator can be written using the relationship between harmonic polynomials in different Jacobi systems (see Eqs. (2.26) and (2.27) in chapter 2). This leads to

$$Q_{1M_1}(\boldsymbol{y}) = -\left(\frac{4\pi}{3}\right)^{1/2} 2(\cos\varphi_{23}) Z_2 e \frac{\sqrt{m a_{y2}}}{m_2} y Y_{1M_1}(\widehat{y}), \tag{B.112}$$

for 1 and 2 being the identical charged particles, and 3 referring to the remaining particle. Here, φ_{23} is the mass-dependent phase given by Eq. (2.27). This expression is analogous in form to Eq. (B.102), but including a factor $2(\cos\varphi_{23})$. Therefore, the sum rule in this case can be easily obtained as

$$S_T(E1) = \frac{3}{4\pi}\frac{Z_2^2 e^2 m a_{y2}}{m_2^2}(2\cos\varphi_{23})^2\langle n_0 j_0 \mu_0 | y^2 | n_0 j_0 \mu_0\rangle. \tag{B.113}$$

Finally, consider now the case of a system comprising three charged particles, being the two particles related by $\boldsymbol{x}$ identical. In that case, the electric dipolar operator is given by the sum of Eqs. (B.102) y (B.112). Notice that the charge and mass factors are different for each term, provided the third particle is different from the previous two. This leads to

$$\widehat{Q}_{1M_\lambda} = \left(\frac{4\pi}{3}\right)^{1/2} \left[Z_3 e \frac{\sqrt{m a_{y_3}}}{m_3} - 2\ Z_2 e \left(\cos\varphi_{23}\right) \frac{\sqrt{m a_{y_2}}}{m_2} \right]\ y Y_{1M_\lambda}(\widehat{y}), \tag{B.114}$$

Then, the sum rule for dipolar transition in this case is

$$S_T(E1) = \frac{3}{4\pi} \left[Z_3 e \frac{\sqrt{m a_{y_3}}}{m_3} - 2\ Z_2 e \left(\cos\varphi_{23}\right) \frac{\sqrt{m a_{y_2}}}{m_2} \right]^2 \langle n_0 j_0 \mu_0 | y^2 | n_0 j_0 \mu_0 \rangle. \tag{B.115}$$

B.4.2 Quadrupole moment

The quadrupole moment of a nucleus is defined as

$$Q = \sqrt{\frac{16\pi}{5}} \langle n_0 j_0 j_0 | \widehat{Q}'_{20} | n_0 j_0 j_0 \rangle, \tag{B.116}$$

where $|n_0 j_0 j_0\rangle$ represents the ground-state with angular momentum j_0 and maximum projection. This is the usual definition of Q, where the quadrupolar operator $\widehat{Q}'_{20}$ does not include the factor $\sqrt{4\pi/(2\lambda+1)}$ used in the notation from Brink and Satchler [82]. In the case of a system comprising two identical charged particles[2] related by coordinate $\boldsymbol{x}$, this operator can be written using the relationship between harmonic polynomials in different Jacobi sets (see Eqs. (2.26) and (2.27)),

$$\widehat{Q}'_{2M_\lambda} = 2 Z_2 e \frac{m a_{y_2}}{m_2^2} \left[\left(\sin\varphi_{23}\right)^2 x^2 Y_{2M_\lambda}(\widehat{x}) + \left(\cos\varphi_{23}\right)^2 y^2 Y_{2M_\lambda}(\widehat{y}) \right]. \tag{B.117}$$

Thus, the evaluation of Eq. (B.116) can be separated into two parts,

$$Q = \sqrt{\frac{16\pi}{5}} 2 Z_2 e \frac{m a_{y_2}}{m_2^2} \left[\left(\sin\varphi_{23}\right)^2 Q_x + \left(\cos\varphi_{23}\right)^2 Q_y \right], \tag{B.118}$$

[2] The only case considered in chapter 2 for the quadrupole moment is ^{9}Be, comprising two identical α particles.

where

$$Q_x = \langle n_0 j_0 j_0 | x^2 Y_{2M_\lambda}(\widehat{x}) | n_0 j_0 j_0 \rangle, \tag{B.119}$$

$$Q_y = \langle n_0 j_0 j_0 | y^2 Y_{2M_\lambda}(\widehat{y}) | n_0 j_0 j_0 \rangle. \tag{B.120}$$

Expanding explicitly the wave functions, the first term gives

$$\begin{aligned} Q_x = & \sum_{\beta\beta' ii'} C_{n_0}^{i\beta j_0} C_{n_0}^{i'\beta' j_0} \sum_{\nu\nu'\iota\iota'} \langle j_{ab}\nu I_k \iota | j\mu\rangle \langle j'_{ab}\nu' I_k \iota' | j'\mu'\rangle \delta_{\iota\iota'} \\ & \times \sum_{m_l m'_l \sigma\sigma'} \langle l m_l S_x \sigma | j_{ab}\nu\rangle \langle l' m'_l S'_x \sigma' | j'_{ab}\nu'\rangle \delta_{S_x S'_x} \delta_{\sigma\sigma'} \\ & \times \sum_{m_x m'_x} \sum_{m_y m'_y} \langle l_x m_x l_y m_y | l m_l\rangle \langle l'_x m'_x l'_y m'_y | l' m'_l\rangle \\ & \times \int (\sin\alpha)^2 (\cos\alpha)^2 \, d\alpha \; d\rho \; \varphi_K^{l_x l_y}(\alpha) U_{i\beta}(\rho) x^2 U_{i'\beta'}(\rho) \varphi_{K'}^{l'_x l'_y}(\alpha) \\ & \times \int d\widehat{x} Y^*_{l_x m_x}(\widehat{x}) Y_{2M_\lambda}(\widehat{x}) Y_{l'_x m'_x}(\widehat{x}) \int d\widehat{y} Y^*_{l_y m_y}(\widehat{y}) Y_{l'_y m'_y}(\widehat{y}). \end{aligned} \tag{B.121}$$

Using Eq. (B.72) and considering that

$$\begin{aligned} & \int d\widehat{x} Y_{l_x m_x}(\widehat{x})^* Y_{\lambda M_\lambda}(\widehat{x}) Y_{l'_x m'_x}(\widehat{x}) \\ & \quad = (-1)^{m_x} \frac{\hat{l_x}\hat{\lambda}\hat{l'_x}}{\sqrt{4\pi}} \begin{pmatrix} l_x & \lambda & l'_x \\ 0 & 0 & 0 \end{pmatrix} \begin{pmatrix} l_x & \lambda & l'_x \\ -m_x & M_\lambda & m'_x \end{pmatrix}, \end{aligned} \tag{B.122}$$

the term in x can be written as

$$\begin{aligned} Q_x = & \sqrt{\frac{5}{4\pi}} \sum_{\beta\beta'} \sum_{ii'} C_{n_0}^{i\beta j_0} C_{n_0}^{i'\beta' j_0} \delta_{l_y l'_y} \delta_{S_x S'_x} \hat{l_x} \hat{l'_x} \begin{pmatrix} l_x & 2 & l'_x \\ 0 & 0 & 0 \end{pmatrix} C_x \\ & \times \int\int (\sin\alpha)^2 (\cos\alpha)^2 \, d\alpha \; d\rho \; \varphi_K^{l_x l_y}(\alpha) U_{i\beta}(\rho) x^2 U_{i'\beta'}(\rho) \varphi_{K'}^{l'_x l'_y}(\alpha), \end{aligned} \tag{B.123}$$

where C_x contains the summation over all projections,

$$\begin{aligned} C_x = & \sum_{\nu\nu'\iota} \langle j_{ab}\nu I_k \iota | j\mu\rangle \langle j'_{ab}\nu' I \iota | j'\mu'\rangle \sum_{m_l m'_l \sigma} \langle l m_l S_x \sigma | j_{ab}\nu\rangle \langle l' m'_l S_x \sigma | j'_{ab}\nu'\rangle \\ & \times \sum_{m_x m'_x m_y} \langle l_x m_x l_y m_y | l m_l\rangle \langle l'_x m'_x l_y m_y | l' m'_l\rangle (-1)^{m_x} \begin{pmatrix} l_x & 2 & l'_x \\ -m_x & M_\lambda & m'_x \end{pmatrix}. \end{aligned} \tag{B.124}$$

Equation (B.124) can be reduced to Racah coefficients (see Eq. (B.94) and the preceding derivation), leading to

$$C_x = (-1)^{j_0}\hat{j}_0^2 \begin{pmatrix} 2 & j_0 & j_0 \\ 0 & j_0 & -j_0 \end{pmatrix} \hat{l}\hat{l}'\hat{j}_{ab}\hat{j}'_{ab}(-1)^{l_y+l_x+l'_x+S_x-j_{ab}+j'_{ab}-I+l+l'} \\ \times W(ll'l_xl'_x;2l_y)W(j_{ab}j'_{ab}ll';2S_x)W(j_0j_0j_{ab}j'_{ab};2I). \tag{B.125}$$

Inserting Eq. (B.125) into Eq. (B.123) gives

$$Q_x = \sqrt{\frac{5}{4\pi}}\hat{j}_0^2 \begin{pmatrix} 2 & j_0 & j_0 \\ 0 & j_0 & -j_0 \end{pmatrix} \sum_{\beta\beta'}\sum_{ii'} C_{n_0}^{i\beta j_0}C_{n_0}^{i'\beta' j_0} \\ \times \delta_{l_yl'_y}\delta_{S_xS'_x}\hat{l}_x\hat{l}'_x\hat{l}\hat{l}'\hat{j}_{ab}\hat{j}'_{ab}(-1)^{l_y+l_x+l'_x+S_x-j_{ab}+j'_{ab}-I+l+l'+j_0} \\ \times \begin{pmatrix} l_x & 2 & l'_x \\ 0 & 0 & 0 \end{pmatrix} W(ll'l_xl'_x;2l_y)W(j_{ab}j'_{ab}ll';2S_x)W(j_0j_0j_{ab}j'_{ab};2I) \\ \times \int\int (\sin\alpha)^2(\cos\alpha)^2\, d\alpha\; d\rho\; \varphi_K^{l_xl_y}(\alpha)U_{i\beta}(\rho)x^2U_{i'\beta'}(\rho)\varphi_{K'}^{l'_xl'_y}(\alpha). \tag{B.126}$$

Following a similar derivation for Q_y, the second term in Eq. (B.118) provides

$$Q_y = \sqrt{\frac{5}{4\pi}}\hat{j}_0^2 \begin{pmatrix} 2 & j_0 & j_0 \\ 0 & j_0 & -j_0 \end{pmatrix} \sum_{\beta\beta'}\sum_{ii'} C_{n_0}^{i\beta j_0}C_{n_0}^{i'\beta' j_0} \\ \times \delta_{l_xl'_x}\delta_{S_xS'_x}\hat{l}_y\hat{l}'_y\hat{l}\hat{l}'\hat{j}_{ab}\hat{j}'_{ab}(-1)^{l_x+l_y+l'_y+S_x-j_{ab}+j'_{ab}-I+j_0} \\ \times \begin{pmatrix} l_y & 2 & l'_y \\ 0 & 0 & 0 \end{pmatrix} W(ll'l_yl'_y;2l_x)W(j_{ab}j'_{ab}ll';2S_x)W(j_0j_0j_{ab}j'_{ab};2I) \\ \times \int\int (\sin\alpha)^2(\cos\alpha)^2\, d\alpha\; d\rho\; \varphi_K^{l_xl_y}(\alpha)U_{i\beta}(\rho)y^2U_{i'\beta'}(\rho)\varphi_{K'}^{l'_xl'_y}(\alpha). \tag{B.127}$$

These expressions enable the computation of the quadrupole moment for a system comprising two identical charged particles.

B.5 Magnetic transitions

The magnetic multipole operarator can be expressed as a sum of two terms: the orbital and spin parts. Following the notation of Brink and Satchler [82], this operator in the preferred Jacobi set k for a system comprising three particles is

$$\widehat{M}_{\lambda M_\lambda}(\boldsymbol{x}_k, \boldsymbol{y}_k) = \frac{e\hbar}{2mc}\sqrt{4\pi\lambda} \times \sum_{q=1}^{3} r_q^{\lambda-1} \left[g_s \left(Y_{\lambda-1} s \right) + \frac{2g_l}{\lambda+1} \left(Y_{\lambda-1} l \right) \right]^{(q)}_{(\lambda-1,1)\lambda,M_\lambda} \tag{B.128}$$

where l and s are the orbital angular momentum and spin of each particle. The two separated terms are

$$\widehat{M}^{\text{orb}}_{\lambda M_\lambda}(\boldsymbol{x}_k, \boldsymbol{y}_k) = \frac{e\hbar}{2mc}\sqrt{4\pi\lambda} \sum_{q=1}^{3} r_q^{\lambda-1} \frac{2g_l^{(q)}}{\lambda+1} \left[Y_{\lambda-1} l \right]^{(q)}_{(\lambda-1,1)\lambda,M_\lambda} , \tag{B.129}$$

$$\widehat{M}^{\text{spin}}_{\lambda M_\lambda}(\boldsymbol{x}_k, \boldsymbol{y}_k) = \frac{e\hbar}{2mc}\sqrt{4\pi\lambda} \sum_{q=1}^{3} r_q^{\lambda-1} g_s^{(q)} \left[Y_{\lambda-1} s \right]^{(q)}_{(\lambda-1,1)\lambda,M_\lambda} . \tag{B.130}$$

Here g_l and g_s are the orbital and spin g factors, and $[Y_{\lambda-1} j]_{(\lambda-1,1)\lambda,M_\lambda}$ is a tensorial product of order 1,

$$\left[Y_{\lambda-1} j \right]_{(\lambda-1,1)\lambda,M_\lambda} \equiv \sum_{\eta\xi} Y_{(\lambda-1)\eta} \widehat{j}_\xi \langle (\lambda-1)\eta 1\xi | \lambda M_\lambda \rangle. \tag{B.131}$$

Using 3-j symbols, this product can be written as

$$\left[Y_{\lambda-1} j \right]_{(\lambda-1,1)\lambda,M_\lambda} = \sum_{\eta\xi} Y_{(\lambda-1)\eta} \widehat{j}_\xi (-1)^{\lambda+M_\lambda} \times \hat{\lambda} \begin{pmatrix} \lambda-1 & 1 & \lambda \\ \eta & \xi & -M_\lambda \end{pmatrix}, \tag{B.132}$$

which is equivalent to the tensorial product definiton in Ref. [82], considering that λ is an integer. Then, the computation of magnetic transitions requires the definition of the spherical components ξ ($\xi = -1, 0, 1$) of the angular momentum $\widehat{j}_\xi$ acting on its eigenstates,

$$\widehat{j}_\xi |jm\rangle = \sum_{j'm'} |j'm'\rangle \langle j'm' | \widehat{j}_\xi | jm \rangle. \tag{B.133}$$

Using the Wigner-Eckart theorem (B.81),

$$\widehat{j}_\xi|jm\rangle = \sum_{j'm'} |j'm'\rangle(-1)^2\langle j'm'|jm1\xi\rangle\langle j'||\widehat{j}||j\rangle. \tag{B.134}$$

The reduced matrix element of the total angular momentum, according to Brink and Satchler, is

$$\langle j'||\widehat{j}||j\rangle = \delta_{jj'}\sqrt{j(j+1)}. \tag{B.135}$$

Then, transforming the Clebsh-Gordan coefficients into 3-j symbols,

$$\widehat{j}_\xi|jm\rangle = \sum_{m'} |jm'\rangle(-1)^{j-1+m'}\sqrt{(2j+1)j(j+1)}\begin{pmatrix} j & 1 & j \\ m & \xi & -m' \end{pmatrix}. \tag{B.136}$$

Note that Eq. (B.129) involves the angular momentum of the particle q. This can be expressed, in a three-body system, as a function of l_{y_q} by

$$\widehat{l}_q = \frac{M_T - m_q}{M_T}\widehat{l}_{y_q}. \tag{B.137}$$

Finally, $\boldsymbol{r}_q$ is the position of particle q, which in the Jacobi-q set is given by Eq. (B.80). As a consequence, the computation of magnetic operator matrix elements in the preferred Jacobi system k requires the transformations between Jacobi sets described in section B.2 and already employed for electric transitions.

The orbital part of the magnetic operator can be expressed as a function of $\boldsymbol{y}_q$ and l_{y_q} as

$$\begin{aligned}\widehat{M}^{orb}_{\lambda M_\lambda} = \frac{e\hbar}{2mc}\sqrt{4\pi\lambda}\sum_{q=1}^{3}\left(\frac{M_T - m_q}{M_T}\right)^{\lambda}\left(\frac{m}{a_{y_q}}\right)^{\frac{\lambda-1}{2}} \\ \times\, y_q^{\lambda-1}\frac{2g_l^{(q)}}{\lambda+1}\left[Y_{\lambda-1}l_y\right]^{(q)}_{(\lambda-1,1)\lambda,M_\lambda},\end{aligned} \tag{B.138}$$

so its matrix element between states of good total angular momentum j and projection μ is

$$\langle nj\mu|\widehat{M}^{orb}_{\lambda M_\lambda}|n'j'\mu'\rangle = \frac{e\hbar}{2mc}\frac{\sqrt{4\pi\lambda}}{\lambda+1}\sum_{q=1}^{3}\left(\frac{M_T-m_q}{M_T}\right)^{\lambda}\left(\frac{m}{a_{y_q}}\right)^{\frac{\lambda-1}{2}} 2g_l^{(q)} \times \langle nj\mu|y_q^{\lambda-1}\left[Y_{\lambda-1}l_y\right]^{(q)}_{(\lambda-1,1)\lambda,M_\lambda}|n'j'\mu'\rangle. \tag{B.139}$$

In order to compute these matrix elements, the system states $|nj\mu\rangle$ can be rotated to the Jacobi-q set following the same derivation presented for electric transitions. For simplicity, indexes and coefficients regarding these transformation will be omitted, i.e., the case of a particle k in the preferred Jacobi-k set will be shown. Using Eq. (B.132), the previous matrix element is

$$\langle nj\mu|y^{\lambda-1}\left[Y_{\lambda-1}l_y\right]_{(\lambda-1,1)\lambda,M_\lambda}|n'j'\mu'\rangle = \sum_{\eta\xi}(-1)^{\lambda+M_\lambda}\hat{\lambda}\begin{pmatrix}\lambda-1 & 1 & \lambda\\ \eta & \xi & -M_\lambda\end{pmatrix} \times \langle nj\mu|y^{\lambda-1}Y_{(\lambda-1)\eta}\widehat{l}_{y_\xi}|n'j'\mu'\rangle. \tag{B.140}$$

Expanding the states explicitly,

$$\begin{aligned}
&\langle nj\mu|y^{\lambda-1}\left[Y_{\lambda-1}l_y\right]_{(\lambda-1,1)\lambda,M_\lambda}|n'j'\mu'\rangle\\
&=\sum_{\eta\xi}(-1)^{\lambda+M_\lambda}\hat{\lambda}\begin{pmatrix}\lambda-1 & 1 & \lambda\\ \eta & \xi & -M_\lambda\end{pmatrix}\\
&\times\sum_{\beta\beta'}\sum_{ii'}C_n^{i\beta j}C_{n'}^{i'\beta'j'}\sum_{\nu\nu'}\sum_{\iota}\langle j_{ab}\nu I\iota|nj\mu\rangle\langle j'_{ab}\nu' I\iota|j'\mu'\rangle\\
&\times\sum_{m_lm'_l}\sum_{\sigma}\delta_{S_xS'_x}\langle lm_lS_x\sigma|j_{ab}\nu\rangle\langle l'm'_lS_x\sigma|j'_{ab}\nu'\rangle\\
&\times\sum_{m_ym'_y}\sum_{m_x}\delta_{l_xl'_x}\langle l_xm_xl_ym_y|lm_l\rangle\langle l_xm_xl'_ym'_y|l'm'_l\rangle\\
&\times\langle l_ym_y|Y_{(\lambda-1)\eta}\widehat{l}_{y_\xi}|l'_ym'_y\rangle\\
&\times\int\int(\sin\alpha)^2(\cos\alpha)^2d\alpha d\rho U_{i\beta}(\rho)\varphi_K^{l_xl_y}(\alpha)y^{\lambda-1}U_{i'\beta'}(\rho)\varphi_{K'}^{l_xl'_y}(\alpha),
\end{aligned}$$

and using Eq. (B.136),

$$
\begin{aligned}
&\langle nj\mu|y^{\lambda-1}\left[Y_{\lambda-1}l_y\right]_{(\lambda-1,1)\lambda,M_\lambda}|n'j'\mu'\rangle \\
&=\sum_{\eta\xi}(-1)^{\lambda+M_\lambda}\hat{\lambda}\begin{pmatrix}\lambda-1 & 1 & \lambda\\ \eta & \xi & -M_\lambda\end{pmatrix} \\
&\times\sum_{\beta\beta'}\sum_{ii'}C_n^{i\beta j}C_{n'}^{i'\beta'j'}\sum_{\nu\nu'}\sum_{\iota}\langle j_{ab}\nu I\iota|nj\mu\rangle\langle j'_{ab}\nu' I\iota|j'\mu'\rangle \\
&\times\sum_{m_l m'_l}\sum_{\sigma}\delta_{S_xS'_x}\langle lm_lS_x\sigma|j_{ab}\nu\rangle\langle l'm'_lS_x\sigma|j'_{ab}\nu'\rangle \\
&\times\sum_{m_ym'_y}\sum_{m_x}\delta_{l_xl'_x}\langle l_xm_xl_ym_y|lm_l\rangle\langle l_xm_xl'_ym'_y|l'm'_l\rangle \\
&\times\sum_{m'}(-1)^{l'_y-1+m'}\sqrt{(2l'_y+1)l'_y(l'_y+1)}\begin{pmatrix}l'_y & 1 & l'_y\\ m'_y & \xi & -m'\end{pmatrix}\langle l_ym_y|Y_{(\lambda-1)\eta}|l'_ym'\rangle \\
&\times\int\int(\sin\alpha)^2(\cos\alpha)^2d\alpha d\rho U_{i\beta}(\rho)\varphi_K^{l_xl_y}(\alpha)y^{\lambda-1}U_{i'\beta'}(\rho)\varphi_{K'}^{l_xl'_y}(\alpha).
\end{aligned}
$$

Using now relation (B.88), $\langle l_ym_y|Y_{(\lambda-1)\eta}|l'_ym'\rangle$ can be expanded leading to

$$
\begin{aligned}
&\langle nj\mu|y^{\lambda-1}\left[Y_{\lambda-1}l_y\right]_{(\lambda-1,1)\lambda,M_\lambda}|n'j'\mu'\rangle \\
&=\sum_{\eta\xi}(-1)^{\lambda+M_\lambda}\hat{\lambda}\begin{pmatrix}\lambda-1 & 1 & \lambda\\ \eta & \xi & -M_\lambda\end{pmatrix} \\
&\times\sum_{\beta\beta'}\sum_{ii'}C_n^{i\beta j}C_{n'}^{i'\beta'j'}\sum_{\nu\nu'}\sum_{\iota}\langle j_{ab}\nu I\iota|nj\mu\rangle\langle j'_{ab}\nu' I\iota|j'\mu'\rangle \\
&\times\sum_{m_l m'_l}\sum_{\sigma}\delta_{S_xS'_x}\langle lm_lS_x\sigma|j_{ab}\nu\rangle\langle l'm'_lS_x\sigma|j'_{ab}\nu'\rangle \\
&\times\sum_{m_ym'_y}\sum_{m_x}\delta_{l_xl'_x}\langle l_xm_xl_ym_y|lm_l\rangle\langle l_xm_xl'_ym'_y|l'm'_l\rangle \\
&\times\sum_{m'}(-1)^{l'_y-1+m'+m_y}\sqrt{(2l'_y+1)l'_y(l'_y+1)}\frac{\hat{l}_y\hat{l}'_y(\hat{\lambda-1})}{\sqrt{4\pi}} \\
&\times\begin{pmatrix}l'_y & 1 & l'_y\\ m'_y & \xi & -m'\end{pmatrix}\begin{pmatrix}l_y & \lambda-1 & l'_y\\ -m_y & \eta & m'\end{pmatrix}\begin{pmatrix}l_y & \lambda-1 & l'_y\\ 0 & 0 & 0\end{pmatrix} \\
&\times\int\int(\sin\alpha)^2(\cos\alpha)^2d\alpha d\rho U_{i\beta}(\rho)\varphi_K^{l_xl_y}(\alpha)y^{\lambda-1}U_{i'\beta'}(\rho)\varphi_{K'}^{l_xl'_y}(\alpha).
\end{aligned}
$$

Reorganizing,

$$\begin{aligned}
&\langle njm|y^{\lambda-1}\left[Y_{\lambda-1}l_y\right]_{(\lambda-1,1)\lambda,M_\lambda}|n'j'm'\rangle \qquad \text{(B.141)}\\
&=\sum_{\beta\beta'}\sum_{ii'}C_n^{i\beta j}C_{n'}^{i'\beta'j'}\sqrt{(2l'_y+1)l'_y(l'_y+1)}\frac{\hat{l}_y\hat{l}'_y(\hat{\lambda-1})}{\sqrt{4\pi}}\begin{pmatrix} l_y & \lambda-1 & l'_y\\ 0 & 0 & 0\end{pmatrix}\\
&\times\delta_{S_xS'_x}\delta_{l_xl'_x}\int\int(\sin\alpha)^2(\cos\alpha)^2d\alpha d\rho U_{i\beta}(\rho)\varphi_K^{l_xl_y}(\alpha)y^{\lambda-1}U_{i'\beta'}(\rho)\varphi_{K'}^{l_xl'_y}(\alpha)\ \Delta,
\end{aligned}$$

where

$$\begin{aligned}
\Delta&=\sum_{\eta\xi}(-1)^{\lambda+M_\lambda}\hat{\lambda}\begin{pmatrix}\lambda-1 & 1 & \lambda\\ \eta & \xi & -M_\lambda\end{pmatrix}\sum_{\nu\nu'}\sum_{\iota}\langle j_{ab}\nu I\iota|j\mu\rangle\langle j'_{ab}\nu' I\iota|j'\mu'\rangle\\
&\times\sum_{m_lm'_l}\sum_{\sigma}\langle lm_lS_x\sigma|j_{ab}\nu\rangle\langle l'm'_lS_x\sigma|j'_{ab}\nu'\rangle\\
&\times\sum_{m_ym'_y}\sum_{m_x}\langle l_xm_xl_ym_y|lm_l\rangle\langle l_xm_xl'_ym'_y|l'm'_l\rangle \qquad \text{(B.142)}\\
&\times\sum_{m'}(-1)^{l'_y-1+m'+m_y}\begin{pmatrix}l'_y & 1 & l'_y\\ m'_y & \xi & -m'\end{pmatrix}\begin{pmatrix}l_y & \lambda-1 & l'_y\\ -m_y & \eta & m'\end{pmatrix}.
\end{aligned}$$

Using expression (B.91) to relate the Clebsh-Gordan coefficients with 3-j symbols, the factor Δ can be reduced following a derivation similar to that presented for electric transitions. This leads to

$$\begin{aligned}
\Delta&=(-1)^{-j'+l_y+l-2S_x+l'+2j'_{ab}+2j_{ab}-2I-\mu}\\
&\times\hat{\lambda}\hat{j}\hat{j}'\hat{j}_{ab}\hat{j}'_{ab}\hat{l}\hat{l}'\begin{pmatrix}j & \lambda & j'\\ -\mu & M_\lambda & \mu'\end{pmatrix} \qquad \text{(B.143)}\\
&\times W(l'_y1l_y(\lambda-1);l'_y\lambda)W(ll_x\lambda l'_y;l_yl')W(\lambda l'j_{ab}S_x;lj'_{ab})W(\lambda j'_{ab}jI;j_{ab}j').
\end{aligned}$$

Inserting this in Eq. (B.141) and computing the reduced matrix element,

$$\begin{aligned}
&\langle j||y^{\lambda-1}\left[Y_{\lambda-1}l_y\right]_{(\lambda-1,1)\lambda}||j'\rangle \qquad \text{(B.144)}\\
&=(-1)^{-j+\lambda-\mu}\hat{j}^{-1}\begin{pmatrix}j' & \lambda & j\\ \mu' & M_\lambda & -\mu\end{pmatrix}^{-1}\langle j\mu|y^{\lambda-1}\left[Y_{\lambda-1}l_y\right]_{(\lambda-1,1)\lambda,M_\lambda}|j'\mu'\rangle\\
&=(-1)^{\lambda-\mu+j'+\lambda}\hat{j}^{-1}\begin{pmatrix}j & \lambda & j'\\ -\mu & M_\lambda & \mu'\end{pmatrix}^{-1}\langle j\mu|y^{\lambda-1}\left[Y_{\lambda-1}l_y\right]_{(\lambda-1,1)\lambda,M_\lambda}|j'\mu'\rangle.
\end{aligned}$$

Then, the orbital part of the magnetic operator matrix element, with all its constants, is given by

$$\begin{aligned}
\langle nj||\widehat{M}^{orb}_{\lambda}||n'j'\rangle &= \frac{e\hbar}{2mc}\left(\frac{M_T-m_q}{M_T}\right)^{\lambda}\frac{\sqrt{\lambda}}{\lambda+1}(\lambda\hat{-}1)\hat{\lambda}\hat{j}'\left(\frac{m}{a_y}\right)^{\frac{\lambda-1}{2}}2g_l \\
&\times\sum_{\beta\beta'}\sum_{ii'}C^{i\beta j}_{n}C^{i'\beta'j'}_{n'}\sqrt{l'_y(l'_y+1)}\hat{l}_y\hat{l}'^2_y\hat{j}_{ab}\hat{j}'_{ab}\hat{l}\hat{l}'\delta_{S_xS'_x}\delta_{l_xl'_x}\begin{pmatrix} l_y & \lambda-1 & l'_y \\ 0 & 0 & 0\end{pmatrix} \\
&\times(-1)^{2j+l_y+l-2S_x+l'+2j'_{ab}+2j_{ab}-2I} \qquad \text{(B.145)} \\
&\times W(l'_y1l_y(\lambda-1);l'_y\lambda)W(ll_x\lambda l'_y;l_yl')W(\lambda l'j_{ab}S_x;lj'_{ab})W(\lambda j'_{ab}jI;j_{ab}j') \\
&\times\int\int(\sin\alpha)^2(\cos\alpha)^2d\alpha d\rho U_{i\beta}(\rho)\varphi_K^{l_xl_y}(\alpha)y^{\lambda-1}U_{i'\beta}(\rho)\varphi_{K'}^{l_xl'_y}(\alpha).
\end{aligned}$$

Reorganizing the Racah coefficients and phase factors, the previous expression leads to

$$\begin{aligned}
\langle nj||\widehat{M}^{orb}_{\lambda}||n'j'\rangle &= \frac{e\hbar}{2mc}\left(\frac{M_T-m_k}{M_T}\right)^{\lambda}\frac{\sqrt{\lambda}}{\lambda+1}(\lambda\hat{-}1)\hat{\lambda}\hat{j}'\left(\frac{m}{a_y}\right)^{\frac{\lambda-1}{2}}2g_l \\
&\times\sum_{\beta\beta'}\sum_{ii'}C^{i\beta j}_{n}C^{i'\beta'j'}_{n'}\sqrt{l'_y(l'_y+1)}\hat{l}_y\hat{l}'^2_y\hat{j}_{ab}\hat{j}'_{ab}\hat{l}\hat{l}'\delta_{S_xS'_x}\delta_{l_xl'_x}\begin{pmatrix} l_y & \lambda-1 & l'_y \\ 0 & 0 & 0\end{pmatrix} \\
&\times(-1)^{2j-j'+l_y-l_y-S_x+j'_{ab}+j_{ab}-I+l_x+\lambda} \qquad \text{(B.146)} \\
&\times W(l_yl'_y(\lambda-1)1;\lambda l'_y)W(ll'l_yl'_y;\lambda l_x)W(ll'j_{ab}j'_{ab};\lambda S_x)W(j_{ab}j'_{ab}jj';\lambda I) \\
&\times\int\int(\sin\alpha)^2(\cos\alpha)^2d\alpha d\rho U_{i\beta}(\rho)\varphi_K^{l_xl_y}(\alpha)y^{\lambda-1}U_{i'\beta}(\rho)\varphi_{K'}^{l_xl'_y}(\alpha).
\end{aligned}$$

This corresponds to the contribution to the orbital part of a single particle k in the Jacobi-k set. Introducing all three particles, the final expression can be written as

$$\begin{aligned}
\langle nj||\widehat{M}^{\rm orb}_{\lambda}||n'j'\rangle &= \frac{e\hbar}{2mc}\frac{\sqrt{\lambda}}{\lambda+1}(\lambda\hat{-}1)\hat{\lambda}\hat{j}'(-1)^{\lambda}\sum_{q=1}^{3}\left(\frac{M_T-m_q}{M_T}\right)^{\lambda}\left(\frac{m}{a_{y_q}}\right)^{\frac{\lambda-1}{2}}2g_l^{(q)} \\
&\times\sum_{\beta\beta'}\sum_{\beta_q\beta'_q}N_{\beta\beta_q}N_{\beta\beta'_q}\delta_{S_{x_q}S'_{x_q}}\delta_{l_{x_q}l'_{x_q}}\times(-1)^{2j-j'+l'_{y_q}-l_{y_q}+l_{x_q}-S_{x_q}+j_{ab_q}+j'_{ab_q}-I_q} \\
&\times\sqrt{l'_{y_q}\left(l'_{y_q}+1\right)}\hat{l}_{y_q}\hat{l}'^2_{y_q}\hat{j}_{ab_q}\hat{j}'_{ab_q}\hat{l}_q\hat{l}'_q\begin{pmatrix} l_{y_q} & \lambda-1 & l'_{y_q} \\ 0 & 0 & 0\end{pmatrix}W(l_{y_q}l'_{y_q}(\lambda-1)1;\lambda l'_{y_q}) \\
&\times W(l_ql'_ql_{y_q}l'_{y_q};\lambda l_{x_q})W(l_ql'_qj_{ab_q}j'_{ab_q};\lambda S_{x_q})W(j_{ab_q}j'_{ab_q}jj';\lambda I_q)\sum_{ii'}C^{i\beta j}_{n}C^{i'\beta'j'}_{n} \\
&\times\int\int d\alpha d\rho(\sin\alpha)^2(\cos\alpha)^2U_{i\beta}(\rho)\varphi_{K_q}^{l_{x_q}l_{y_q}}(\alpha)y^{\lambda-1}U_{i'\beta'}(\rho)\varphi_{K'_q}^{l'_{x_q}l'_{y_q}}(\alpha). \qquad \text{(B.147)}
\end{aligned}$$

The spin part of the magnetic operator can be expressed as a function of $\boldsymbol{y}_q$ and l_{y_q} as

$$\begin{aligned}\widehat{M}^{spin}_{\lambda M_\lambda} = \frac{e\hbar}{2mc}\sqrt{4\pi\lambda}\sum_{q=1}^{3}\left(\frac{M_T-m_q}{M_T}\right)^{\lambda-1}\left(\frac{m}{a_{y_q}}\right)^{\frac{\lambda-1}{2}} \\ \times\, y_q^{\lambda-1} 2g_s^{(q)}\,[Y_{\lambda-1}s]^{(q)}_{(\lambda-1,1)\lambda,M_\lambda}\,,\end{aligned} \tag{B.148}$$

so its matrix element between states of good total angular momentum j and projection μ is

$$\begin{aligned}\langle nj\mu|\widehat{M}^{spin}_{\lambda M_\lambda}|n'j'\mu'\rangle = \frac{e\hbar}{2mc}\sqrt{4\pi\lambda}\sum_{q=1}^{3}\left(\frac{M_T-m_q}{M_T}\right)^{\lambda-1}\left(\frac{m}{a_{y_q}}\right)^{\frac{\lambda-1}{2}} 2g_s^{(q)} \\ \times\,\langle nj\mu|y_q^{\lambda-1}\,[Y_{\lambda-1}s]^{(q)}_{(\lambda-1,1)\lambda,M_\lambda}\,|n'j'\mu'\rangle.\end{aligned} \tag{B.149}$$

The reduced matrix element for the spin part can be easily obtained following the same derivation presented for the orbital part. After working out the algebra, the final expression for the contribution of all three particles can be written as

$$\begin{aligned}&\langle nj||\widehat{M}^{\rm spin}_{\lambda}||n'j'\rangle = \frac{e\hbar}{2mc}\sqrt{\lambda}(\lambda\hat{-}1)\hat{\lambda}\hat{j}'\sum_{q=1}^{3}\left(\frac{M_T-m_q}{M_T}\right)^{\lambda-1}\left(\frac{m}{a_{y_q}}\right)^{\frac{\lambda-1}{2}} g_s^{(q)} \\ &\times\sum_{\beta\beta'}\sum_{\beta_q\beta'_q} N_{\beta\beta_q}N_{\beta\beta'_q}\delta_{S_{x_q}S'_{x_q}}\delta_{l_{x_q}l'_{x_q}}(-1)^{j+j'+l_{x_q}-S_{x_q}-j_{ab_q}+2I_q} \\ &\times\sqrt{I_q\,(I_q+1)}\hat{I}_q\hat{l}_{y_q}\hat{l}'_{y_q}\hat{j}_{ab_q}\hat{j}'_{ab_q}\hat{l}_q\hat{l}'_q\begin{pmatrix} l_{y_q} & \lambda-1 & l'_{y_q}\\ 0 & 0 & 0\end{pmatrix} W(l_q l'_q l_{y_q} l'_{y_q};(\lambda-1)l_{x_q}) \\ &\times W(l_q l'_q j_{ab_q} j'_{ab_q};(\lambda-1)S_{x_q})\begin{Bmatrix} j & j' & \lambda\\ j_{ab_q} & j'_{ab_q} & \lambda-1\\ I_q & I_q & 1\end{Bmatrix}\sum_{ii'} C_n^{i\beta j}C_n^{\prime i'\beta' j'} \\ &\times\int\int d\alpha d\rho(\sin\alpha)^2(\cos\alpha)^2 U_{i\beta}(\rho)\varphi_{K_q}^{l_{x_q}l_{y_q}}(\alpha)y^{\lambda-1}U_{i'\beta'}(\rho)\varphi_{K'_q}^{l'_{x_q}l'_{y_q}}(\alpha).\end{aligned} \tag{B.150}$$

Appendix C

Reaction rates

Considering a reaction going from N to M particles,

$$A_1 + A_2 + \cdots + A_N \longrightarrow B_1 + B_2 + \cdots + B_M,$$

the reaction rate per unit volume can be written accordingly to Refs. [104, 176] as

$$R(E) = \frac{2\pi}{\hbar} \frac{1}{g_1 g_2 \ldots g_N} \int \delta(E - E_f) |\langle \Psi | W | \Psi_f \rangle|^2 \frac{d^3\boldsymbol{p}_1}{(2\pi)^3} \ldots \frac{d^3\boldsymbol{p}_{M-1}}{(2\pi)^3}, \quad \text{(C.1)}$$

where E and E_f are the initial and final energies in the center of mass frame, Ψ and Ψ_f are the initial and final wave functions, and W is the interaction responsible for the reaction. Here, g_i are the spin degeneracies of the N initial particles, and $\boldsymbol{p}_j$ are the $M-1$ relative moments between the M particles in the final state.

C.1 Three-body radiative capture

The radiative capture reaction of three particles (abc), into a bound nucleus A of binding energy ε_B,

$$a + b + c \longrightarrow A + \gamma,$$

is a pure electromagnetic process. If the center of mass energy of the initial particles is denoted by ε, the reaction rate of such process is given by Eq. (C.1) as

$$R_{abc}(\varepsilon) = \frac{2\pi}{\hbar}\frac{1}{g_a g_b g_c}\int \delta(\varepsilon - \varepsilon_f)|\langle\Psi|W|\Psi_f\rangle|^2 \frac{d^3\boldsymbol{p}_\gamma}{(2\pi)^3}, \tag{C.2}$$

where $\boldsymbol{p}_\gamma$ is the momentum of the emitted photon, and

$$\varepsilon_f = \varepsilon_B + \varepsilon_\gamma. \tag{C.3}$$

Note that ε_B is negative (see for instance Fig. 3.1). Considering that $p_\gamma = \varepsilon_\gamma/\hbar c$ and $d^3\boldsymbol{p}_\gamma = p_\gamma^2 dp_\gamma d\Omega_\gamma$, the previous integral can be computed making use of Eq. (C.3), which leads to

$$R_{abc}(\varepsilon) = \frac{1}{\pi\hbar}\frac{1}{g_a g_b g_c}\frac{\varepsilon - \varepsilon_B}{(\hbar c)^3}|\langle\Psi|W|\Psi_f\rangle|^2. \tag{C.4}$$

Analogously, for the inverse photodissociation process,

$$A + \gamma \longrightarrow a + b + c,$$

the reaction rate given by Eq. (C.1) is

$$R_\gamma(\varepsilon_f) = \frac{2\pi}{\hbar}\frac{1}{2g_A}\int \delta(\varepsilon_f - \varepsilon)|\langle\Psi_f|W|\Psi\rangle^2 \frac{d^3\boldsymbol{p}_x}{(2\pi)^3}\frac{d^3\boldsymbol{p}_y}{(2\pi)^3}, \tag{C.5}$$

where $\boldsymbol{p}_x$ is the relative momentum between particles a and b, and $\boldsymbol{p}_y$ is that between the center of mass of the (a, b) subsystem and the particle c. Here, the energy in the final state satisfies

$$\varepsilon = T_x + T_y = \frac{\hbar^2 p_x^2}{2a_x} + \frac{\hbar^2 p_y^2}{2a_y}, \tag{C.6}$$

where T_x and T_y are the kinectic energy associated to x and y, respectively. From Eq. (C.4) it is possible to express $|\langle\Psi|W|\Psi_f\rangle|^2$ as a function of $R_{abc}(\varepsilon)$. Inserting this into Eq. (C.5) leads to

$$R_\gamma(\varepsilon_f) = 2\pi^2\frac{(\hbar c)^3}{\varepsilon_\gamma^2}\frac{g_a g_b g_c}{2g_A}\int \delta(\varepsilon_f - \varepsilon)R_{abc}(\varepsilon)\frac{d^3\boldsymbol{p}_x}{(2\pi)^3}\frac{d^3\boldsymbol{p}_y}{(2\pi)^3}. \tag{C.7}$$

Taking into account that

$$d^3\boldsymbol{p}_x = p_x^2 dp_x d\Omega_x = \left(\frac{2a_x T_x}{\hbar^2}\right)^{1/2}\frac{a_x}{\hbar^2}dT_x d\Omega_x, \tag{C.8}$$

$$d^3\boldsymbol{p}_y = p_y^2 dp_y d\Omega_y = \left(\frac{2a_y T_y}{\hbar^2}\right)^{1/2} \frac{a_y}{\hbar^2} dT_y d\Omega_y, \tag{C.9}$$

and $\delta(\varepsilon_f - \varepsilon) = \delta(\varepsilon - T_x - T_y)$, the integration of Eq. (C.7) over Ω_x, Ω_y and p_y (or T_y) provides

$$\begin{aligned} R_\gamma(\varepsilon_f) = \frac{1}{2\pi^2}\frac{(\hbar c)^3}{\varepsilon_\gamma^2}\frac{a_x}{\hbar^2}\frac{a_y}{\hbar^2}\left(\frac{2a_x}{\hbar^2}\right)^{1/2}\left(\frac{2a_y}{\hbar^2}\right)^{1/2} \\ \times \frac{g_a g_b g_c}{2g_A} R_{abc}(\varepsilon)\int_0^\varepsilon dT_x \sqrt{T_x\,(\varepsilon - T_x)}. \end{aligned} \tag{C.10}$$

The preceding integral can be computed analytically, leading to

$$R_\gamma(\varepsilon_\gamma) = \frac{c^3}{\hbar^3}\frac{(a_x a_y)^{3/2}}{8\pi}\left(\frac{\varepsilon}{\varepsilon_\gamma}\right)^2 \frac{g_a g_b g_c}{2g_A} R_{abc}(\varepsilon). \tag{C.11}$$

This reaction rate corresponds to a two-body capture process, which can be expressed as the relevant cross section times the relative velocity between the constituents, i.e. $R_\gamma(\varepsilon_\gamma) \equiv c\sigma_\gamma(\varepsilon_\gamma)$, where σ_γ is the photodissociation cross section of the nucleus A. Thus, the final expression for the three-body reaction rate is

$$R_{abc}(\varepsilon) = \frac{\hbar^3}{c^2}\frac{8\pi}{(a_x a_y)^{3/2}}\left(\frac{\varepsilon_\gamma}{\varepsilon}\right)^2 \frac{2g_A}{g_a g_b g_c}\sigma_\gamma(\varepsilon_\gamma). \tag{C.12}$$

The previous expression does not take into account the possibility of (abc) comprising identical particles. In that case, the reaction rate has to be multiplied by $\nu!$, where ν is the number of identical particles in the three-body system. The reaction rate at a given temperature T can be obtained from Eq. (C.12) averaging $R_{abc}(\varepsilon)$ with a Maxwell-Boltzmann distribution,

$$F_B(\varepsilon, T) = \frac{1}{2}\left(\frac{1}{k_B T}\right)^3 \varepsilon^2 e^{\frac{-\varepsilon}{k_B T}}. \tag{C.13}$$

This leads to

$$\begin{aligned} \langle R_{abc}(\varepsilon)\rangle(T) = \nu!\frac{\hbar^3}{c^2}\frac{8\pi}{(a_x a_y)^{3/2}}\frac{g_A}{g_a g_b g_c}\frac{1}{(k_B T)^3} e^{\frac{|\varepsilon_B|}{k_B T}} \\ \times \int_{|\varepsilon_B|}^\infty \varepsilon_\gamma^2\ \sigma_\gamma(\varepsilon_\gamma) e^{\frac{-\varepsilon_\gamma}{k_B T}} d\varepsilon_\gamma. \end{aligned} \tag{C.14}$$

Bibliography

[1] *Radioactive Nuclear Beam Facilities* (Report from the Nuclear Physics European Collaboration Committee [NuPECC], Europe, 2000).

[2] M. G. Mayer, Phys. Rev. **75**, 1969 (1949).

[3] E. H. S. Burhop, D. H. Davis, J. Sacton, and G. Schoronchoff, Nucl. Phys. A **132**, 625 (1969).

[4] D. J. Millener, J. W. Olness, E. K. Warburton, and S. S. Hanna, Phys. Rev. C **28**, 497 (1983).

[5] I. Tanihata *et al.*, Phys. Lett. B **160**, 380 (1985).

[6] E. Arnold *et al.*, Phys. Lett. B **281**, 16 (1992).

[7] K. Riisager, Rev. Mod. Phys. **66**, 1105 (1994).

[8] P. G. Hansen, A. S. Jensen, and B. Jonson, Annu. Rev. Nucl. Part. Sci. **45**, 591 (1995).

[9] B. M. Sherrill, Nucl. Phys. A **685**, 134 (2001).

[10] J. S. Al-Khalili, Lect. Notes Phys. **651**, 77 (2004).

[11] M. V. Zhukov, B. V. Danilin, D. V. Fedorov, J. M. Bang, I. J. Thompson, and J. S. Vaagen, Phys. Rep. **231**, 151 (1993).

[12] M. Cubero *et al.*, Phys. Rev. Lett. **109**, 262701 (2012).

[13] A. M. Moro and J. A. Lay, Phys. Rev. Lett. **109**, 232502 (2012).

[14] J. P. Fernández-García *et al.*, Phys. Rev. C **92**, 044608 (2015).

[15] T. Matsumoto, T. Kamizato, K. Ogata, Y. Iseri, E. Hiyama, M. Kamimura, and M. Yahiro, Phys. Rev. C **68**, 064607 (2003).

[16] M. Rodríguez-Gallardo, J. M. Arias, and J. Gómez-Camacho, Phys. Rev. C **69**, 034308 (2004).

[17] A. M. Moro, J. M. Arias, J. Gómez-Camacho, and F. Pérez-Bernal, Phys. Rev. C **80**, 054605 (2009).

[18] J. A. Lay, A. M. Moro, J. M. Arias, and J. Gómez-Camacho, Phys. Rev. C **82**, 024605 (2010).

[19] T. Matsumoto, E. Hiyama, M. Yahiro, K.Ogata, Y. Iseri, and M. Kamimura, Nucl. Phys. A **738**, 471 (2004).

[20] R. Y. Rasoanaivo and G. H. Rawitscher, Phys. Rev. C **39**, 1709 (1989).

[21] E. Nielsen, D. V. Fedorov, A. S. Jensen, and E. Garrido, Phys. Rep. **347**, 373 (2001).

[22] P. Descouvemont, C. Daniel, and D. Baye, Phys. Rev. C **67**, 044309 (2003).

[23] M. Rodríguez-Gallardo, J. M. Arias, J. Gómez-Camacho, A. M. Moro, I. J. Thompson, and J. A. Tostevin, Phys. Rev. C **72**, 024007 (2005).

[24] I. J. Thompson, B. V. Danilin, V. D. Efros, J. S. Vaagen, J. M. Bang, and M. V. Zhukov, Phys. Rev. C **61**, 024318 (2000).

[25] J. Casal, M. Rodríguez-Gallardo, and J. M. Arias, Phys. Rev. C **88**, 014327 (2013).

[26] J. A. Lay, A. M. Moro, J. M. Arias, and J. Gómez-Camacho, Phys. Rev. C **85**, 054618 (2012).

[27] R. de Diego, J. M. Arias, J. A. Lay, and A. M. Moro, Phys. Rev. C **89**, 064609 (2014).

[28] *Perspective of Nuclear Physics in Europe* (Nuclear Physics European Collaboration Committee [NuPECC] Long Range Plan, Europe, 2010).

[29] C. Iliadis, *Nuclear Physics of Stars*, 2$^{\text{nd}}$ ed. (Willey-VCH, Weinheim, 2015).

[30] A. Aprahamian, K. Langanke, and M. Wiescher, Prog. Part. Nucl. Phys. **54**, 535 (2005).

[31] F. Hoyle, Astrophys. J. Suppl. **1**, 121 (1954).

[32] K. Ogata, M. Kan, and M. Kamimura, Prog. Theor. Phys. **122**, 1055 (2009).

[33] C. Angulo *et al.*, Nucl. Phys. A **656**, 3 (1999).

[34] E. Garrido, R. de Diego, D. V. Fedorov, and A. S. Jensen, Eur. Phys. J. A **47**, 102 (2011).

[35] N. B. Nguyen, F. M. Nunes, I. J. Thompson, and E. F. Brown, Phys. Rev. Lett. **109**, 141101 (2012).

[36] S. Ishikawa, Phys. Rev. C **87**, 055804 (2013).

[37] K. Langanke and M. Wiescher, Rep. Prog. Phys. **64**, 1657 (2001).

[38] S. E. Woosley, J. R. Wilson, G. J. Mathews, R. D. Hoffman, and B. S. Meyer, Astrophys. J. **433**, 229 (1994).

[39] Y.-Z. Qian and S. E. Woosley, Astrophys. J. **471**, 331 (1996).

[40] K. Sumiyoshi, M. Terasawa, G. J. Mathews, T. Kajino, S. Yamada, and H. Suzuki, Astrophys. J. **562**, 880 (2001).

[41] J. M. Lattimer and D. N. Schramm, Astrophys. J. **192**, L145 (1974).

[42] A. Bartlett, J. Görres, G. J. Mathews, K. Otsuki, M. Wiescher, D. Frekers, A. Mengoni, and J. Tostevin, Phys. Rev. C **74**, 015802 (2006).

[43] T. Sasaki, K. T. Kajino, G. Mathews, K. Otsuki, and T. Nakamura, Astrophys. J. **634**, 1173 (2005).

[44] E. M. Burbidge, G. R. Burbidge, W. A. Fowler, and F. Hoyle, Rev. Mod. Phys. **29**, 547 (1957).

[45] H. Schatz *et al.*, Phys. Rep. **294**, 167 (1998).

[46] J. Görres and M. Wiescher and F. K. Thielemann, Phys. Rev. C **51**, 392 (1995).

[47] L. V. Grigorenko and M. V. Zhukov, Phys. Rev. C **72**, 015803 (2005).

[48] M. Arnould and K. Takahashi, Rep. Prog. Phys. **62**, 395 (1999).

[49] K. Sumiyoshi, H. Utsunomiya, S. Goko, and T. Kajino, Nucl. Phys. A **709**, 467 (2002).

[50] V. D. Efros, W. Balogh, H. Herndl, R. Hofinger, and H. Oberhummer, Z. Phys. A **355**, 101 (1996).

[51] I. J. Thompson, F. M. Nunes, and B. V. Danilin, Comput. Phys. Commun. **161**, 87 (2004).

[52] S. Quaglioni, C. Romero-Redondo, and P. Navrátil, Phys. Rev. C **88**, 034320 (2013).

[53] C. H. Dasso and A. Vitturi, Lect. Notes Phys. **652**, 157 (2004).

[54] R. de Diego, E. Garrido, D. V. Fedorov, and A. S. Jensen, Eur. Phys. Lett. **90**, 52001 (2010).

[55] E. P. Wigner and L. Eisenbud, Phys. Rev. **72**, 29 (1947).

[56] P. Descouvemont, E. Tursunov, and D. Baye, Nucl. Phys. A **765**, 370 (2006).

[57] N. Austern, Y. Iseri, M. Kamimura, M. Kawai, G. Rawitsher, and M. Yahiro, Phys. Rep. **154**, 125 (1987).

[58] O. I. Tolstikhin, V. N. Ostrovsky, and H. Nakamura, Phys. Rev. Lett **79**, 2026 (1997).

[59] A. U. Hazi and H. S. Taylor, Phys. Rev. A **1**, 1109 (1970).

[60] R. S. Mackintosh and S. G. Cooper, Nucl. Phys. A **589**, 377 (1995).

[61] S. G. Cooper and R. S. Mackintosh, Nucl. Phys. A **592**, 338 (1995).

[62] V. I. Kukulin, V. N. Pomerantsev, K. D. Razikov, V. T. Voronchev, and G. G. Ryzhikh, Nucl. Phys. A **586**, 151 (1995).

[63] J. M. Bang, J. J. Benayoun, C. Gignoux, and I. J. Thompson, Nucl. Phys. A **405**, 126 (1983).

[64] D. Baye, Phys. Rev. Lett **58**, 2738 (1987).

[65] E. Garrido, D. V. Fedorov, and A. S. Jensen, Nucl. Phys. A **617**, 153 (1996).

[66] M. Hesse, D. Baye, and J. M. Sparenberg, Phys. Lett. B **455**, 1 (1999).

[67] M. Yahiro, Y. Iseri, H. Kameyama, M. Kamimura, and M. Kawai, Prog. Theor. Phys. Suppl. **89**, 32 (1986).

[68] L. D. Faddeev, Sov. Phys. JETP **12**, 1014 (1961).

[69] E. O. Alt, P. Grassberger, and W. Sandhas, Nucl. Phys. B **2**, 167 (1967).

[70] A. Deltuva, A. M. Moro, E. Cravo, F. M. Nunes, and A. C. Fonseca, Phys. Rev. C **76**, 064602 (2007).

[71] I. Thompson and A. Barnett, J. Comput. Phys. **64**, 490 (1986).

[72] G. R. Satchler, *Direct Nuclear Reactions* (Clarendon Press, Oxford, 1983).

[73] I. J. Thompson, Comput. Phys. Rep. **7**, 167 (1988).

[74] J. S. Al-Khalili and J. A. Tostevin, in *Scattering*, edited by P. Pike and P. Sabatier (Academic Press, 2001).

[75] L. F. Canto and M. S. Hussein, *Scattering Theory of Molecules, Atoms and Nuclei* (World Scientific, Singapore, 2013).

[76] F. Pérez-Bernal, I. Martel, J. M. Arias, and J. Gómez-Camacho, Phys. Rev. A **63**, 052111 (2001).

[77] A. M. Moro, J. M. Arias, J. Gómez-Camacho, I. Martel, F. Pérez-Bernal, R. Crespo, and F. Nunes, Phys. Rev. C **65**, 011602(R) (2001).

[78] A. M. Moro, F. Pérez-Bernal, J. M. Arias, and J. Gómez-Camacho, Phys. Rev. C **73**, 044612 (2006).

[79] M. Rodríguez-Gallardo, J. M. Arias, J. Gómez-Camacho, R. C. Johnson, A. M. Moro, I. J. Thompson, and J. A. Tostevin, Phys. Rev. C **77**, 064609 (2008).

[80] S. Karataglidis, K. Amos, and B. G. Giraud, Phys. Rev. C **71**, 064601 (2005).

[81] J. Suhonen, in *From Nucleons to Nucleus*, Theoretical and Mathematical Physics (Springer Berlin Heidelberg, 2007) pp. 117–156.

[82] D. M. Brink and G. R. Satchler, *Angular Momentum* (Clarendon, Oxford, 1994).

[83] A. Bohr and B. R. Mottelson, *Nuclear Structure* (W. A. Benjamin, Inc., Reading (MA), 1969).

[84] J. Raynal and J. Revai, Nuovo Cim. **68A**, 612 (1970).

[85] C. Romero-Redondo, E. Garrido, D. V. Fedorov, and A. S. Jensen, Phys. Rev. C **77**, 054313 (2008).

[86] R. de Diego, E. Garrido, A. S. Jensen, and D. V. Fedorov, Phys. Rev. C **77**, 024001 (2008).

[87] O. Bohigas, A. M. Lanes, and J. Martorel, Phys. Rep. **51**, 267 (1979).

[88] E. Lipparini and S. Stringari, Phys. Rep. **175**, 103 (1989).

[89] M. Rodríguez-Gallardo and A. M. Moro, Int. J. Mod. Phys. E **20**, 947 (2011).

[90] A. Macías, F. Martín, A. Riera, and M. Yañez, Phys. Rev. A **36**, 4179 (1987).

[91] P. Descouvemont, E. Pinilla, and D. Baye, Prog. Theor. Phys. Suppl. **196**, 1 (2012).

[92] T. Bjerge and K. J. Broström, Nature **138**, 400 (1936).

[93] D. Tilley, C. Cheves, J. Godwin, G. Hale, H. Hofmann, J. Kelley, C. Sheu, and H. Weller, Nucl. Phys. A **708**, 3 (2002).

[94] B. V. Danilin, S. N. Ershov, and J. S. Vaagen, Phys. Rev. C **71**, 057301 (2005).

[95] M. Brodeur *et al.*, Phys. Rev. Lett. **108**, 052504 (2012).

[96] Y. C. Tang and D. R. Thompson, Phys. Rep. **47**, 167 (1978).

[97] V. D. Efros, W. Leidemann, and G. Orlandini, Phys. Lett. B **338**, 130 (1994).

[98] C. Romero-Redondo, S. Quaglioni, P. Navrátil, and G. Hupin, Phys. Rev. Lett. **113**, 032503 (2014).

[99] D. Gogny, P. Pires, and R. De Tourreil, Phys. Lett. B **32**, 591 (1970).

[100] J. Bang and C. Gignoux, Nucl. Phys. A **313**, 119 (1979).

[101] I. Angeli and K. P. Marinova, Atomic Data and Nuclear Data Tables **99**, 69 (2013).

[102] I. J. Thompson, Program `sturmxx` Available at http://fresco.org.uk/related.htm.

[103] J. P. Fernández-García *et al.*, Phys. Rev. Lett. **110**, 142701 (2013).

[104] R. de Diego, *Sistemas de tres cuerpos en el continuo y reacciones de interés astrofísico*, Ph.D. thesis, Instituto de Estructura de la Materia, CSIC (2010).

[105] T. Myo, K. Kato, S. Aoyama, and K. Ikeda, Phys. Rev. C **63**, 054313 (2001).

[106] D. Baye, P. Capel, P. Descouvemont, and Y. Suzuki, Phys. Rev. C **79**, 024607 (2009).

[107] T. Aumann *et al.*, Phys. Rev. C **59**, 1252 (1999).

[108] D. R. Tilley, J. H. Kelley, J. L. Godwin, D. J. Millener, J. E. Purcell, C. G. Sheu, and H. R. Weller, Nucl. Phys. A **745**, 155 (2004).

[109] I. Tanihata *et al.*, Phys. Lett. B **206**, 592 (1988).

[110] E. Liatard *et al.*, Europhys. Lett. **13**, 401 (1990).

[111] D. Sundholm and J. Olsen, Chem. Phys. Lett. **177**, 91 (1991).

[112] E. Garrido, D. V. Fedorov, and A. S. Jensen, Phys. Lett. B **684**, 132 (2010).

[113] Y. Hirayama *et al.*, Phys. Rev. C **91**, 024328 (2015).

[114] S. Ali and A. R. Bodmer, Nucl. Phys. **80**, 99 (1966).

[115] J. S. Al-Khalili and J. A. Tostevin, Phys. Rev. Lett **76**, 3903 (1996).

[116] P. Descouvemont, T. Druet, L. F. Canto, and M. S. Hussein, Phys. Rev. C **91**, 024606 (2015).

[117] C. W. Arnold, T. B. Clegg, C. Iliadis, H. J. Karwowski, G. C. Rich, J. R. Tompkins, and C. R. Howell, Phys. Rev. C **85**, 044605 (2012).

[118] E. Garrido, D. V. Fedorov, and A. S. Jensen, Nucl. Phys. A **733**, 85 (2004).

[119] K. Tanaka *et al.*, Phys. Rev. C **82**, 044309 (2010).

[120] F. Ajzenberg, Nucl. Phys. A **523**, 1 (1991).

[121] V. Guimarães *et al*, Phys. Rev. C **58**, 116 (1998).

[122] M. Chromik *et al.*, Phys. Rev. C **66**, 024313 (2002).

[123] F. Ajzenberg, Nucl. Phys. A **460**, 1 (1986).

[124] A. Ozawa *et al*, Nucl. Phys. A **693**, 32 (2001).

[125] W. Geithner *et al*, Phys. Rev. Lett. **101**, 252502 (2008).

[126] L. V. Grigorenko, Y. L. Parfenova, and M. V. Zhukov, Phys. Rev. C **71**, 051604 (2005).

[127] R. E. Warner *et al.*, Nucl. Phys. A **635**, 292 (1998).

[128] C. Forssén, N. B. Shul'gina, and M. V. Zhukov, Phys. Rev. C **67**, 045801 (2003).

[129] J. Casal, M. Rodríguez-Gallardo, J. M. Arias, and I. J. Thompson, Phys. Rev. C **90**, 044304 (2014).

[130] J. M. Blatt and V. F. Weisskopf, *Theoretical Nuclear Physics* (John Wiley and Sons, Inc., New York, 1966).

[131] J. Marganiec *et al.*, Acta. Phys. Pol. B **45**, 229 (2014).

[132] B. S. Meyer, G. J. Mathews, W. M. Howard, S. E. Woosley, and R. D. Hoffman, Astrophys. J. **399**, 656 (1992).

[133] B. S. Meyer, Annu. Rev. Astron. Astrophys. **32**, 153 (1994).

[134] S. E. Woosley and R. D. Hoffman, Astrophys. J. **395**, 202 (1992).

[135] H. Utsunomiya, Y. Yonezawa, H. Akimune, T. Yamagata, M. Ohta, M. Fujishiro, H. Toyokawa, and H. Ohgaki, Phys. Rev. C **63**, 018801 (2000).

[136] O. Burda, P. von Neumann-Cosel, A. Richter, C. Forssén, and B. A. Brown, Phys. Rev. C **82**, 015808 (2010).

[137] R. de Diego, E. Garrido, D. V. Fedorov, and A. S. Jensen, Eur. Phys. J. A **50**, 93 (2014).

[138] L. Grigorenko, K. Langanke, N. Shul'gina, and M. Zhukov, Phys. Lett. B **641**, 254 (2006).

[139] E. Garrido and R. de Diego, private communication (2015).

[140] M. Wiescher, J. Görres, and H. Schatz, J. Phys. G: Nucl. Part. Phys. **25**, R133 (1999).

[141] K. Alder and A. Winther, *Electromagnetic excitation: Theory of Coulom excitation with heavy ions* (North-Holland, Amsterdam, 1975).

[142] J. P. Fernández-García, *Análisis de los canales de ruptura de la reacción* $^{11}Li+^{208}Pb$ *a energías entorno a la barrera de Coulomb*, Ph.D. thesis, Universidad de Sevilla (2013).

[143] H. Oberhummer, W. Balogh, V. D. Efros, H. Herndl, and R. Hofinger, Few-body Systems Suppl. **8**, 317 (1995), open access at arXiv.

[144] T. Nakamura *et al.*, Phys. Rev. Lett **96**, 252502 (2006).

[145] S. Shimoura *et al.*, Nucl. Phys. A **348**, 29 (1995).

[146] M. Smith *et al.*, Phys. Rev. Lett **101**, 202501 (2008).

[147] S. Woosley and T. Janka, Nature Phys. **1**, 147 (2005).

[148] J. A. Lay, *Descripción de la estructura y reacciones de núcleos exóticos en una base de oscilador armónico transformado*, Ph.D. thesis, Universidad de Sevilla (2012).

[149] L. Acosta *et al.*, Phys. Rev. C **84**, 044604 (2011).

[150] L. Standyło *et al.*, Phys. Rev. C **87**, 064603 (2013).

[151] M. Rodríguez-Gallardo, J. M. Arias, J. Gómez-Camacho, A. M. Moro, I. J. Thompson, and J. A. Tostevin, Phys. Rev. C **80**, 051601(R) (2009).

[152] A. Lane and R. Thomas, Rev. Mod. Phys. **30**, 257 (1958).

[153] P. Descouvemont and D. Baye, Rep. Prog. Phys. **73**, 036301 (2010).

[154] R. J. Woolliscroft *et al.*, Phys. Rev. C **69**, 044612 (2004).

[155] N. Yu *et al.*, J. Phys. G: Nucl. Part. Phys. **37**, 075108 (2010).

[156] A. J. Koning and J. P. Delaroche, Nucl. Phys. A **713**, 231 (2003).

[157] A. R. Barnett and J. S. Lilley, Phys. Rev. C **9**, 2010 (1974).

[158] P. Descouvemont, T. Druet, L. F. Canto, and M. S. Hussein, J. Phys. Conf. Ser. **590**, 012008 (2015).

[159] E. F. Aguilera *et al.*, Phys. Rev. C **63**, 061603(R) (2001).

[160] A. M. Sánchez-Benítez *et al.*, Nucl. Phys. A **803**, 30 (2008).

[161] M. J. G. Borge *et al.*, JPS Conf. Proc. **6**, 020036 (2015).

[162] O. R. Kakuee *et al.*, Nucl. Phys. A **728**, 339 (2003).

[163] R. J. Woolliscroft *et al.*, Phys. Rev. C **68**, 014611 (2003).

[164] P. R. S. Gomes *et al.*, Phys. Rev. C **70**, 054605 (2004).

[165] S. Kailas, Reference Input Parameter Library (RIPL-2), available online at http://www-nds.iaea.org/RIPL-2/.

[166] U. Atzrott, P. Mohr, H. Abele, C. Hillenmayer, and G. Staudt, Phys. Rev. C **53**, 1336 (1996).

[167] A. Arazi *et al.*, private communication (2015).

[168] K. C. C. Pires *et al.*, Phys. Rev. C **83**, 064603 (2011).

[169] F. Ajzenberg, Nucl. Phys. A **506**, 1 (1990).

[170] M. Chernykh, H. Feldmeier, T. Neff, P. von Neumann-Cosel, and A. Richter, Phys. Rev. Lett. **98**, 032501 (2007).

[171] D. J. Marín-Lámbarri, R. Bijker, M. Freer, M. Gai, T. Kokalova, D. J. Parker, and C. Wheldon, Phys. Rev. Lett. **113**, 012502 (2014).

[172] R. Bijker and F. Iachello, Phys. Rev. C **61**, 067305 (2000).

[173] T. Akahori, Y. Funaki, and K. Yabana, Phys. Rev. C **92**, 022801 (2015).

[174] A. Dotter and B. Paxton, Astron. Astrophys. **507**, 1617 (2009).

[175] T. Suda, R. Hirschi, and M. Fujimoto, Astrophys. J. **741**, 61 (2011).

[176] S. Weinberg, *The Quantum Theory of Fields I* (Cambridge University Press, Cambridge, 1995).

Publications, contributions and other research activities

Publications

- Authors: **J. Casal**, M. Rodríguez-Gallardo and J. M. Arias
  Title: *Three-body nuclei and their astrophysical implications: the case of ^{6}He*
  Conference: La Rábida 2012. International Scientific Meeting on Nuclear Physics
  Reference: AIP Conference Proceedings **1541** (2013) 171.
  Proceeding

- Authors: **J. Casal**, M. Rodríguez-Gallardo and J. M. Arias
  Title: *Analytical transformed harmonic oscillator basis for three-body nuclei of astrophysical interest: Application to ^{6}He*
  Reference: Physical Review C **88** (2013) 014327.
  Article

- Authors: **J. Casal**, M. Rodríguez-Gallardo, J. M. Arias and I. J. Thompson
  Title: *Astrophysical reaction rate for ^{9}Be formation within a three-body approach*
  Reference: Physical Review C **90** (2014) 044304.
  Article

- Authors: **J. Casal**, M. Rodríguez-Gallardo and J. M. Arias
  Title: *^{9}Be elastic scattering on ^{208}Pb and ^{27}Al within a four-body reaction framework*

Reference: Physical Review C **92** (2015) 054611.
Article

- Authors: **J. Casal**, M. Rodríguez-Gallardo, J. M. Arias and J. Gómez-Camacho
  Title: *Determining astrophysical three-body radiative capture reaction rates from inclusive Coulomb breakup measurements*
  Reference: Physical Review Letters (2015) Submitted.
  Article

- Authors: **J. Casal**, M. Rodríguez-Gallardo and J. M. Arias
  Title: *Reactions induced by* ^{9}*Be in a four-body continuum-discretized coupled-channels framework*
  Conference: La Rábida 2015. International Scientific Meeting on Nuclear Physics
  Reference: Springer Proceedings in Physics (2015) Submitted.
  Proceeding

- Authors: **J. Casal**, M. Rodríguez-Gallardo and J. M. Arias
  Title: ^{9}*Be scattering within a four-body continuum-discretized coupled-channels framework*
  Conference: NN2015. International Conference on Nucleus-Nucleus Collisions
  Reference: Italian Physical Society, Conference Proceedings series (2015) Submitted.
  Proceeding

- Authors: A. Arazi *et al*, **J. Casal** *et al.*
  Title: *Quasielastic scattering of* ^{9}*Be on* ^{120}*Sn at the TANDAR laboratory*
  In preparation (2016).

- Authors: **J. Casal**, E. Garrido, M. Rodríguez-Gallardo, R. de Diego and J. M. Arias
  Title: *Radiative capture reaction for* ^{17}*Ne formation within a full three-body model*
  In preparation (2016).

Contributions to conferences

- Authors: **J. Casal**, M. Rodríguez-Gallardo and J. M. Arias
  Title: *Three-body nuclei and their astrophysical implications: the case of ^{6}He*
  Conference: International Scientific Meeting on Nuclear Physics (RABIDA12), "Basic concepts in Nuclear Physics: theory, experiments and applications"
  Place: La Rábida (Huelva), Spain
  Date: 9-13 September 2012, Poster

- Authors: **J. Casal**, M. Rodríguez-Gallardo and J. M. Arias
  Title: *Three-body nuclei and their astrophysical implications: the case of ^{6}He*
  Conference: VII Encuentros de Física Nuclear (EFN12)
  Place: La Rábida (Huelva), Spain
  Date: 14-16 September 2012, Poster

- Authors: **J. Casal**, M. Rodríguez-Gallardo and J. M. Arias
  Title: *Descripción de sistemas de tres cuerpos en una base analítica de oscilador armónico transformado y su aplicación en astrofísica*
  Conference: XXXIV Reunión Bienal de la Real Sociedad Española de Física, Simposio de Física Nuclear
  Place: Valencia, Spain
  Date: 15 July 2013, Talk

- Authors: **J. Casal**, M. Rodríguez-Gallardo, J. M. Arias and I. J. Thompson
  Title: *Description of three-body radiative capture reactions using an analytical transformed harmonic oscillator basis*
  Conference: Direct Reactions with Exotic Beams (DREB2014)
  Place: Darmstadt, Germany
  Date: 2 July 2014, Talk

- Authors: **J. Casal**, M. Rodríguez-Gallardo, J. M. Arias and I. J. Thompson
  Title: *Three-body radiative capture reactions and four-body CDCC calculations using the analytical THO method: Application to ^{9}Be*

Conference: VI CPAN Days
Place: Sevilla, Spain
Date: 20 October 2014, Talk

- Authors: **J. Casal**, M. Rodríguez-Gallardo, J. M. Arias
  Title: *Continuum treatment for weakly-bound systems*
  Conference: Complex Systems: from the Nanoscale to the Continuum (CS:N2C)
  Place: Münster, Germany
  Date: 10 February 2015, Talk

- Authors: **J. Casal**, M. Rodríguez-Gallardo, J. M. Arias
  Title: *Reactions induced by ^{9}Be in a four-body CDCC framework*
  Conference: International Scientific Meeting on Nuclear Physics (RABIDA15), "Basic concepts in Nuclear Physics: theory, experiments and applications"
  Place: La Rábida (Huelva), Spain
  Date: 1 June 2015, Talk

- Authors: **J. Casal**, M. Rodríguez-Gallardo, J. M. Arias
  Title: *^{9}Be scattering within a four-body CDCC framework*
  Conference: 12th International Conference on Nucleus-Nucleus collisions (NN2015)
  Place: Catania, Italy
  Date: 21-26 June 2015, Poster

Research stays

- Reacciones nucleares de interés astrofísico
  (Nuclear reactions of astrophysical interest)
  Lawrence Livermore National Laboratory (LLNL)
  Livermore, California, EEUU.
  Duration: 90 days
  Period: September 15 to December 13, 2013.
  Supervisor: I. J. Thompson, staff member, Nuclear Theory and Modeling Group.

- Tratamiento del continuo en sistemas de tres cuerpos de interés en Astrofísica Nuclear
  (Continuum treatment in three-body systems of interest in Nuclear Astrophysics)
  Université Libre de Bruxelles (ULB)
  Brussels, Belgium.
  Duration: 36 days
  Period: November 14 to December 19, 2014.
  Supervisor: P. Descouvemont, Director of FNTFM
  (Physique Nucléaire Théorique et Physique Mathématique)

Seminars

- "Astrophysical reaction rate for three-body systems using an analytical transformed harmonic oscillator basis", Dpto. FAMN, Universidad de Sevilla, April 10, 2014.
- "Three-body radiative capture reactions and four-body CDCC calculations using the analytical THO method: Application to ^{9}Be", Université Libre de Bruxelles (ULB), November 27, 2014.
- "Three-body systems in nuclear reactions and their astrophysical implications", Technische Universität (TU) Darmstadt, October 15, 2015.

Courses

- ISOLDE Nuclear Reactions and Nuclear Structure course, CERN, April 22-25, 2014.
- HPC (high performance computing) course, Universidad de Sevilla, Sevilla, Spain, October 21 to December 16, 2015.